A unified analytical approach for the acoustic conceptual design of fans of modern aero-engines

vorgelegt von
Dipl.-Ing.
Antoine Moreau
geb. in Paris

von der Fakultät V – Verkehrs- und Maschinensysteme
der Technischen Universität Berlin
zur Erlangung des akademischen Grades

Doktor der Ingenieurwissenschaften
– Dr.-Ing. –

genehmigte Dissertation

Promotionsausschuss:

Vorsitzender:	Prof. Dr.-Ing. Andreas Bardenhagen
Gutachter:	Prof. Dr. rer. nat. Lars Enghardt
Gutachter:	Prof. Dr.-Ing. Dieter Peitsch
Gutachter:	Prof. Phillip Joseph

Tag der wissenschaftlichen Aussprache: 18. Juli 2016

Berlin 2017

'Essentially, all models are wrong, but some are useful.'

George Box, statistician

(quote from his book
'Empirical Model-Building and Response Surfaces'
written with Norman Draper in 1987)

Abstract

This thesis proposes a set of theoretical models to predict, during the conceptual design phase, the sound emitted by the fan stage of an aero-engine, which is due to the interaction of its solid surfaces with the flow. The models are analytical or semi-analytical in nature, and cover a range of disciplines that span between aerodynamics and acoustics. Various fan architectures, such as the conventional ducted turbofan, the ducted contra-rotating fan and the contra-rotating open rotors, are addressed on a common basis, where the sensitivity of the radiated noise to the fan design is investigated at given thrust and optimal aerodynamic performance.

The main part of the thesis provides a detailed description of the models that have been selected, adapted and implemented with appropriate formulations to form a consistent prediction environment. Fan aerodynamics is considered via a meanline approach, where a given streamline is assumed to be representative of the whole flow passage. A procedure to obtain a realistic and aerodynamically sound fan geometry based on a reduced number of parameters, typical of the preliminary design phase, is proposed. For each investigated fan, the aerodynamic performance map is explored to locate the off-design points relevant for acoustic certification. The flow perturbations generated by the blades are described as decaying wakes and potential fields that propagate down to the neighboring blade row and interact with it in form of acoustic waves.

The formulation of the sound pressure radiated by the blades has been completely derived anew from the linear theory of the Acoustic Analogy. The acoustic pressure, expressed in the frequency domain, presents strong analogies in the ducted problem compared with the free-field case. The mathematical derivation also shows that the expressions of tonal and broadband noise assume very similar forms. Finally, a term common to all problems, identified as the source strength, only depends on the flow around the blades, and can therefore be directly related to the aerodynamic quantities deduced from the fan design procedure mentioned above.

The capabilities of that unified prediction approach are illustrated by two parametric studies, which deal with the acoustic implications of a modification of the design speed of the fan for the three main architectures. The motivation for addressing this topic is twofold: first, fan speed is known to be an essential key driver for noise emission; second, it is a parameter that strongly affects design and thus is a good candidate to test the entire calculation chain. The speed reduction is realized either by decreasing the fan pressure ratio, hence increasing the bypass ratio of the engine, or by increasing the aerodynamic loading of the blades, if the fan diameter cannot be further increased. It turns out that the results obtained feature realistic, sensible, and smooth trends that are in line with past theoretical and experimental studies.

As a consequence, the feasibility of acoustic assessment based on analytical models during a preliminary design phase is demonstrated. The virtues of the contra-rotating concepts over the conventional turbofan in terms of broadband and tonal self-noise can be directly attributed to the lower aerodynamic loading and Mach numbers. The open rotors do not by themselves generate more noise, the source strength is relatively similar to that of ducted fans, but lack the benefits of a nacelle equipped with sound damping liners. Finally, fan designs with a low pressure ratio tend to be significantly less noisy, thus the acoustic optimum lies far below the optimum of fuel-consumption. A low-noise design alternative to the reduction of the pressure ratio, is increasing the loading of the fan, which however must result from a careful compromise between broadband and tonal noise.

Acknowledgements

I would firstly like to thank my colleague Dr. Sébastien Guérin for his continuous support during the many years we have been working together. I often remember the fruitful discussions we had in the most various circumstances, especially those in the evening, after a day of business trip, in the airplane or in the bus bringing us home. From the beginning, we naturally shared a common view on what our research work should be and how to realize it. Merci à toi.

Much of the work presented in this thesis has profited from the participation and the technical support of several students from the Technical University of Berlin: Behnam Nouri, Nadja Wagner, Robert Meier zu Ummeln, Sebastian Oertwig, Arne Matschke, Claas Koep, and last but not least, my most committed student and now colleague, Robert Jaron; to all of you, vielen Dank für eure Unterstützung!

Thanks also go to my colleagues Dr. Robert Meyer and Prof. Lars Enghardt for trusting me as I started to work for them, first as a student, then as an employee, at the Department of Engine Acoustics. The kind support provided by Balbir Kaur, Brig Pilger, and Horst Mettchen in every-day work life is sincerely acknowledged, too.

I am also grateful to the people that form the international community of Aeroacoustics research. This is a pleasant, vivid, and human-scale community, full of passionate scholars and committed engineers. I have learned much from them, and from all the interactions I could have with the academic and industrial partners during conferences and meetings.

Finally, I would like to say some words in French to my parents. Maman, Papa, votre bienveillance éternelle à l'égard de votre fils est inestimable et, je dois dire, m'a aidé à surmonter la dernière ligne droite avant de finaliser cette thèse. Je vous en suis très reconnaissant.

Nomenclature

Here are presented the main symbols and notations occuring in the models and the corresponding physical quantities they describe. Some symbols may refer to different quantities depending on the context.

Latin symbols

A	cross-sectional area (m^2)
	wake area (-)
	position upstream of an engine component
A_{mn}	modal amplitude (Pa)
a_0	sound speed (m/s)
B	number of blades (-)
	position downstream of an engine component
C_L, C_D	lift and drag coefficients (-)
C_f	skin friction coefficient (-)
c	blade chord length (m)
c_p	specific heat capacity of air $c_p = 1004.5kg/s$
d	wake depth (-)
D	diffusion factor (-)
	diameter (m)
	drag (N)
f	frequency (Hz)
	force per unit area (Pa)
G	Green's function (1/m)
g_m^ω	modal Green's function (1/m)
h	wake harmonic (-)
	streamtube height (m)
	non-dimensional chordwise distribution of sound sources (-)
H	enthalpy (J/kg)
H_{12}	boundary layer shape factor
i	blade incidence (rad)
	imaginery unit number $i^2 = -1$
J_m	Bessel function of order m (-)
k	wavenumber (1/m)
	acoustic scattering index (-)
ℓ	chordwise or streamwise position (m)
	turbulent correlation length (m)
M	Mach number (-)
m	circumferential mode order (-)
n	radial mode order (-)
	power split exponent (-)
	direction normal to blade chord (-)
N	number of engines, blades, or modes (-)
o	throat width (m)

P	pressure (Pa)
p	fluctuation pressure (Pa)
Q	mass flow rate (kg/s)
r	radial position or direction (m)
	specific gas constant of air $r = 287.04 J/kg/K$
R	duct casing or blade tip radius (m)
s	blade pitch spacing (m)
	subscript for source position
S	Sears' function (-)
	non-dimensional entropy (-)
	wetted surface (m^2)
St	Strouhal number (-)
t	blade thickness (m)
	subscript for total (or stagnation) thermodynamic quantities
	subscript for tangential or circumferential velocity component
T	temperature (K)
	time period (s)
	thrust (N)
u	fluctuation velocity in streamwise direction (m/s)
U	blade rotation speed (m/s)
W	flow velocity (m/s)
	weight (kg)
V	flow velocity (m/s)
x	axial direction (m)
y	tangential direction (opposed to circumferential direction) (m)
z_s	noise source position (m)

Greek symbols

α_{mn}	modal cut-on factor
β	flow angle (rad)
	factor $\beta = \sqrt{1 - M^2}$
γ	heat capacity ratio of air $\gamma = 1.4$
Γ	blade circulation (m^2/s)
δ	blade deviation angle (rad)
δ_1,δ_2	displacement and momentum thickness of the boundary layer (m)
Δ	difference
ζ_0	aerodynamic excitation pressure (Pa)
η	aerodynamic efficicency (-)
	hub-to-tip ratio (-)
θ	circumferential position (rad)
Λ	turbulent integral length scale (m)
ν	kinematic viscosity of air (m^2/s)
	blade index (-)
Π	power (W)
ρ	density (kg/m^3)
σ	pitch-to-chord ratio or solidity (-)
	non-dimentional frequency (-)
	throttling coefficient (-)
	source term (Pa)
σ_{mn}	$(n+1)^{th}$ zero of Bessel function of order m (also called Bessel eigenvalue) (-)
τ	flow turning coefficient (-)
ϕ	flow coefficient (-)

	phase term (-)
χ	blade stagger angle (rad)
ψ	acoustic emission angle (rad)
	loading coefficient (-)
Ψ	acoustic chordwise correlation function (-)
ω	aerodynamic loss coefficient (-)
	pulsation frequency (rad/s)
Ω	rotation frequency of rotor (rad/s)

Contents

List of Figures

List of Tables

Chapter 1

Introduction

1.1 Objectives

Since the early days of civil-aircraft aero-engine turbofans the evolution of their design has been characterized by a continuous increase in engine diameter. This development was pushed mostly by fuel-saving considerations: larger engines operate with lower exhaust jet velocity, so less kinetic energy is imparted to the air for the same amount of energy effectively used for propulsion (higher propulsive efficiency). Moreover, the low jet velocity is associated with reduced jet noise, because of smaller velocity gradients and lower turbulence production within the shear layer between the jet and the ambient air. As a result, increasing engine diameter has improved so far both fuel consumption and noise emission.

Nowadays, the growth rate of air traffic and the need for more stringent noise regulations put pressure on the civil aircraft industry to propose adequate technological solutions. These demands can only be coped with by steadily improving the aerodynamics and acoustics of the engines. However, the engine size cannot be much further increased without unacceptable weight and drag penalties resulting from the enlarged nacelle. The strong reduction in jet noise has also bolstered the importance of fan noise. As a consequence, alternative approaches must be considered, which involve either new engine concepts, or other design parameters proper to the geometry and operating conditions of the fan. Because modern fans have reached a very high aerodynamic efficiency well above 90%, improving the acoustics without degrading the aerodynamics is a really challenging task.

The main objective of the present work is to provide a platform for the assessment and reduction of fan noise during the pre-design development phase of an engine. Since noise and fuel consumption have become uncorrelated, and sometimes even competing aspects, a multi-disciplinary approach called the 'design-to-noise' can integrate the acoustic assessment at an early phase of the design process and result in so-called 'quiet-by-design' fans. The main objective is articulated by the following four aspects that must be addressed by the platform:

- **Comparison of innovative fan concepts**: alternative concepts to the conventional rotor–stator-stage turbofan (TF) are currently considered by the industry as candidates for the future low-emission engines. These are the counter-rotating turbofan (CRTF) composed of a ducted rotor–rotor-stage, and the counter-rotating open rotors (CROR) composed of two unducted large-diameter propellers. These concepts represent a technological challenge, especially from the acoustic point of view.

- **Identification of acoustically relevant design parameters**: a parametric description of the physical processes is necessary at a level sufficiently detailed to capture the essential aerodynamics-acoustics trade-offs. The identification of key drivers relies on the quantitative assessment of the relative importance of the different parameters.

- **Support of an analysis competence**: the correct assessment of fan noise sources and their relative importance depending on the design and operating conditions is still a strongly debated

topic. The present approach should be pedagogical and help the user, engineer or researcher to get more insight. Computational simulations such as CFD and CAA provide detailed and sometimes very accurate results, but their interpretation is difficult as they basically contain vast and untreated datasets. Thus, they are often used as black-box models inside which one cannot easily look and get insight into the driving mechanisms.

- **The long-term perspective:** represented by explorative studies performed in order to identify which configurations within the design space have the best potential and are worth being refined and investigated with a more demanding and accurate approach (for example CFD/CAA or measurements).

1.2 Challenges

There are two major challenging aspects associated with the objectives detailed in the previous section. The first is the ability to provide a comparison between different concepts and configurations which is made on a fair basis: for example, the noise assessment of two engines has to be carried out for the same engine performance (required thrust, optimal efficiency, etc.). The second challenge is computation time: the aerodynamic and acoustic calculations have to be performed within a reasonable amount of time for parameter studies to cover a sufficiently large design space. More specifically, the points related to these challenges are:

- Fan noise strongly depends on fan aerodynamics and should not be interpreted alone: noise prediction does not only rely on good acoustic models but also on a sensible description of aerodynamic performance, of the steady and unsteady flow inside the fan.
- The number of parameters and their range of variation is large: conventional turbofans have high-solidity blades whereas open rotors have low-solidity blades, and the variations in pressure ratio and relative flow Mach number may extend from the incompressible to the supersonic flow regimes.
- Some of the physical problems considered are different in nature: the generation of tonal and broadband noise, the generation of noise inside a duct or in the free field.

1.3 The analytical approach

Given the objectives and the challenges linked to them, the prediction based on an analytical approach has been chosen. Here, the word 'analytical' has to be understood as opposed to both 'empirical' and 'computational'. An introduction to the different approaches described by each of those adjectives is given by Envia [1].

An empirical model is usually based on statistical correlations of high-level (global) parameters derived from experimental data. As the description of the problem is not causal, the driving mechanisms cannot be identified more than on a very basic level. Furthermore, the domain of validity of the model is limited and extrapolation is not possible a priori.

On the other side, a computational model is based on a low-level (local) description of the physics, often in form of a set of differential equations (such as the Navier-Stokes equations). The challenge is then concentrated on the correct numerical implementation of the mathematical description and on the data post-processing. Due to the low-level description, gaining physical insight is difficult.

The analytical approach is located somewhere in between: the models are mathematically simple enough to avoid major numerical problems, still they remain causal and provide a sufficiently detailed description for design studies to be performed. The challenge of this approach is to estimate the highest possible degree of simplification allowed to still address the problem properly. The following items highlight the main advantages of analytical models:

- Mathematical formula of analytical models already give indications about the driving mechanisms before the calculation has been performed. Moreover, they provide the connection between the acoustic and the aerodynamic parameters.
- As all models are relatively simple, they can be easily integrated in a single prediction platform and more attention can be paid to the derivation of unified formulations of the different problems considered.
- At last, simple models can be implemented in fewer lines of code and their behaviour can be better controlled over a wide range of applications: this ensures fast and robust calculation routines.

1.4 State of the art on prediction models

The question of fan noise prediction by means of analytical models has been addressed by the industry and other research entities, and some were communicated in conference papers or public reports. We will consider two categories of prediction methods to illustrate the current state of the art.

1) The fan noise prediction tool developed at NASA by Heidmann [2] (later improved by Kontos, Janardan and Gliebe [3] or adapted to small engines by Hough and Weir [4]) is based on empirical correlations derived from static tests [5] on a series of eight different full-scale fans, all having the same rotor–stator architecture. This model is part of the Aircraft Noise Prediction Program 'ANOPP' developed by NASA. Due to the relatively few and simple engine data required as input, this public-domain prediction model is now widely used among the industry and the universities.

Heidmann observed that the measured sound power approximately scaled with the shaft power $P_{shaft} = Q \cdot \Delta T_t$, but he noticed that fans with a higher pressure ratio (lower mass flow rate Q and higher total temperature rise ΔT_t) emit more noise. Thus, he proposed the following scaling law for the overall sound power: $P_{sound} = K \cdot Q \cdot \Delta T_t^2$, where K is an empirical coefficient.

This scaling law is a statistical correlation involving very high-level parameters of the engine. Of course, the temperature rise across the fan cannot be regarded as the source of noise by itself. However, this choice is justified on the ground that the temperature rise correlates well with the flow velocities and their fluctuations, which are the main physical cause for fan noise. The empirical coefficient K sets the absolute noise level and also contains various empirical corrections to account for the blade count, the axial distance between the rotor and the stator, and other effects. The ranking of noise sources is possible to some extent because a distinction is made between the different noise components (for example tonal and broadband components, rear-arc and forward-arc emissions) but they are neither related to the physical noise mechanisms nor to the noise emitters, the rotor and the stator. Moreover, this model cannot be applied to counter-rotating or unducted concepts without neglecting essential aspects of the problem.

2) The second category of prediction methods is formed by the more theoretical approaches that have been developed as an alternative to Heidmann's model. Some of the prediction codes and research teams involved in this field in the USA and in Europe are listed below.

Here is a list of the codes developed in the USA:

- Codes used by NASA and developed in collaboration with the industry or universities. This list can be found on the websites of the Glenn and Langley research centers:
  - V072 and RSI deal with tonal and broadband models for dipole-type interaction noise. V072 focuses on tonal noise and is one the first analytical fan noise prediction models developed at NASA. It was developed by Ventres et al. [6] and enhanced by Edmane Envia [7]. It includes a two-dimensional linear-cascade response model to account for scattering by neighbouring blades during the noise generation process. The RSI tool developed by Envia [8] extends the capabilities of V072 to broadband noise prediction.

  - TFANS/BFANS are respectively tonal and broadband cascade noise model used by Pratt & Whitney. The code TFANS was written by David Topol [9, 10, 11] from Pratt & Whitney. BFANS is based on the work by Donald Hanson [12, 13, 14] from Pratt & Whitney and Stewart Glegg from the Florida Atlantic University [15, 16, 17]. An overview of BFANS is presented by Bruce Morin [18]. The tool has the specificity to account for the cascade response to a three-dimensional gust, and to model the transmission and reflection of acoustic modes through a blade row (and the mode trapping phenomenon).
  - FanBB is the broadband prediction code developed by Ramani Mani and Philip Gliebe [19, 20, 21, 22, 23] from General Electric. FanBB includes a model for the quadrupole-type interaction of incoming turbulence with the potential fields of blades and a model for anisotropic large-scale incoming disturbances.
  - WOBBLE is a propeller noise prediction tool based on the work by Hanson [24, 25, 26].
  - LINPROP/QPROP is also dedicated to the prediction of dipole and quadrupole sources for propellers; it is based on the work by Envia [27].
  - ASSPIN was developed by Feri Farassat and Kenneth Brentner [28, 29, 30] in Langley to provide a time-domain prediction of propellers and open rotor noise. This is the only tool from the list given here that does not work in the frequency domain.

- Codes developed by American universities:
  - Broadband noise models at the University of Notre Dame: annular cascade response model supervised by Hafiz Atassi [31, 32, 33] in collaboration with Pratt & Whitney, and an anisotropic turbulence model by David Stephens and Scott Morris [34].

Here is a non-exhaustive list of the analytical work performed in Europe:

- France: a series of airfoil, propeller and fan noise prediction models was initiated and supervised by Michel Roger from Ecole Centrale de Lyon. He published in collaboration with Stéphane Moreau on airfoil noise and automotive fans [35, 36], with Yannick Rozenberg on trailing edge noise [37], with Hélène Posson on cascade response [38] (work supported by Snecma), and with Arnulfo Carazo on open rotor tonal interaction noise [39] (work supported by Airbus). Part of this set of models has been applied in noise assessment and optimization studies, for example by Pagano et al. at CIRA (Italian aerospace research center) [40], Marinus et al. at the Von Karman Institute in Brussels [41], or Magne et al. at the University of Sherbrooke in Québec [42].
- England: Rolls-Royce has supported a number of studies at the following universities:
  - Cambridge University: David Crighton, Nigel Peake working with Anthony Parry focused their studies on the tonal self- and interaction-noise of propellers and open rotors [43, 44, 45, 46].
  - Institute of Sound and Vibration in Southampton: Christopher Morfey provided essential contributions [47, 48, 49] in the 1970's to the theory of fan noise generation. More recently, Phil Joseph, Vincent Blandeau, and Michael Kingan [50, 51, 52, 53, 54] focused on broadband noise of fans and open rotors.
- The Netherlands: work on propeller tonal noise models by Schulten [55] and Brouwer [56] from NLR (national Dutch aerospace research center).
- Germany: Klaus Heinig from MTU published a cascade model for compressor noise prediction [57].

These models all have in common a strong theoretical fundament and rely, at least for the acoustic part of the prediction, very weakly on empirical coefficients, unlike Heidmann's model. They are basically exact analytical solutions of a simplified problem, which most of the time addresses one specific noise source or a limited number of sources. As a result, the formulation and program implementation of each model are strongly focused on the problem considered and cannot be extended easily to other noise

sources or to a wider range of applications. For example, few models address the problem of tonal and broadband noise simultaneously and with a similar formulation, and no model deals with the ducted und unducted problems at the same time.

In order to get the 'global picture' (for example a source ranking) or compare different concepts, it is necessary to run and analyse every model separately, and finally cross-compare their results, which can be a delicate task due to the variety of input and output data proper to each model.

Moreover, these analytical models cannot be run on their own. They need to be coupled to flow models or computational solvers since the aerodynamic input data required are much more detailed than those needed by Heidmann's empirical model. In the author's view, these more advanced analytical acoustic models only partly fit into the philosophy presented before. Especially the dependence on external aerodynamic tools and the need for implementing several models to obtain the overall picture of fan noise generation is regarded as an obstacle to future noise assessment and also an obstacle to a didactic approach.

1.5 New prediction tool: PropNoise

A novel tool for the prediction of noise produced by rotating or non-rotating blade rows has been developed since 2008 [58, 59, 60, 61, 62, 63, 64, 65, 66]. It was named 'PropNoise' standing for Propulsion Noise. Its description and application is the object of the present work.

Attention has been paid to the establishment of a unified approach with strong connections between the aerodynamics and the acoustics, and a comprehensive description of the different fan noise sources for assessing correctly the trade-offs the engineer may be confronted to during the 'design-to-noise' process. Moderately detailed but equally accurate models covering the main aspects of fan noise have been prefered to highly accurate models covering a smaller range of aspects. PropNoise forms a framework integrating various aerodynamic and acoustic models and is coded in form of Matlab routines. The large majority of the models is inspired from already existing work available in the literature but reformulated in a way to provide homogeneity and continuity between the different fields.

The structure of the tool is presented in Figure 1.1. The three modules for fan design, steady, and unsteady aerodynamics are dedicated to the generation of input data for the acoustic calculations. These modules are based on a meanline approach, which means that the aerodynamic calculations are performed at a single radial position considered to be representative of the complete flow. The validity of this assumption will be discussed later. The acoustic models are based on a radial-strip approach: the response of the blades to an excitation is calculated for each radial strip as if the problem was two-dimensional, however the emission of sound waves by the different strips and their interferences are calculated with a three-dimensional model. An intermediate module ensures the radial extrapolation of the meanline aerodynamic data required by the acoustic models.

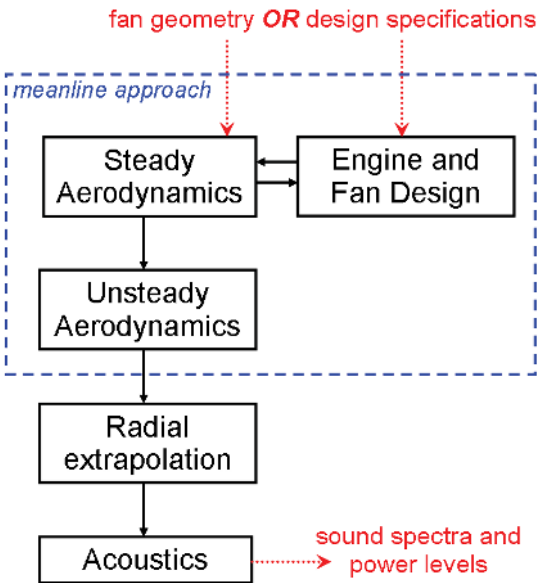

Figure 1.1: Modular structure of the prediction tool 'PropNoise'

This structure refers to the 'stand-alone' mode of the tool, in which no other program needs to be coupled to 'PropNoise'. The acoustic-relevant aerodynamic input data are generated inside the tool. It is also possible to disactivate some of the internal aerodynamic calculations and to provide the acoustic module with flow data coming from another tool, as in the case of a RANS-informed noise prediction [67]. However, this aspect is beyond the scope of the present work.

The following chapters of this document will present each of the modules contained in the 'stand-alone' version of the program.

Chapter 2

Steady aerodynamics

2.1 Motivation and approach

In the field of aeroacoustics, the knowledge of the steady and unsteady flow quantities is necessary to determine the sound sources and the conditions of sound propagation that will affect the noise emission perceived by an observer. The purpose of this chapter is to present a set of analytical models for the steady aerodynamic quantities relevant for aero-engine fan noise and to precise how these quantities are related to fan geometry and operating conditions.
The models for steady aerodynamics prediction provide two different types of information: the first concerns the aerodynamic performance of the fan, in terms of mass flow rate, pressure rise and efficiency, and more globally engine thrust and fuel consumption; the second type of output data delivered by the models concerns more refined quantities such as boundary layer thickness and flow velocities around the blades. These quantities are the source of flow perturbations within the engine, which propagate to neighbouring blade rows, interact with them, and this finally results in sound emission.
Beyond the necessity of generating the appropriate input data for calculating flow perturbations and eventually noise, the module for steady aerodynamics aims at establishing a link between the aerodynamic performance of an engine and its noise emission. A clear view on the relation between those two essential aspects may help the engineer to identify suited configurations very early during the design process of an engine.
The approach adopted here relies on simple analytical models, which present the advantage of being fast, robust, and easier to understand than more accurate tools. Attention has been paid to physically-based descriptive models, which are able to provide some level of understanding. No claim is made here to compete with modern flow solvers like MISES (coupled Euler-Boundary Layer cascade code) or TRACE (DLR in-house code, full 3D RANS solver). Such tools provide nowadays reliable predictions for most fan or compressor applications and are extensively used among the industry to improve and design new components. However, the massive use of CFD is identified by Cumpsty [68] as a possible cause for the lack of insight associated with modern fan designs.
The use of simple descriptive models is not new. The development of analytical fan prediction models based on empirical correlations experienced a significant growth up to the 1980's and such models formed then the basis for most designs, before they became superseded by CFD. The aero-engine manufacturers developed each their own set of correlations, like those of Swan at Boeing [69], Grieb at MTU [70], Koch & Smith at General Electric [71], or Miller, Wasdell and Wright at Rolls-Royce [72, 73]. In a continuous effort to provide more accurate predictions, the correlations became more complex while simultaneously losing their link to first-principles aerodynamics. We intend to avoid this flaw by sticking to fundamental theoretical studies such as the pioneering work of Lieblein [74], completed by the more general considerations of Denton [75].

2.2 Definition of parameters and assumptions

A number of simplifications are made in order to keep the computations rapid and robust, and to limit the use of empirical correlations. These assumptions are listed below:

- Meanline approach: all quantities are calculated at a given radial station, specified by the user in percent of the duct height. This radial station is assumed to be representative of the fan operating condition and of its performance. It is usually referred to as the meanline radius (see Fig. 2.1). The meanline approach does not allow accounting for the strong radial variations in geometry and flow typical of fans with a low hub-to-tip ratio, but we will see on an application that the major features of the aerodynamic fan map can still be correctly reproduced.

- Steady flow: only the time-averaged part of the flow is calculated. At first, the flow is calculated in the relative reference frame (rotating with the blade row) and then converted into the fixed frame. Flow perturbations such as wakes and potential fields are treated in a different module and will be described in chapter 4 dedicated to unsteady aerodynamics. The steady flow quantities far upstream and downstream of a blade row are considered axisymmetric (constant in the circumferential direction). As a result, the impact of the circumferential variation of incidence on rotor blade performance (as might be the case in the presence of a fan inflow distortion) cannot be addressed by the models.

- No engine core: only the bypass flow of the fan is considered. Hence, the bypasss ratio of the engine cannot be directly determined from the geometry but may be estimated at the design point based on the fan pressure ratio (see the next chapter 3 on engine and fan design for the details).

- Axial-flow compressor: the radial component of flow velocities is neglected, as is the variation of the streamline radius. These assumptions are not suited for radial compressors. The aerodynamic influence of blade sweep and lean is not considered.

- The axial velocity component must be subsonic everywhere: $M_x < 1$. Supersonic business jets and compressors with supersonic axial inflow cannot therefore be treated.

- No bleed air, no blade cooling: the mass of airflow entering each component is entirely conserved at the outflow as no air extraction system is modelled. Also, no blade cooling system is considered for the compressors. This means that the total temperature in the relative reference frame is constant across a blade row.

- The outflow regime of each of the engine components must be subsonic in the rotating reference frame linked to the blade row. This condition is satisfied for most compressors, except for supersonic low-solidity propellers or axial-flow rotors with an extremely low degree of reaction.

- The fan performance is calculated based on the blade profile loss (which is the sum of shock loss and boundary layer loss) and the endwall loss (which is the sum of the annulus loss due to endwall friction, and secondary flow loss). For unducted configurations, the endwall loss model has to be replaced by a tip vortex model.

- Flow conditions at which blade stall or choking within the blade passage is detected are not permitted. The routines return an error status. An exception is made for the exhaust nozzle, which may operate in choked condition.

- The thermodynamic properties of the air are considered constant: the specific gas constant is $r = 287.04$ J/K/kg, the heat capacity ratio is $\gamma = 1.4$, and the specific heat capacity is $c_p = \frac{\gamma r}{\gamma - 1} = 1004.6$ J/K/kg.

The following part of the present paragraph will now introduce some important quantities related to the mean flow around a blade row. Figure 2.2 presents the definition of flow velocities and flow angles

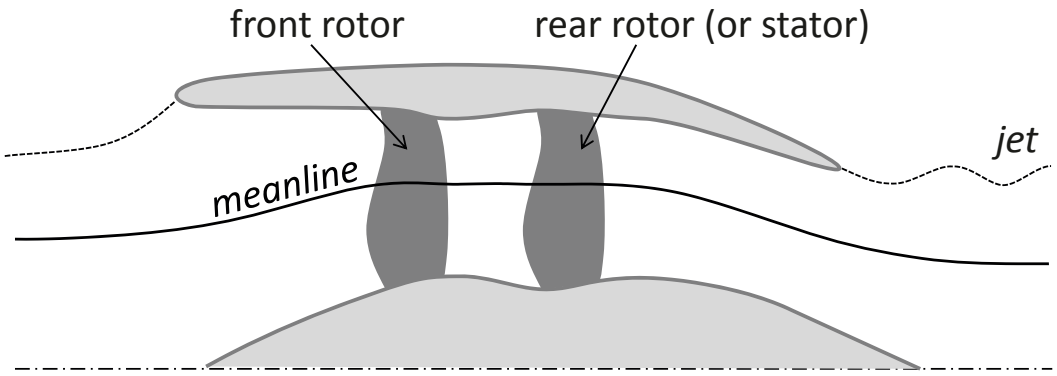

Figure 2.1: Simplified engine model [76]

considered in the rotating frame of reference linked to the blades. The subscripts A and B refer to flow conditions upstream and downstream of the blade row, respectively. The quantities $\overline{W}_{SS}$ and $\overline{W}_{PS}$ denote the blade surface velocities on the suction and pressure side, respectively. They will be defined more precisely later in this chapter. The quantities s, h, i and δ refer to the blade spacing, outflow streamtube height, blade incidence, and deviation, respectively.

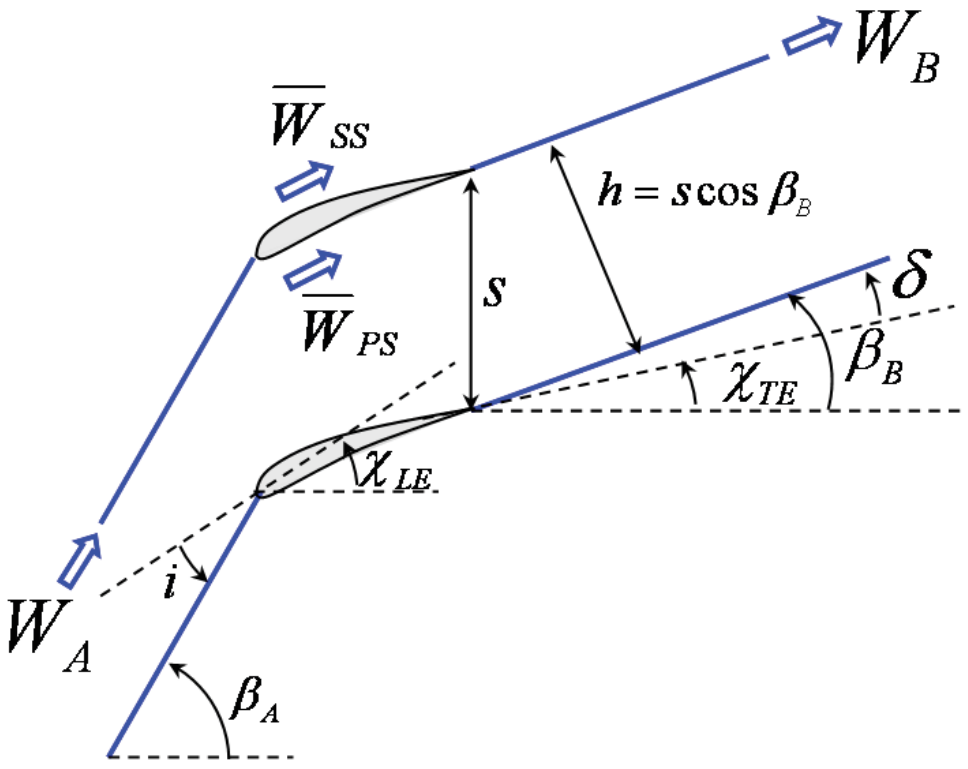

Figure 2.2: Flow angles and velocities in the relative frame linked to the blade row

As no air extraction/injection occurs within the engine, the mass flow rate Q is conserved between positions A and B:

$$Q_B = Q_A \tag{2.1}$$

Similarly, as the blades are not cooled, the flow within the blade passage is considered adiabatic and the total temperature T_t is conserved between positions A and B in the rotating frame. This is verified both for rotors and stators as the radius change of the streamlines is neglected.

$$T_{tB} = T_{tA} \tag{2.2}$$

The incidence is defined as the difference between the inflow angle (expressed in the rotating frame) and the metal angle of the blade leading edge.

$$i = \beta_A - \chi_{LE}$$

We will define later the so-called design incidence i_{des}, which is comprised between the minimum-loss incidence and the incidence of maximum lift-to-drag ratio. The deviation angle is the difference between the outflow angle and the blade metal angle at the trailing edge. It has a significant effect on the performance of a blade row at off-design incidence.

$$\delta = \beta_B - \chi_{TE}$$

The prediction of this parameter has been subject to numerous studies, which can be associated historically to two different approaches: the german school, represented by the work of Weinig [77] and Scholz [78], developed exact theoretical models to predict the lift of a cascade of arbitrary solidity. However, the assumptions made are strong (inviscid flow, circular arc profiles, incompressible flow). The anglo-american school (see Carter [79, 80] and Lieblein [81, 74, 82]) proposed an empirical approach based on correlations gained from low-speed cascade experiments. These correlations inherently feature a lack of universality (they are specific to certain types of NACA profiles and are not valid for the low-solidity blade rows of propellers and open rotors) but they were very popular among the engine design community as long as standard blade profiles were used. Extensions developed for transonic compressors (see Çetin [83]) further reduced the gap between prediction and measurements but they were not accompanied with an increase of insight. For the sake of keeping the routines simple, fast and robust, we choose here to consider the deviation angle to be a linear function of the incidence:

$$\begin{cases} \delta(i = i_{des}) = 0 \\ \dfrac{\partial \delta}{\partial i} \underset{\sigma \to 0}{\to} 1 - \pi\sigma\cos\chi \end{cases} \Rightarrow \delta = \frac{i - i_{des}}{1 + \pi\sigma\cos\chi}$$

For simplicity the deviation at design conditions is neglected. The present model fulfills two well-known results: at large solidities, the deviation tends to zero, whereas the variations of deviation and incidence are identical at vanishing solidity. The outflow angle β_B can be calculated from the deviation and the outflow velocity magnitude W_B can be directly obtained from the continuity equation Eq.(2.1).

Lakshminarayana [84] introduced the following mean quantities (average between upstream and downstream positions) to determine the lift and drag forces on cascade blades:

$$\begin{aligned} \mathbf{W}_m &\equiv \frac{\mathbf{W}_A + \mathbf{W}_B}{2} \text{ (vector averaging)} \\ \tan\beta_m &\equiv \frac{\tan\beta_A + \tan\beta_B}{2} \\ \rho_m &\equiv \frac{2\rho_A\rho_B}{\rho_A + \rho_B} \end{aligned} \tag{2.3}$$

An important parameter for the design of fans is the so-called meridional-velocity–density ratio, denoted MVDR. As we consider axial-flow fans without change of the radius through the compression

process, the meridional velocity is identical to the axial velocity, and the MVDR is equivalent to the AVDR (axial-velocity–density ratio). So we have:

$$MVDR = AVDR \equiv \frac{\rho_B W_{xB}}{\rho_A W_{xA}} = \frac{A_A}{A_B} \tag{2.4}$$

If the flow blockage due to endwall boundary layers is neglected, the MVDR is inversely proportional to the ratio A_B/A_A of the duct cross-sectional areas (duct contraction) across the blade row.

2.3 Relation between pressure rise, flow turning and lift

According to the Euler turbomachinery equation (more details can be found in the books by Laksminarayana [84], Cumpsty [85], and Grieb [86]), the change in angular momentum caused by a rotor is related to the energy received by the fluid. The specific total enthalpy rise (expressed in the fixed frame) across an axial-flow rotor with no meanline-radius change is given by:

$$\Delta H_t = U \cdot \Delta W_t \tag{2.5}$$

The variation of the circumferential flow velocity across the blade row is $\Delta W_t = W_{tA} - W_{tB}$ and is usually referred to as flow turning; its value is identical in the rotating and in the fixed reference frames. U is the meanline circumferential speed of the rotor blades. Alternatively, the enthalpy rise in the absolute frame can be expressed in terms of the pressure ratio PR achieved by the rotor and its isentropic efficiency η_{ise}:

$$\Delta H_t = c_p T_{tA} \cdot \frac{PR^{\frac{\gamma-1}{\gamma}} - 1}{\eta_{ise}}$$

The pressure ratio PR is defined as the ratio of the outflow to the inflow total pressures taken in the fixed frame. The inflow total temperature T_{tA} is here expressed in the fixed reference frame, too. From the last two equations, we observe that the pressure rise accross an axial-flow compressor rotor is generated by turning the flow (non-zero ΔW_t). This is usually achieved in two ways, depending on the Mach number domain for which the compressor is designed. In the case of subsonic compressors, the duct contours impose at the design point a nearly constant axial velocity across the blade row (this is done to limit diffusion and avoid flow separation), hence the turning can only be obtained by deflecting the flow in the rotating frame. In supersonic compressors, the flow angles are hardly modified in the rotating frame because the blades are thin and straight to avoid the formation of strong shocks responsible for high losses. The turning is obtained through the reduction of the axial velocity and the strong deceleration of the flow from supersonic to subsonic conditions induced by the shock system. Figure 2.3 illustrates the working principles of the low-speed subsonic and supersonic axial-flow compressors.

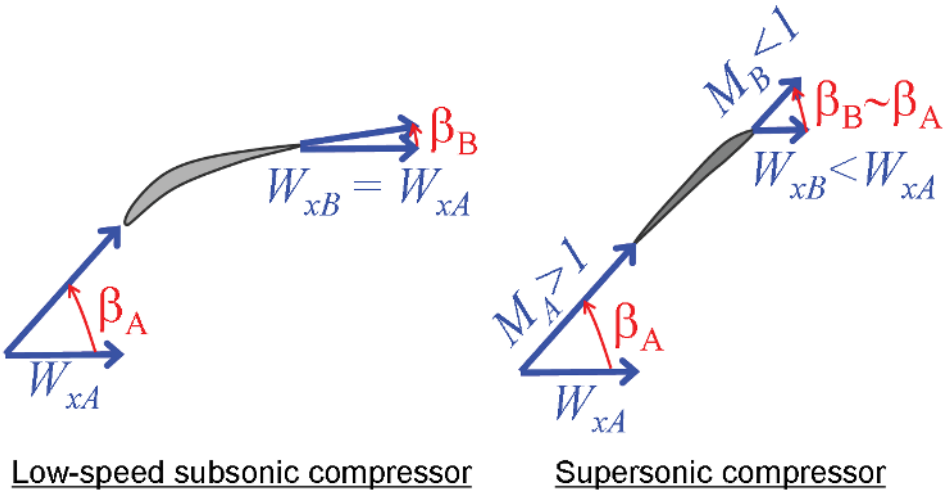

Figure 2.3: Working principle of a subsonic and supersonic rotor blade row

We will now establish a relation between the flow turning and the lift coefficient of the blades. Lakshminarayana [84] has shown that the sectional lift L can be expressed in terms of circulation Γ:

$$\rho_m W_m \Gamma = L = \frac{1}{2}\rho_m W_m^2 C_L \cdot c$$

Moreover, the circulation around an airfoil can be related to the flow turning of the blade row:

$$\Gamma \equiv \oint W d\ell = \Delta W_t \cdot s \tag{2.6}$$

We obtain the following relation between flow turning and lift coefficient:

$$C_L = \frac{2\Delta W_t}{\sigma W_m} = \frac{\tau \cos\beta_m}{\sigma}, \text{ where } \tau \equiv \frac{2\Delta W_t}{W_x} = 2(\tan\beta_A - \tan\beta_B) \tag{2.7}$$

This equation indicates that the change in flow angles (flow turning coefficient) is closely related to the lift coefficient through the quantity $\sigma = c/s$ called the solidity of the cascade, which is the ratio of the blade chord c to the blade spacing s. Because the lift coefficient must assume finite values, there can be no flow turning for an isolated airfoil (which is equivalent to a blade row of vanishing solidity). For a blade row of increasing solidity, the flow turning tends to be solely determined by the metal angles of the blades, so the lift coefficient continuously decreases and tends to zero. This fundamental behaviour is described in more details by the analytical model of Scholz [78] including an estimation of the inviscid deviation. Note that the isolated airfoil can indeed generate flow turning if we consider a finite-span wing with tip vortices; in that case the two-dimensional flow assumption is not sastisfied.

2.4 Definition of design and off-design conditions

A blade row operates at design conditions if its incidence assumes a particular value, named the design incidence. In that case, the flow overspeeds around the blade (see Eq.(2.8)) are determined by the global lift coefficient of the airfoil without consideration of local accelerations responsible for a loss penalty. This is basically a case of near-minimum loss or near-maximum efficiency for the blade. In the low subsonic regime, the design incidence is zero. In the high subsonic and supersonic regimes, the design incidence is

larger than the choking incidence and this has to be modelled by the following approach. The choking incidence primarily depends on the throat width o of the blade passage and on the inflow Mach number:

$$o = s\cos(0.8\chi_{LE} + 0.2\chi_{TE}) - \bar{t}$$

$$i_{chok} = \arccos\left(\frac{o/s}{\alpha_{cr}}\right) - \chi_{LE} \text{ , where } \alpha_{cr} \equiv \frac{Q_r(M_A)}{Q_r(1)} \text{ and } Q_r \equiv \frac{Q \cdot \sqrt{\gamma r T_t}}{P_t \cdot A}$$

The quantity Q_r is the reduced mass flow, it is solely a function of the Mach number. In subsonic flow, choking occurs if the throat area ratio is smaller than a critical value and the calculation is interrupted in that case. With supersonic inflow, the calculation is broken up if the throat area ratio decreases below unity. In reality, the choking limiting condition in supersonic flow is defined by an even more stringent case of minimum incidence called the unique incidence, which further reduces the range of operation as the Mach number is increased. The unique incidence is explained more extensively by Freeman and Cumpsty [87], and Levine [88]. When a cascade operates at unique incidence, it is called started and features a shock system attached to the blade leading edge. Operation at larger incidence is called unstarted and is characterized by a detached bow shock upstream of the blade leading edge.

The design incidence is defined as:

$$i_{des} = \max\left(0, \frac{i_{chok} + i_0}{2} + \Delta i\right)$$

The reference incidence i_0 denotes the incidence at which there is no flow area contraction. The empirical constant Δi specifies the distance between design and choking in terms of incidence angle at supersonic flow conditions, a value of 2 degrees gives a good match with actual fan maps.

$$i_0 = \arccos(o/s) - \chi_{LE}$$

The stalling incidence i_{stall} gives a rough estimate of incidence at which stall is detected, it is calculated by:

$$i_{stall} = \max(i_{des}, K_{offdes}\,(1 + \pi\sigma\cos\chi))$$

The empirical constant K_{offdes} has a value around 8 degrees.

2.5 Distribution of flow velocities around the blades

As described by Denton [75] the production of loss is closely related to the distribution of flow velocities around the blades. On each side of the blade (pressure and suction sides), we will consider a single chordwise-averaged value of the velocity, that is assumed to be representative of the losses. The choice of a scalar rather than a full chordwise distribution was adopted by Lieblein [74] and Koch and Smith [71], and is supported by the fact that the entropy production is proportional to the third power of velocity [75], therefore is it essentially determined by the region of maximum velocity. We write this chordwise-average velocity in a form similar to that proposed by Koch and Smith [71] but extended to off-design incidence conditions:

$$\overline{W} = W_A \cdot \left(1 + f(\frac{\bar{t}}{h}, M_x) \pm \frac{1}{4}C_L + \Delta_{offdes}\right) \tag{2.8}$$

The second term in the parenthesis corresponds to the acceleration due to the flow area contraction in the blade passage, it depends on the chordwise-average blade thickness and on the axial Mach number. The third term represents the overspeed due to lift: it is positive on the suction side and negative on the pressure side. The last term is attributable to off-design incidence and proximity to choking. At design conditions (zero incidence at low Mach numbers, small positive value at high mach number depending on throat width), the relation of Eq.(2.6) is retrieved by taking the difference between the suction and pressure side velocities:

$$\Gamma \equiv \oint W d\ell = \left(\overline{W}_{SS} - \overline{W}_{PS}\right) \cdot c = \frac{1}{2}W_m C_L \cdot c$$

This equality is not exactly satisfied at off-design conditions because Δ_{offdes} assumes different values on the pressure side and suction of the blades. Physically, the off-design velocity distribution departs from the optimal distribution of velocities established at zero incidence, and is responsible for an additional loss penalty. The off-design overspeed factor is given by:

$$\Delta_{offdes} = \begin{cases} 0.5\frac{i-i_{des}}{i_{stall}-i_{des}}, \text{ on the suction side if } i > i_{des} \\ \max\left(0.5\frac{i_{des}-i}{i_{stall}-i_{des}}, 1.5\frac{i_{des}-i}{i_{des}-i_{chok}}\right), \text{ on the pressure side if } i < i_{des} \\ 0, \text{ otherwise} \end{cases} \tag{2.9}$$

2.6 Losses

2.6.1 Relation between loss, drag and entropy production

The loss coefficient characterising the performance of a rotating blade row is usually defined as a normalized total pressure loss:

$$\omega \equiv \frac{\Delta P_t}{\frac{1}{2}\rho_m W_m^2}$$

where $\Delta P_t = P_{tA} - P_{tB}$ is the difference between the inflow and outflow total pressures in the relative reference frame rotating with the blade row. This definition is less suited for endwall loss, which usually scales with W_x^2 instead of W_m^2. By considering the integral over the streamtube height of the momentum equation in chordwise direction, we obtain a relation between the total pressure loss and the drag force applied on the blades (see the derivation detailed by Grieb [86], Cumpsty [85] and Lakshminarayana [84]):

$$\Delta P_t \cdot s\cos\beta_m = D = \frac{1}{2}\rho_m W_m^2 C_D \cdot c$$

By combining these last two equations, we obtain an equation linking the drag coefficient to the loss coefficient:

$$C_D = \frac{\omega\cos\beta_m}{\sigma} \tag{2.10}$$

Similarly to Eq.(2.7) this equation relates a quantity usually defined for isolated airfoils, C_D, to a quantity typical for cascades, ω. If both equations (2.7) and (2.10) are combined, we can observe that the ratio of flow turning to loss coefficient, which directly affects the isentropic efficiency of a rotor (this is shown in Eq.(2.21)), is equivalent to the well-known lift-to-drag ratio characterising airfoil performance:

$$\frac{C_L}{C_D} = 2\frac{\Delta W_t/W_x}{\omega} = 2\frac{\tan\beta_A - \tan\beta_B}{\omega} = \frac{\tau}{\omega} \tag{2.11}$$

It should be noted that this relation has been obtained after assuming a constant axial velocity accross the blade row. This condition is usually satisfied to limit diffusion and avoid flow separation.

We will now present the models used to calculate the losses generated by a cascade. As stated by Cahill [89] and Denton [75], the loss of total pressure is related to the production of entropy. The flow through a blade row considered in the rotating reference frame locked to the blades can be regarded as an adiabatic process (no total temperature change), so the entropy rise is solely determined by the variation of the total pressure:

$$\Delta S = \frac{\gamma}{\gamma-1}\frac{\Delta T_t}{T_t} - \frac{\Delta P_t}{P_t} = -\frac{\Delta P_t}{P_t} = \frac{\frac{1}{2}\rho_m W_m^2 \omega}{P_t} = -\log\left(\frac{P_{tB}}{P_{tA}}\right) \tag{2.12}$$

The entropy denoted S is the usual specific entropy, non-dimensionalized by the mass flow rate and by the specific gas constant r. Correlatively, the total pressure loss is linked to the entropy rise through:

$$\Delta P_t = P_{tA}(1 - e^{-\Delta S})$$

In the present models, we consider that the sources of entropy are represented by the profile and endwall losses. They are formed by the boundary layers developing on the blade surfaces and their convected wakes, and the shocks appearing within the blade passage if the inflow Mach number is beyond the critical Mach number. By superimposition of the entropy sources, the overall entropy rise is simply given by the sum of three contributions:

$$\Delta S = \Delta S_{BL} + \Delta S_{shock} + \Delta S_{endwall}$$

2.6.2 Blade loading, diffusion factor and stall

A fundamental aspect of compressor aerodynamics is the positive streamwise pressure gradient imposed to the flow as it passes through the blade rows. This increases the size of the blade boundary layer and limits the pressure rise. The pioneering work of Lieblein [74] offereda a better understanding of this effect and provided a quantitative prediction for it. Based on the integral momentum equation of the boundary layer Lieblein derived a relation between the momentum thickness at the blade trailing edge and a parameter called the diffusion factor which represents the intensity of flow deceleration (or diffusion) over the blade. He applied his relation to experimental data gained during a series of low-speed cascade measurements and he obtained a strikingly good match in view of the diversity of the cascade geometries considered. We will use here a modified version of Lieblein's diffusion factor. For each side of the blade, we define a diffusion factor D as:

$$D \equiv \frac{\overline{W} - W_B}{W_A} \tag{2.13}$$

The classical diffusion factor DF introduced by Lieblein [90] can be directly retrieved from Eq.(2.13) with thin profiles working at zero-incidence and in subsonic flow, by approximating $\overline{W} \approx W_A(1 + \frac{1}{4}C_L)$ in Eq.(2.8) and $C_L \approx \frac{2\Delta W_t}{\sigma W_A}$ in Eq.(2.7):

$$DF = 1 + \frac{1}{4}C_L - \frac{W_B}{W_A} = 1 - \frac{W_B}{W_A} + \frac{\Delta W_t}{2\sigma W_A}$$

The diffusion factor D proposed here is a more general version of DF, and is applicable for thick airfoils working at off-design subsonic or supersonic inflow conditions. Turbines are characterized by very low values for the diffusion factor D. Compressor blades are typically designed for a value around 0.5, where the boundary layer is on the verge of separation, which usually starts from the trailing edge of the blades and moves upstreams as the incidence is increased. Increasing the loading well beyond this point leads to massive separation; the pressure rise of the rotor abruptly drops: this is the so-called stall.

The detection of stall is still a very delicate problem and there is no criterion accepted universally. The diffusion factor has been recognized as an acceptable although very inaccurate candidate to detect stall. The concern of the present approach is to dispose of a robust criterion that indicates unacceptably high losses and interrupts the calculation to avoid convergence problems. This is provided by a stability criterion which is based on the work of several authors like Greitzer [91] or Day [92] and was used by Freeman and Cumpsty [87] to predict supersonic compressor performance. This criterion stipulates that the blades operate in the stable domain as long as an increase in incidence at constant rotation speed (equivalently, a decrease in axial flow speed) leads to an increase in outflow static pressure (or at least a decrease small enough). The blade row operates in the stable domain as long as the following criterion is satisfied:

$$\frac{W_{xA}}{P_{tA}} \frac{\partial P_B}{\partial W_{xA}} < 0.2$$

During the development and testing of the aerodynamic routines, this stability criterion has proven to be more reliable than the diffusion factor, especially at high supersonic speeds where the diffusion factor does not correlate well with the shock loss.

2.6.3 Loss caused by boundary layers

The entropy created in the boundary layer developing on the blades is given by Denton [75]:

$$rT_t \cdot \Delta S_{blade} = \frac{\int C_d \rho W^3 d\ell}{\rho W_x s}$$

The entropy rise depends on the third power of the external flow velocity at the edge of the boundary layer. As mentionned by Denton, this term does not include the entropy generation during the mixing process of the wake, which may represent up to one third of the total loss from compressor blades with an adverse pressure gradient. An alternative but equivalent approach by Lieblein [74] proposes to correlate the one-sided momentum thickness δ_2 with the diffusion factor defined previously.

$$\delta_2 = \frac{C_f}{2} L \cdot F(D), \text{ where } F(D) = 0.5 + 0.5 \cdot \exp\left(3D + 2D^2\right) \tag{2.14}$$

The airfoil semi-perimeter L can be approximated by $L = c\frac{(\chi_{LE}-\chi_{TE})/2}{\sin((\chi_{LE}-\chi_{TE})/2)}$. It roughly corresponds to the chord length but may be significantly larger for highly cambered stator or turbine blades. The function F is empirical and several versions of it were proposed by Lieblein and other authors. At zero-pressure gradient, $D = 0$ and $F = 1$, so we retrieve the flat-plate result $\delta_2 = \frac{C_f}{2} L$. We propose the following model for the chordwise-averaged skin friction coefficient C_f for turbulent boundary layer :

$$C_f = C_{f0} \cdot \left(\frac{10^6}{Re}\right)^{0.2} \cdot \frac{1}{\sqrt{1 + \frac{\gamma-1}{2} M^2}} \tag{2.15}$$

Various studies suggest a value of $C_{f0} = 0.0045$ (see Schlichting [93]). Figure 2.4 presents a comparison of the correlations used to estimate the momentum thickness. The quantity depicted as the loss factor is basically the term $F(D)$ of Eq.(2.14) summed on the suction and pressure sides. The first correlation was proposed by Lieblein [74]; alternative correlations were later proposed by Grieb [86], Wright and Miller [73], Koenig [94], and Koch and Smith [71]. The correlation presently implemented is very close to the others.

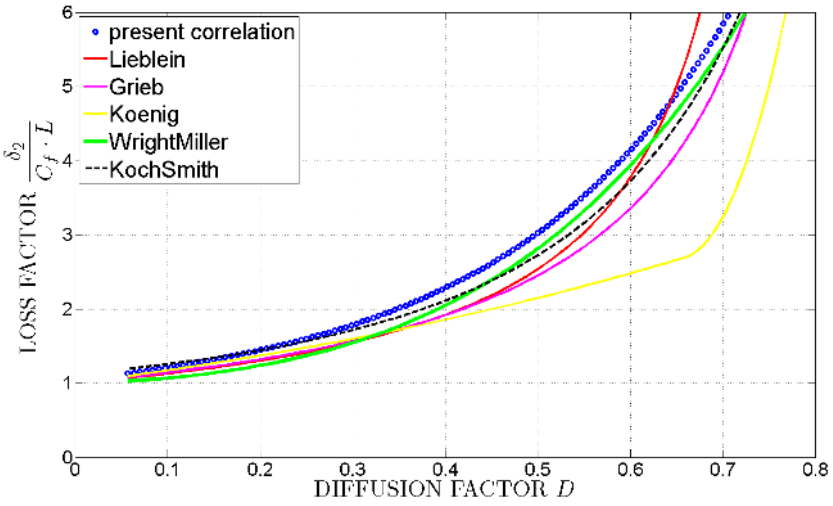

Figure 2.4: Comparison of the loss correlations

The 99% boundary layer thickness δ_0, the displacement thickness δ_1 and energy thickness δ_3 are obtained from the momentum thickness through the shape factors H_{12}, H_{32}, and H_{10} which are defined

as follows:

$$H_{12} \equiv \frac{\delta_1}{\delta_2} \ , \ H_{32} \equiv \frac{\delta_3}{\delta_2} \ , \ H_{10} \equiv \frac{\delta_1}{\delta_0} \tag{2.16}$$

We propose a model for calculating the shape factors as functions of the diffusion factor D only. The dependence on the Reynolds number Re is ignored here, which is a reasonable assumption for boundary layer mostly turbulent over the airfoil without laminar bubble separation. It has been observed from experiments that the shape factors can be roughly correlated to the intensity of the pressure gradient over an airfoil. The following table summarizes the experimental observations:

loading	asymptotic values for accelerating BL ($D < 0$)	zero-pressure gradient ($D = 0$)	near separation ($D \approx 0.55$)
H_{12}	1	1.3	2.7
H_{32}	2	1.8	1.5
H_{10}	0	0.13	0.45

Table 2.1: Shape factors of a turbulent boundary layer for different values of the pressure gradient

A model respecting the experimental observations, and the contuinity of the functions is given here:

$$\begin{aligned} H_{12} &= 1 + 2.795 \log\left(1 + 0.1133 e^{3.63D}\right) \\ H_{32} &= \frac{4H_{12}}{3H_{12} - 1} \\ H_{10} &= 0.5 \left(\frac{H_{12} - 1}{2}\right)^{0.7} \end{aligned} \tag{2.17}$$

According to Lieblein [74], the entropy generated in the boundary layer of the blade and its wake reads:

$$\Delta S_{BL} = \frac{2\delta_2}{h} \cdot \frac{H_{32}^{wake}/2}{\left(1 - \frac{H_{12}^{wake}\delta_2}{h}\right)^3} \cdot \frac{\frac{1}{2}\rho_m W_m^2}{P_{tA}} \ , \text{ where } H_{12}^{wake} = 1.08 \text{ and } H_{32}^{wake} = 1.93$$

2.6.4 Loss caused by shocks

There is no generally accepted method to describe analytically the entropy generated by the complex shock system formed in transonic compressors. One of the first attempts by Miller et al. [95] simplified the shock system to a single normal shock for which analytical formula are available. This model fails to describe correctly the rapid loss rise with increasing incidence, as pointed out by Freeman and Cumpsty [87]. They also explained that shock loss is inherently a combination of entropy rise within the shock itself and entropy created by the shock–boundary-layer interaction. Here, we propose a correlation for the shock-only entropy rise :

$$\Delta S_{shock} = 0.06 \cdot \frac{2\gamma}{3(\gamma+1)^2} \cdot \left(\max(0, M_{max}^2 - 1)\right)^2$$

The pre-shock Mach number on the surface blades is calculated based on the maximum surface velocities from Eq(2.8):

$$M_{max} = \max(\overline{M}_{SS}, \overline{M}_{PS})$$

2.6.5 Endwall loss

The physics associated with endwall flows is highly complex due to three-dimensionnal and unsteady flow. This is still not well understood and there is no analytical or empirical model recognized as being both accurate and reliable on different configurations. The endwall loss is usually divided into two components:

the annulus loss due to skin friction on the endwalls and secondary losses including all other loss sources. An extensive review of the various models existing is presented by Grieb [86]. The model we propose here is reduced to the annulus friction loss. The secondary losses are not modelled because we focus on the meanline approach and do not acccount for the tip flow as a noise source.

$$dS_{endwall} = 2C_f \cdot \frac{\frac{1}{2}W_x^2}{rT_t}$$

The secondary losses depend on the lift coefficient of the blades and on the adverse pressure gradient. It should be also noted that the model does not account for the influence of blade aspect ratio. Wennerstrom [96] has identified it is a major parameter driving endwall loss and the stall limit. The author knows from the literature no analytical or semi-empirical model that would include these aspects thoroughly. A diffusor analogy as proposed by Koch [97] might be implemented to predict the boundary layer development on the wall. In that case, an essential parameter is the initial value of the endwall boundary layer thickness at the beginning of the diffusion.

2.7 Fan performance

The following quantities are commonly used as design parameters to analyze and characterize the aerodynamic behaviour of a compressor:

- The first parameter is the stage loading coefficient ψ. The german definition adopted here differs from the english one by a factor 2. In multiple-stage compressors, the number of stages required is directly linked to this parameter.
- The second parameter ϕ is called the flow coefficient. It is generally desirable to maximize this parameter as it implies a higher mass flow per unit area and therefore a more compact engine. The flow coefficient is limited by choking within the blade passage. The flow coefficient is similar to the advance ratio J defined for unducted propellers and open rotors.
- The degree of reaction $\Re$ is the third parameter free to be chosen during the design phase of a multiple-stage compressor. It represents the balance of work (and loss) between the rotor and the stator. It is also related to the choice of the flow angle between two successive stages. In the case of purely axial inflow typically encountered in single-stage fans, this parameter is not free but depends on the stage loading coefficient.
- The last parameter τ will be called the turning angle coefficient. The loss coefficient and the lift-to-drag ratio of the blades are primarily determined by τ. It is a measure of the aerodynamic loading of the whole blade row and of the flow turning.
- The parameter σ is called the throttling coefficient or 'Drosselziffer' in the german literature (see Grieb [86]). It is an important stability parameter and we will see it is a measure of the impact of endwall losses.
- The parameter π is the power coefficient and is an indication of the compactness of the stage relative to its work output.

$$
\begin{aligned}
\psi &\equiv \frac{\Delta H_t}{U^2/2} = \frac{2\Delta W_t}{U} \\
\phi &\equiv \frac{W_x}{U} \\
\Re &\equiv \frac{(\Delta H)_{rotor}}{(\Delta H)_{rotor} + (\Delta H)_{stator}} \qquad \underbrace{= 1 - \frac{\psi}{4}}_{\text{axial inflow only}} \qquad \text{(ratio of static-enthalpy rise)} \\
\tau &\equiv \frac{\psi}{\phi} = \frac{2\Delta W_t}{W_x} = 2(\tan\beta_A - \tan\beta_B) \\
\sigma &\equiv \frac{\Delta H_t}{W_x^2} = \frac{\psi}{2\phi^2} \\
\pi &\equiv \frac{Q \cdot \Delta H_t}{\rho A U \cdot U^2/2} = \phi \cdot \psi
\end{aligned}
\tag{2.18}
$$

The parameters presented here will strongly affect the performance of a compressor, which is measured mainly through two figures of merit: the pressure ratio and the efficiency. The pressure ratio is defined as the ratio of the outflow to the inflow total pressure expressed in the fixed frame of reference: $PR \equiv \frac{P_{tB}}{P_{tA}}$. The efficiency measures the quality of the compression with respect to a thermodynamically ideal process. Two different efficiencies are usually considered, which also have a slightly different physical meaning: the isentropic efficiency η_{ise} and the polytropic efficiency η_{pol}.

$$
\begin{aligned}
\eta_{ise} &\equiv \frac{(\Delta H_t)^{ise}}{\Delta H_t} = \frac{\int_A^B (dT_t)^{ise}}{\int_A^B dT_t} = \frac{T_{tB}^{ise} - T_{tA}}{T_{tB} - T_{tA}} \\
\eta_{pol} &\equiv \frac{(dH_t)^{ise}}{dH_t} = \frac{\int_A^B \left(\frac{dT_t}{T_t}\right)^{ise}}{\int_A^B \frac{dT_t}{T_t}} = \frac{\log\left(\frac{T_{tB}^{ise}}{T_{tA}}\right)}{\log\left(\frac{T_{tB}}{T_{tA}}\right)}
\end{aligned}
\tag{2.19}
$$

where the mass-specific total enthalpy is $H_t = c_p T_t$ and the parameter T_{tB}^{ise} is the fictive outflow total temperature that would be required if the compression process were ideal; it is smaller than the actual outflow total temperature T_{tB}, and is given by:

$$
T_{tB}^{ise} = T_{tA} \cdot \left(\frac{P_{tB}}{P_{tA}}\right)^{1-1/\gamma}
$$

The polytropic efficiency is defined similarly to the isentropic efficiency but for an infinitely small compression process. Its dependence on pressure ratio is much weaker, therefore it can be used to compare the quality of compressors having different pressure ratios. The polytropic efficiency is directly related to the entropy generated during an infinitesimal compression process:

$$
(dH_t)^{ise} = dH_t - \frac{\gamma - 1}{\gamma} H_t dS
$$

$$
\eta_{pol} = 1 - \frac{\gamma - 1}{\gamma} \frac{dS}{dH_t/H_t} = 1 - \frac{\frac{1}{2}W_m^2}{dH_t}\omega
$$

We will now derive a simple relation linking the polytropic efficiency to the lift-to-drag ratio $\frac{C_L}{C_D}$ and to the design parameters ϕ and $\Re$. We consider an incompressible flow with constant axial velocity across the stage. The entropy rise dS can be formulated in terms of loss coefficient according to Eq.(2.12). The

expressions for the entropy rise of the first rotor, stator and second rotor, respectively, are given by:

$$\begin{aligned} dS_{rotor1} &= \omega \cdot \frac{\rho}{2P_t} \cdot \left(W_x^2 + \left(U - \frac{\Delta W_t}{2} \right)^2 \right) \text{ , for a TF or CRTF} \\ dS_{stator} &= \omega \cdot \frac{\rho}{2P_t} \cdot \left(W_x^2 + \left(\frac{\Delta W_t}{2} \right)^2 \right) \text{ , for a TF} \\ dS_{rotor2} &= \omega \cdot \frac{\rho}{2P_t} \cdot \left(W_x^2 + \left(U + \frac{\Delta W_t}{2} \right)^2 \right) \text{ , for a CRTF} \end{aligned} \tag{2.20}$$

The loss coefficient ω is assumed identical for all blade rows. The rotation speed of the second rotor is equal in magnitude and opposite in sign to that of the first rotor U. As the second rotor operates at higher flow velocities than the first rotor, it produces more losses. This explains why the efficiency of the second rotor is usually lower than that of the first rotor.

We can now further simplify the expression of the polytropic efficiency by using Euler turbomachinery equation $dH_t = U\Delta W_t$ (see Eq.(2.5)) and identifying $\frac{\omega}{2\Delta W_t/W_x} = \frac{C_D}{C_L}$ (see Eq.(2.11)). We obtain for a rotor–stator stage:

$$\eta_{pol} = 1 - \frac{C_D}{C_L} \left(2\phi + \frac{\Re^2 + (1-\Re)^2}{\phi} \right) \tag{2.21}$$

The details of the derivation are given by Grieb [86]. We observe from this equation that two terms determine the efficiency: the lift-to-drag ratio of the blades, which is a decreasing function of the turning angle coefficient τ and depends on the detailed blade geometry, and a second term depending on global design parameters (flow coefficient and degree of reaction). This second term reaches an optimum for $\phi = 0.5$ and $\Re = 0.5$, which is indeed the design point usually chosen for multiple-stage compressors. However, in the case of a fan stage with purely axial inflow, this design would imply a turning angle coefficient of 4 which is far too large to ensure a good lift-to-drag ratio. Therefore, axial-inflow fans are usually designed for a stage loading around 0.9 and a flow coefficient of 0.8 (see Grieb [86]), in order to maintain an affordable value of τ below 1.5. They operate at a relatively high degree of reaction around 0.8 which means that most of the static pressure rise (and most of the loss) comes from the rotor, making the overall fan performance more sensitive to the rotor design than to the stator design.

A similar expression can be derived for a rotor–rotor stage. In that case, each rotor contributes to the total enthalpy rise, which is then given by $dH_t = 2U\Delta W_t$. The degree of reaction of a rotor–rotor stage with axial inflow is given by: $\Re = \frac{1}{2}\left(1 - \frac{\psi}{4}\right)$. We obtain a similar relation:

$$\eta_{pol} = 1 - \frac{C_D}{C_L} \left(\phi + \frac{1 + (1-2\Re)^2}{\phi} \right)$$

Here again the second term has an optimum for $\Re = 0.5$ but for a higher flow coefficient $\phi = 1$ and this represents a fundamental advantage of the contra-rotating turbofans compared to the single-rotating ones. Designing at higher mass flow rate implies a more compact engine and a lower stage loading. Moreover, the blades can be designed at a significantly lower turning angle coefficient, which means a better lift-to-drag ratio, and less blades, which presents the advantage of delaying choking.

The qualitative advantage of the CRTF is detailed in a more quantitative way now. Let us consider the design space (ϕ,ψ), also called the Smith chart [98]. Figure 2.5 depicts the variation of polytropic efficiency as a function of the the flow and loading coefficients. It is a usual representation in compressor design and is called the Smith chart. The chart has been calculated based on the aerodynamic models presented so far and assuming incompressible flow and constant axial velocity across the fan stage. Moreover, the endwall loss generated by the mere friction has been here additionally taken into account (the axial aspect ratio of the blades is 4 and the drag coefficient for endwall loss is assumed constant). Over the

whole design space, CRTF presents roughly 2% higher efficiency than a conventional rotor–stator stage. Moreover, the region of maximum efficiency is more flat and located at higher flow coefficients.

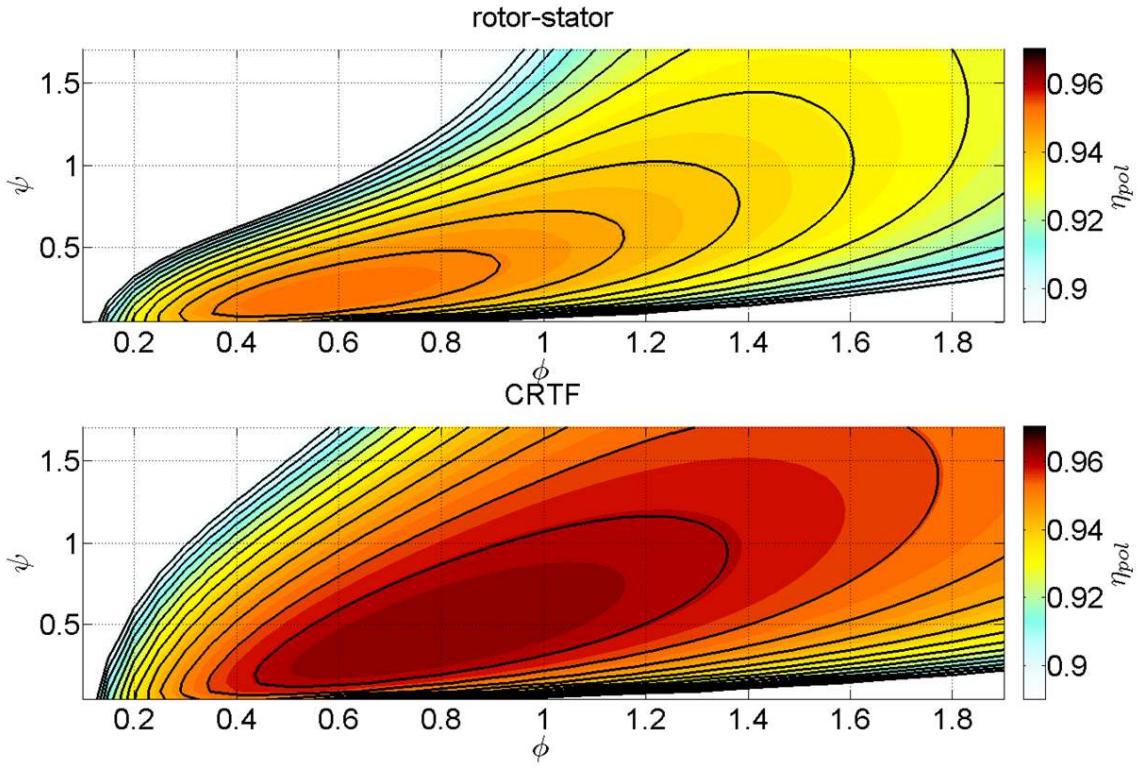

Figure 2.5: Smith Chart for CRTF(lower) and SRTF(upper)

The maximum efficiency obtained from those simplifed formulas lies around 0.96, which is significantly better than the actual efficiency of rotors. As reported by Cumpsty, the meanline approach underestimates the loss, because a large part is attributable to endwall losses and the interaction loss between endwall and the blades. This reminds us that the results obtained from a meanline prediction should be regarded cautiously.

2.8 Application of the models

The aerodynamic models described so far will now be illustrated and applied to the performance prediction of the so-called DLR UHBR fan, which is a research rotor–stator stage developed and manufactured in 2006 by the DLR Institute of Propulsion Technology. The design procedure is detailed by Kaplan [99]. The UHBR fan is designed to equip a ultra-high-bypass ratio engine ($BPR \approx 12$). The main characteristics of the UHBR fan geometry and performance in cruise are listed in Table 2.2. The aerodynamic design point (ADP) is Top of Climb (or Max Climb). At Take-off the fan is operated at a relative tip Mach number below 1.05, thus preventing the emission of strong shock-induced buzz-saw noise. A second fan developed by DLR is also considered: the counter-rotating fan concept named CRISP2, whose design is the result of an automated multidisciplinary optimization by Goerke and Le Denmat [100].

The calculations are performed on a 1/3-scale model of the UHBR fan measured at the M2VP compressor test facility of the DLR Institute of Propulsion Technology in Cologne. The full-scale diameter of the fan is 2.4 m. The performance is evaluated for the meanline position at 70% of the blade height

model fan diameter [m]	0.8	0.8
rotor hub-to-tip ratio	0.27	0.24
rotor blade count	22 / 38	12 / 10
axial aspect ratio of rotor blades	2.5 / 2.6	3.1 / 2.6
reduced speed of rotors [rpm] in cruise	-7300 / 0	-5045 / 3982
reduced mass flow [kg/s] in cruise	98	158

Table 2.2: Geometry parameters of UHBR (left) and CRISP2 (right) fans

fan pressure ratio	1.38	1.30
fan isentropic efficiency	0.90	0.93
rotor-face axial Mach number	0.63	0.66
rotor tip relative Mach number	1.13	1.04
flow coefficient ϕ	0.85	1.04
loading coefficient ψ	0.99	0.61
degree of Reaction $\Re$	0.75	0.49
turning angle coefficient τ	1.16	0.59

Table 2.3: Design parameters in Cruise of the UHBR (left) and CRISP2(right) fans

($KML = 0.7$). In a first time, we will show the aerodynamic performance of the rotor blade row alone, considered in the relative frame of reference. In a second time, the performance of the whole fan stage will be described.

2.8.1 Cascade performance

The aerodynamic performance of a cascade is usually characterized by the variation of losses and other flow quantities depending on the incidence of the blades and on the inflow Mach number in the reference frame locked to the blade row. Figure 2.6 presents the two-dimensional map of the cascade losses of the UHBR stator. Non-coloured domains are outside the domain of operation of the cascade (due to stall or choking). Regions of high losses are marked in brown colours.

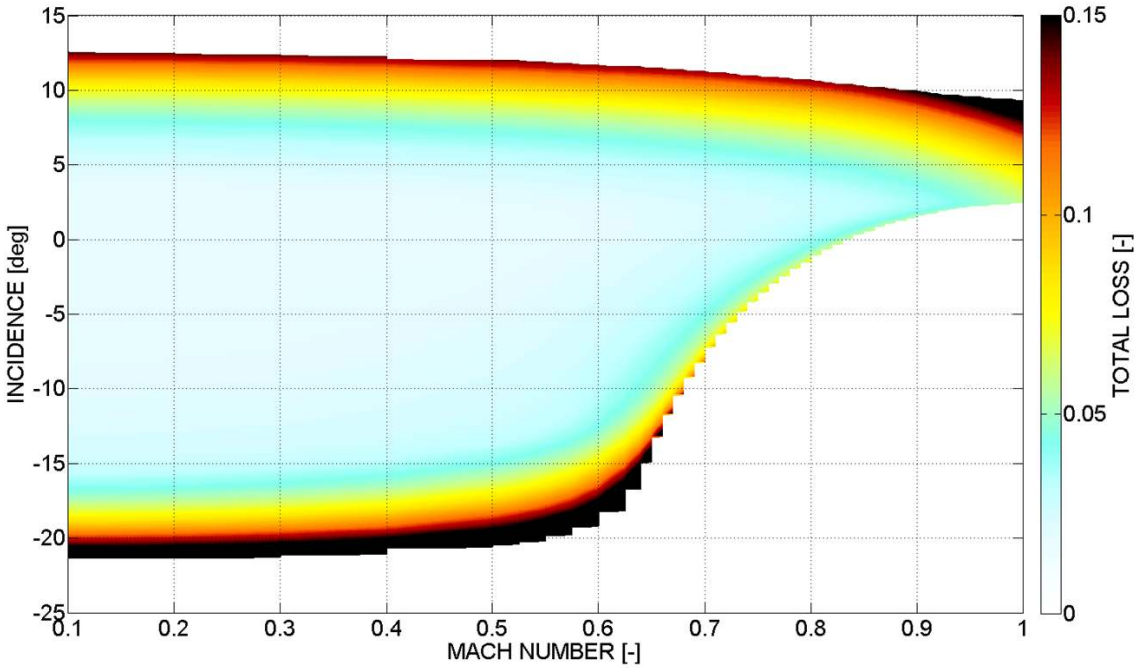

Figure 2.6: Cascade map representing the variation of loss as a function of the inflow Mach number and incidence angle

Several general remarks can be made:

- The reduction of the working range as Mach number is increased is clearly visible on such cascade diagrams. For low Mach numbers, the upper and lower incidence limits correspond to stall on the suction and pressure sides, respectively. They change weakly with the Mach number. Beyond a certain value of Mach number related to the throat area of the cascade, the working range on the negative incidence side starts to be drastically reduced as a result of choking within the blade passage.

- The loss characteristics presents a relatively flat minimum centered near the zero-incidence case. The minimum loss incidence is not prescribed a priori using empirical correlations but results from the superimposition of the contributions of the pressure and suction side boundary layers, which follow opposite trends as incidence is increased. The loss produced on the suction side of the blades dominates at positive incidence, whereas it is mostly determined by the pressure side at negative incidence.

- Increasing the inflow Mach number significantly modifies the loss characteristics. The extent of the low loss region (also called working range) is reduced as the Mach number approaches unity. The reduction in working range is more pronounced on the negative incidence side, which is attributable to the shift of the choking limit towards positive incidence values as supersonic inflow conditions are reached, see Cumpsty [85].

- The minimum loss incidence slightly increases from zero at low Mach number towards roughly 3 degrees at sonic inflow. The choking incidence strongly increases and the incidence at which stall is detected decreases slightly. These results are in agreement with other empirically-based models such as the one developed at Rolls-Royce by Wasdell, Wright and Miller [72, 73].

- Also the shape of the loss characteristics is affected by the inflow Mach number. At low Mach numbers, the curves have a relatively flat minimum. At high Mach numbers, the loss curve is more suitably described by a parabolic curve of order 2. This is in agreement with the observation of Grieb [86].
- At supersonic inflow conditions, the choking incidence and minimum-loss incidence are identical and the loss curve does not feature a minimum with zero derivative. This was also observed by Bloch [101] when performing 2D-simulations of supersonic cascades. Bloch attributed the smooth transition between started and unstarted flow observed in a real fan map to three-dimensional effects and the spanwise transfer of airflow from started regions to unstarted regions.

2.8.2 Fan performance at off-design conditions

The present section is dedicated to the assessment of the prediction at off-design conditions. The performance maps of two different fans designed by the compressor department of DLR [99, 102] have been calculated and depicted in Fig. 2.7. Lines of constant rotor speed at plotted in the space fan pressure ratio vs. mass flow rate Q. The left side of the figure contains the map of a rotor-stator fan stage with a design pressure ratio of 1.38. The right side of the figure shows the map of a contra-rotating fan with a design pressure ratio of 1.3. The predicted iso-speed lines are colored in gray and the actual performance is marked with symbols and thin black lines. The iso-speed lines of the fan isentropic efficiency are plotted in Fig. 2.8. The following conclusions are given:

- The prediction of the fan pressure ratio is acceptable in the vicinity of the design point and at part speeds in the domain of moderate loading. At high speeds where the flow is transonic and features a complex system of shocks interacting with detached boundary layers, the discrepancy is more pronounced.
- A significant overprediction of the pressure rise is done near the surge limit, which is probably due to the strong flow deviation caused by thick boundary layers developing on the blades. The deviation model currently used relies on simple theoretical considerations and only accounts for incidence and solidity: deviation vanishes in the limit of high solidity, and flow turning vanishes in the single-airfoil limit. Empirical corrections available in the literature might be added in the future to better model the performance near surge.
- The choking limit is slightly overpredicted at design and part speeds. Since choking is the consequence of flow blockage over the whole span and since its onset is very sensitive to cascade throat width and local Mach number, this limit cannot be predicted accurately by a meanline approach. The author prefers a simple robust approach over an empirical correlation tuned for a particular case but that would likely be unsuited in the more general case.
- Fan efficiency is overestimated by 1% to 2 % near the design point. This may be attributed to the underprediction of the endwall losses, which do not only consist of a skin-friction component but also boundary layer thickening through diffusion and interaction with the complex tip and hub vortex flows. The drop in efficiency at lower and higher speeds is fairly well predicted.

The off-design points particularly relevant during the flight mission are the mid-cruise or aerodynamic design point (DP), max-climb or top-of-climb (TP), and the three acoustic certification points: take-off sideline (SL), take-off cutback (CB) and approach (AP). The flight conditions and thrust requirements at each of these points (see Table 2.4) are the same for all engine configurations considered in the following studies; in particular, the noise levels will be compared at the same thrust condition. These conditions correspond to a single-aisle medium-range civil aircraft equipped with two engines (Airbus A320 or Boeing 737). The typical positions of the off-design points within the fan map are marked in Fig. 2.7 by black circles. Typical values of some flow parameters are summarized in Table 2.5 in the particular case of the DLR UHBR fan [99]. Top of climb (TC) is often considered as the true dimensioning point, as the fan must provide more thrust than in cruise (hence a higher pressure ratio) with a more severe mass flow

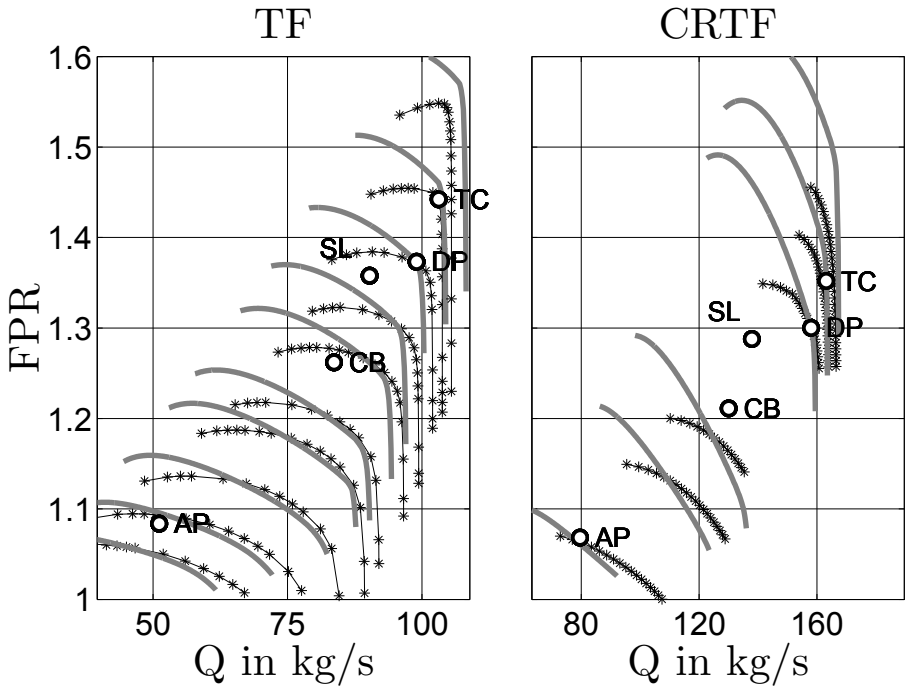

Figure 2.7: Validation of predicted pressure ratio at off-design conditions (prediction: solid gray lines, reference: black lines with icons) [76]

capacity (higher axial Mach number) which forces the fan to operate closer to the choking limit. The three points relevant for the noise certification are all situated at part speed and with a larger incidence than in cruise especially at approach, which is due to the weaker acceleration of the flow over the spinner as the Mach number is reduced. The sideline point (SL) is aerodynamically more critical as it is located at fairly high speed and closer to the surge limit as in cruise.

Table 2.4: Flight conditions and thrust requirements common to all configurations at specific operating conditions

	DP	TC	SL	CB	AP
Total net thrust in kN	37	44	170	110	38
Flight Mach number	0.78	0.78	0.21	0.35	0.21
Flight height in m	10500	10500	0	500	120

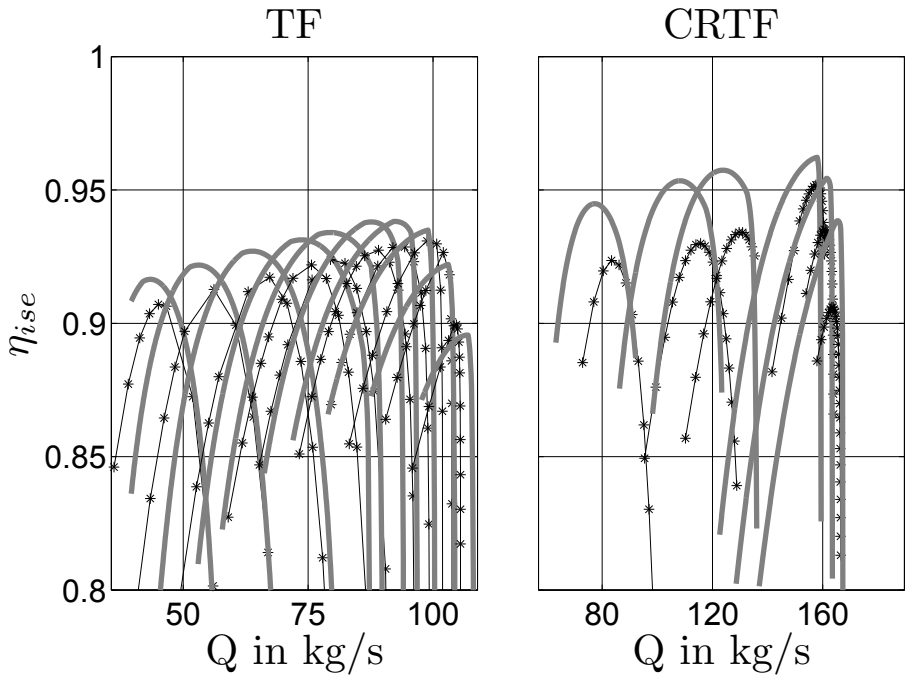

Figure 2.8: Validation of predicted efficiency at off-design conditions (prediction: solid gray lines, reference: black lines with icons) [76]

Table 2.5: Predicted fan parameters at off-design operating conditions in the particular case of the DLR UHBR fan

	DP	TC	SL	CB	AP
N_{corr} in %	100	106	95	85	54
FPR	1.38	1.44	1.35	1.26	1.09
η_{ise}	0.93	0.91	0.93	0.94	0.92
M_x	0.64	0.68	0.54	0.48	0.28
i in deg	3.1	2.9	6.0	5.8	7.8

2.9 Conclusion

The present models deliver realistic trends for the prediction of the fan aerodynamic characteristics of single- or counter-rotating fans. Despite of being a strong simplification, the meanline approach on which the models are based, captures several fundamental properties of the flow inside a turbofan stage and of its aerodynamic performance. The fact that the interpretation of the results is rendered more straightforward by the meanline approach supports the general philosophy presented in introduction 1: relating the acoustic features of a fan to its aerodynamic performance and deriving design guidelines.

Apart from the inherent limitations of the meanline approach that were discussed before, some aspects of the models could be improved while still being addressed on a meanline level:

- Deviation: this quantity is generally not zero at design conditions, especially for low-solidity blades. These blades do not only show high losses at high loading, they also have poor turning capabilities, even at design conditions. Introducing a model for the design deviation angle depending on blade solidity would move the designs of loaded fans to blades with a higher solidity.

- Shock loss: separating shock-only loss from the shock–boundary layer interaction loss is not physically well grounded and leads to difficulties in deriving empirical prediction methods that reproduce correctly the variations with incidence, Mach number and blade geometries. The theoretical approach proposed by Freeman and Cumpsty [87] could be extended to account for airfoil camber, arbitrary solidity, duct contraction, while covering the subsonic and supersonic regimes equally. In that case this so-called extended Freeman model would include both the shock and boundary layer loss, and address the off-design flow conditions without any additional loss model.
- The effect of the duct contraction (MVDR) on the shock loss is not modelled presently. It is known that increasing the MVDR reduces the choking limit but may significantly improve the performance at design conditions. This effect could also be captured by the extended Freeman model.

Chapter 3

Engine and fan aerodynamic design

3.1 Motivation and approach

In the previous chapter 2, aerodynamic models were proposed to compute the flow and performance of a given fan once its geometry and operating conditions (mass flow rate and rotation speed) are known. However, at an early design stage, only a few global parameters concerning the engine architecture and thermodynamic cycle can be specified. The purpose of the present module is precisely to find the optimal geometry and operating conditions satisfying the global design specifications for the engine.

These specifications consist of the number of engines, their type (TF, CRTF, CROR), the pressure ratio of the fan and some parameters concerning the flight conditions such as Mach number and altitude, and the thrust required by the aircraft to maintain its flight path. For ducted configurations, the axial Mach number upstream of the first rotor is an important additional design parameter. For unducted configurations, this parameter is constrained by the thrust and cannot be chosen freely.

The quantities determined by the design module are essentially the diameter and length of the engine, as well as geometry parameters proper to the fan like blade number, chord length, stagger angles and the operating conditions.

The acoustic comparison of different engines is made in general difficult by the strong discrepancy existing in aerodynamic and flow conditions in which the engines operate. With the help of the present design module, a common criterion based on the selection of the best aerodynamic design for each engine configuration can be drawn to compare the noise emission of different engine architectures.

3.2 Design constraints

The engine design procedure consists of an optimization of the engine and fan parameters associated with the lowest fuel consumption for the specified user requirements. The constraints listed below define the design space in which the search for the optimum is carried out. The optimal solutions found depend on this set of constraints.

- Design point: the design of the engine is performed at only one operating point, called the aerodynamic design point (ADP), which usually corresponds to mid-cruise flight conditions. The following design constraints are imposed at ADP but may not be maintained at off-design points.
- Optimization for best fan efficiency: the fitness function (or quantity to be optimized) during the procedure is basically the fuel consumption of the engine. In the case of a swirl-free exhaust flow, this is equivalent to searching for the engine with the best fan efficiency. In the present version of the module, the design is performed based on aerodynamic considerations solely. Future versions may include some acoustic criteria (for example as an additional fitness function).

- Stability margin: apart from being located in the region of best efficiency the design must also be robust, that means its performance has to remain stable over a range of positive incidences. The rotation speed and mass flow characterizing the stability point are as follows:

$$N_{off} = N_{ADP}$$
$$Q_{off} = Q_{ADP} \cdot (1 - SM/100)$$

  The user-defined parameter SM is called the stability margin and is expressed in percent of the design mass flow rate. During the design of a blade row (cascade design procedure), an average efficiency based on the contributions of the design and stability points (weighted by the relative loss level) is maximized and the corresponding solidity is determined. A design with a large margin (typically 20%) presents high-solidity blades, stable operation over a wide range (well beyond the usual off-design flight points), but this is compensated by a lower efficiency in cruise conditions. Such a design choice (also called stall margin) is an essential aspect of fan design and explains for example why the rear-rotor of a CRTF-concept has a higher solidity than the front-rotor. It should be noted that no stability margin is defined in that sense for a CROR engine: the off-design operations are regulated by a variable-pitch system so that the blades are operated near their optimal incidence at all flight points.

- However, no system for adapting the blade stagger angle or the exhaust nozzle area is modelled here. Once determined at the design point, the geometry of the fan is frozen and constant for all other off-design points.

- Engine architecture: the engine is composed of five components, depicted in Figure 3.1. The intake, the first rotor (R1), an inter-stage section, the second rotor or the stator (R2), and finally a convergent exhaust nozzle. The engine can be a conventional turbofan with a rotor–stator stage (TF), a counter-rotating fan (CRTF) or a counter-rotating open rotor (CROR). In the latter case, there is no outer duct enveloping the rotors. For the sake of simplicity, neither pylons are modelled with the CROR nor structural struts are modelled with the ducted configurations TF and CRTF.

- The meanline radius R_m is constant across the fan stage. The duct contours are designed to impose streamlines parallel to the engine axis. This restriction is of course not applicable to radial compressors.

- The variation of axial velocity W_x across a blade row is an essential aspect of fan design. Allowing for constant axial velocity limits flow diffusion and thus separation but it imposes a marked duct contraction and increases the flow velocities impinging the downstream blade row. A compromise is usually found by selecting an appropriate value of the meridional-velocity–density ratio ($MVDR$, see Eq.(2.4)). A correlation based on the density ratio is used to set the design value of the $MVDR$ and finally determine the duct contours that satisfy this condition:

$$(MVDR)_{des} = \left(\frac{\rho_B}{\rho_A}\right)^{n_{MVDR}}$$

  The value of the user-defined exponent n_{MVDR} is comprised between 0 (no duct contraction) and 1 ($W_x = const$). A value of 0.5 is representative of modern fans.

- The blades operate at a specific incidence providing the minimum loss: this is the design incidence presented in the previous chapter 2. For small Mach numbers, the design incidence is zero. For higher Mach numbers approaching choking condition, the design incidence may assume moderate positive values up to 5 degrees. Note that the incidence for best efficiency is usually slightly higher than the design incidence, however the difference in efficiency is negligible due to the flat shape of the optimum.

- Swirl-free exhaust: the outflow angle of the fan (behind the second rotor or the stator) is zero. In that case, searching the engine with the lowest fuel consumption is equivalent to searching the fan

with the highest isentropic efficiency. This constraint is not applicable for the design of a single propeller, as the appropriate choice for the exhaust swirl is an essential aspect of the optimization.

- Rotor inflow Mach number: the optimal relative inflow Mach number M_{rel} of a rotor (at the meanline radius) is searched within the range $M_x < M_{rel} < 1.5$. This corresponds to a maximum relative tip Mach number $M_{tip,rel}$ of roughly 1.7, and a maximum fan pressure ratio around 1.9.

- The number of blades is determined by the axial aspect ratio of the blades (specified by the user) and by the solidity of the blade row which is found automatically by the optimization routines. No acoustic criterion is implemented in the present version of the module. The axial aspect ratio varies for modern rotors between 2 and 2.5 (before the 1990s the blades had higher values between 3 and 4). Low-aspect-ratio blades are characterized by good aerodynamic and aero-mechanical stability (see Wennerstrom [96]). For a CROR, slender blades with a high axial aspect-ratio around 4 or 5 are important to keep a low tip vortex drag. However the associated loss is not modelled in the present version.

- Off-design points: after the engine has been designed at ADP, calculations are performed at the following off-design points: top of climb and the three acoustic certification points take-off and cut-back and approach. The design is discarded if the calculation does not converge or returns an error status. This may be an indication that the stability margin chosen is too low: especially at the take-off and approach points, the fan may operate at strong positive incidence and needs a sufficient blade surface to avoid flow separations and loss of performance. Convergence problems obtained at top of climb are usually attributable to the proximity to choking conditions (too large values of axial Mach number or too high flow blockage inside the blade rows).

- For the counter-rotating fan architectures CRTF and CROR, the ratio of rotation speed of the rotors is kept constant for all off-design points and identical to that obtained at ADP. The speed ratio at ADP results from the aerodynamic optimization without taking into account the constraints imposed by the low-pressure turbine or a gear-box.

- Because only the bypass flow of the fan is modelled, it is not possible to compute the bypass ratio directly. However, it can be roughly estimated at the design point by correlation with the fan pressure ratio (FPR). The shaft power on the low-pressure turbine (LPT) and on the fan are given by:

$$\begin{aligned} \Pi_{LPT} &= Q_{core} \cdot c_p \cdot (\Delta T_t)^{LPT} \\ \Pi_{fan} &= (Q_{core} + Q_{bypass}) \cdot c_p \cdot (\Delta T_t)^{fan} = \Pi_{LPT} \\ (\Delta T_t)^{fan} &= T_{t0} \cdot (FPR^{(\gamma-1)/(\gamma\eta_{pol})} - 1) \end{aligned}$$

The LPT power is considered to be entirely transferred to the fan. The bypass ratio BPR is defined as the ratio of the bypass to the core mass flow rate. We obtain:

$$BPR \equiv \frac{Q_{bypass}}{Q_{core}} = \frac{(\Delta T_t)^{LPT}}{T_{t0}} \cdot \frac{1}{FPR^{(\gamma-1)/(\gamma\eta_{pol})} - 1} - 1 \tag{3.1}$$

The first term of the correlation is the ratio of the LPT total temperature drop to the inflow total temperature and is assumed to have a constant typical value of 1.36. The polytropic efficiency of the fan is also assumed constant with a value of 0.93.

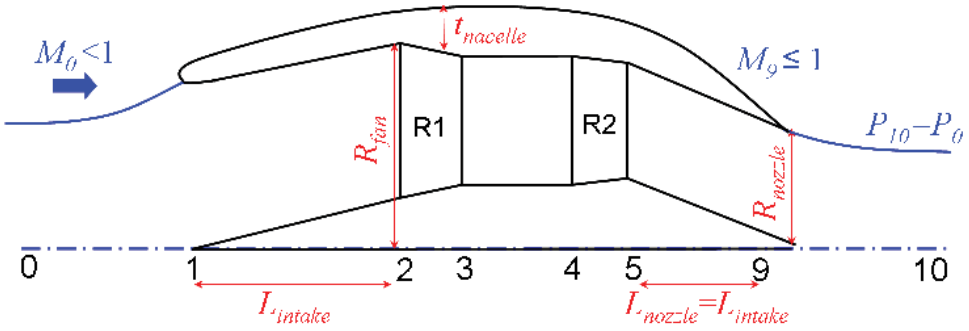

Figure 3.1: schematic view of the ducted-fan engine configuration.

Figure 3.1 depicts schematically the architecture of a ducted-fan engine as modelled in the module. For unducted configurations, the outer fan cowl is replaced by a streamline. The different stations are listed from 0 to 10. The stations 0 and 10 correspond to the far upstream and far downstream positions, respectively. The engine entry plane is located at position 1. The fan entry plane is located at position 2. Position 9 is the engine exhaust plane at which the jet exhaust pressure and the ambient pressure are identical $P_9 = P_0$ if the jet is subsonic $M_9 < 1$. For critical convergent nozzles with exactly sonic flow at the nozzle exist, we have $M_9 = 1$ and $P_9 > P_0$.

3.3 Preliminary engine design

3.3.1 Methodology

Before optimizing the geometry of the fan blades, the global dimensions of the engine have to be determined during a preliminary design phase, as shown in Figure 3.2. The most important parameter to meet the thrust requirements of the aircraft is the mass of airflow entering the engine. Based on this quantity, it is possible to determine the fan diameter. Subsequently, the nozzle diameter is determined to meet the condition $P_9 = P_0$ or $M_9 = 1$ at the exhaust plane. All other dimensions of the engine are derived by simple scaling. The wetted surface of the nacelle and the engine weight affect the drag produced by the engine itself, which in turn is added to the original thrust requirement and the airflow is corrected. This iterative process is repeated until the size of the engine has converged.

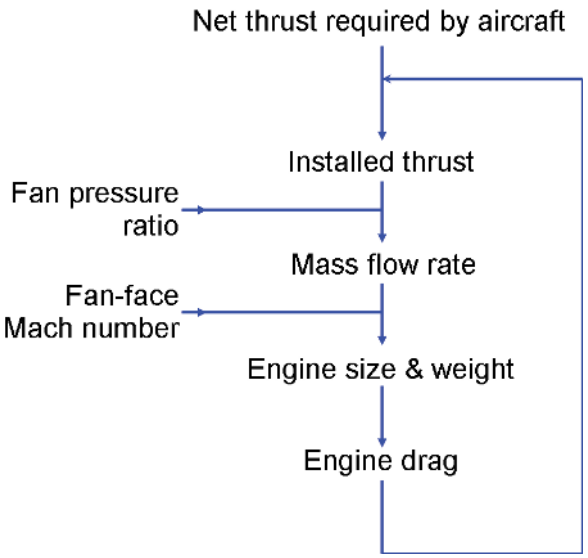

Figure 3.2: Principle of the engine preliminary design

The calculation steps presented in Figure 3.2 will now be detailed.

3.3.2 Engine thrust

The thrust required by the aircraft for each engine is called the net thrust or installed thrust. It is to be distinguished from the uninstalled thrust, which is usually the quantity guaranteed by the engine manufacturer. The uninstalled thrust, which is for example described in a book by Mattingly et al. [103], depends on the airflow Q ingested by the engine and the so-called specific thrust $V_{10} - V_0$ representing the acceleration of the flow by the engine:

$$T_{uninst} = Q(V_{10} - V_0) \tag{3.2}$$

The term QV_{10} is usually referred to as gross thrust, and is the thrust obtained during static tests. The term QV_0 is sometimes called the ram drag. The net thrust is the difference between the uninstalled thrust and the drag produced by the engine itself. The net thrust is usually calculated by the aircraft designer. In the present model, we propose to consider two terms for the engine drag: the nacelle drag D_n due to flow spillage and the friction surfaces enveloping the engine and the additional induced drag D_i which is the vortex-induced drag generated at the aircraft wing tips but caused by the engine weight. The interaction drag between the nacelle, the pylon and the wing is considered constant and already included in the net thrust requirements, so it will not be modelled.

$$T_{net} = T_{uninst} - D_n - D_i \tag{3.3}$$

The specific thrust can be determined prior to the engine sizing as it solely depends on the thermodynamic cycle of the engine (mostly the pressure ratio and to a lesser extent the fan isentropic efficiency). For the sake of simplicity, we will consider here that the engine pressure ratio is the fan pressure ratio

FPR specified by the user. The specific thrust can be calculated by using the following relations:

$$\begin{aligned} V_{10} - V_0 &= (V_9 - V_0) + \frac{P_9 - P_0}{\rho_9 V_9} \\ V_9 &= \sqrt{2c_p(T_{t9} - T_9)} \\ T_{t9} &= T_{t0} \cdot \left(1 + \frac{FPR^{\frac{\gamma-1}{\gamma}} - 1}{\eta_{ise}}\right) \\ P_{t9} &= P_{t0} \cdot FPR \\ T_9 &= T_{t9} \cdot \left(\frac{P_9}{P_{t9}}\right)^{\frac{\gamma-1}{\gamma}} \end{aligned} \tag{3.4}$$

The isentropic efficiency of the fan η_{ise} defined in Eq.(2.19) is a priori unknown and will be obtained from the fan design routines. Only a few iterations are necessary to converge as the efficiency of well-designed fans is fairly high and can be regarded from the point of view of the thermodynamic cycle as nearly constant.

3.3.3 Engine airflow and fan diameter

Based on the uninstalled thrust and specific thrust, Eq.(3.2) can be reformulated to provide the airflow Q, and subsequently the cross-section area in front of the first rotor:

$$A_2 = \frac{Q}{\rho_2 V_2}$$

In the case of ducted configurations the rotor-face axial velocity V_2 is specified by the user in form of the axial Mach number. For the unducted CROR configuration, this velocity is not a free design parameter but is constrained by the pressure ratio. According to the actuator disk theory, the CROR is modelled by a disk producing a static pressure jump $\Delta P = P_{t0}(FPR - 1)$ in axial incompressible flow, the axial velocity in the disk plane is then:

$$V_2 = \frac{1}{2}\left(V_0 + \sqrt{V_0^2 + 2\frac{P_{t0}}{\rho_0}(FPR - 1)}\right)$$

Due to the incompressible flow assumption, the axial velocity is slightly underestimated. Moreover it must be below the sonic limit. As a result the pressure ratio of the CROR has to be limited to a maximum value around 1.3 at cruise flight conditions (35000 ft altitude and flight Mach number of 0.78).

The diameter of the first rotor is:

$$D_{fan} = 2\sqrt{\frac{A_2}{\pi(1-\eta)}}$$

The parameter η is the hub-to-tip ratio at the entry of the fan and is a free design parameter specified by the user. Similarly, the diameter of the exhaust nozzle is given by:

$$R_{nozzle} = \sqrt{\frac{A_9}{\pi}} \text{ , where } A_9 = \frac{Q}{\rho_9 V_9}$$

3.3.4 Engine length and nacelle dimensions

As indicated in Figure 3.1, the axial length of the intake and of the nozzle are considered equal. A simple approach could be to scale these lengths with the fan diameter, but this would yield a too long and too

heavy nacelle for engines with a very low fan pressure ratio. For that reason, the length is assumed to scale with the square root of the engine thrust for dimensionality reasons:

$$\begin{aligned} L_{intake} &= L_{REF} \cdot \sqrt{\frac{T_{uninst}}{T_{REF}} \frac{P_{REF}}{P_0}} \\ L_{nozzle} &= L_{intake} \end{aligned} \tag{3.5}$$

The intake length L_{REF}, thrust T_{REF}, and pressure P_{REF} are those of a well-known reference engine used to calibrate the scaling. The axial length of the blade rows R1 and R2 are equal to the axial chord, and they are computed from the axial aspect ratio specified by the user:

$$c_{ax} = \frac{R_{fan}(1-\eta)}{AR_{ax}}$$

The axial length of the inter-stage duct between R1 and R2 depends on the axial chord of the blade and a user-defined parameter K_{cax}:

$$\Delta L = K_{cax} \cdot \max(c_{ax,R_1}, c_{ax,R_2})$$

This scaling is motivated by acoustic considerations: the value of K_{cax} should be at least 1 to ensure a sufficient distance and a weak interaction between the blade rows, which is required for low-noise emission.

The external surface of the nacelle is given by:

$$S_{nac} = 2\pi \cdot R_{fan} \cdot L_{nac}$$

The mean thickness of the nacelle is computed using the following correlation:

$$t_{nac} = t_{REF} \cdot \sqrt{\frac{T_{uninst}}{T_{REF}} \frac{P_{REF}}{P_0}}$$

3.3.5 Engine weight

The overall weight of the engine is the sum of three terms:

$$W_{eng} = W_{fan} + W_{core} + W_{nac}$$

The first term is the weight of the fan blades, assumed to be made out of titanium. Like for the intake length and nacelle thickness, the weight of the engine core W_{core} is assumed to scale with some power of the engine thrust. The third term is part of the engine weight directly scaling with the volume of the external nacelle, whose average density is estimated around 400 kg/m^3.

$$\begin{aligned} W_{fan} &= \rho_{blade} \cdot B \cdot \mathcal{V}_{blade} \text{ , where } \mathcal{V}\text{: blade volume} \\ W_{core} &= W_{REF} \cdot \left(\frac{T_{uninst}}{T_{REF}} \frac{P_{REF}}{P_0} \right)^{3/2} \\ W_{nac} &= \rho_{nac} \cdot S_{nac} \cdot t_{nac} \end{aligned}$$

3.3.6 Engine drag

The drag of the engine is composed of different terms: the drag of the nacelle, which includes the friction and spillage drag, and the additional aircraft induced drag caused by the weight of the engine.

The friction drag of the external nacelle is computed assuming a constant flow velocity equal to the flight velocity V_0. The skin friction coefficient C_f is obtained from Eq.(2.15) taking the flight Mach number and a Reynolds number based on the size of the nacelle. The internal friction drag of the nacelle is already included in the isentropic efficiency of the fan (blade row endwall loss).

$$D_{friction} = \frac{1}{2}\rho_0 V_0^2 \cdot S_{nac} \cdot C_f(Re_{nac}, M_0)$$

The spillage drag is the result of the partial recovery of additive drag (or pre-entry drag) through the suction force at the lip of the nacelle. Physically, this drag is related to the entropy produced in the boundary layer and in the shocks as a result of the flow spillage around the lips and the associated overspeeds. More details can be found in the book on aircraft engine design by Mattingly [103] or that of Ward on aerospace propulsion systems [104]. A reaslistic estimation for the spillage coefficient K_{spill} is around 0.4.

$$D_{spillage} = K_{spill}\left(Q(V_1 - V_0) + A_1(P_1 - P_0)\right)$$

The last term, the induced drag, is not directly generated on the engine, but corresponds to the additional induced drag of the aircraft caused by the weight of the engine added to the aircraft weight. Assuming an ideal elliptic distribution of lift L, the total induced drag of the airplane having a wing span b is given by:

$$D_i = \frac{L^2}{\frac{1}{2}\rho_0 V_0^2 \cdot \pi b^2}$$

In cruise, the lift exactly compensates the total weight of the aircraft: $L = (W_a + N \cdot W_{eng})g$. The aircraft weight in cruise without its engines is W_a and must be specified by the user. The acceleration constant is $g = 9.81\ m/s^2$. We assume that the weight of the engines is very small compared to the aircraft weight:

$$(W_a + N \cdot W_{eng})^2 \approx W_a^2 + 2N \cdot W_{eng} \cdot W_a$$

As a result, the additional induced drag caused by every engine separately is given by:

$$D_i = \frac{2W_a \cdot W_{eng} \cdot g^2}{\frac{1}{2}\rho_0 V_0^2 \cdot \pi b^2}$$

3.4 Fan design

3.4.1 Principles

As mentioned in the introduction of the present chapter, the design of the fan relies on an iterative process which searches for the configuration with the highest fan efficiency. This iterative process is presented in Figure 3.3 for the conventional ducted turbofan (rotor–stator stage) and the counter-rotating turbofan (ducted or unducted). The approach consists of varying successively the meanline inflow relative Mach number M_{rel} of the first rotor, between a minimum value corresponding to the axial Mach number (specified by the user or imposed) and a maximum value fixed arbitrarily in the program (the maximum value is limited to 1.5, which is large enough to cover fan pressure ratios up to 1.9). After systematic variation of M_{rel}, the value yielding the best fan efficiency is chosen for design. In the case of counter-rotating turbofans, the power split n between the first and the second rotor must be varied, too. It increases when the pressure ratio of the first rotor increases and it is equal to 0.5 if both rotors have the same pressure ratio. Experience shows that the optimal power split is usually located between 0.5 and 0.7. The power split is mathematically defined as follows:

$$n \equiv \frac{1}{1 + \frac{\log(PR_2)}{\log(PR_1)}} \text{ , where } PR_1 \cdot PR_2 = FPR$$

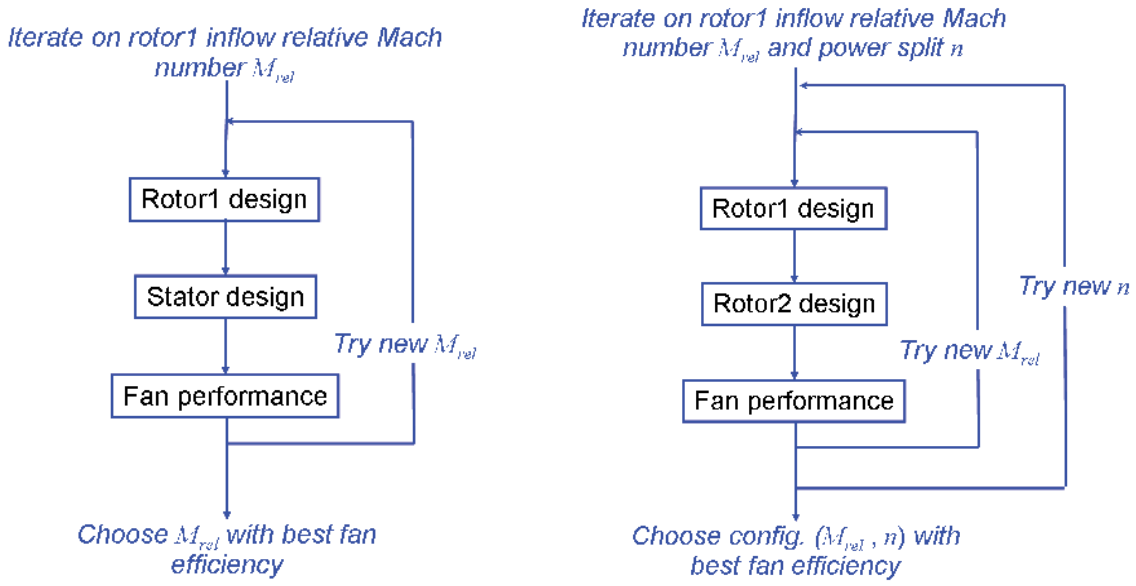

Figure 3.3: Principle of the design of a single-rotating (left) and counter-rotating (right) turbofan stage

Inside the global iteration loop, each component has its own design procedure which is summarized in Figure 3.4. The relative Mach number is used to calculate the rotational speed of the first rotor, and to deduce the flow turning based on Euler's turbomachinery equation, see Eq.(2.5). In order to ensure a swirl-free exhaust flow, the flow turning of the second rotor (or stator) must be exactly equal in magnitude and opposite in sign to that of the first rotor. The optimal lift coefficient which provides the lowest loss for the specified flow turning is found by means of a gradient-based search algorithm. Using the relation of Eq.(2.7), the optimal solidity can be obtained and subsequently all parameters describing the geometry of the blades.

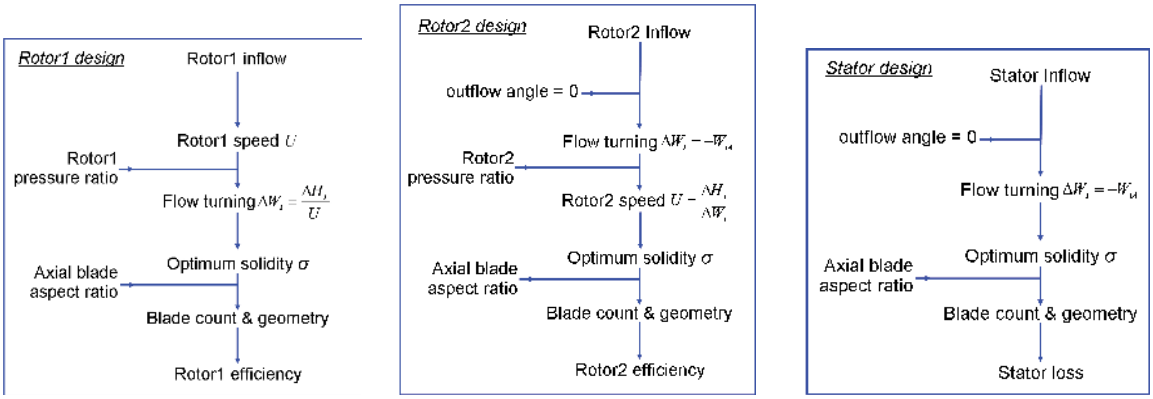

Figure 3.4: Principle of the design of rotors and stators

3.4.2 Exemplary results

The design principles described in the previous section will now be illustrated through parameter studies performed on a typical turbofan application.

We focus first on the cascade design routine which looks for the optimal lift coefficient and cascade solidity for given inflow Mach number and flow turning. Figure 3.5 presents the results of a parameter study in which the solidity of a stator cascade has been continuously varied from 0 to 4 and the performance and flow quantities calculated with the module for Steady Aerodynamics described in the previous chapter 2. The various coloured curves correspond to different values of flow turning varying from 5 degrees (blue) to 40 degrees (dark red).

- Each curve presents an optimal solidity for which the total cascade loss has a minimum. Low-solidity cascades operate at a high lift coefficient and consequently high diffusion factor associated with flow separation over the blades.
- Inversely, high-solidity cascades work at a lower lift coefficient and diffusion factor, so separation is avoided but the wetted blade surfaces are larger than necessary and are responsible for increased skin-friction loss. Moreover, the flow at cascade throat approaches sonic conditions (choking limit) which is accompanied by overspeeds and an additional increase of the losses.
- As flow turning increases, the optimum is shifted towards larger solidity and diffusion factor. This trend presents some analogy with the increase of wing loading observed on aircraft designs as the weight (hence the lift) is increased.
- These results reproduce the trends observed in 1959 by Lieblein [74] as he introduced his concept of diffusion factor and illustrated in a similar parameter study the implications of his new correlation on cascade design. However, Lieblein did not account for compressibility effects at the time, which in particular may result in choking and increased losses as the throat flow becomes sonic.

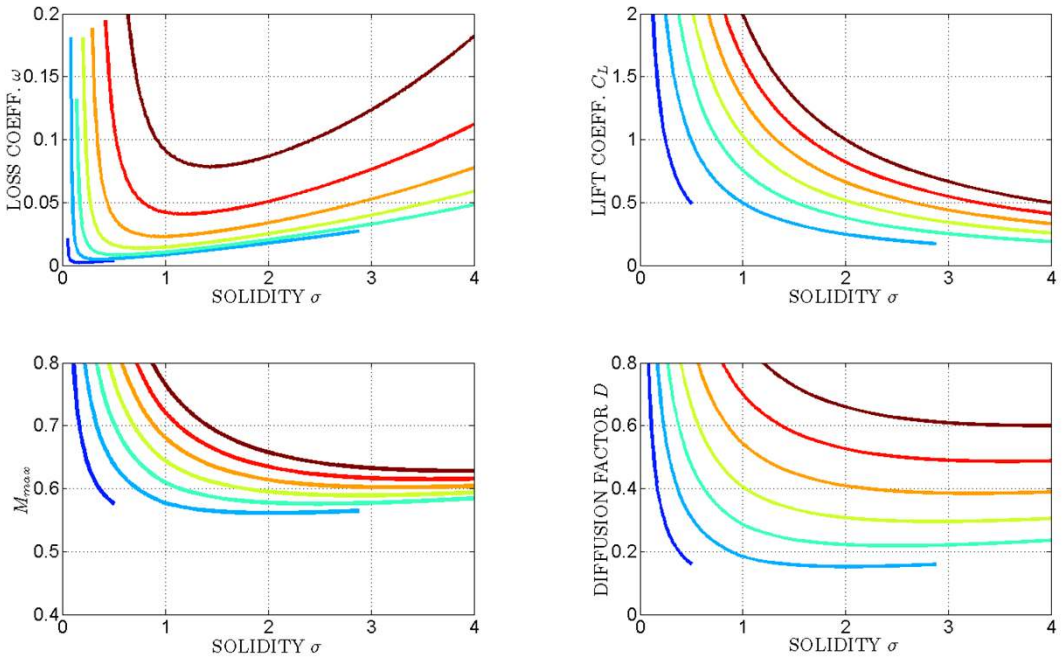

Figure 3.5: Variation of stator performance for different geometries (solidity) and inflow angles

This parameter variation is carried out automacially by the cascade design routine. The optimal solidity corresponding to minimum loss is found through an algorithm fitting the curve to a polynom of second order which enables the robust determination of the optimal solidity even if the curve is not

continuous and presents small jumps. Figure 3.6 presents the behaviour of the optimal solution depending on the flow turning (each colour corresponds to a different inflow Mach number). The following remarks can be made:

- At low values of the flow turning, the optimal solidity increases nearly linearly. The asymptotic case of zero flow turning thus yields a cascade of vanishing solidity which corresponds to the isolated airfoil.
- The optimal diffusion factor increases with the flow turning. This is in agreement with the observations of Denton [75] who stated that the optimal compressor cascade should operate at high loading, on the verge of separation.
- For very high flow turning angles above 40 deg, the optimal cascade is found to operate with significant losses and presumably some separated regions. The prediction of the correct trends is much less reliable in this domain due to the inaccuracy of the loss models with detached flow. The optimal solutions found by the routine should therefore be considered with caution if the losses become too large.
- At high values of the inflow Mach number, the optimal lift coefficient becomes smaller in order to avoid too high supersonic velocities and shock losses.

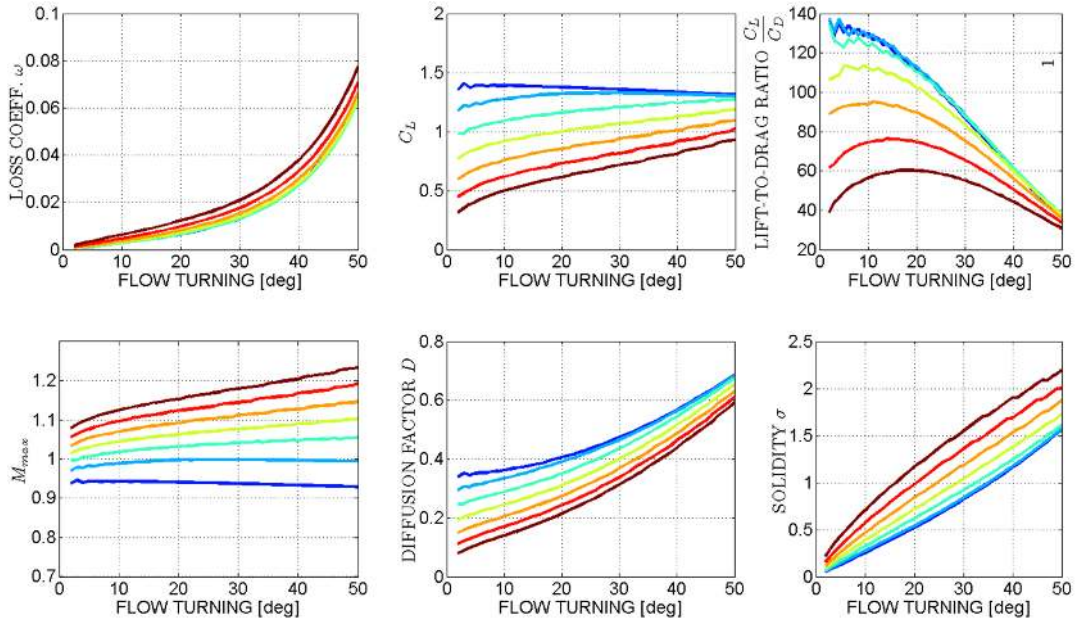

Figure 3.6: Variation of stator performance for flow turning requirements

The parameter study presented in Figure 3.7 illustrates how the optimal rotor inflow relative Mach number M_{rel} is selected which is an essential step of the fan design routine depicted in Figure 3.3. The specifications for the rotor–stator stage were a constant fan pressure ratio of 1.35, and constant rotor inflow axial Mach number of 0.6. The rotor inflow relative Mach number is continuously varied from 0.6 to 1.1. The main features can be summarized here:

- According to the Euler's turbomachinery equation, design at low Mach number (low rotor speed) must be compensated by a high flow turning: the flow is strongly deflected by the rotor and may be even accelerated. The rotor efficiency remains high but the strong swirl has to be recovered by the stator, resulting in high stator losses and a poor overall fan efficiency.

- Inversely, designing the rotor for high Mach numbers allows to operate the fan with a smaller inter-stage swirl and good stator efficiency. However, this is limited by the loss penalty associated with the shocks forming around the rotor blades at transonic and supersonic speeds.
- The optimal value for M_{rel} thus results from a balance between rotor and stator losses. This compromise is a well-known aspect of fan design and is related to the selection of the proper degree of reaction $\mathcal{R}$ for the stage. Rotor–stator stages operate at relatively high degree of reaction around 0.8, whereas counter-rotationg rotors operate around $\mathcal{R} = 0.5$.
- For large Mach numbers above 0.9, the optimal diffusion factor decays because the flow turning decreases and large values of peak Mach numbers associated with strong shock loss must be avoided.

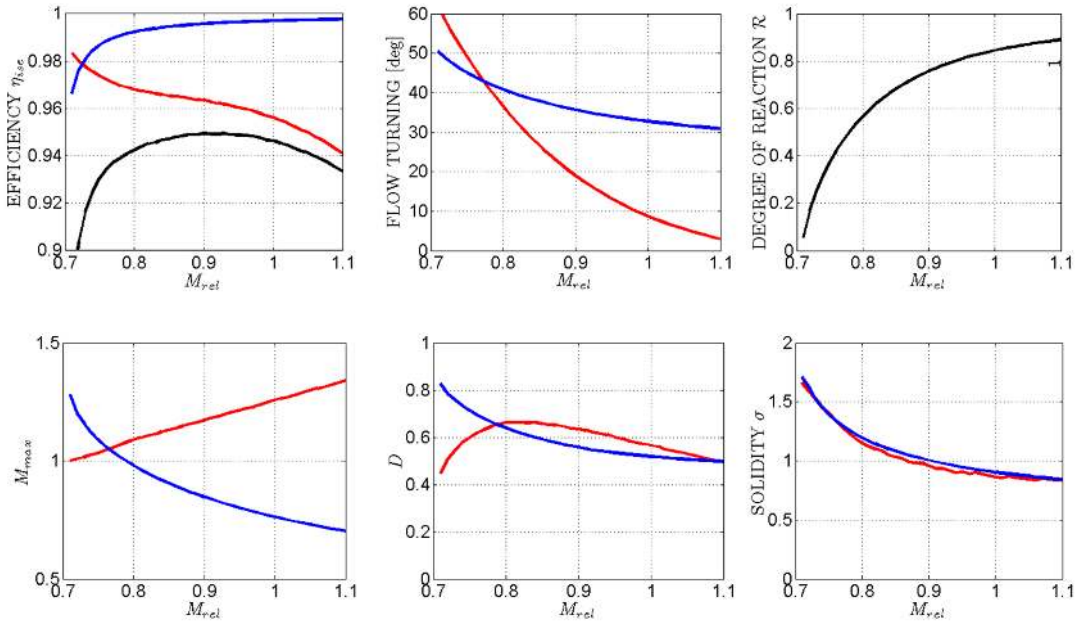

Figure 3.7: Variation of rotor–stator design: effect of inflow Mach number at constant FPR

The parameter study presented in Figure 3.8 presents the design parameters for increasing fan pressure ratio. Practically, the optimum inflow Mach number from Figure 3.7 is selected for each value of the pressure ratio. The rotor inflow axial Mach number is maintained constant at a value of 0.6. The following remarks are given:

- The main design parameters such as Mach number, solidity, flow turning, or diffusion factor tend to increase with increasing fan pressure ratio.
- The total fan efficiency slightly increases at very low values of the pressure ratio: this is attributable to the endwall annulus loss which does not scale with the pressure ratio. Then, the efficiency reaches a maximum. At higher pressure ratio, the efficiency decreases as a consequence of the increase in flow turning which is necessary to provide the desired compression. This represents more demanding aerodynamic conditions.

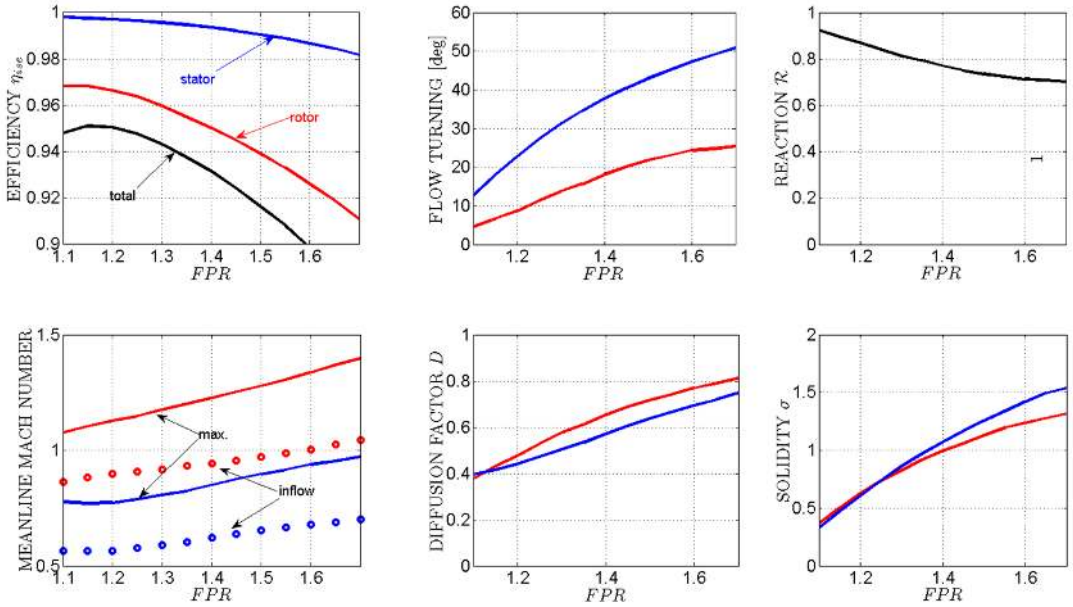

Figure 3.8: Variation of rotor–stator design: effect of fan pressure ratio at constant M_x

3.5 Engine performance

The ultimate figure of merit characterizing the aerodynamic performance of an engine for a given aircraft application is the fuel consumption, denoted FC. We will show in this section that this quantity is directly related to the overall efficiency of the engine, which is defined as the ratio of output power formed by the net propulsive power and the input power contained in the fuel injected inside the combustion chamber.

$$\eta_{eng} \equiv \frac{\Pi_{out}}{\Pi_{in}} = \frac{T_{net} \cdot V_0}{FC \cdot HV}$$

The parameter HV is the heating value of kerozine ($HV = 40 \cdot 10^6 J/kg$). The engine efficiency is written as a product of four terms:

$$\eta_{eng} = \frac{\Pi_{out}}{\Pi_{uninst}} \cdot \frac{\Pi_{uninst}}{\Pi_{kin}} \cdot \frac{\Pi_{kin}}{\Pi_{th}} \cdot \frac{\Pi_{th}}{\Pi_{in}}$$

The installation, propulsive, aero-thermal and combustion efficiencies are defined as follows:

$$\begin{aligned}
\eta_{inst} &\equiv \frac{\Pi_{out}}{\Pi_{uninst}} = \frac{T_{net}}{T_{uninst}} \\
\eta_{prop} &\equiv \frac{\Pi_{uninst}}{\Pi_{kin}} = \frac{2V_0}{V_{10} + V_0} \\
\eta_{aerotherm} &\equiv \frac{\Pi_{kin}}{\Pi_{th}} = \frac{(V_{10}^2 - V_0^2)/2}{c_p(T_{t10} - T_{t0})} \\
\eta_{comb} &\equiv \frac{\Pi_{th}}{\Pi_{in}} = \frac{Qc_p(T_{t10} - T_{t0})}{FC \cdot HV} = 1
\end{aligned}$$

The first term is the installation efficiency, it depends on the aerodynamic design of the nacelle, flow spillage, and the engine weight relative to the total aircraft weight. The second term is the propulsive efficiency and is directly related to the exhaust velocity of the flow and tends to be higher for low pressure ratio fans. The aero-thermal efficiency includes the loss of efficiency due to the high temperature of the

jet and due to the transverse kinetic energy contained in the turbulence and the exhaust swirl (which may be present at off-design conditions). The isentropic efficiency of the fan is part of the engine aero-thermal efficiency. At last, the combustion process inside modern burners has become so efficient that we will consider it as ideal. We define the specific fuel consumption as the fuel consumption required to produce of net thrust of one Newton. It is inversely proportional to the engine efficiency:

$$SFC \equiv \frac{FC}{T_{net}} = \frac{V_0}{\eta_{eng} \cdot HV}$$

Note that this relation is not valid in static conditions where the flight velocity is zero (for example at Take-off). In that case the specific fuel consumption reads:

$$SFC = \frac{V_{10}/2}{\eta_{inst} \cdot \eta_{aerotherm} \cdot \eta_{comb} \cdot HV}$$

Finally the fuel consumption for each engine is given by:

$$FC = SFC \cdot T_{net}$$

Figure 3.9 presents the variation with fan pressure ratio of some quantities provided by the preliminary design routine previously described in Figure 3.2. This routine is practically responsible for the sizing of the engine (most importantly the fan diameter and the nacelle length). There exists an optimum fan pressure ratio at which the fuel consumption is minimal. Low pressure ratio engines have a high propulsive efficiency but have a large drag penalty due to their size. High pressure ratio engines are more compact, but have a low propulsive and aero-thermal efficiency.

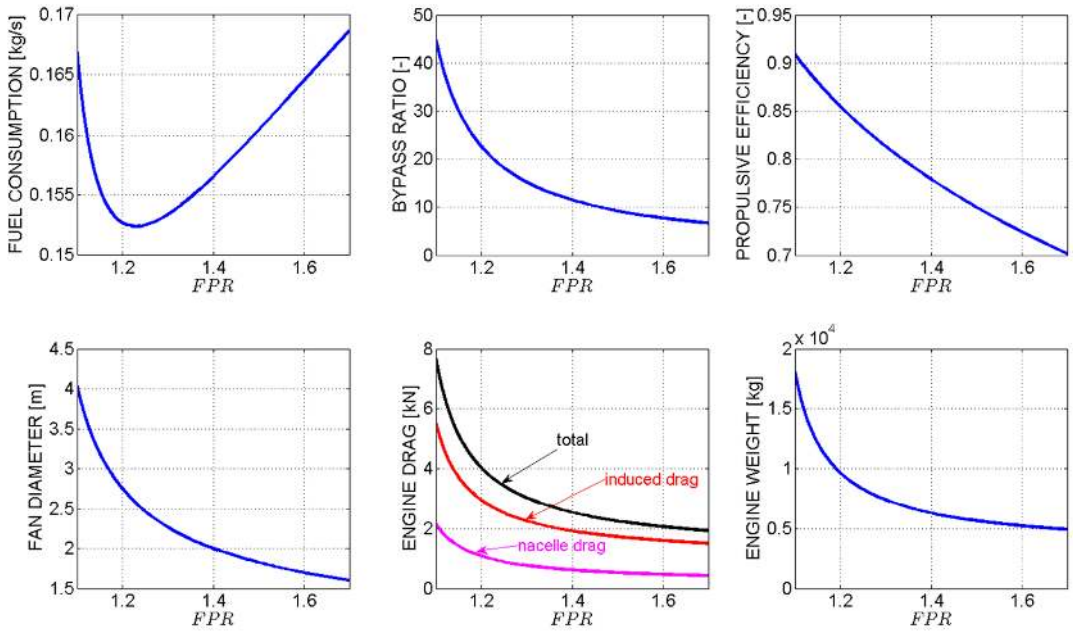

Figure 3.9: Typical results of pre-design

3.6 Off-design operating points

After the aerodynamic design has been performed, the geometry of the fan blades is fixed and it is possible to calculate the performance of the engine at off-design flight conditions. The off-design points

are listed in Table 3.1 with their corresponding flight Mach numbers, altitudes, aircraft overall net thrust requirements and some approximate values of the reduced fan speed N_{red} at which the engine is operated (expressed in percent of the Cruise speed). The off-design specifications listed in this table are given for a typical commercial jet airliner with short- to medium-range.

	Cruise (ADP)	Top of climb	Take-off	Cut-back	Approach
flight altitude [m]	10500	10500	0	500	120
flight Mach number	0.78	0.78	0.21	0.35	0.21
required thrust [kN]	37	44	170	110	38
approx. N_{red} [%]	100	110	90	80	50

Table 3.1: Definition of the flight conditions for a given short- to medium-range airliner

The Top of climb (or max climb) flight condition is of particular interest for the aerodynamic performance of the engine: it is usually the most demanding point, as the engine must be operated at very high speed (typically 5 to 10% higher than the cruise speed) with nearly choked fan blades. For the acoustic assessment, three other off-design points being part of the noise certification are considered: Take-off, Cut-back and Approach. The Take-off point may also be challenging aerodynamically as the fan operates there near the stall limit. This is particularly the case for the CRTF-concept with low-solidity blades. If the aerodynamic performance cannot be achieved (due to choking or stall), the subsequent calculations cannot carried out: an assessment of the fan at the corresponding operating point is not possible.

For each off-design point, an iterative procedure looks for the set of operating conditions (fan speed and airflow) that delivers the required thrust and satisfies an additional criterion (the procedure is illustrated in Figure 3.10). For ducted configurations, this criterion concerns the jet expansion at the nozzle exit: if the exit Mach number is below one $M_9 < 1$, the exhaust static pressure must be equal to the ambient pressure $P_9 = P_0$. For turbofan engines with a fan pressure ratio larger than 1.3 approximately, the exhaust nozzle is usually choked in cruise and top of climb conditions. In that case, the throat flow of the nozzle is exactly sonic $M_9 = 1$ and the exhaust pressure is larger than the ambient pressure. For unducted configurations, no nozzle controls the expansion of the jet so an alternative criterion is applied: the axial velocity must match the velocity induced by the thrust of the rotors.

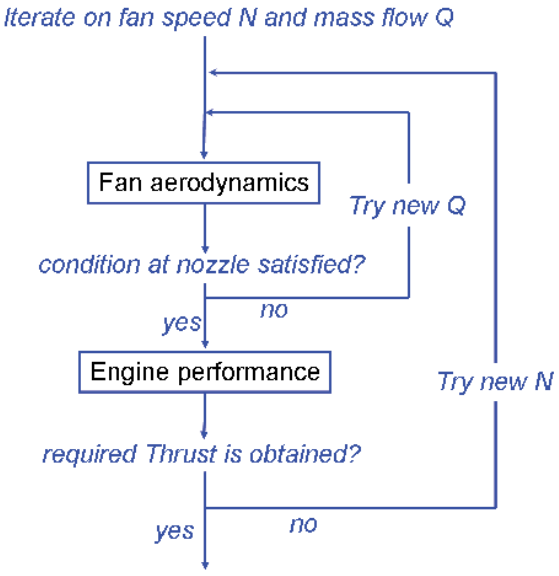

Figure 3.10: Procedure to determine the fan speed and mass flow rate at off-design conditions.

The configurations with counter-rotating rotors (CRTF and CROR) are assumed to operate at constant speed ratio (ratio of rotation speeds between front- and rear-rotor) irrespective of the off-design point considered. Thus, the speed of the rear-rotor is simply scaled from its value in cruise.

3.7 Validation at design conditions

In order to verify how accurate the predictions can be in terms of design, a series of existing ducted fans have been simulated for which the design parameters are known. The pressure ratio of these fans ranges from 1.3 to 1.7 for the single-rotating configurations, and from 1.2 to 1.45 for the contra-rotating cases. Fig. 3.11 compares the solidity and relative Mach number predicted by the tool with the actual values observed on the real design, note that the meanline values are considered here again. The different symbol styles are related to either the front or rear blade row of the fan. Perfectly accurate predictions are located along the center dashed line while the upper resp. lower dashed lines correspond to an overestimation resp. underestimation by 10%.

- The first conclusion of this comparison is the fairly good prediction of the relative Mach number over a broad range of values (right part of the figure): as expected, the stators of the conventional fans have a low inflow Mach number and the rotors are characterized by high values, the rotors of the contra-rotating concept operate in a more moderate Mach number domain.
- The second conclusion concerns the prediction of the blade solidity (left side of the figure): we observe a significant dispersion, especially on the rotor-stator stages. The solidity of the stator tends to be overestimated whereas that of the rotor is underestimated. This may be explained by two important design parameters: the stall margin and the meridional-velocity–density ratio known as MVDR. These parameters strongly affect the flow diffusion allowed at design condition and thus impact directly the solidity; the choice of these parameters is part of the experience gained over the years by the engine manufacturers, which makes it a more challenging task to predict with a simplified approach. Stators do not deliver power input and generate low losses, this is probably why one can afford to design them with lower solidities, keeping thereby the cruise efficiency as high as possible. Nevertheless, the trend of increasing solidity with increasing fan pressure ratio is globally respected; the higher solidity of the rear rotor compared to the front rotor of the CRTF is also well reproduced (this too is a result of designing for a sufficient stall margin).

The next aspect deals with the validation of the fan isentropic efficiency predicted by our aerodynamic model. Fig. 3.12 shows the comparison between the conventional fan TF with the contra-rotating fan CRTF over a wide range of design fan pressure ratio and fan-face axial Mach number. A similar but much more detailed study performed with a 3D RANS solver has been published by Timea Lengyel [105] recently. A result from her study is shown in Fig. 3.13. Although the present approach relies on simple models and a one-dimensional description at meanline, the same trends are observed in both studies and similar conclusions can be drawn.

- The maximum fan efficiency is obtained for low pressure ratio and low Mach number. However, the pressure ratio should not be too low, otherwise the endwall loss would dominate and nullify the aerodynamic benefit; in the case of a very low pressure ratio, an unducted configuration (CROR) is recommended.
- Designing for high fan-face axial Mach number reduces the fan diameter and makes the engine more compact, but there is an efficiency penalty on the fan that leads to a compromise. Current designs are located around 0.6-0.65. For the unducted CROR, this parameter is constrained by the thrust and must be above the flight Mach number.
- The contra-rotating ducted fan presents a significant efficiency benefit over the conventional fan by at least 1%. Interestingly, the higher the pressure ratio or axial Mach number is, the larger is the benefit, which can reach up to 3%. This makes the CRTF a more serious competitor in the range of moderate bypass ratio rather than at ultra high bypass ratio.

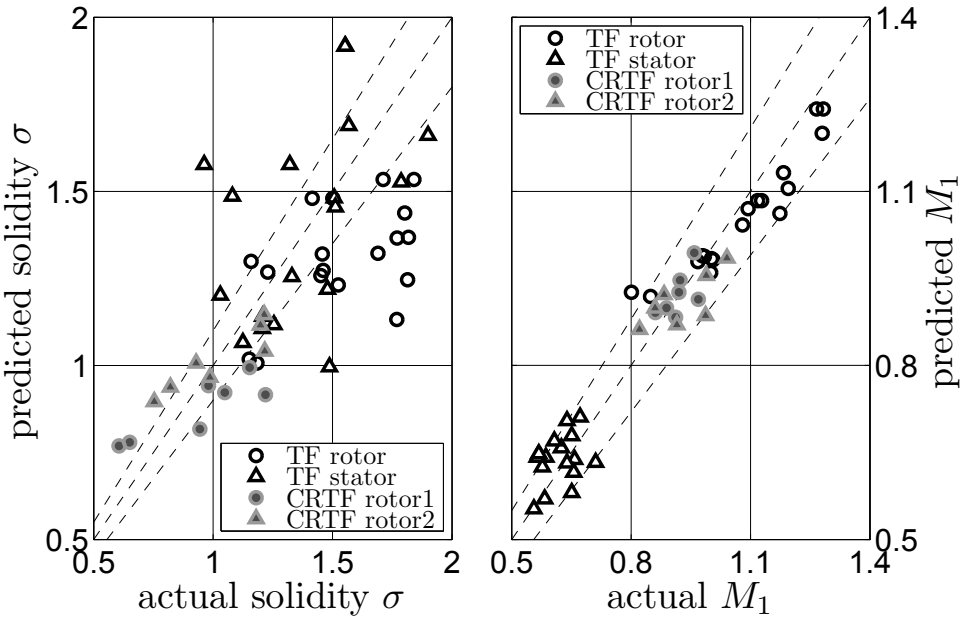

Figure 3.11: Accuracy of the prediction of some fan design parameters [76]

- The reasons for the aerodynamic superiority of the CRTF over the TF are twofold: first, the work input can be split over both rotors, meaning that each rotor needs less flow turning, a lower diffusion factor, and a lower solidity (less blades) which also reduces the blockage and delays choking; in all, less friction and mixing loss is produced for the same overall work input. The second reason lies in the nature of the velocity triangles: let consider the Smith chart [98] in the (ϕ,ψ) design space, the TF has its optimum around $\phi = 0.5$ and $\psi = 1$, a region never chosen for compressor stages with axial inflow because the loading is too high and the lift-to-drag ratio is too low there. The Smith chart of the CRTF is better suited for axial-inflow fans, since the optimum is at $\phi = 1$ and $\psi \to 0$, a region with higher mass flow, low loading and a better lift-to-drag ratio for the blades.

3.8 Conclusion

A procedure that includes the sizing of the engine nacelle and the design of the fan blades has been presented in this chapter. The optimized engine presents a minimal fuel consumption for the specified thrust requirement, flight conditions, fan pressure ratio, and fan stability margin. Only the bypass flow of the engine is considered here, which is a realistic assumption for high-bypass-ratio engines. Parameter variations have been performed and the consistency of the trends has been discussed. The integration of some acoustic design criterion, based for example on a cut-off design for the blade-passing frequencies, may constitute an extension of the present procedure, in the future.

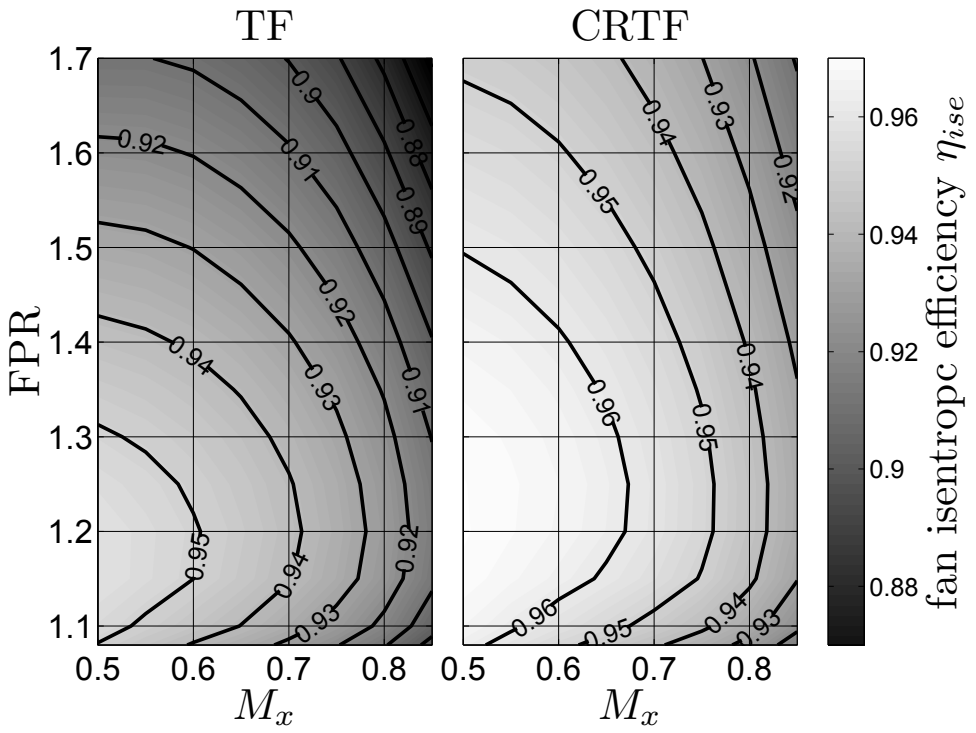

Figure 3.12: Variations of single- and contra-rotating fan efficiency with pressure ratio and axial Mach number [76]

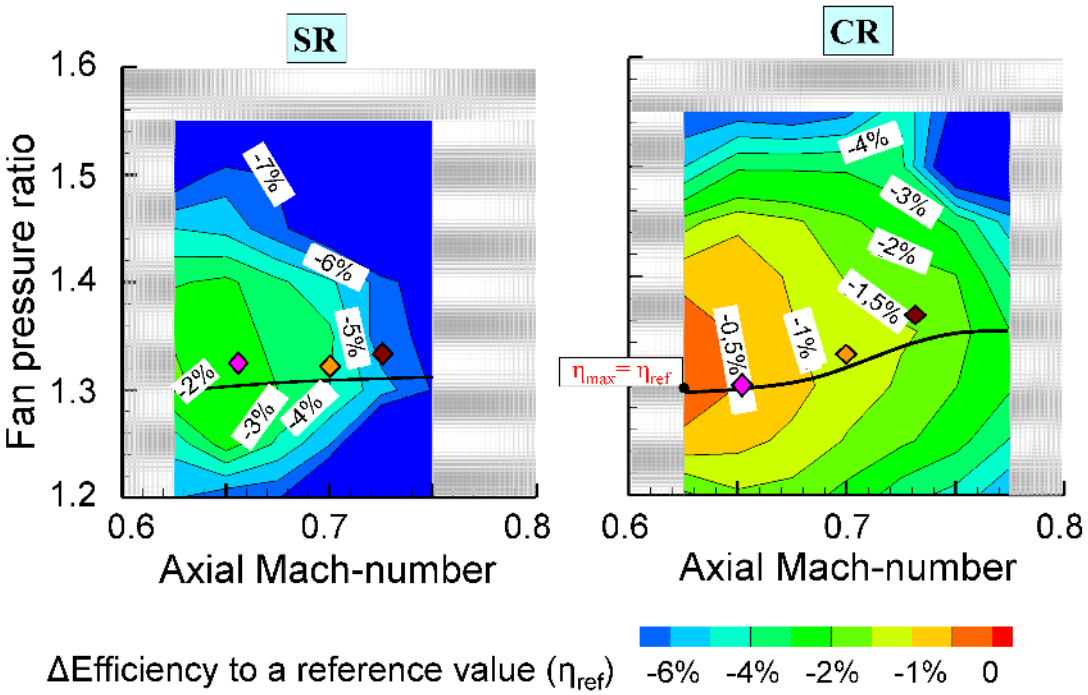

Figure 3.13: Results of a similar study [105] obtained after optimization with a 3D RANS flow solver

Chapter 4

Unsteady aerodynamics

4.1 Introduction

The models presented in this chapter establish the connection between the mean flow quantities and the acoustic calculations. Turbofan noise basically arises from flow perturbations that fluctuate in time in the reference frame of the observer. The expression 'unsteady aerodynamics' will be used hereafter to refer to the acoustically relevant components of the flow. The perturbations of two different parts of the flow are considered: the viscous flow (blade boundary layers, wakes and turbulence) and the potential field (pressure field bound to each blade row). The fluctuations of the temperature field can be neglected in the fan and compressors of an engine. Flow velocity fluctuations are sometimes described as gusts.

Similarly to the steady aerodynamics module, the initial strength of the wakes and potential fields and their decay in axial direction are calculated on a meanline radius. The perturbations are expressed in terms of flow velocity spectra depending on frequency and circumferential mode order. It will be shown that circumferential variations of a steady velocity field locked to a rotor result in time fluctuations if observed in the fixed reference frame. This chapter will also present the lift response of blades to these fluctuations.

Generally, it should be mentioned that the domain of unsteady aerodynamics covers a relatively wide range of problems and is one of the fundamental pillars for accurate noise predictions. However, the development of theoretically-based analytical solutions has not received as much attention in the literature as its purely acoustic counterpart. Therefore, unlike the acoustic models which provide an exact analytical solution of a simplified problem, the models for unsteady aerodynamics are partly based on empirical correlations, involving constants that need to be calibrated and possibly adapted to the application considered.

4.2 Potential field

The potential field is often regarded as the counterpart of the viscous flow field: by definition, it is the irrotational component of the velocity field, which can be written as a gradient of a scalar quantity called the velocity potential. In a well-designed fan with limited separations and weak shocks, the potential field is almost independent of the viscous flow. We will consider here only the steady part of the potential field that is bound to the blade row and rotates with it. It is generated by the flow displacement due to airfoil thickness and by the blade circulation due to lift. At subsonic mean-flow velocities, the propagation takes place linearly but in the supersonic regime, shocks are formed and there is an energy decay due to the dissipation inside the shocks.

4.2.1 Initial strength of the potential field

As long as the perturbations of the steady pressure field bound to a blade row are small, the thickness and lifting problems can be treated separately. Each blade is then represented by a distribution of steady monopoles and dipoles, respectively. This is the approach adopted by Parry and Crighton [44]. Kemp and Sears [106] detailed the derivation of the lifting model. Morfey [47] provided analytical estimations but distinguishing between the low-solidity and high-solidity limits. For simplicity and consistency with the models for Steady Aerodynamics, we choose to evaluate the potential field on a meanline radius and based on the spatial distribution of flow overspeeds around the blade. For that purpose, the source strength of the quadrupole term introduced by Hanson [24] forms the starting point:

$$\overline{\rho u_\ell^2} = \frac{1}{c^2} \int_{\ell=-\infty}^{+\infty} \int_{n=0}^{h} \rho u_\ell^2(\ell, n) dn d\ell \tag{4.1}$$

where u_ℓ is the streamwise disturbance velocity. The surface integral is approximated by:

$$\overline{\rho u_\ell^2} = K_{quad} \cdot \rho_m \left[(\overline{W}_{SS} - W_m)^2 + (\overline{W}_{PS} - W_m)^2 \right]$$

The scalar quantities $\overline{W}_{SS}$, $\overline{W}_{PS}$, are the averaged blade velocities on the suction and pressure side, they have been already introduced in chapter 2 on Steady Aerodynamics and can be calculated based on the thickness, lift cofficient and off-design incidence, see Eq.(2.8). The background flow parameters ρ_m, W_m have also already been presented in Eq.(2.3). The constant K_{quad} must be determined empirically, a value around 0.5 seems appropriate. Finally, the root-mean-square value (in the sense of circumferential averaging) of the initial velocity perturbation is given by:

$$u_0 = \sqrt{\frac{\overline{\rho u_\ell^2}}{\rho_m} \cdot \sigma}$$

The solidity σ of the blade row appears from averaging over a blade passage with a width equal to the blade spacing s. The root-mean-square value of the velocity perturbation vanishes for single airfoils and increases with increasing solidity, which agrees with the model of Morfey [47].

4.2.2 Circumferential distribution and modes

In addition to a scalar quantity representing the energy, the prediction of noise requires to describe the distribution of this energy among the harmonics. Due to the 2π-periodicity of the problem in circumferential direction, the harmonics are integers denoted m and called circumferential or azimuthal modes. The perturbation associated to a mode of order m is obtained by Fourier decomposition:

$$u(m) \equiv \frac{1}{2\pi} \int_{\theta=0}^{2\pi} u(\theta) e^{im\theta} d\theta \equiv \frac{1}{s} \int_{y=0}^{s} u(y) e^{i\frac{m}{r}y} dy$$

By definition, the root-mean-square value of the velocity perturbation in circumferential direction is:

$$|u_0|^2 \equiv \frac{1}{2\pi} \int_{\theta=0}^{2\pi} u(\theta)^2 d\theta = \sum_{m=-\infty}^{+\infty} |u(m)|^2$$

We assume that all blades are identical, which implies that the mode orders are multiples of the blade count: $m = h \cdot B$. Moreover, we assume that the entire energy is contained solely in the first harmonic order, which is a reasonable hypothesis as higher harmonics decay very rapidly and practically do not show up in the noise spectra.

$$u(m) = \begin{cases} u_0 \text{ , if } |m| = B \\ 0 \text{ , otherwise} \end{cases}$$

The assumption of identical blades is less acceptable at supersonic speeds. From each blade a shock is emitted, whose intensity and position depend on the blade camber and thickness. The non-linear propagation effects associated with the shocks amplify the differences between the shocks. As a result, minor geometry variations from blade to blade lead, after some distance, to a pressure pattern with a rich modal content, as energy is transferred from the main harmonics to all other mode orders (also called multiple pure tones). Pickett [107] proposed a statistical model to relate analytically the spectrum of multiple pure tones to the variations in blade geometry.

4.2.3 Decay of the potential field

If the mean flow is subsonic in the reference frame locked to the blade rows, the potential field sources emit waves interfering destructively and the resulting pressure field cannot propagate without a decay. The amplitude decrease of the perturbation velocity depends on the axial distance Δx to the leading edge of the blades, the circumferential mode order m and the flow conditions. The decay model presented here is derived from the analytical axial wavenumber inside an infinitely long duct with uniform axial flow in the fixed reference frame (see the chapter 6 dedicated to Acoustics for further details).

$$u(\Delta x) = u_0 \cdot \exp(-\alpha \Delta x), \text{ where } \alpha = \frac{|m|}{r_{mn}} \frac{\sqrt{1 - M_{rel}^2}}{1 - M_x^2} \text{ , for } M_{rel} < 1 \tag{4.2}$$

The quantity r_{mn} is the caustic radius, which will be defined later in the chapter 6 dedicated to Acoustics. It is approximated by the meanline radius. It should be noted that the decay law presented here is not rigorously valid for unducted configurations in the free field, despite its reproduction of the main qualitative trends. The exact solution can be obtained from the near-field theory as developed by Hanson [108] or Schulten [55] for propeller noise prediction. The axial decay coefficient α decreases with increasing relative Mach number, and vanishes as the mean flow becomes sonic: beyond this point the pressure perturbations can propagate in form of cut-on acoustic modes and are characterized by shocks. The non-linear effects associated to their large amplitudes and gradients result in energy dissipation whose intensity can be quantified by either the weak shock theory or the one-dimensional non-linear acoustic theory (see the work of Morfey [109]). A quantity called the 'time of flight' is defined:

$$T(\Delta x) = \frac{\Delta x}{s} \frac{M_{rel}^2}{\sqrt{M_{rel}^2 - 1}} \frac{1}{\left(\sin \beta_{rel} - \cos \beta_{rel} \sqrt{M_{rel}^2 - 1}\right)^2} \tag{4.3}$$

The relative Mach number is calculated from the axial Mach number and the rotation speed: $M_{rel}^2 = M_x^2 + \frac{\Omega \cdot r}{a_0}$. The relative flow angle is given by: $\cos \beta_{rel} = \frac{M_x}{M_{rel}}$. The decay of shock pressure rise inside a duct is given by:

$$\frac{\Delta P}{P}(\Delta x) = \frac{(\Delta P/P)_0}{1 + \frac{\gamma+1}{2\gamma} \cdot T(\Delta x) \cdot (\Delta P/P)_0} \rightarrow \frac{2\gamma}{\gamma + 1} \frac{1}{T(\Delta x)} \tag{4.4}$$

At large distances, the pressure perturbation does not depend on its initial value ΔP_0 anymore, and decays inversely to the ratio of axial distance Δx to blade spacing s. The perturbation velocity can be related to the perturbation pressure through:

$$\Delta P = -\rho W_{rel} u \tag{4.5}$$

where W_{rel} is the circumferential average of the streamwise velocity component, which is also the velocity computed by the Steady Aero module. In the following, it will be denoted W_{mean} or W_0.

4.3 Mean-flow wakes

The boundary layer generated on the blade surface is convected in form of a wake from the trailing edge of the blades. It is well known that the impingement of wakes on a blade row located further

downstream may be an important noise contributor. The wake is characterized by a mean velocity deficit and stochastic velocity fluctuations amplified by the velocity gradients within the wake. In this part, we consider the mean part of the wake and adopt a simple model to describe it: the mean wake has a Gaussian shape and is symmetric (same width on the pressure and suction sides). Therefore, the wake quantities (width, depth and area) will be easily related to the boundary layer thickness and shape factor. A review on existing semi-empirical models has been given by Carazo [110]: the models are applicable to either isolated airfoils, cascades or rotors, and do not account for pressure-gradient effects. To remedy this partly, a new model will be proposed to determine analytically the decay of the wake in the streamwise direction. The evolution of the wake is considered in the reference frame locked to the blade row where the wake is generated.

4.3.1 Wake model

We consider the steady wake formed by the blades in the rotating frame of reference. The velocity perturbation convected behind a blade row is modelled by a train of identical Gaussian-shaped symmetrical wakes. This model has been experimentally confirmed by Raj [111], Ravindranath [112], and Reynolds [113] based on two-dimensional cascade measurements. Real wakes are non-symmetrical as the boundary layer on the suction and pressure sides have a different thickness; the impact of non-symmetrical wakes has been analyzed by Roger [114] and shown to be significant only for higher harmonics. The streamwise velocity perturbation expressed as a function of the circumferential position $y = r\theta$ is then given by:

$$u(y) = u_{max} \cdot \sum_{k=-\infty}^{+\infty} e^{-\pi\left(\frac{y-k\cdot s}{w\cdot s}\right)^2} \tag{4.6}$$

where u_{max} is the peak perturbation velocity (also called maximum deficit velocity), s the blade spacing and w the non-dimensional wake width which is defined more precisely hereafter. The sum represents the train of wakes. The streamwise component W of local flow velocity is:

$$W(y) = W_{max} - u(y)$$

The figure 4.1 illustrate how these quantities are defined. A symmetrical Gaussian wake can be characterized by three non-dimensional parameters: the area A, depth d and width w.

$$\begin{aligned} A &\equiv \int_0^s \frac{u(y)}{W_{mean}} \frac{dy}{s} \\ d &\equiv \frac{u_{max}}{W_{max}} \\ w &\equiv \frac{A}{d} \end{aligned}$$

The quantity W_{mean} is the circumferentially averaged velocity: it is equal to the outflow velocity W_B introduced in the chapter 2. The non-dimensional wake parameters can be related to the displacement and momentum thickness of the wake. These are defined as follows:

$$\begin{aligned} \delta_1 &= \frac{h}{s} \int_{y=0}^{s} \left(1 - \frac{u(y)}{W_{max}}\right) dy \\ \delta_2 &= \frac{h}{s} \int_{y=0}^{s} \frac{u(y)}{W_{max}} \left(1 - \frac{u(y)}{W_{max}}\right) dy \end{aligned}$$

The boundary layer thicknesses are defined in the direction normal to the direction of convection; this explains the appearance of the ratio of the streamtube height h to the blade spacing s. We can now express the wake parameters in terms of boundary layer quantities:

$$\begin{aligned} A &= \frac{\delta_1}{h - \delta_1} \\ d &= \sqrt{2}(1 + A)\left(1 - \frac{1}{H_{12}}\right) \end{aligned} \tag{4.7}$$

The wake area depends on the blockage of the flow channel by the wake, which in turn depends on the viscous drag coefficient of the blade. The wake depth depends on the shape factor H_{12} and increases with increasing blade aerodynamic loading. This is consistent with experimental observations by the research team of Lakshminarayana ([112], [113]). The initial value of the wake parameters (at the trailing edge) can therefore be calculated using the momentum thickness and shape factor of Eq.(2.14) and Eq.(2.16). It should be noticed that the definition of the wake parameters is valid for wakes clearly separated from each other, if the wake width increases beyond a certain value (typically around 0.4) the wakes start to merge and the wake deficit decays more rapidly as observed experimentally by Raj [111].

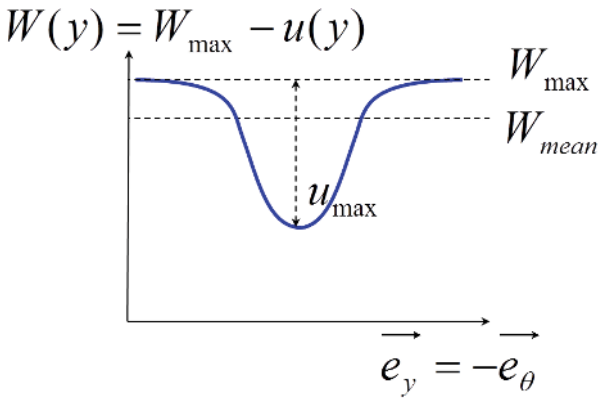

Figure 4.1: Representation of a wake over a blade passage and the associated mean flow and deficit velocities

4.3.2 Spectral content

The Fourier transform of the train of Gaussian wakes from Eq.(4.6) is calculated analytically:

$$u(h) = W_{mean} \cdot A \cdot e^{-\pi \cdot w^2 \cdot h^2} \tag{4.8}$$

The wake harmonic order is denoted h. Parseval's theorem (or Rayleigh's identity) stating the conservation of energy is verified:

$$\frac{1}{s}\int_0^s u(y)^2 dy = \sum_{h=-\infty}^{+\infty} u(h)^2$$

4.3.3 Wake decay

The problem of predicting the decay rate of wakes has been treated by a large number of authors. Theoretical considerations by Prandtl and Schlichting [93] lead to a scaling law for a two-dimensional wake such that the velocity defect scales with the square-root of the blade drag coefficient. Due to the strong interaction between the mean velocity deficit and the local turbulence, most approaches rely on empirical correlations. One of the first quantitative models was proposed by Silverstein [115] for a wake convected behind an isolated airfoil. He correlated the wake decay to the drag coefficient of the airfoil. Wygnanski [116] reported on extensive velocity measurements behind isolated obstacles (airfoil, cylinder, etc.) and formulated the correlation in terms of the boundary layer thickness. Measurements have been performed downstream of two-dimensional cascade blades [113] of fan rotors [112, 117]. They confirm that the wake deficit scales fairly well with the square-root of the blade drag coefficient if the distance considered is large enough. In that case, the far-wake models provide streamwise variations of the wake

parameters in the following form:

$$\begin{aligned} w(\ell) &= \sqrt{w_{TE}^2 + K \cdot C_D \cdot \frac{\ell}{c}}, \\ w(\ell) \cdot d(\ell) &= const, \end{aligned} \tag{4.9}$$

where ℓ is the distance to the trailing edge. The product of wake width and depth (which is by definition the wake area) is assumed constant, the wake width slowly increases with distance. However this approach strongly relies on the experimental determination of the constant K. Moreover, the rapid decay observed close to the trailing edge (near-wake region) is not modelled correctly and the impact of a non-zero pressure gradient cannot be included.

We have chosen here to describe the decay on a more theoretical basis based on the integral boundary layer equation. This approach was widely used in the 60's and 70's to predict the performance of two-dimensional diffusers. In this problem, the mean flow can be reasonably well described by the one-dimensional version of the continuity equation in incompressible flow, coupled to the momentum equation to predict the growth of the boundary layer along the diffuser walls and the flow blockage. A third equation is usually required to close the problem, and there have been a number of auxiliary equations proposed for this closure. The method of Head [118] complemented by Green [119] has received some success: the volume flow rate (also called the entrainment) transported within the boundary layer is correlated to some shape factor representing the current state of the boundary layer. We apply this approach to describe the decay of the wake. We further assume incompressible flow, no wall, and that the boundary layer is fully turbulent.

$$\begin{aligned} \text{Continuity equation: } & \frac{d(W(h-\delta_1))}{d\ell} = 0 \\ \text{Momentum equation: } & \frac{d\delta_2}{d\ell} = -(H_{12}+2)\frac{\delta_2}{W}\frac{dW}{d\ell} \\ \text{Entrainment equation: } & \frac{1}{W}\frac{d(W(\delta_0-\delta_1))}{d\ell} = 2E \end{aligned} \tag{4.10}$$

These equations are applied along a streamtube, in the direction of wake convection. The velocity W denotes the velocity outside of the boundary layer, here W_{max}. The entrainment coefficient E is related to the shape factor through the following empirical relation:

$$E = K_E(H_{12} - 1)$$

where the constant K_E is calibrated to match experimental measurements of a small-deficit wake with zero pressure-gradient (see Townsend [120]). In that case we have:

$$\delta_2 \frac{dH_{12}}{d\ell} = -0.468(H_{12}-1)^3 = -2E \cdot \frac{(H_{21}-1)^2}{1.3}$$

As explained by Lyrio [121] and detailed more mathematically by Veldman [122], the equations (4.10) must be solved simultaneously in order to avoid convergence problems, especially when the coupling between the inviscid mean flow and the boundary layer is strong (typically near separation). The approach presented here enables to account for the interaction between neighbouring wakes and for non-zero pressure-gradient. Moreover, it reproduces the rapid decay observed near the trailing edge of blades and the more moderate variations in the far-wake region.

We will now illustrate the capabilities of this model through three parameter studies. In Figure 4.2 is presented the streamwise decay of the non-dimensional wake parameters. The streamwise distance ℓ is normalized by the streamtube height h. Near the trailing edge of the blades ($\ell/h < 1$), the more intensive mixing is responsible for rapid variations. Especially the wake area decays very fast in this region. Further downstream ($\ell/h > 1$) the decay is markedly slower. The wake flattens as the width

increases and the depth decreases, but the wake area is nearly constant in this region which is still called the near-wake region. The far wake is not depicted here (width $w > 0.4$). It corresponds to the region where the wakes of adjacent blades start to merge; in that case the decay accelerates and the wake area decreases again. The various colour lines in Figure 4.2 correspond to a variation of the streamwise pressure gradient. The blade loading and the initial parameters of the wakes are maintained constant. For a given streamwise position, the wake depth and the shape factor are larger in the presence of an adverse pressure gradient. This result is in agreement with the experimental observations of Raj [111] made on cascade of airfoils, which stated that the decay is less rapid in presence of an adverse pressure gradient.

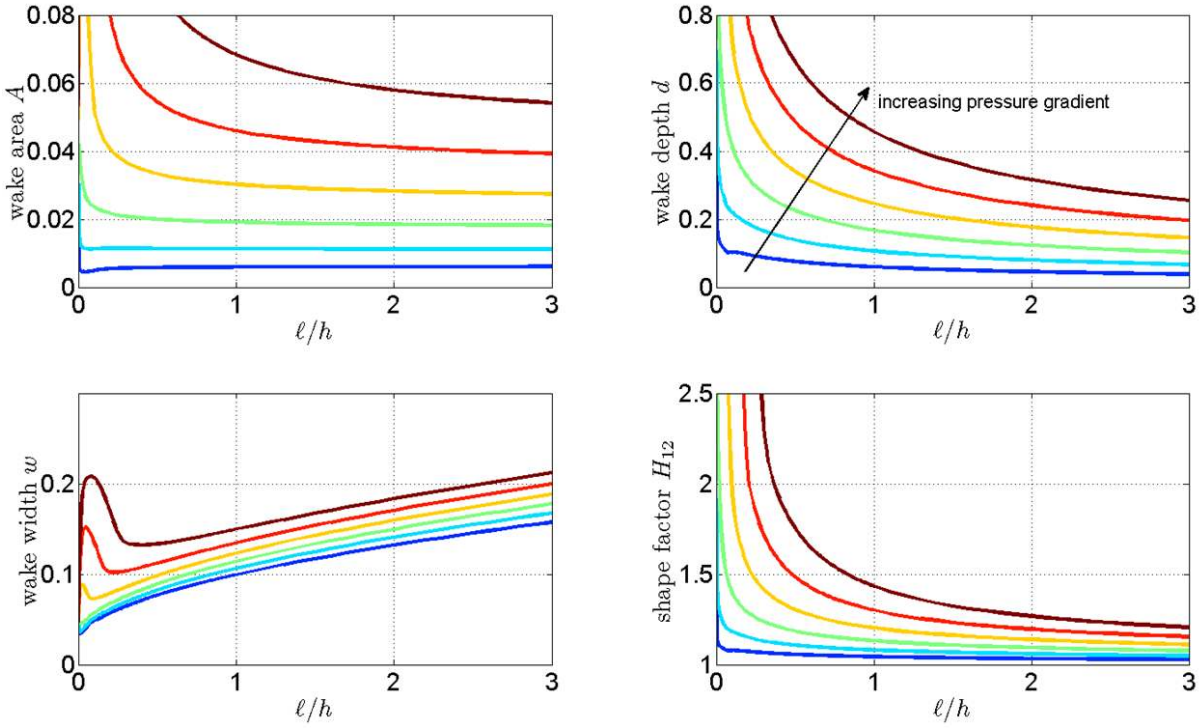

Figure 4.2: Streamwise evolution of wake parameters for different values of pressure gradient (initial wake parameters kept constant)

The effect of blade loading on the streamwise evolution of the wake parameters can be examined in Figure 4.3. For a given blade geometry, the blade loading is directly related to the drag coefficient and to the boundary layer thickness at the trailing edge of the blades. Several measurements on compressor rotors carried out by the research team of Lakshminarayana [113, 112, 123] have confirmed that a higher blade loading slows down the decay and induces a larger depth and width of the wakes. This is also what the present model predicts: for a given streamwise position, the depth and shape factor increases with the blade loading, however the effect seems not to be as pronounced as for the pressure gradient.

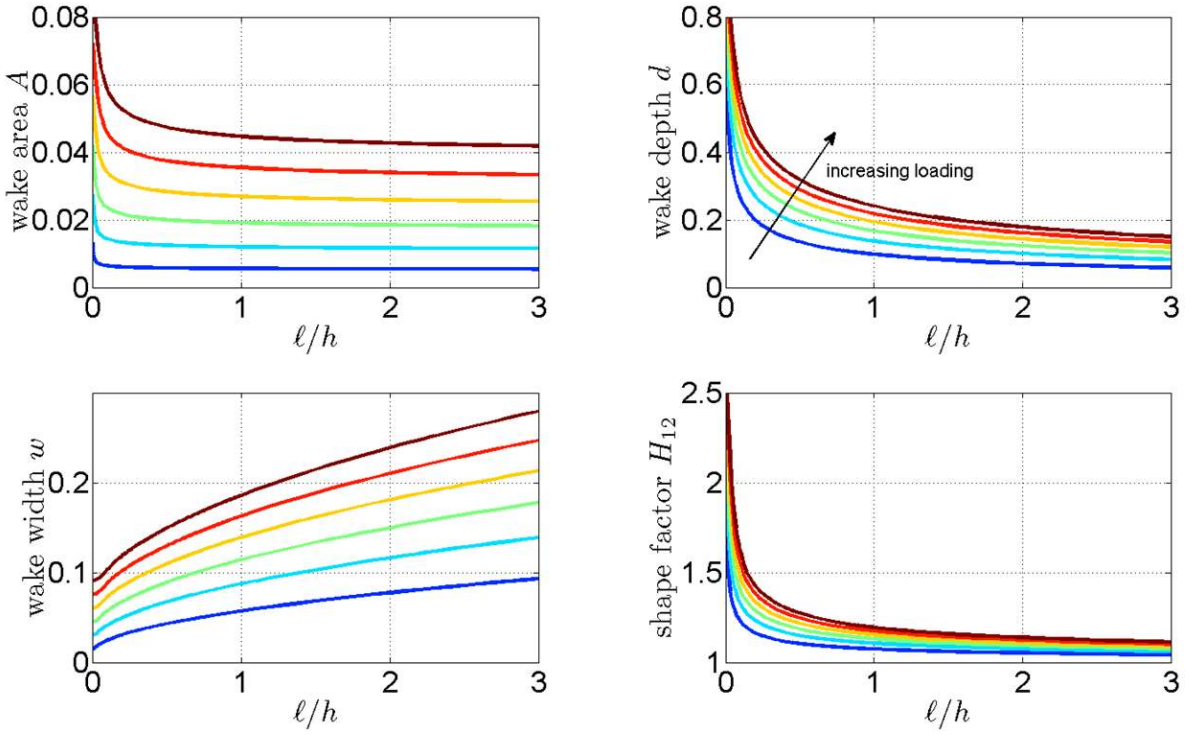

Figure 4.3: Streamwise evolution of wake parameters for different values of blade loading

Finally, the scaling of the wake width with the blade drag coefficient is shown in Figure 4.4. The solid lines depict the results of the model whereas the dashed lines represent the empirical scaling law of Eq.(4.9), with $K = 0.3$. A good agreement is observed for the low solidity cases (blue lines $\sigma = 0.1$ and green curves $\sigma = 0.2$). For the higher solidity typical of a compressor blade row (brown curves $\sigma = 1$) the empirical scaling law underpredicts the wake decay. These results are also in agreement with the measurements of Ravindranath [112] who stated that the wake width roughly scales with the square root of the drag coefficient.

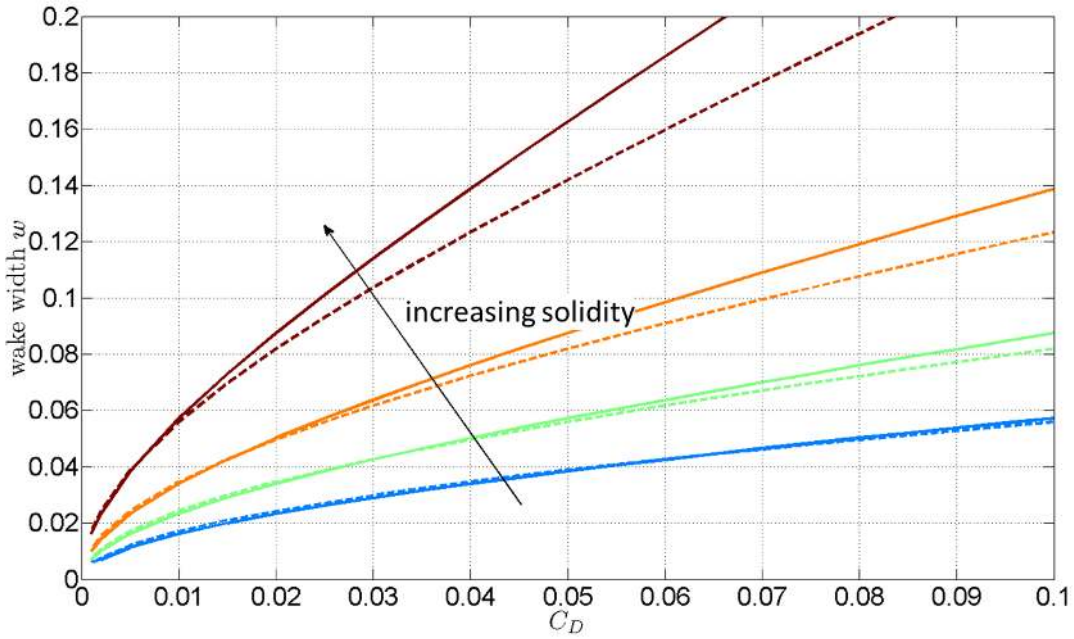

Figure 4.4: Variation of wake width on blade drag coefficient for the fixed streamwise position $\ell/h = 1$) and for different solidity. (solid line: correlation of Eq.(4.9), dashed line: solution of Eq.(4.10))

4.4 Turbulence

Stochastic velocity fluctuations proper to turbulence are the source of broadband noise. Three different categories will be considered in this section: inflow turbulence generated in the atmosphere and ingested by the fan, the turbulence present in the blade wakes, and turbulence generated inside the boundary layer developing on the blade and interacting with the trailing edge. In all cases, the turbulence is assumed isotropic with a small correlation length, and it can therefore be fully described by the turbulent kinetic energy, the integral length scale, and a non-dimensional function for the spectral content. The expression of turbulence in the frequency domain is preferred to that in the time domain as it enables more easily an interpretation of the theoretical results and suits the acoustic formulation presented in chapter 6. Glegg [124] has recently pointed out the difficulties associated to this choice and proposes an alternative description based on time correlations.

4.4.1 Inflow turbulence ingested by the fan

We assume the turbulence ingested from the atmosphere to be isotropic and homogeneous. The root-mean-square of the turbulent velocity fluctuations in the streamwise and transverse direction are identical and equal to 2/3 of the turbulent kinetic energy k, i.e. $\overline{u^2} = \overline{v^2} = \overline{w^2} = \frac{2}{3}k$. The homogeneity assumption implies that the entire energy is contained in the circumferential mode of zero order $m = 0$. The one-dimensional power spectral density of the velocity fluctuations and the turbulence correlation length are described by the Von Karman model utilized by Amiet [125].

$$\Phi_{uu}(\omega) = \overline{u^2} \cdot \frac{\Lambda}{W_0} \cdot \frac{0.656}{(1+1.8z^2)^{5/6}}$$
$$\ell(\omega) = \Lambda \cdot \frac{5.01z^2}{\sqrt{1+z^2}\left(1+\frac{8}{3}z^2\right)} \rightarrow 1.4\frac{W_0}{\omega}$$

where W_0 is the mean flow velocity, the reduced frequency is $z = \frac{St}{St_0}$, the Strouhal number $St = \frac{f\Lambda}{W_0}$ and a reference Strouhal number $St_0 = 1/2\pi \approx 0.16$. The quantities $\overline{u^2}$ and Λ are properties of the

atmospheric turbulence and do not depend on the fan considered. At high frequencies the correlation length does not depend on the integral length scale. Note that the power spectral density Φ_{uu} has the dimension of a squared velocity divided by a frequency and verifies:

$$\int_{-\infty}^{+\infty} \Phi_{uu}(\omega) d\omega = \overline{u^2} \tag{4.11}$$

Wake turbulence

The characteristics of turbulence convected behind rotor blades has been documented by Reynolds [126] and Ganz [117]. It was shown in these studies that the wake turbulence presents some similarities with isotropic free turbulence. More recently, hot-wire measurements inside a low-speed rotor-stage [127] at various operating conditions have provided an extensive set of wake turbulence data for the cyclo-stationary analysis applied by Jurdic [128]. He showed that the wake turbulence spectra can be represented as a product of a one-dimensional frequency spectrum and a Gaussian-shaped modulation function depending on the circumferential mode order m, which he called cyclic order. This may be written mathematically as:

$$\Phi_{uu}(\omega, m) = \Phi_{uu}(\omega) \cdot e^{-2\pi \cdot w^2 \cdot h^2} \text{ , where } h = m/B \tag{4.12}$$

Note that the Gaussian function is the square of the mean-flow Gaussian wake mentioned in Eq.(4.8). The non-dimensional width w is assumed to be identical for the mean wake and the turbulent wake. The one-dimensional spectrum $\Phi_{uu}(\omega)$ is that utilized by Amiet [125] for turbulence-airfoil interaction noise.

The peak turbulent kinetic energy (assumed to be on the center axis of the wake) and the integral length scale are determined empirically. Experimental observations by Ganz [117] and Wygnanski [116] indicate that the wake turbulent velocity scales proportionally to the wake deficit velocity $u(y)$ defined in Eq.(4.6):

$$\overline{u^2}(y) = \left(K_{Uturb} \cdot u(y)\right)^2$$

After averaging the quantity $\overline{u^2}(y)$ over a blade passage we obtain:

$$\overline{u^2} = \sum_{h=-\infty}^{+\infty} \left(K_{Uturb} \cdot u(h)\right)^2 \text{ , see Eq.(4.8)}$$

The integral length scales with the wake width and the blade passage streamtube height.

$$\Lambda = K_{Lturb} \cdot w \cdot h$$

Qualitatively, this model correctly reproduces the increase of turbulence intensity and length scale as the blade drag coefficient or loading increases, which was observed by Ganz [117] and Camp [129]. The empirical constants have a fairly wide range of values reported in the literature: K_{Uturb} varies between 0.2 and 0.4, and K_{Lturb} varies between 0.2 and 0.6. In this model, the turbulence is assumed to adapt instantaneously to changes in the mean-wake flow, so the history of turbulence is ignored. Moreover, the coupling between the decay of the mean-flow wake and the turbulence production is not accounted for. There is a potential for an improved analytical description of the wake decay, which could for example be based on a standard two-equation turbulence model coupled to the integral boundary layer equation.

4.4.2 Wall-pressure fluctuations

The prediction of trailing edge broadband noise strongly depends on the appropriate definition of a source strength to serve as an input for the acoustic model. The quantity usually considered is the local surface pressure spectrum, which can be obtained by one-point measurements with a surface pressure sensor located near the trailing edge. The correlation proposed is the following:

$$\Phi_{pp}(\omega) = \left(\frac{1}{2}\rho_0 W_0^2 C_D\right)^2 \cdot \frac{\delta_1}{W_0} \cdot F(z) \text{ , where } F(z) = \frac{1}{1 + z + 0.217z^2 + 0.00562z^4}$$

The reduced frequency z is defined similarly to the previous section. The Strouhal number is based on the boundary layer displacement thickness at the blade trailing edge: $St = \frac{f \cdot \delta_1}{W_0}$. The non-dimensional spectrum $F(z)$ is that given by Willmarth and Roos [130]. In their model, as in the model of Goody [131], the drag coefficient has a constant value $C_D = 0.0045$ or $C_D = C_f$, which is suited for flat plate with zero-pressure gradient but not for loaded fan blades. An extension of Goody's model was proposed by Rozenberg [37] to account for a pressure-gradient effect. However, the pressure fluctuations also scale with the local skin friction coefficient C_f near the trailing edge, leading to an unrealistic noise decrease as blade separation occurs (in that case $C_f = 0$). For this reason, we have chosen the drag coefficient C_D as scaling parameter: it increases continuously as blade loading increases beyond the separation point. The quantity Φ_{pp} is expressed in squared Pascal per Herz.

For the spanwise correlation length, we use at high frequencies the model of Amiet [132] based on the work of Corcos [133]:

$$\ell(\omega) = 1.7 \frac{U_c}{\omega} \tag{4.13}$$

The parameter U_c is the convection speed of the eddies, it lies between 60 and 80 percent of the external flow velocity outside of the boundary layer. The coefficient 1.7 is empirical and may vary between 1.4 and 2.1 depending on the pressure-gradient.

A less empirical model might be derived from the streamwise development of the boundary layer along the blade. This approach was adopted by Remmler et al. [134] to calculate the pressure fluctuations from a RANS simulation. They started from the Poisson equation for the fluctuating pressure. The procedure is based on the integral within the boundary layer in the direction normal to the wall of the streamwise velocity profile $W(y)$ and turbulent kinetic energy (which both can be extracted from a RANS simulation). An alternative approach proposed by Glegg [135] also provides the ability to predict trailing edge noise from RANS calculations.

4.5 Change of reference frame

The flow perturbations mentioned previously were expressed in the frame of reference locked to the blades that create them. However the interaction mechanism resulting in sound emission has to be calculated in the reference frame locked to the blades that generate sound. For that reason, it is necessary to convert the perturbation from one reference frame to another. Let denote $p(t, \theta)$ the circumferential distribution of flow perturbation expressed in the time domain.

$$p_m^\omega = \frac{1}{2\pi T_{ref}} \int_{t=-\infty}^{+\infty} \int_{\theta=0}^{2\pi} p(t,\theta) e^{i(\omega t - m\theta)} d\theta dt$$

This quantity can be formulated in a different reference frame moving with a speed Ω relative to the first one. In that case, the circumferential position is expressed as $\tilde{\theta} = \theta - \Omega t$. The flow perturbation becomes:

$$p_m^\omega = \frac{1}{2\pi T_{ref}} \int_{t=-\infty}^{+\infty} \int_{\tilde{\theta}=-\Omega t}^{-\Omega t+2\pi} p(t,\theta) e^{i((\omega - m\Omega)t - m\tilde{\theta})} d\tilde{\theta} dt$$

Hence, we obtain by identification:

$$p_m^\omega = p_{\tilde{m}}^{\tilde{\omega}} \text{ , where } \begin{cases} \tilde{m} = m \\ \tilde{\omega} = \omega - m\Omega \end{cases}$$

Changing the reference frame is therefore equivalent to a frequency shift similar to the Doppler shift of a sound source in rectilinear motion. It also means that the circumferential mode decomposition of a perturbation is necessary to change the reference frame. Technically, the transformation may lead

to negative values of the pulsation frequency; in that case the negative part can be mirrored into the positive part by changing the sign of the circumferential mode and taking the complex conjugate. The spectrum shows such a symmetry property because the signal $p(t,\theta)$ is real. The conversion from negative to positive frequencies reads:

$$p_m^{-\omega} = \left(p_{-m}^{\omega}\right)^* \Rightarrow \left|p_m^{-\omega}\right|^2 = \left|p_{-m}^{\omega}\right|^2$$

An example is now presented to illustrate the effect of transforming the reference frame on the spectrum of turbulence. We consider the wake turbulence spectrum of Eq.(4.12) written as a Von Karman spectrum modulated by the Gaussian-shaped mean-flow wake behind rotor blades. Figure 4.5 shows the original spectrum in blue dashed line as observed in the rotor reference frame, the spectrum after transformation into the fixed reference frame is depicted by the thick red line. On the left-hand side of the figure, the integral length scale Λ is small compared to the blade spacing and on the right-hand side it is much higher, corresponding to conditions with large flow separation on the rotor blades. Strong humps appear in the spectrum observed the fixed frame for the large integral length scale and they are centered on the harmonics of the blade passing frequency (BPF). No hump is observed for the small length scale. The formation of humps centered on the BPF harmonics is driven by two non-dimensional parameters:

- The primary parameter is the Strouhal number based on the BPF: $St_{BPF} \equiv \frac{\Lambda f_{rot} B}{W_0} \propto \frac{\Lambda}{s}$. This parameter is directly proportional to the ratio of integral length scale to blade spacing. If the Strouhal number is very small, typically below 0.02, the spectrum is hardly modified by changing the reference frame. As the Strouhal number increases, energy is progressively transferred from the low to the high frequencies, and from the circumferential mode zero to modes rotating in the same direction as the rotor. If the Strouhal number exceeds a value around 0.4, humps arise near the BPF-harmonics.
- The width w of mean wake drives the decay of BPF harmonics. The larger the width is, the faster is the decay. This usually occurs in combination with large values of the integral length scale.

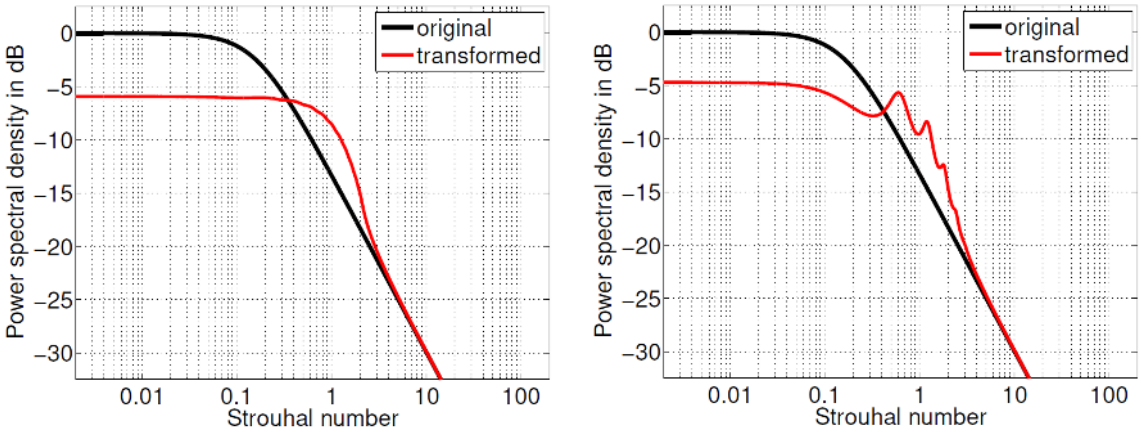

Figure 4.5: Modification of a wake turbulence spectrum through transformation of the reference frame (left: moderate length scale $St_{BPF} = 0.2, w = 0.07$, right: large length scale $St_{BPF} = 0.6, w = 0.2$)

4.6 Airfoil response function

The next step on the way toward noise emission is to determine how the blades respond to an incoming velocity perturbation (also called gust). This process can be regarded as a transfer function between flow velocity fluctuations as input and the surface pressure on the blade as output. We will see in chapter 6 dedicated to the acoustic models that the source strength is formed by the force per unit area exerted by

the fluid on the blades. For the present application, this chordwise distribution of the force is the normal component $f_n^\omega(\ell)$, at the pulsation frequency ω. This quantity can be written as a local pressure jump Δp and is proportional to the inflow dynamic pressure:

$$f_n^\omega(\ell) = \Delta p(\omega, \ell) = \frac{1}{2}\rho_0 W_0^2 C_L(\omega) h_L(\ell)$$

The quantity $C_L(\omega)$ is the unsteady lift coefficient and $h_L(\ell)$ is the non-dimensional distribution of lift along the blade chord, independent of the frequency. The original model developed by Sears [136] assumes a chordwise distribution in the form:

$$h_L(\ell) = \frac{\pi}{2}\sqrt{\frac{c-\ell}{\ell}} \text{ , note that } \frac{1}{c}\int_{\ell=0}^{c} h_L(\ell)d\ell = 1$$

This is the distribution of the response to a perturbation propagating downstream (the peak loading is located at the leading edge). The unsteady lift coefficient is given by the two-dimensional incompressible-flow linear theory:

$$C_L(\omega) = 2\pi\frac{u_n(\omega)}{W_0}S(\omega)$$

where u_n is the velocity fluctuation normal to the airfoil chord and S is the Sears function [136] for incompressible flow.

$$S(\omega) = \frac{1}{\sqrt{1+2\pi\sigma}} \text{ , where } \sigma = \frac{\omega c}{2W_0} \tag{4.14}$$

This is the low frequency approximation for the incompressible Sears function as given in Goldstein [137] but modified to take reference at the airfoil leading edge instead of the mid-chord (explaining why the phase of S is constant and equal to 0: the airfoil response to a gust is immediate at low frequencies). Further assumptions underlay this model:

- The blade is approximated by an infinitely thin flat plate operating at zero mean-flow incidence. The effects of thickness, camber, and mean loading have been investigated by Goldstein and Atassi [138] or Kerschen et al. [139].
- The solution proposed here is valid for low values of $M_0 \cdot \sigma$ (low Mach number and low frequencies). This parameter can be easily written in terms of a non-dimensional acoustic wavenumber: $M_0 \cdot \sigma = kc/2$. So the problem of compressibility is closely related to the compactness of the source. As we will see in the chapter 6 presenting the acoustic models, the source non-compactness is accounted for via a chordwise correlation function that depends on the non-dimensional wavenumber kc.
- The gusts impinge the blade normally to its span or the blade is unswept. Solutions for oblique gusts have been derived by Graham [140] or Adamczyk [141]. Moreover, only harmonic gusts are considered: this a reasonable assumption in the case of wakes or turbulence, which decay very slowly during their convection, but the exponential decay of potential fields would require a generalized model as done by Kemp and Homicz [142].
- The presence of neighbouring blades and their effect on the unsteady lift response function are neglected. Significantly more complex models called cascade response model are available in the literature (see for example the work of Glegg [17] or Posson [38]).

.

The velocity fluctutation normal to the airfoil is obtained by appropriate projection of the streamwise and transverse velocity components u and w:

$$u_n = u \cdot \sin(\chi - \beta_{rel}) + w \cdot \cos(\chi - \beta_{rel})$$

The second term is neglected during the calculation as the streamwise velocity perturbations inside a wake are usually much higher than the transverse ones. The term inside the sine and cosine functions is

the difference between the stagger angle of the excited blades and the flow angle expressed in the relative system of the wake-generating blade row (which is approximately the stagger angle of the upstream blade row). This difference is around 90 degrees on a counter-rotating fan stage and around 60 degrees on a rotor-stator stage, thus more excitation may be expected from a counter rotating stage.

For broadband noise, the unsteady lift coefficient is related to the spectral density of velocity fluctuations:

$$\overline{|C_L|^2}(\omega) = 4\pi^2 \frac{\Phi_{uu}(\omega)}{W_0^2} |S(\omega)|^2$$

Note that we assumed $\Phi_{u_n u_n} = \Phi_{uu}$ which is a reasonable approximation in isotropic turbulence.

Chapter 5

Extrapolation of meanline data

5.1 Need for a radial extrapolation

As described in the previous chapters, the steady and unsteady aerodynamic calculations are based on a meanline approach. The information delivered by this kind of approach is sufficient to get an estimate of the overall aerodynamic performance of a fan, however acoustic calculations require a more detailed set of flow data, even for the prediction of global trends. This is mainly due to the acoustic interference effects, which result from the superimposition of sound waves emitted from sources distributed in space, especially in the radial direction. The inteference of sound waves may lead to very significant reductions in tonal noise levels compared to the case with compact sources. This effect becomes more pronounced if the amplitude of radial geometry variations are in the same order of magnitude as the acoustic wavelength, typically at high frequencies. For that reason, a smooth radial distribution of the source strength is necessary and the flow data obtained at meanline radius must be extrapolated in radial direction. For broadband noise, this effect is less important due to the small correlation length of the flow turbulence structures, but there are still strong radial variations of the source strength due to the large differences in Mach numbers between the tip and the hub of a fan stage. We will now detail the assumptions and the models used to extrapolate the meanline data.

5.2 Steady flow velocities

The sound speed a_0 and the static air density ρ_0 are considered radially constant. The radial variation of the flow velocities in the absolute reference frame is described by a potential flow model (see Grieb [86]). This is also known as free-vortex design and assumes that no vortices are shed by the blade along the radius. This assumption is acceptable for ducted rotors and stators with very small clearance at their blade ends, but it may not be correct for open rotors where a strong leakage of blade circulation is observed toward the tip:

$$\begin{aligned} U(r) &= \Omega \cdot r \\ W_x &= const \\ W_t(r) &= \frac{\Gamma}{r} \\ W_0(r) &= \sqrt{W_x^2 + (W_t(r) - U(r))^2} \end{aligned}$$

The circumferential velocity of the blade is U and Ω is the rotation frequency in radians per second. The quantity Γ is the radially constant blade circulation and can be calculated from Eq.(2.6) at the meanline radius. Combining this equation with Eq.(2.5) shows that this model corresponds to a radially constant enthalpy rise $\Delta H_t = \frac{\Omega}{2\pi} B\Gamma$, which is an acceptable approximation except near the hub and near the tip of an unducted rotor. The hub region is usually unloaded on purpose to avoid too large secondary-flow

disturbances, and the tip of open rotors cannot produce lift. The relative velocity magnitude W_0 will be used as scaling parameter to extrapolate the perturbation velocities.

5.3 Blade geometry

The extrapolation of the geometry is based on the radial variations of the flow velocities. The blade stagger angle χ is extrapolated assuming that the blade operates approximately zero incidence, i.e. the blades are aligned with the inflow angle:

$$\tan\chi = \frac{W_t - U}{W_x}$$

In practical cases, it is observed that rotors operating with an axial inflow have twisted blades to satisfy the zero-incidence conditions. Stators or rotors located downstream of the first rotor operate with non-axial inflow: in that case, we consider untwisted blades as the inflow angle in the relative reference framce is reasonably constant in radial direction.

$$\tan\chi(r) = \begin{cases} \tan\chi_{ML} \cdot \frac{r}{r_{ML}} \text{ , for twisted blades} \\ \tan\chi_{ML} = const \text{ , for untwisted blades} \end{cases}$$

The variations of the blade stagger angle determine the twist. The axis along which blades are twisted can be specified through the quantity PCA, which stands for pitch change axis and indicates the chordwise position of the axis as a fraction of the blade chord. A value around 0.5 is usual. The radial variation of the blade chord is linear and described by the chord taper ratio (CTR), which is the ratio of the tip chord to the hub chord. The radial variations of solidity are given by:

$$\sigma(r) = \frac{B \cdot c(r)}{2\pi r}$$

The blade thickness is calculated similarly based on the ratio of the tip to hub relative thickness (TTR). For a ducted rotor-stator stage, the value of CTR is usually slightly above 1, and TTR is around 0.5. For a CROR, the geometry of the blades shows a more pronounced taper. The position of the leading and trailing edge of each blade row is calculated from the radial twist and the sweep and lean angles, whose values are assumed constant in radial direction.

5.4 Lift, drag and unsteady flow velocities

The lift and drag coefficients, and the quadrupole term determine the rotor-alone tonal noise levels, and to some extent the strength of the potential field at the origin. We propose the following simple models:

$$C_L = const$$
$$C_D = const$$
$$\overline{\rho u_t^2}(r) \propto W_0^2$$

The quadrupole term is assumed to scale with the square of the relative flow velocity W_0. The unsteady perturbation velocities and surface pressure fluctuations are also assumed to scale with a certain power of the relative flow velocity, we propose:

$$\Phi_{pp}(r) \propto W_0^4$$
$$\Phi_{uu}(r) \propto W_0^2 \cdot \sigma$$
$$u_{wake}(r) \propto W_0 \cdot \sigma$$
$$u_{pfield}(r) \propto W_0 \cdot \sqrt{\sigma}$$

The flow perturbation also scales with some power of the solidity because the drag coefficient of blades is assumed radially constant. It should noted that the flow perturbations due to endwall losses are not taken into account and cannot therefore contribute to noise emission. The amplitude of velocity fluctuations induced in the wake and potential field decay axially but are assumed constant radially. Their phase, however, features significant radial variations as a result of the tilting of the wakes. This latter aspect is modelled in more details in the next chapter dedicated to Acoustics, and is responsible for substantial sound wave cancellations in tonal interaction noise.

Chapter 6

Acoustics

6.1 Modelling approach

The purpose of this chapter is to present a fully analytical formulation of noise generated by rotating blades. A unified approach is adopted to handle various engine configurations such as ducted fans or counter-rotating open rotors, and to treat the tonal and broadband noise components on the same modelling basis. Apart from the ability of predicting noise very rapidly, the present approach also provides a theoretical description of the different noise generation and propagation mechanisms with a special attention given to their relation to the aerodynamic parameters and mean flow quantities. The previous chapters were dedicated to Steady and Unsteady Aerodynamics, we now treat and describe the Acoustics as a by-product of the aerodynamics of the engine.

This is essentially the point of view taken by the acoustic analogy of Lighthill [143]. From the continuity and momentum equations, which basically describe any flow motion, Lighthill derived a relation equivalent in form to a wave equation in a medium at rest:

$$\frac{\partial^2 \rho}{\partial t^2} - a_0^2 \nabla^2 \rho = \frac{\partial^2 T_{ij}}{\partial x_i \partial x_j,} \tag{6.1}$$

where ρ is the density, a_0 the propagation velocity, and T_{ij} is the Lighthill's stress tensor. By analogy he identified the left-hand term of Eq.(6.1) as the propagation of sound and the right-hand term composed of perturbation flow quantities as the source of aerodynamic sound. His work marks the birth date of Aeroacoustics as a distinct research domain. As explained by Morfey [48] and Goldstein [137], the fundamental aspect of the acoustic analogy is the causal link established between noise and the aerodynamic sources, and the implicit assumption, for the theory to be of any practical use, that the sources can be evaluated a priori independently of noise. Of course, this approach is not rigorously exact, and represents an interpretation of the continuity and momentum equations, and there exist situations in which the propagation and generation of sound are interrelated without any clear causal link. Still, the acoustic analogy has been very successful in enhancing our physical understanding of aerodynamic sound and forms the theoretical framework for the present modelling approach.

More precisely, we adopt the solution of the acoustic analogy that was derived by Goldstein [144, 137]. This is a generalized version of the Ffowcs-Williams & Hawkings solution of Lighthill's equation with moving solid boundaries. Goldstein utilizes Green's functions to better distinguish between acoustic propagation and sound sources, and to adapt the solution to the specific problem considered. Through the choice of the appropriate Green's function, it is possible to obtain a solution for the sound pressure in the free space or in a duct. Furthermore, we choose a formulation of Goldstein's work in the frequency domain, as first applied by Hanson [25]. The frequency-domain formulation is prefered to the time-domain formulation (see for example Farassat [28]) as it provides more insight into the driving parameters of noise.

A brief history of the rotating-blade noise prediction is presented schematically in Fig. 6.1. Propeller noise is an old problem that has attracted attention since the 30's. Gutin [145] was the first to publish

a quantitative prediction of propeller noise, where he identified that sound was produced by the rotation of steady dipoles related to the blade forces. Accompanying the rapid growth of turbojet civil aircraft, Aeroacoustics research exploded during the 50's, relying on Lighthill's powerful concept of the acoustic analogy and its extensions to moving flow and solid boundaries [146]. But the first turbojets of that time were single-stream engines with no bypass, so the jet was the major source of noise and represented the main focus of aeroacoustic research. As technology shifted to larger, two-stream engines with a bypass (this was an improvement in terms of both fuel consumption and noise), the relative importance of jet noise compared to the other sources decreased and more attention was paid to rotating-blade noise. The work of Ffowcs-Williams and Hawkings [147] marks the return to the old propeller noise problem, now tackled from the point of view of the acoustic analogy. This new approach enabled to identify and to separate the aerodynamic mechanisms responsible for the noise emission, and under which conditions some of them can be neglected for the sake of computational efficiency. Goldstein [144] extended Ffowcs-Williams & Hawkings' equation to problems with boundary conditions like in a duct.

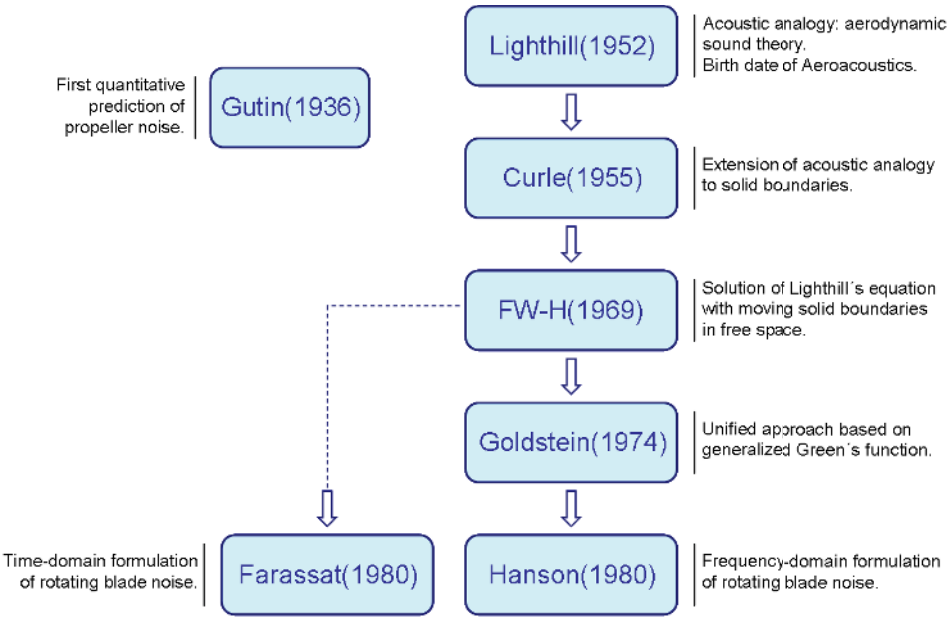

Figure 6.1: History of rotating-blade noise prediction based on the acoustic analogy

Several studies after Hanson [25] also adopted the frequency-domain formulation of Goldstein's solution, they are presented in Table 6.1 and sorted according to the specific problem they tackle. Except for the in-duct tonal self noise (supersonic rotor noise associated to non-linear shock propagation, prediction models not based on the acoustic analogy can be found in [107, 148]), all problems have been treated in this way by at least one research team. However, because of some specificity associated to each problem, the governing equations are generally expressed in very different forms (including different notation conventions), which makes the comparison between the problems as well as the general understanding of rotating-blade noise more difficult. The present work provides similar analytical formulations for the in-duct and free-field, tonal and broadband, interaction and self-noise problems. Some attention will be given to the similarities that can be observed when treating problems of open rotor and ducted fan noise. In the propeller problem the sound is radiated in the free space while it propagates inside a duct before radiating to the far field in the fan noise problem. The presence of a duct modifies not only the propagation but also the generation of sound.

Furthermore, we will extensively use the cylindrical system of coordinates, which is well suited for rotor noise problems. In this system of coordinates, the 2π-periodicity in circumferential (or azimuthal)

direction allows to decompose the pressure into a discrete sum of Fourier components called azimuthal modes. We will consider a purely axial uniform flow in the reference frame fixed to the engine. The boundary conditions will be either those of the free space (with the far-field approximation) or those of an infinitely long annular duct with hard walls. The presence of the blades as sound scatterers will be ignored.

problem	free-field	in-duct
tonal self noise	Hanson(1980) [25] Parry&Crighton(1989) [44]	- -
tonal interaction noise	Hanson(1984) [26] Parry(1988) [43] Carazo(2011) [39]	Ventres(1982) [6] Meyer&Envia(1996) [7]
broadband self noise	Zhou(2004) [51]	Glegg(1998) [16]
broadband interaction noise	Blandeau(2009) [52] Kingan(2012) [54]	Glegg(1993) [15] Joseph(2003) [50] Lowis(2006) [149] Ventres(1982) [6] Mani(1997) [150]

Table 6.1: Some applications of the frequency-domain formulation of Golstein's version of the acoustic analogy

As mentioned in the previous paragraph, alternative approaches not based on the acoustic analogy of Lighthill may be more appropriate in situations where there is a strong coupling between noise propagation and noise generation. For example the work of Atassi [151] presents some general aspects of this approach and a practical application. In his book on Aeroacoustics, Goldstein [137] dedicates an entire chapter to alternative theories based on the solution of the linearized vorticity-acoustic field equations.

6.2 Assumptions

The acoustic models derived in this chapter are exact solutions of a simplified problem. The assumptions underlying the simplification of the problem are listed below:

- Uniform axial flow: This assumption is linked to the level of accuracy used for modelling the propagation of sound in the moving medium, which is represented by the Green's function. Physically, any deviation from this model results in sound scattering, but in the acoustic analogy approach, this effect is interpreted as a source (typically contained in the quadrupole term). The assumption of uniform axial flow neglects in particular the interstage swirl, the tip vortex flow of open rotors and the supersonic regions and shocks on the suction side of the blades.
- For unducted configurations, the far-field approximation of the free-space solution is taken. For ducted configurations, the duct is formed by infinitely long and hard walls with no sound absorption.

As a result no reflections at the end are considered. Moreover, the presence of the blades as sound scatterers is not modelled, which means that cascade resonance and shielding effects are neglected.

- Thin and slightly cambered airfoils: the sources located on the blades all have the same orientation along the chordline. Blade of turbines, at a rotor hub with low hub-to-tip ratio, or stators of highly loaded stages depart significantly from this assumption. However the blades may be twisted in radial direction, and have a sweep and a lean angle.
- Small angle of attack: the blades and the inflow are oriented in the same direction.
- Radial forces and radial flow components are neglected. This is acceptable as long as the blade lean angle is moderate.
- All blades of a given rotor or stator are geometrically identical and equally spaced in circumferential direction and located at the same axial position.
- Small turbulence length scale: the spanwise and circumferential correlation lengths are identical and considered small compared to the duct height and to the blade spacing, which means that the blades are uncorrelated for the broadband noise component.
- Taylor's turbulence hypothesis: the turbulence is considered frozen as it convects over the blade, which corresponds to infinite correlation length in streamwise direction.

6.3 Noise propagation

6.3.1 The convective and flyover problems

The problem of sound emitted by an engine moving relative to a medium can be usually formulated from two different points of view: Wells and Han [152] distinguish between the moving-medium problem, which we call here the convective problem, and the moving-observer problem, also called flyover problem. As the present work is basically dealing with the emitted sound power at given engine operating conditions, we adopt in the present work the formulation of the convective problem. The flyover problem formulation is more suited for describing the noise emission along a flight path towards a fixed observer.

In the convective problem, the observer and the engine are steady in a moving medium with uniform axial Mach number M_x. In the flyover problem, the observer is fixed in a steady medium while the engine is moving with a constant axial Mach number M_x. Although both problems are equivalent, the convective problem offers more simple formulations for noise generation because the emission and observation angles do not depend on time and the frequency emitted by the source is identical to that perceived by the observer as the Doppler shift is removed. Moreover, according to Wells and Han [152], this approach presents some advantages in terms of computational efficiency. A more recent work by Weckmueller et al. [153] also explains why the convective formulation leads to reduced computation time and a higher accuracy for tonal noise problems. Figure 6.2 illustrates the convective and flyover problems, and precises the physical meaning of the propagation angles.

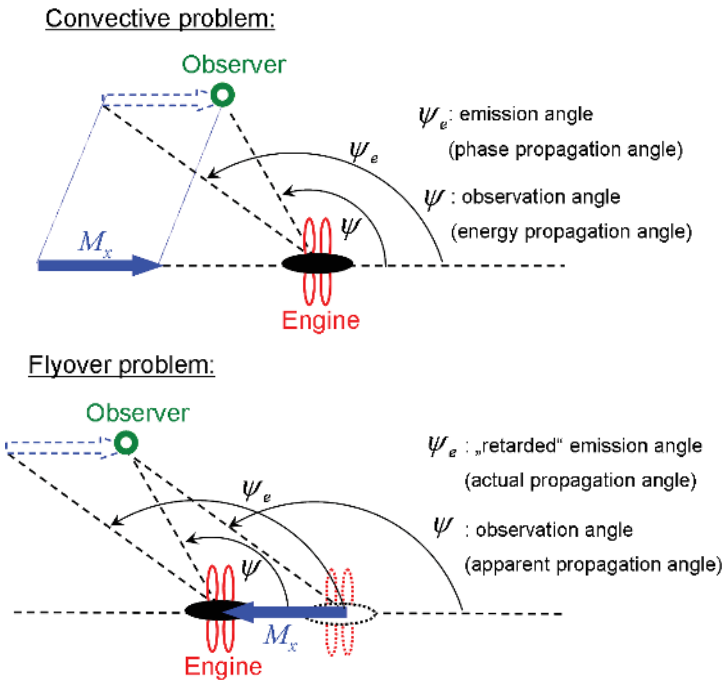

Figure 6.2: Two different points of view for formulating the sound emission

In the convective problem, the emission angle ψ_e and the observation angle ψ correspond to the phase and energy propagation angles in the moving medium, respectively. In the flyover problem, as the medium is steady, these angles are identical and are represented by ψ_e. In this case, ψ is an apparent propagation angle as would be perceived by the observer. The relation between these angles is given by Rienstra and Hirschberg [154]:

$$\frac{\sin\psi}{\sqrt{1-M_x^2\sin^2\psi}} = \frac{\sin\psi_e}{\mathcal{D}}$$
$$\frac{\cos\psi}{\sqrt{1-M_x^2\sin^2\psi}} = \frac{M_x+\cos\psi_e}{\mathcal{D}}$$

where the quantity $\mathcal{D}$ is called the Doppler factor:

$$\mathcal{D} = 1 + M_x\cos\psi_e \tag{6.2}$$

These angles are comprised between 0 (rearward radiation) and π (forward radiation), and are defined as presented in Figure 6.2. It should be noted that the results given by several authors (Hanson [25], Parry [44]) are formulated in terms of the emission angle ψ_e, whereas we choose here the observation angle ψ, which is more appropriate in the convective problem.

6.3.2 Dispersion relation

The dispersion relation that describes the sound propagation in a medium with uniform and purely axial flow has been derived by Morfey [155] from the linearized Euler equations applied to a harmonic sound wave. In the cylindrical coordinate system, the following relation is established between the axial and radial wavenumbers:

$$k^2 = k_r^2 + (1-M_x^2)k_x^2 + 2M_x k k_x \tag{6.3}$$

As the dispersion relation is a property of the medium, it is equally valid in the free space and in a duct. Based on the dispersion relation in a steady medium, we define an apparent wave number:

$$\tilde{k}^2 \equiv k_x^2 + k_r^2 = (k - M_x k_x)^2 = \frac{k^2}{\mathcal{D}^2} \tag{6.4}$$

6.3.3 Sound propagation

Because the boundary conditions impose certain wave forms for the problem considered, the free-space and in-duct wavenumbers are usually formulated in different ways. However, we will show that these formulations present a strong similarity.

Free-field propagation

In the free space, no constraints are imposed on the wavenumbers. The axial and radial wavenumbers are given by:

$$\begin{aligned} k_r &= k\frac{\sin\psi}{\sqrt{1 - M_x^2 \sin^2\psi}} = \tilde{k}\sin\psi_e \\ k_x &= \frac{k}{\beta^2}\left(-M_x + \frac{\cos\psi}{\sqrt{1 - M_x^2\sin^2\psi}}\right) = \tilde{k}\cos\psi_e \end{aligned} \tag{6.5}$$

The complex Fourier coefficient of the pressure is written as a sum of azimuthal modes:

$$p^\omega(x, r, \theta) = \sum_{m=-\infty}^{+\infty} p_m^\omega(x, r) e^{im\theta}$$

In-duct propagation

In a duct, the acoustic velocity is specified at the duct walls depending on the wall properties. This implies that only certain wave patterns are able to propagate within the duct without decaying. These are called modes and are described through the circumferential (also azimuthal) order m and the radial order n, which indicate the number of zeros of the acoustic pressure in circumferential and radial directions, respectively. In case of hard walls, the normal component of the acoustic velocity must be zero at the wall. This imposes the radial and axial wavenumbers to assume discrete values in the form:

$$\begin{aligned} k_r &= \frac{\sigma_{mn}}{R} \\ k_x^\pm &= \frac{k}{\beta^2}\left(-M_x \pm \alpha_{mn}\right) \end{aligned} \tag{6.6}$$

The quantity σ_{mn} represents the $(n+1)^{th}$ zero of the first derivative of the Bessel function J_m (in case of a hollow duct). The superscript sign $\pm$ above the axial wavenumber specifies the direction of propagation of the sound wave: + for downstream propagation, and - for upstream propagation. The quantity α_{mn} is called the mode cut-on factor and is defined as:

$$\alpha_{mn} \equiv \sqrt{1 - (1 - M_x^2)\left(\frac{\sigma_{mn}}{kR}\right)^2} \tag{6.7}$$

For propagating modes, the cut-on factor is a real number between 0 and 1. For non-propagating modes, the cut-on factor is purely imaginary. In that case, the axial wavenumber has a non-zero imaginary

component which is responsible for the exponential decay of the pressure amplitude along the duct. The Fourier coefficient of the acoustic pressure taken at the frequency ω is usually decomposed in the form:

$$p^{\omega}(x,r,\theta) = \sum_{m=-\infty}^{+\infty} \sum_{n=0}^{+\infty} A_{mn}^{\pm} \frac{J_m(k_r r) + Q_{mn} Y_m(k_r r)}{\sqrt{F_{mn}}} e^{ik_x^{\pm} x + im\theta}$$

The pressure associated to a mode of azimuthal order m (which will be called modal pressure from now on) is given by:

$$p_m^{\omega}(x,r) = \sum_{n=0}^{+\infty} A_{mn}^{\pm} \frac{J_m(k_r r) + Q_{mn} Y_m(k_r r)}{\sqrt{F_{mn}}} e^{ik_x^{\pm} x} \tag{6.8}$$

Note that the quantities $p^{\omega}(x,r,\theta)$, $p_m^{\omega}(x,r)$ and $A_{mn}^{\pm}$ are complex numbers. J_m and Y_m are the Bessel and Neumann functions, respectively. The quantity Q_{mn} is equal to zero for a hollow duct (no center-body) and is defined as:

$$Q_{mn} \equiv -\frac{J_m'(\sigma_{mn})}{Y_m'(\sigma_{mn})}$$

The quantities F_{mn} are normalization factors introduced to verify the following equation:

$$\frac{1}{R^2} \int_{\eta R}^{R} \frac{|J_m(k_r r) + Q_{mn} Y_m(k_r r)|^2}{F_{mn}} r \mathrm{d}r = 1 \tag{6.9}$$

they are related to the factors C_{mn} of Holste [156] by $2\pi R^2 F_{mn} = C_{mn}$. Then:

$$F_{mn} = \begin{cases} \frac{1}{2}[1-\eta^2], \text{ for the plane wave } m=n=0 \\ \frac{1}{2}\left[\left(1-\frac{m^2}{\sigma_{mn}^2}\right)\left(J_m(\sigma_{mn}) + Q_{mn}Y_m(\sigma_{mn})\right)^2 \right. \\ \qquad \left. -\left(\eta^2 - \frac{m^2}{\sigma_{mn}^2}\right)\left(J_m(\eta\sigma_{mn}) + Q_{mn}Y_m(\eta\sigma_{mn})\right)^2\right], \text{ otherwise} \end{cases} \tag{6.10}$$

The wavenumbers presented in Eq.(6.6) can also be formulated in terms of the modal energy propagation angle $\psi_{mn}^{\pm}$ which was previously used by the authors [61] (and denoted $\chi_x^{\pm}$) to compute the trajectory of rays and the number of bounces experienced by a mode propagating in a duct:

$$\begin{aligned} k_r &= k \frac{\sin\psi_{mn}^{\pm}}{\sqrt{1 - M_x^2 \sin^2\psi_{mn}^{\pm}}} \\ k_x^{\pm} &= \frac{k}{\beta^2}\left(-M_x + \frac{\cos\psi_{mn}^{\pm}}{\sqrt{1 - M_x^2\sin^2\psi_{mn}^{\pm}}}\right) \end{aligned} \tag{6.11}$$

The analogy with the free-field axial and radial wavenumbers given in Equation (6.5) is obvious when identifying the in-duct modal energy propagation angle $\psi_{mn}^{\pm}$ with the free-field observation angle ψ. The angle $\psi_{mn}^{\pm}$ is one of the two angles specifying the propagation of a ray in a duct. The equivalence of modes and rays, particularly relevant at high frequencies, was proposed by Chapman [157]. According to his work, every cut-on mode can be described by a polar and an azimuthal angle, a mode may be mathematically written as a bundle of rays and vice versa. The energy propagation angle in the case of a purely axial flow (no swirl) can be related to the phase propagation angle $\zeta_{mn}^{\pm}$ and to the mode cut-on factor α_{mn}:

$$\cos\psi_{mn}^{\pm} = \frac{M_x + \cos\zeta_{mn}^{\pm}}{\sqrt{1 + M_x^2 + 2M_x\cos\zeta_{mn}^{\pm}}} = \pm\alpha_{mn}\frac{\sqrt{1-M_x^2}}{\sqrt{1-\alpha_{mn}^2 M_x^2}}, \text{ where } \begin{cases} 0 \le \psi_{mn}^{+} < \pi/2 \\ \pi/2 \le \psi_{mn}^{-} \le \pi \end{cases}$$

This is also the angle at which the peak of radiation is located in the far field with the same uniform flow inside and outside of the duct. This equation is equivalent to Equation 27 in the paper by Rice et al. [158]. The phase propagation angles and their range of values are given by:

$$\cos\zeta_{mn}^{\pm} = \frac{-M_x \pm \alpha_{mn}}{1 \mp \alpha_{mn} M_x}, \text{ where } \begin{cases} 0 \leq \zeta_{mn}^{+} \leq \zeta_{mn}^{-} \\ \pi/2 \leq \zeta_{mn}^{-} \leq \pi \end{cases}$$

It should be noted that the case $\zeta_{mn}^{+} > \pi/2$ is possible and corresponds to wave fronts propagating upstreams whereas the energy propagates in the downstream direction. The caustic radius r_{mn}, introduced by Chapman [157], will be of some use:

$$r_{mn} = \frac{|m|}{\sigma_{mn}} R \tag{6.12}$$

The phase velocity $\mathbf{c}_\zeta$, and the group velocity $\mathbf{c}_\psi$ are given by:

$$\begin{aligned} \mathbf{c}_\zeta &= a_0(1 + \mathbf{M}\cdot\mathbf{n}_\zeta)\mathbf{n}_\zeta \\ \mathbf{c}_\psi &= a_0(\mathbf{M} + \mathbf{n}_\zeta) \\ \text{where } \mathbf{M} &= M_x \mathbf{e_x} \end{aligned}$$

where $\mathbf{n}_\zeta$ is the unity vector of the phase velocity. In the outer region of the duct defined by $r > r_{mn}$, Chapman showed that the propagation of modes can be mathematically described by the piecewise linear propagation of rays. In that region, the radial wavenumber k_r can be decomposed into an azimuthal and a purely radial component. The phase velocity vector can then assume the form:

$$\mathbf{n}_\zeta(r) = \frac{k_x}{\tilde{k}}\mathbf{e_x} + \frac{k_\theta(r)}{\tilde{k}}\mathbf{e}_\theta + \frac{\sqrt{k_r^2 - k_\theta(r)^2}}{\tilde{k}}\mathbf{e_r}$$

where $k_\theta(r) = \frac{m}{r}$ is a circumferential wavenumber. This relation is defined only for cut-on modes and in the outer part of the duct where r is larger than the caustic radius. The angles $\psi_{mn}^{\pm}$ and $\zeta_{mn}^{\pm}$ can be calculated from:

$$\begin{aligned} \cos\psi_{mn}^{\pm} &= \mathbf{n}_\psi \cdot \mathbf{e_x} \\ \cos\zeta_{mn}^{\pm} &= \mathbf{n}_\zeta \cdot \mathbf{e_x} \end{aligned}$$

6.3.4 Overall sound power

The magnitude of the free-field and in-duct pressure cannot be directly compared as the sound intensity is constant in a hard-walled duct while it decays with the square of the distance to the source in the free space (provided the dissipative effects are negligible). An appropriate quantity suited for quantitative comparisons is the overall modal sound power Π_m^ω emitted by the source at a given azimuthal mode m and pulsation frequency ω.

Acoustic intensity

To compute the acoustic intensity in a uniform medium at a large distance from the source, Morfey [159] indicates that the geometric acoustic approximation can be used. According to this, the acoustic intensity vector $\mathbf{I}$ is obtained from the Blokhintsev invariant [160] which states that acoustic energy is constant along a ray tube :

$$\mathbf{I} = \frac{\frac{1}{2}|p^\omega|^2}{\rho_0 a_0^2}\mathcal{D}\mathbf{c}_\psi$$

where p^ω is the peak amplitude of the pressure, $\mathcal{D}$ is the Doppler factor defined in Eq.(6.2), and $\mathbf{c}_\psi$ the ray or group velocity vector (pointing in the direction of acoustic energy propagation). The sound power Π^ω radiated through a surface S is given by:

$$\Pi^\omega = \iint_S (\mathbf{I}\cdot\mathbf{n}_S)dS$$

where $\mathbf{n}_S$ is the unity vector normal to the surface element dS.

Free-field sound power

In the free field, the overall sound power is obtained after integration of the sound intensity over a sphere of radius ρ centered on the engine as shown in Figure 6.3.

$$\Pi^{\omega} = \int_{\theta=0}^{2\pi} \int_{\psi=0}^{\pi} \frac{\frac{1}{2}|p^{\omega}|^2}{\rho_0 a_0^2} \mathcal{D}(\mathbf{c}_{\psi} \cdot \mathbf{n}_S) \rho^2 \sin\psi d\psi d\theta$$

The Doppler factor is written as $\mathcal{D} = \frac{(1-M_x^2)\sqrt{1-M_x^2\sin^2\psi}}{\sqrt{1-M_x^2\sin^2\psi}-M_x\cos\psi}$.
The projection of the group velocity vector onto a spherical surface is: $\mathbf{c}_{\psi}\cdot\mathbf{n}_S = a_0\left(\sin\psi_e \sin\psi + (M_x + \cos\psi_e)\cos\psi\right) = a_0 \cdot \frac{1-M_x^2}{\sqrt{1-M_x^2\sin^2\psi}-M_x\cos\psi}$.
Using the energy conservation property of the Fourier transform (known as Parseval's theorem or Rayleigh's identity), the integral along θ can be written as a discrete sum of circumferential modes:

$$\int_{\theta=0}^{2\pi} |p^{\omega}|^2 d\theta = 2\pi \sum_{m=-\infty}^{+\infty} |p_m^{\omega}|^2$$

The final expression for the overall modal sound power emitted in the free field is:

$$\Pi_m^{\omega} = 2\pi \int_{\psi=0}^{\pi} \left[\frac{\frac{1}{2}|p_m^{\omega}|^2}{\rho_0 a_0^2} \mathcal{D}(\mathbf{c}_{\psi} \cdot \mathbf{n}_S) \right] \rho^2 \sin\psi d\psi \tag{6.13}$$

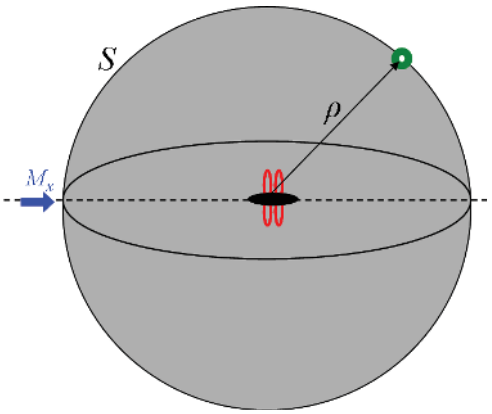

Figure 6.3: Integration surface for calculation of free-field sound power

In-duct sound power

In the ducted case, the overall sound power is calculated through integration over two duct cross-sections S^- and S^+ located upstream and downstream of the fan, respectively. This case is depicted in Figure 6.4. The integrand contains the amplitudes of the modes propagating in the upstream and downstream directions. The sound power carried by a cut-on mode (m,n) of amplitude $A_{mn}^{\pm}$ is derived by Morfey [155]. No sound power is propagated by cut-off modes. The sound power carried by all cut-on modes of azimuthal order m is of the form:

$$\Pi_m^{\omega\,\pm} = \sum_{n=0}^{n_{max}} \pi R^2 \frac{|A_{mn}^{\pm}|^2}{\rho_0 a_0} \alpha_{mn} C_{mn}^{\pm} \tag{6.14}$$

The quantity α_{mn} is the mode cut-on factor defined in Equation (6.7). The coefficients $C^{\pm}_{mn}$, called modal convection factors, depend on the axial Mach number and represent the energy amplification or attenuation due to flow convection. The energy of downstream propagating modes is increased due to the presence of flow, whereas modes propagating against the flow carry less energy.

$$C^{\pm}_{mn} = \frac{(1 - M_x^2)^2}{(1 \mp \alpha_{mn} M_x)^2}$$

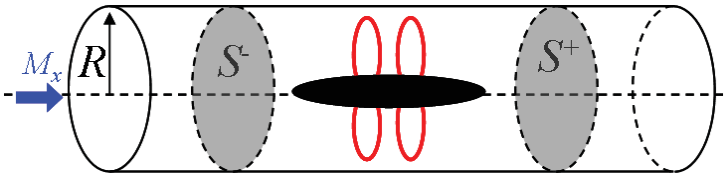

Figure 6.4: Integration surface for calculation of the in-duct sound power

The sound power of a mode (m,n) transmitted at the duct ends into the far field can be approximated by the modal transmission coefficient proposed by Morfey [155]:

$$\left(\Pi^{\omega}_{mn}{}^{\pm}\right)_{transmitted} = \Pi^{\omega}_{mn}{}^{\pm} \cdot T_{mn}, \text{ where } T_{mn} = \frac{4\alpha_{mn}}{(1 + \alpha_{mn})^2} \tag{6.15}$$

Although the exact geometry of the duct ends cannot be considered in this formula, it provides a realistic trend: the modes well above cut-off ($\alpha_{mn} \approx 1$) are nearly completely transmitted, but the modes near cut-off ($\alpha_{mn} << 1$) - despite their strong excitation at source and large pressure levels inside the duct - do not particularly show up in the far field due to their poor transmission at the duct end.

6.4 Noise generated by rotating blades

6.4.1 Derivation of the modal pressure

Fundamental equation for noise generation

The general purpose of this chapter is to establish an analytical formulation of the acoustic pressure generated by a rotating blades as encountered in open rotors or a rotor–stator fan stage. The derivation of the modal pressure begins with the fundamental equation governing the generation of sound in the presence of solid boundaries which was derived by Goldstein [137]. The sound pressure p received at time t by an observer located at the point z is expressed in Eq.(6.16) as a sum of three terms: a monopole (volume displacement or thickness noise), a dipole term (surface force noise), and a quadrupole term (sources located in a volume around the blades). Note that the sign of the monopole and dipole terms is opposed to that of Goldstein because we have chosen here the point of view of the aerodynamicist who usually considers the action applied by the flow on the blades.

$$p(z,t) = \frac{1}{T_{ref}} \int_{-\infty}^{+\infty} \left[- \iint \left[\rho_0 W_n \frac{DG}{Dt_s} + f_i \frac{\partial G}{\partial z_{si}} \right] dz_s + \iiint \left[T_{ij} \frac{\partial^2 G}{\partial z_{si} \partial z_{sj}} \right] dz_s \right] dt_s \tag{6.16}$$

The variables z_s and t_s denote the position of the source and the time of emission, respectively. The term $f_i = f_i(z_s, t_s)$ is the i^{th} component of force per unit area exerted by the fluid on the blade. f_i has the dimension of a pressure, and can be steady or unsteady in the reference frame locked to the rotor. $W_n = W_n(z_s, t_s)$ is the flow velocity normal to the blade surface element, it is independent of time in

the rotating reference frame if blade vibrations are neglected. $T_{ij} = T_{ij}(z_s, t_s)$ is the $(i,j)^{th}$ Lighthill's stress tensor element, which is the quadrupole term containing steady and unsteady terms in the rotor reference frame such as flow turbulence passing over the blades. The Green's function corresponding to the problem considered (duct or free space) is $G = G(z, t, z_s, t_s)$ and has the dimension of an inverse length. The reference time T_{ref} is introduced to match the dimension on both sides of Eq.(6.16).

Formulation in the frequency domain and cylindrical coordinates

The sound pressure and the Green's function are decomposed in Fourier series in the frequency domain and in the azimuthal direction:

$$p(z,t) = \frac{T_{ref}}{2\pi} \int_{-\infty}^{+\infty} \sum_{m=-\infty}^{+\infty} p_m^\omega(x,r) e^{im\theta - i\omega t} d\omega$$

$$G(z,t,z_s,t_s) = \frac{T_{ref}}{2\pi} \int_{-\infty}^{+\infty} \sum_{m=-\infty}^{+\infty} G_m^\omega(x,r,x_s,r_s) e^{im(\theta-\theta_s) - i\omega(t-t_s)} d\omega$$

The quantities p_m^ω and G_m^ω have the same dimension as p and G. Furthermore, we assume that the modal Green's function can be written as follows:

$$G_m^\omega(x,r,x_s,r_s) = g_m^\omega(x,r,r_s) e^{-ik_x x_s}$$

An auxiliary quantity $\aleph$ is introduced to simplify the notations:

$$\aleph \equiv g_m^\omega(x,r,r_s) e^{-ik_x x_s - im\theta_s + i\omega t_s}$$

Using these expressions, Eq.(6.16) is now formulated in terms of modal quantities:

$$p_m^\omega(x,r) = \frac{1}{T_{ref}} \int_{-\infty}^{+\infty} \left[-\iint \left[\rho_0 W_n \frac{D\aleph}{Dt_s} + f_i \frac{\partial \aleph}{\partial z_{si}} \right] dz_s + \iiint \left[T_{ij} \frac{\partial^2 \aleph}{\partial z_{si} \partial z_{sj}} \right] dz_s \right] dt_s$$

The forces and flow terms can be decomposed into axial, circumferential and radial components. The relative importance of the radial component was assessed by Carazo [39] to be small on the tonal noise produced by a CROR engine. However, these effects may become significant on highly leaned blades. Here we assume that the radial terms are negligible, so the surface force and volume stress terms reduce to:

$$f_i \frac{\partial \aleph}{\partial z_{si}} = f_x \frac{\partial \aleph}{\partial x_s} + f_\theta \frac{1}{r_s} \frac{\partial \aleph}{\partial \theta_s}$$

$$T_{ij} \frac{\partial^2 \aleph}{\partial z_{si} \partial z_{sj}} = T_{xx} \frac{\partial^2 \aleph}{\partial x_s^2} + 2T_{x\theta} \frac{1}{r_s} \frac{\partial^2 \aleph}{\partial x_s \partial \theta_s} + T_{\theta\theta} \frac{1}{r_s^2} \frac{\partial^2 \aleph}{\partial \theta_s^2}$$

Using the assumption of uniform and purely axial flow in the whole domain, the derivatives of the auxiliary quantity $\aleph$ are given by:

$$\frac{D\aleph}{Dt_s} = \frac{\partial \aleph}{\partial t_s} + W_x \frac{\partial \aleph}{\partial x_s} = i(\omega - k_x W_x)\aleph$$

$$\frac{\partial \aleph}{\partial x_s} = -ik_x \aleph$$

$$\frac{1}{r_s} \frac{\partial \aleph}{\partial \theta_s} = -i \frac{m}{r_s} \aleph = -ik_\theta \aleph$$

After injecting these expressions, the equation for the modal pressure becomes:

$$p_m^\omega(x,r) = \frac{1}{T_{ref}} \int_{-\infty}^{+\infty} \left[\begin{array}{l} -i \iint \rho_0 W_n (\omega - k_x W_x) \aleph dz_s \\ +i \iint (f_x k_x + f_\theta k_\theta) \aleph dz_s \\ - \iiint (T_{xx} k_x^2 + 2T_{x\theta} k_x k_\theta + T_{\theta\theta} k_\theta^2) \aleph dz_s \end{array} \right] dt_s$$

Expression of the source term in the rotating frame of reference

As the acoustic sources are locked to the rotor, it is convenient to describe their position in the rotating frame of reference attached to it. The source position $\tilde{z}_s$ reads:

$$\tilde{z}_s = \begin{pmatrix} \tilde{x}_s \\ \tilde{\theta}_s \\ \tilde{r}_s \end{pmatrix} = \begin{pmatrix} x_s \\ \theta_s - \Omega t_s \\ r_s \end{pmatrix}$$

Thus, the auxiliary quantity $\aleph$ can be written as:

$$\aleph = g_m^\omega(x, r, r_s) e^{-ik_x x_s - im\tilde{\theta}_s + i\tilde{\omega}t_s}$$

The quantity $\tilde{\omega} = \omega - m\Omega$ that appears through this transformation is the frequency observed in the rotating frame of reference locked to the rotor. Ω is the signed rotation speed of the rotor in [rad/s]. When the sources rotate, a shift in frequency is observed similarly to that occuring with translating sources, the factor $1 - \frac{m\Omega}{\omega}$ is analog to the Doppler factor defined in Eq.(6.2). After switching the time and space integrals, the modal pressure is then written as follows for the thickness, surface force and potential flow terms respectively:

$$p_m^\omega(x, r) = \begin{cases} -i \iint \left[\rho_0 W_n(\tilde{z}_s)(\omega - k_x W_x) g_m^\omega(x, r, r_s) e^{-ik_x x_s - im\tilde{\theta}_s} \frac{1}{T_{ref}} \int_{-\infty}^{+\infty} e^{i\tilde{\omega}t_s} dt_s \right] d\tilde{z}_s \\ +i \iint \left[k_i g_m^\omega(x, r, r_s) e^{-ik_x x_s - im\tilde{\theta}_s} \frac{1}{T_{ref}} \int_{-\infty}^{+\infty} f_i(\tilde{z}_s, t_s) e^{i\tilde{\omega}t_s} dt_s \right] d\tilde{z}_s \\ - \iiint \left[k_i k_j g_m^\omega(x, r, r_s) e^{-ik_x x_s - im\tilde{\theta}_s} \frac{1}{T_{ref}} \int_{-\infty}^{+\infty} T_{ij}(\tilde{z}_s, t_s) e^{i\tilde{\omega}t_s} dt_s \right] d\tilde{z}_s \end{cases}$$

The time integrals are interpreted in the form of Fourier coefficients of the three terms respectively:

$$\frac{1}{T_{ref}} \int_{-\infty}^{+\infty} e^{i\tilde{\omega}t_s} dt_s = \delta(\tilde{\omega})$$

$$\frac{1}{T_{ref}} \int_{-\infty}^{+\infty} f_i(\tilde{z}_s, t_s) e^{i\tilde{\omega}t_s} dt_s = f_i^{\tilde{\omega}}(\tilde{z}_s)$$

$$\frac{1}{T_{ref}} \int_{-\infty}^{+\infty} T_{ij}(\tilde{z}_s, t_s) e^{i\tilde{\omega}t_s} dt_s = T_{ij}^{\tilde{\omega}}(\tilde{z}_s)$$

It is worth mentioning here again that the normal velocity and the Lighthill's tensor (or Reynolds tensor if some sources neglected) for the velocity field bound to the rotor are both independent of time in the rotating frame of reference. The integral over the emission time t_s can be interpreted as a Fourier decomposition. For the thickness and potential flow terms, the Fourier transform of the unity function is a Dirac pulse centered on 0. This means that only frequencies verifying $\tilde{\omega} = 0$ or $\omega = m\Omega$ are excited. In that case, the frequency and the azimuthal mode are coupled. For the surface force term, $f_i^{\tilde{\omega}}$ is the Fourier component of the force per unit area exerted by the fluid on the blades, observed at a frequency ω in the fixed reference frame and at a frequency $\tilde{\omega} = \omega - m\Omega$ in the rotating reference frame. Note that like for the thickness and potential flow terms, the steady force (lift and drag) terms produce only modes verifying $\omega = m\Omega$. For the quadrupole term, $T_{ij}^{\tilde{\omega}}$ is the Fourier component of the Lighthill's tensor.

The modal pressure p_m^ω of the azimuthal mode m at the pulsation frequency ω reads as follows for each source:

$$p_m^\omega(x, r) = \begin{cases} -i \iint \rho_0 W_n(\tilde{z}_s)(\omega - k_x W_x) g_m^\omega(x, r, r_s) e^{-ik_x x_s - im\tilde{\theta}_s} d\tilde{z}_s \\ +i \iint \left[f_x^{\tilde{\omega}}(\tilde{z}_s) k_x + f_\theta^{\tilde{\omega}}(\tilde{z}_s) k_\theta \right] g_m^\omega(x, r, r_s) e^{-ik_x x_s - im\tilde{\theta}_s} d\tilde{z}_s \\ - \iiint \left[T_{xx}^{\tilde{\omega}}(\tilde{z}_s) k_x^2 + 2T_{x\theta}^{\tilde{\omega}}(\tilde{z}_s) k_x k_\theta + T_{\theta\theta}^{\tilde{\omega}}(\tilde{z}_s) k_\theta^2 \right] g_m^\omega(x, r, r_s) e^{-ik_x x_s - im\tilde{\theta}_s} d\tilde{z}_s \end{cases} \quad (6.17)$$

H

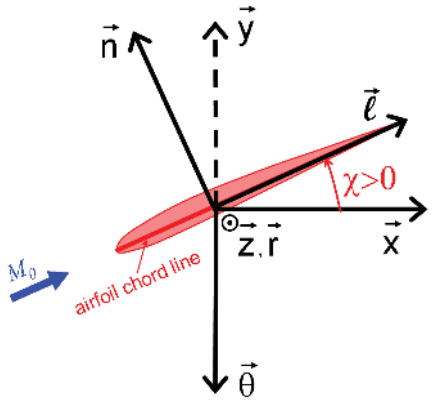

Figure 6.5: airfoil system of coordinates

The surface force term of Eq.(6.17) is similar to that found by Lowis and Joseph [149], which they derived in the particular case of in-duct noise generation.

Projection in the system of coordinates of the airfoil

The integrals occurring in Equation (6.17) are now formulated along the radial, chordwise and transverse (normal to the chord line) directions. We denote ℓ the chordwise position of the source on the blades, n the transverse position, ν the blade index, and project the coordinates x_s and θ_s of the source position in the airfoil system of coordinates (see Figure 6.5). We assume that the blades are thin and slightly cambered so that they can be approximated by flat plates staggered at an angle χ from the engine axis. Furthermore, all blades of a given blade row are identical (but can at this point still be located at different axial and azimuthal positions).

$$x_s = x_{LE}(\nu, r_s) + \ell(r_s)\cos\chi(r_s) - n(r_s)\sin\chi(r_s)$$
$$\tilde{\theta}_s = \tilde{\theta}_{LE}(\nu, r_s) - \frac{\ell(r_s)\sin\chi(r_s)}{r_s} + \frac{n(r_s)\cos\chi(r_s)}{r_s}$$

$$\text{thickness and surface force terms: } d\tilde{z}_s \overset{S}{=} d\ell dr_s$$
$$\text{quadrupole term: } d\tilde{z}_s \overset{V}{=} d\ell dn dr_s$$

The chordwise and transverse wave numbers are obtained by projecting the axial wavenumber and azimuthal wavenumber $k_\theta = m/r_s$ onto the airfoil axis:

$$\begin{aligned} k_\ell &= k_x\cos\chi - k_\theta\sin\chi \\ k_n &= -k_x\sin\chi - k_\theta\cos\chi = \tilde{\mathbf{k}}\cdot\mathbf{n} = \tilde{k}\sin(\zeta^{\pm}_{mn} - \chi) \end{aligned} \tag{6.18}$$

The normal wavenumber k_n is the scalar product between the apparent wavevector and the unit vector normal to the flat plates. As we will see in Eq.(6.22), the lift-related noise depends on k_n, hence this equation indicates that acoustic modes whose wavefront direction of propagation is aligned with the blade are weakly excited, whereas modes whose wavefront direction of propagation is normal to the blades are strongly excited. That result is a direct consequence of the radiation pattern of a dipole, which radiate sound best along its axis, and radiate no sound in the direction perpendicular to its axis. Now, the exponential terms in Eq.(6.17) can be written for the different terms:

$$\text{thickness and surface force terms: } e^{-ik_x x_s - im\tilde{\theta}_s} = e^{-ik_x x_{LE} - im\tilde{\theta}_{LE}}\cdot e^{-ik_\ell \ell}$$
$$\text{quadrupole term: } e^{-ik_x x_s - im\tilde{\theta}_s} = e^{-ik_x x_{LE} - im\tilde{\theta}_{LE}}\cdot e^{-ik_\ell \ell - ik_n n}$$

These results are inserted in Eq.(6.17) and the integral over the source domain is decomposed in a sum over B rotor blades and integrals for each blade expressed along the radial direction and the airfoil chordwise and transverse directions:

$$p_m^\omega(x,r) = \begin{cases} -i \sum_{\nu=1}^{B} \int_{r_s=\eta R}^{R} \left[g_m^\omega(x,r,r_s) e^{-ik_x x_{LE} - im\tilde{\theta}_{LE}} \int_{\ell=0}^{c} (\omega - k_x W_x) \rho_0 W_n \cdot e^{-ik_\ell \ell} d\ell \right] dr_s \\ +i \sum_{\nu=1}^{B} \int_{r_s=\eta R}^{R} \left[g_m^\omega(x,r,r_s) e^{-ik_x x_{LE} - im\tilde{\theta}_{LE}} \int_{\ell=0}^{c} \left[f_x^{\tilde{\omega}}(\tilde{z}_s) k_x + f_\theta^{\tilde{\omega}}(\tilde{z}_s) k_\theta \right] \cdot e^{-ik_\ell \ell} d\ell \right] dr_s \\ - \sum_{\nu=1}^{B} \int_{r_s=\eta R}^{R} \left[g_m^\omega(x,r,r_s) e^{-ik_x x_{LE} - im\tilde{\theta}_{LE}} \int_{\ell=-\infty}^{+\infty} \int_{n=-\infty}^{+\infty} \left[T_{xx}^{\tilde{\omega}} k_x^2 + 2T_{x\theta}^{\tilde{\omega}} k_x k_\theta + T_{\theta\theta}^{\tilde{\omega}} k_\theta^2 \right] \cdot \right. \\ \left. e^{-ik_\ell \ell - ik_n n} d\ell dn \right] dr_s \end{cases} \tag{6.19}$$

Source terms and chordwise integrals

We now evaluate the chordwise integrals of the aerodynamic excitation terms $\rho_0 W_n$, $f_i^{\tilde{\omega}}$ and $T_{ij}^{\tilde{\omega}}$ which appear in Eq.(6.19). We first consider the thickness term. The local velocity normal to the blades is in the thin blade approximation: $W_n = W_0 \frac{\partial t}{\partial \ell}$, where t is the airfoil thickness distribution. Furthermore, we assume that the blades and the inflow are oriented in the same direction, which is a reasonable approximation for moderate angles of attack.

$$\cos\chi \approx \frac{W_x}{W_0} \text{ and } \sin\chi \approx \frac{W_t}{W_0}$$

W_x is the mean flow axial velocity, $W_t = \Omega r_s$ is the tangential velocity of the rotor blades, $W_0 = \sqrt{W_x^2 + W_t^2}$ is the streamwise mean flow velocity in the rotating reference frame (it is also the mean flow chordwise component in the hypothesis of small angles of attack). This formula is not rigorously valid for the downstream rotor of a counter-rotating fan as a swirl component is present between the rotors. Moreover, the frequency and mode order are coupled for the thickness term, hence: $\omega = m\Omega$. After injecting these expressions in Eq.(6.18) we obtain:

$$\omega - k_x W_x \approx -k_\ell W_0$$

Moreover, the Fourier transform of the derivative of t is given by:

$$\int_{\ell=0}^{c} \frac{\partial t}{\partial \ell} \cdot e^{-ik_\ell \ell} d\ell = -ik_\ell \int_{\ell=0}^{c} t \cdot e^{-ik_\ell \ell} d\ell$$

We define a quantity σ_T denoting the source term, which includes the strength of the aerodynamic excitation $\rho_0 W_0^2 t$, the effects of acoustic radiation efficiency (through the term k_ℓ^2), and the non-compactness of the sources along the chordwise direction:

$$\sigma_T = k_\ell^2 \int_{\ell=0}^{c} \rho_0 W_0^2 t \cdot e^{-ik_\ell \ell} d\ell \tag{6.20}$$

For the quadrupole term, Hanson [24] proposes to retain only the chordwise component as it is the dominant term for thin blades at a moderate incidence angle. Hence we get:

$$T_{xx}^{\tilde{\omega}} k_x^2 + 2T_{x\theta}^{\tilde{\omega}} k_x k_\theta + T_{\theta\theta}^{\tilde{\omega}} k_\theta^2 = T_{\ell\ell}^{\tilde{\omega}} k_\ell^2 + 2T_{\ell n}^{\tilde{\omega}} k_\ell k_n + T_{nn}^{\tilde{\omega}} k_n^2 \approx T_{\ell\ell}^{\tilde{\omega}} k_\ell^2 \tag{6.21}$$

Similarly to the thickness term, we introduce the quantity σ_Q for the quadrupole term, σ_L for the lift noise component, and σ_D for the drag noise component:

$$\sigma_Q = k_\ell^2 \int_{\ell=-\infty}^{+\infty} \int_{n=-\infty}^{+\infty} T_{\ell\ell}^{\tilde{\omega}} \cdot e^{-ik_\ell \ell - ik_n n} dn d\ell$$

$$\sigma_L = ik_n \int_{\ell=0}^{c} f_L^{\tilde{\omega}} \cdot e^{-ik_\ell \ell} d\ell \tag{6.22}$$

$$\sigma_D = ik_\ell \int_{\ell=0}^{c} f_D^{\tilde{\omega}} \cdot e^{-ik_\ell \ell} d\ell$$

Modelling these terms (the lift term in particular) is a central problem in addressing the wake or turbulence interaction noise and the trailing-edge noise. This will be done later on. The source terms σ given by the equations (6.20,6.22) for the different noise terms depend on the radius, the blade, and on the frequencies in the fixed and rotating frame of reference:

$$\sigma = \sigma(r_s, \nu, \omega, \tilde{\omega})$$

Final expression for the modal pressure.

After injecting the quantities of the previous section in Equation (6.19), we obtain the modal pressure created by a rotor for the thickness, surface force (lift and drag), and quadrupole sources:

$$p_m^\omega(x, r) = -\sum_{\nu=1}^{B} \int_{r_s=\eta R}^{R} g_m^\omega \cdot e^{-ik_x x_{LE} - im\tilde{\theta}_{LE}} \cdot \sigma \cdot dr_s \tag{6.23}$$

The modal pressure is expressed as a sum over the rotor blades and an integral along the radius of three terms: g_m^ω represents the propagation of sound from the source to the observer, $e^{-ik_x x_{LE} - im\tilde{\theta}_{LE}}$ induces phase cancellation due to the geometrical distribution of the sources in radial and azimuthal direction, and the term σ represents the sources including the amplitude of the aerodynamic excitation, the phase shift due to flow effects (for example wakes tilted along the radius) and the source non-compactness in the chordwise direction. Eq.(6.23) is very similar to that derived by Hanson. Hanson's studies were focused on tonal noise generated at blade passing frequencies (BPF) either by a single rotor [25] or by counter-rotating rotors [26]. The equation presented here is more general and valid for tonal noise with non-uniform inflow perturbation (where tones other than the BPF-harmonics are excited) and is also valid for broadband noise. In the latter case, the phase of the aerodynamic excitation σ contains a random part which can be modelled by a probability density function as shown hereafter. Eq.(6.23) is valid in the free field or in a duct provided the correct Green's function is used.

6.4.2 Application to the free-field and in-duct problems

Free-field Green's function

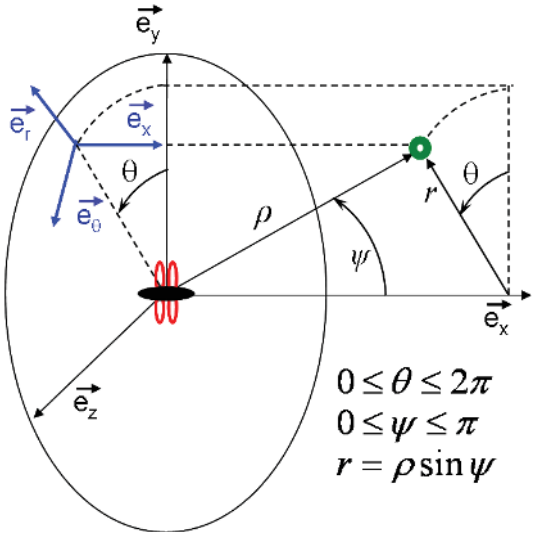

Figure 6.6: cylindrical and spherical system of coordinates

In this section, we derive the far-field approximation of the modal Green's function in the free space. The near-field solution is given by Hanson [108], Peake and Crighton [45], Schulten [55], or by Farassat in the time domain [29]. The flow is assumed subsonic axial and uniform in the whole space, which means that sound refraction due to velocity gradients (related to the thrust-induced axial velocity, or to the potential field around the blades) or sound scattering due to solid surfaces (rotor, hub, airplane) cannot be described by this solution. Blokhintsev [161] has presented the free-space Green's function with uniform axial flow in the time domain:

$$G(z,t,z_s,t_s) = \frac{1}{4\pi R^*}\delta\left(t - t_s - \frac{R_e}{a_0}\right)$$

where $R_e = \frac{R^* - M_x(x-x_s)}{\beta^2}$ and $R^{*2} = (x-x_s)^2 + \beta^2(r\cos\theta - r_s\cos\theta_s)^2 + \beta^2(r\sin\theta - r_s\sin\theta_s)^2$. The Fourier transform of the Green's function and Dirac impulse are given by:

$$G(z,t,z_s,t_s) = T_{ref}\int_{-\infty}^{+\infty} G^\omega(z,z_s)e^{-i\omega(t-t_s)}d\omega$$

$$\delta\left(t - t_s - \frac{R_e}{a_0}\right) = T_{ref}\int_{-\infty}^{+\infty} e^{-i\omega(t-t_s-\frac{R_e}{a_0})}d\omega$$

Hence we retrieve the Green's function in the frequency domain found by Garrick and Watkins [162]:

$$G^\omega(z,z_s) = \frac{e^{ikR_e}}{4\pi R^*} \tag{6.24}$$

We define the distance between the engine and the observer $\rho = \sqrt{x^2 + r^2}$ (see Figure 6.6) and a pseudo-distance $\rho^* = \sqrt{x^2 + \beta^2 r^2}$. Based on the far-field approximation stating that $\rho \gg \rho_s$ and $\rho^* \gg \rho_s^*$, the

quantity R^* appearing in the argument of the exponential term of Eq.(6.24) can be simplified:

$$R^* = \rho^* - \frac{xx_s}{\rho^*} - \beta^2 \frac{rr_s}{\rho^*} \cos(\theta - \theta_s)$$

The term $e^{ik\frac{rr_s}{\rho^*}\cos(\theta-\theta_s)}$ which now appears in the Green's function can be formulated in terms of Bessel functions by using the Jacobi-Anger expansion [163]:

$$e^{iz\cos\theta} = \sum_{m=-\infty}^{+\infty} i^m J_m(z) e^{im\theta}$$

Hence:

$$e^{ik\frac{rr_s}{\rho^*}\cos(\theta-\theta_s)} = \sum_{m=-\infty}^{+\infty} i^m J_m\left(\frac{krr_s}{\rho^*}\right) e^{im(\theta-\theta_s)}$$

The modal decomposition in azimuthal direction yields:

$$G^\omega(z, z_s) = \sum_{m=-\infty}^{+\infty} G_m^\omega(x, r, x_s, r_s) e^{im(\theta-\theta_s)}$$

The modal Green's function is then given by:

$$G_m^\omega(x, r, x_s, r_s) = \frac{1}{4\pi R^*} i^m e^{-\frac{ik}{\beta^2}\left[-\rho^* + \frac{xx_s}{\rho^*} + M_x(x-x_s)\right]} J_m\left(\frac{krr_s}{\rho^*}\right)$$

In the arguments of the exponential and Bessel functions we identify the radial and axial wavenumbers, which were introduced in a previous section dedicated to in-duct propagation (see in Eq.(6.5)). They depend on the axial Mach number and observation angle ψ :

$$k_r \equiv \frac{kr}{\rho^*} = k\frac{\sin\psi}{\sqrt{1 - M_x^2 \sin^2\psi}}$$

$$k_x \equiv \frac{k}{\beta^2}\left(-M_x + \frac{x}{\rho^*}\right) = \frac{k}{\beta^2}\left(-M_x + \frac{\cos\psi}{\sqrt{1 - M_x^2\sin^2\psi}}\right)$$

Furthermore, the quantity R^* is approximated by $R^* \approx \rho^*$ in the denominator of Eq.(6.24). Finally we obtain:

$$G_m^\omega(x, r, x_s, r_s) = \frac{i^m e^{ik_r r + ik_x x}}{4\pi\rho} \frac{J_m(k_r r_s)}{\sqrt{1 - M_x^2\sin^2\psi}} e^{-ik_x x_s}$$

And:

$$g_m^\omega(x, r, r_s) = \frac{i^m e^{-ik_r r - ik_x x}}{4\pi\rho} \frac{J_m(k_r r_s)}{\sqrt{1 - M_x^2\sin^2\psi}}$$

This quantity can be also written as:

$$g_m^\omega(x, r, r_s) = e^{ik_r r + ik_x x} \cdot \hat{g}_m^\omega(\rho, \psi, r_s)$$

where

$$\hat{g}_m^\omega(\rho, \psi, r_s) = \frac{i^m}{4\pi\rho} \cdot \frac{J_m(k_r r_s)}{\sqrt{1 - M_x^2\sin^2\psi}} \tag{6.25}$$

In-duct Green's function

The Green's function valid for an infinitely long hard-wall circular duct with flow is written by Goldstein [137] as a sum of propagating radial modes of order n. The result of Goldstein is adapted to the case of an annular duct with a center-body, we obtain for the modal Green's function:

$$G_m^\omega(x, x_s, r, r_s) = \frac{i}{4\pi R} \sum_{n=0}^{+\infty} \frac{(J_m(k_r r) + Q_{mn} Y_m(k_r r)) \cdot (J_m(k_r r_s) + Q_{mn} Y_m(k_r r_s))}{kR \cdot \alpha_{mn} \cdot F_{mn}} e^{ik_x^\pm (x - x_s)}$$

where the quantities F_{mn} and α_{mn} are respectively the normalization and cut-on factors defined in Equations (6.7) and(6.9). A more general solution valid for an annular duct with uniform mean flow and noise damping walls (liner) is given by Rienstra [164]. The in-duct axial and radial wavenumbers are detailed in Eq.(6.6). The quantity $g_m^\omega(x, r, r_s)$ is written:

$$g_m^\omega(x, r, r_s) = \sum_{n=0}^{+\infty} \frac{J_m(k_r r) + Q_{mn} Y_m(k_r r)}{\sqrt{F_{mn}}} e^{ik_x^\pm x} \cdot \hat{g}_{mn}^\omega(r_s)$$

where

$$\hat{g}_{mn}^\omega(r_s) = \frac{i}{4\pi R} \cdot \frac{J_m(k_r r_s) + Q_{mn} Y_m(k_r r_s)}{kR\, \alpha_{mn}\, \sqrt{F_{mn}}} \tag{6.26}$$

Expressions for the modal pressure

For the free-fied problem, we introduce the quantity $\hat{g}_m$ of Eq.(6.25) into Eq.(6.23) and obtain:

$$p_m^\omega(\rho, \psi) = -i^m e^{ik_r r + ik_x x} \sum_{\nu=1}^{B} \int_{r_s=\eta R}^{R} \hat{g}_m^\omega \cdot e^{-ik_x x_{LE} - im\tilde{\theta}_{LE}} \cdot \sigma \cdot dr_s \tag{6.27}$$

For the in-duct problem, the sound field is most suitably described by a sum of radial modes of orders m and n which are characterized by their complex amplitude $A_{mn}^\pm$:

$$p_m^\omega(x, r) = \sum_{n=0}^{+\infty} A_{mn}^\pm \frac{J_m(k_r r) + Q_{mn} Y_m(k_r r)}{\sqrt{F_{mn}}} e^{ik_x^\pm x}$$

As for the free-field case, we introduce the quantity $\hat{g}_{mn}$ of Eq.(6.26) into Eq.(6.23), and by identification with Eq.(6.8) we obtain an expression for the modal amplitude:

$$A_{mn}^\pm = -i \sum_{\nu=1}^{B} \int_{r_s=\eta R}^{R} \hat{g}_{mn}^\omega \cdot e^{-ik_x x_{LE} - im\tilde{\theta}_{LE}} \cdot \sigma \cdot dr_s \tag{6.28}$$

This expression is valid for all modes: for cut-on modes, the cut-on ratio and the axial wavenumbers are real, for cut-off modes these quantities have a non-zero imaginary part associated to the axial decay of the mode along the axis.

6.4.3 Tonal noise

General result

We will denote ϕ_{exc} the phase of the source term σ appearing in Eq.(6.23). As all blades are assumed identical, located at the same axial position and equally spaced in azimuthal directions, the phase ϕ_{exc} is the only term that depends on the blade index ν; it can be written as the sum of two deterministic

terms, one only depending on the blade index, the other only depending on the radius, and an additional term relevant for broadband noise representing the randomness of the excitation.

$$\phi_{exc}(r_s,\nu) = -m_0\frac{2\pi}{B}\nu + \phi_0(r_s) + \phi_{rand}(\nu, r_s, \varpi)$$

m_0 denotes the azimuthal mode order of the incoming perturbation. ϕ_0 is the phase of the incoming aerodynamic excitation. ϖ denotes the random event considered in the broadband noise case. For tonal noise, the sources are assumed to be fully correlated which means that the phase of the excitation is fully deterministic, the random part ϕ_{rand} is equal to zero. The azimuthal position of the leading edge is given by:

$$\tilde{\theta}_{LE}(r_s,\nu) = \frac{2\pi}{B}\nu + \theta_{LE}(r_s)$$

The quantity θ_{LE} denotes the shift angle of the blade leading edge in azimuthal direction due to lean. For tonal noise we assume that the sources are fully correlated, all blades are identical and equally spaced in the circumferential direction and located at the same axial position. Based on these assumptions, it is possible to extract the term depending on the blade index from the integral along the blade radius in Equation (6.23). We obtain the following expression:

$$p_m^\omega(x,r) = -\sum_{\nu=1}^{B} e^{i(m-m_0)\frac{2\pi}{B}\nu} \cdot \int_{r_s=\eta R}^{R} g_m^\omega \cdot e^{-ik_x x_{LE} - im\theta_{LE}} \cdot \sigma \cdot dr_s$$

The summation term represents the blade-to-blade interference effects which can be destructive or constructive depending on the order m of the acoustic mode and on the order m_0 of the incoming aerodynamic perturbation:

$$\sum_{\nu=1}^{B} e^{i(m-m_0)\frac{2\pi}{B}\nu} = \begin{cases} B, \text{ if } \frac{m-m_0}{B} \text{ is an integer} \\ 0, \text{ else} \end{cases} \tag{6.29}$$

Here, we have derived a more general form of the famous result of Tyler and Sofrin [165] stating that only specific acoustic modes (so-called Tyler & Sofrin modes) can be excited. For identical incoming blade wakes (or potential field) generated by a blade row with N blades, $m_0 = hN$, where h is the harmonic index of the wake. For the self-noise terms (thickness, steady lift and drag, and quadrupole terms), no incoming excitation is defined. The perturbation is localized at each blade and should then be modelled by a train of Dirac functions with $m_0 = hN$, one can show however that for these terms ($f_0 = 0$), this is equivalent to taking $m_0 = 0$, which represents a simpler and more rapid alternative.

Free-field solution

Using this result, we now obtain a simplified form of Eq.(6.27) valid for fully correlated sources and for the so-called Tyler & Sofrin modes:

$$p_m^\omega = i^m e^{ik_r r + ik_x x} \cdot B \int_{r_s=\eta R}^{R} \hat{g}_m^\omega \cdot e^{-ik_x x_{LE} - im\theta_{LE}} \cdot \sigma \cdot dr_s \tag{6.30}$$

In-duct solution

In the in-duct case we obtain for Tyler & Sofrin modes:

$$A_{mn}^{\pm} = i \cdot B \int_{r_s=\eta R}^{R} \hat{g}_{mn}^\omega \cdot e^{-ik_x x_{LE} - im\theta_{LE}} \cdot \sigma \cdot dr_s \tag{6.31}$$

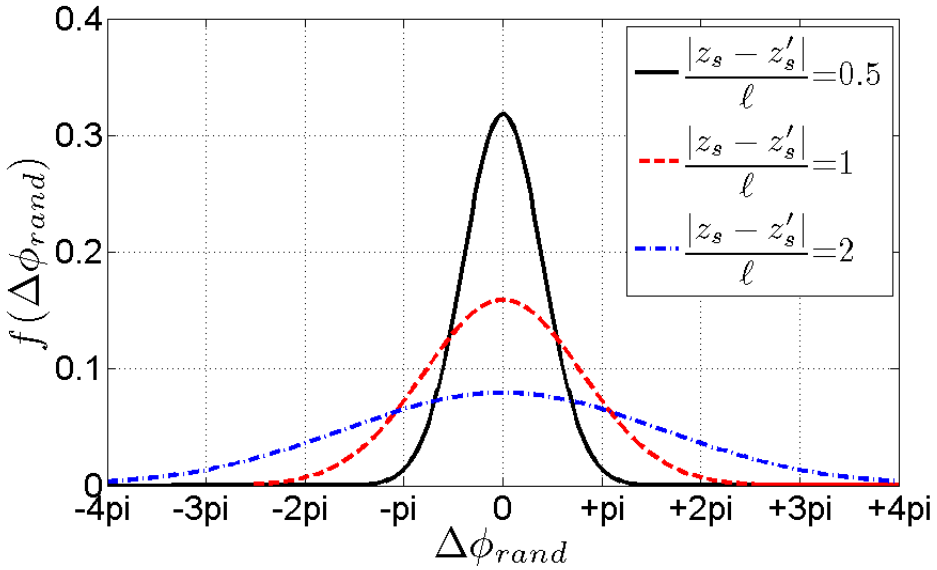

Figure 6.7: Probability density function of $\Delta\phi_{rand}(z_s, z'_s)$

6.4.4 Broadband noise

General derivation

In the broadband noise problem the modal pressure p_m^ω is a random quantity which is not convenient to work with. The deterministic quantity to consider is the expectation of the squared magnitude of the modal pressure, $\overline{|p_m^\omega|^2}$. To derive an expression for this quantity, we start from Eq.(6.23) presented in a simplified form for the sake of clarity. The modal pressure results from an integral of sources of magnitude A and phase Φ.

$$p_m^\omega = \int_{z_s} A(z_s) e^{i\Phi(z_s)} dz_s$$

The conjugate value of the modal pressure is given by:

$$p_m^{\omega\,*} = \int_{z'_s} A(z'_s) e^{-i\Phi(z'_s)} dz'_s$$

Hence the squared magnitude of the modal pressure is:

$$|p_m^\omega|^2 = p_m^{\omega\,*} \cdot p_m^\omega = \int_{z_s}\int_{z'_s} A(z_s)A(z'_s) e^{i(\Phi(z_s)-\Phi(z'_s))} dz'_s dz_s \tag{6.32}$$

For symmetry reasons, this quantity can also be written in this way:

$$|p_m^\omega|^2 = \int_{z'_s}\int_{z_s} A(z'_s)A(z_s) e^{i(\Phi(z'_s)-\Phi(z_s))} dz_s dz'_s = \int_{z_s}\int_{z'_s} A(z_s)A(z'_s) e^{-i(\Phi(z_s)-\Phi(z'_s))} dz'_s dz_s \tag{6.33}$$

After summation of the equations (6.32) and (6.33), and identifying $\cos(x) = \frac{1}{2}(e^{+ix} + e^{-ix})$, we obtain:

$$|p_m^\omega|^2 = \int_{z_s} \int_{z_s'} A(z_s)A(z_s')\cos(\Phi(z_s) - \Phi(z_s'))dz_s'dz_s$$

A statistical averaging is now performed by computing the expectation value of $|p_m^\omega|^2$. The expectation value of random variable X depending on the index of the event ϖ is given by:

$$\overline{X} = E(X) = \lim_{\Omega \to +\infty} \frac{1}{\Omega} \sum_{\varpi=1}^{\Omega} X(\varpi)$$

If X is a continuous real variable, it can be described by a probability density function f and its expectation value is calculated through the following integral:

$$\overline{X} = \int_{-\infty}^{+\infty} X \cdot f(X) \cdot dX \tag{6.34}$$

Furthermore, if we assume that the product of amplitudes and the cosine term are uncorrelated, then the expectation value of their product is equal to the product of their respective expectation values, which yields:

$$\overline{|p_m^\omega|^2} = \int_{z_s} \int_{z_s'} \overline{A(z_s)A(z_s')} \cdot \overline{\cos(\Phi(z_s) - \Phi(z_s'))}dz_s'dz_s \tag{6.35}$$

From this relation, it turns out that two-point correlation statistics over the whole source domain are needed to compute broadband noise in the general case. The direct computation of these quantities is very demanding and their measurement in a real fan or compressor environment is also very challenging. For that reason, there exist a number of models for the two-point correlations, see for example the work of Tam and Auriault [166] or Morse and Ingard [167]. We propose here a simple model for the phase statistics. The phase Φ is first decomposed as a sum of a deterministic and a stochastic or random term:

$$\Phi(z_s) - \Phi(z_s') = \phi(z_s) - \phi(z_s') + \Delta\phi_{rand}(z_s, z_s', \varpi)$$

The continuous random variable $\Delta\phi_{rand}(z_s, z_s')$ is modelled by a probability density function f in the form of a Gaussian-shaped (or normal) distribution, whose mean value is zero and its variance is equal to $\sigma^2 = 2\pi\frac{|z_s - z_s'|^2}{\ell^2}$. The smaller the distance between two sources, the higher is the probability that they have the same phase.

$$f(\Delta\phi_{rand}) = \frac{1}{\sqrt{2\pi\sigma^2}} \cdot e^{-\frac{(\Delta\phi_{rand})^2}{2\sigma^2}} \tag{6.36}$$

where ℓ is a turbulence correlation length which depends on the position considered and on the frequency of the aerodynamic excitation $\tilde{\omega}$. The question of anisotropic turbulence can be handled here by considering a different correlation length for each direction of space. This problem has been treated by Atassi [168] and Stephens [34] in the case of turbulence ingestion by a fan with strongly axially stretched eddies. Previous models based on experimental studies (see the NASA reports by Ganz et al. [117] and Gliebe et al. [23]) have also shown that the turbulence behind a fan rotor exhibits some similarities with isotropic turbulence. We will assume here that the turbulence is isotropic. A model for ℓ is proposed in chapter 4. The two-point correlation of the phase term of Eq.(6.35) is given by:

$$\overline{\cos(\Phi(z_s) - \Phi(z_s'))} = \cos(\phi(z_s) - \phi(z_s'))\overline{\cos(\Delta\phi_{rand})} - \sin(\phi(z_s) - \phi(z_s'))\overline{\sin(\Delta\phi_{rand})}$$

The quantities $\overline{\sin(\Delta\phi_{rand})}$ and $\overline{\cos(\Delta\phi_{rand})}$ are the expectation values of the random variables $\sin(\Delta\phi_{rand})$ and $\cos(\Delta\phi_{rand})$. After calculation, we obtain using Eq.(6.34) and (6.36):

$$\overline{\sin(\Delta\phi_{rand})} = \int_{-\infty}^{+\infty} \sin(\Delta\phi_{rand}) \cdot f(\Delta\phi_{rand}) \cdot d\Delta\phi_{rand} = 0$$

$$\overline{\cos(\Delta\phi_{rand})} = \int_{-\infty}^{+\infty} \cos(\Delta\phi_{rand}) \cdot f(\Delta\phi_{rand}) \cdot d\Delta\phi_{rand} = e^{-\frac{\sigma^2}{2}} = e^{-\pi\frac{|z_s - z'_s|^2}{\ell^2}}$$

This result for the two-point correlation of the phase term presents a form very similar to the models proposed by Tam and Auriault [166], and Morse and Ingard [167]. The final expression for the modal pressure is:

$$\overline{|p_m^\omega|^2} = \int_{z_s}\int_{z'_s} \overline{A(z_s)A(z'_s)}\cos(\phi(z_s) - \phi(z'_s))e^{-\pi\frac{|z_s - z'_s|^2}{\ell^2}} dz'_s dz_s \tag{6.37}$$

This formula is valid for any value of the correlation length ℓ provided the turbulence is isotropic. In the case of a very large turbulence correlation length, the exponential term tends to 1 over the whole source domain, which leads to an expression for the modal pressure in the case of purely tonal noise (fully correlated sources). In the case of a very small turbulence correlation length compared to both the characteristic dimensions of the rotor and the acoutic wavelength, then the amplitude A and deterministic phase ϕ are nearly constant in the domain where the exponential term of Eq.(6.37) is non-negligible. After setting $\eta = z'_s - z_s$, Eq.(6.37) becomes:

$$\overline{|p_m^\omega|^2} = \int_{z_s} \left(\overline{A^2}(z_s) \cdot \int_\eta e^{-\pi\frac{|\eta|^2}{\ell^2}} d\eta \right) dz_s$$

The integral of the Gaussian function is:

$$\int_\eta e^{-\pi\frac{|\eta|^2}{\ell^2}} d\eta = \ell$$

Finally, we obtain with the hypothesis of small-scale turbulence:

$$\overline{|p_m^\omega|^2} = \int_{z_s} \overline{A^2}(z_s) \cdot \ell(z_s) \cdot dz_s \tag{6.38}$$

We assume here that the turbulence responsible for broadband noise is convected over a rotor chord length with no significant modification of its properties. This assumption is known as the frozen turbulence hypothesis (also known as Taylor's hypothesis) and leads the sources to be fully correlated along the streamwise direction (also chordwise direction in the small camber and incidence hypothesis). The sources are fully uncorrelated if they are located on different blades, and correlated in radial direction only if their distance is of the same of magnitude as ℓ.

Free-field solution

The general equation of the modal pressure formulated in the free-field given in Eq.(6.27) is simplified according to the approach of the previous section with the assumption of small scale turbulence. The equivalent of Eq.(6.38) applied to the free-field case then becomes:

$$\overline{|p_m^\omega(\rho,\psi)|^2} = B \int_{r_s=\eta R}^{R} |\hat{g}_m^\omega|^2 \cdot \overline{|\sigma|^2} \cdot \ell \cdot dr_s \tag{6.39}$$

Note that the thickness noise and quadrupole terms generate no broadband noise as their are related to the steady flow around the blades, which is purely deterministic. It should also be noted that all azimuthal modes carry energy contrary to the tonal noise case for which only the Tyler & Sofrin modes are excited. This is due to the small turbulence scale assumption, that leads the sources from different blades to be uncorrelated.

In-duct solution

In the in-duct case, the adaptation of Eq.(6.28) to the broadband formulation yields under the same assumptions as for the free-field case:

$$\overline{|A^{\pm}_{mn}|^2} = B \int_{r_s=\eta R}^{R} |\hat{g}^{\omega}_{mn}|^2 \cdot \overline{|\sigma|^2} \cdot \ell \cdot dr_s \tag{6.40}$$

This expression is similar to that given by Glegg [15] in the case of noise generated from stator vanes.

Broadband noise with partly coherent blades

We can express the relation of Eq.(6.37) if the turbulent correlation length in radial and circumferential directions are different.

$$\overline{|p^{\omega}_m|^2} = \sum_{\nu=1}^{B} \sum_{\nu'=1}^{B} \iint_{r_s, r'_s} \overline{A(r_s)A(r'_s)} \cos\left[\phi(r_s,\nu) - \phi(r'_s,\nu')\right] e^{-\pi\left[\left(\frac{r_s - r'_s}{\ell_r}\right)^2 + \left(\frac{r_s\theta_s - r'_s\theta'_s}{\ell_\theta}\right)^2\right]} dr'_s dr_s \tag{6.41}$$

The overlined quantities are statistical averages. The deterministic part of the phase $\phi(r_s,\nu)$ is assumed to depend only on the blade count and not on the radius. From the relations developed in the section 6.4.3, we have: $\phi(r_s,\nu) = 2\pi \cdot \frac{m-m_0}{B} \cdot \nu$, where m_0 is the circumferential mode order of the incoming turbulence (obtained after Fourier transforming of the statistically averaged turbulent kinetic energy in circumferential direction). By keeping the assumption of small spanwise correlation length, which is still applicable in the case of axially stretched eddies, we can decouple the terms that depend on the radius and those that depend on the blade index ν. The term $r_s\theta_s - r'_s\theta'_s$ in the exponential is written $s(\nu - \nu')$ with s being the radially averaged blade spacing. We obtain:

$$\overline{|p^{\omega}_m|^2} = \Sigma(m) \cdot \int_{r_s} \overline{A^2} \cdot \ell_r \cdot dr_s \text{ , where } \Sigma(m) = \sum_{\nu=1}^{B} \sum_{\nu'=1}^{B} \cos\left(2\pi \cdot \frac{m-m_0}{B} \cdot (\nu - \nu')\right) e^{-\pi\left(\frac{s}{\ell_\theta}\right)^2 (\nu-\nu')^2}$$

$\Sigma(m)$ represents the circumferential correlation function of the blades. In the case of a circumferential correlation length very small compared to the spacing ($\ell_\theta << s$), we retrieve the result of Eq.(6.39) and (6.40): all acoustic modes are equally excited and the squared modal pressure scales with the number of blades B. In the opposite case, where the circumferential correlation length is large compared to the blade spacing ($\ell_\theta >> s$), we retrieve the Tyler and Sofrin mode excitation rule of Eq.(6.29) for tonal noise: only modes verifying $\frac{m-m_0}{B}$ an integer (or equivalently $m = m_0 + kB$) are excited and their squared modal pressure scales with B^2.

The circumferential correlation length is given by:

$$\ell_\theta = \sqrt{(\ell_x \tan\beta_{rel})^2 + \ell_r^2}$$

6.4.5 Summary

Tables 6.2 and 6.3 present a summary of the results obtained so far.

problem	free-field	in-duct
Green's function	$\hat{g}^{\omega}_{m} = \frac{i^m}{4\pi\rho} \cdot \frac{J_m(k_r r_s))}{\sqrt{1-M_x^2 \sin^2\psi}}$	$\hat{g}^{\omega}_{mn} = \frac{i}{4\pi R} \cdot \frac{J_m(k_r r_s)+Q_{mn}Y_m(k_r r_s)}{kR\ \alpha_{mn}\ \sqrt{F_{mn}}}$
tonal noise	$p^{\omega}_{m} = e^{ik_r r + ik_x x} B \cdot \int_{r_s=\eta R}^{R} \hat{g}^{\omega}_{m} e^{-ik_x x_{LE} - im\theta_{LE}} \sigma dr_s$	$A^{\pm}_{mn} = B \cdot \int_{r_s=\eta R}^{R} \hat{g}^{\omega}_{mn} e^{-ik_x x_{LE} - im\theta_{LE}} \sigma dr_s$
broadband noise	$\overline{\lvert p^{\omega}_{m}\rvert^2} = B \int_{r_s=\eta R}^{R} \lvert\hat{g}^{\omega}_{m}\rvert^2 \overline{\lvert\sigma\rvert^2} \ell dr_s$	$\overline{\lvert A^{\pm}_{mn}\rvert^2} = B \int_{r_s=\eta R}^{R} \lvert\hat{g}^{\omega}_{mn}\rvert^2 \overline{\lvert\sigma\rvert^2} \ell dr_s$

Table 6.2: Formula for modal pressure depending on the problem considered

source	σ
thickness noise	$k_\ell^2 \int_{\ell=0}^{c} \rho_0 W_0^2 t e^{-ik_\ell \ell} d\ell$
quadrupole noise	$k_\ell^2 \int_{\ell=-\infty}^{+\infty} \int_{n=0}^{h} T^{\tilde{\omega}}_{\ell\ell} e^{-ik_\ell \ell - ik_n n} dn d\ell$
lift noise	$ik_n \int_{\ell=0}^{c} f^{\tilde{\omega}}_{L} e^{-ik_\ell \ell} d\ell$
drag noise	$ik_\ell \int_{\ell=0}^{c} f^{\tilde{\omega}}_{D} e^{-ik_\ell \ell} d\ell$

Table 6.3: formula for source terms

6.5 Interpretation of the results

6.5.1 Classification of sources

This section presents a summary of the different noise mechanisms and sources which are modelled in the frame of the present study. The first type of classification we will consider is that obtained naturally from the mathematical derivation according to Table 6.3. The following mechanisms are distinguished:

- thickness noise is associated to the volume displacement induced by the rotation of the blades. This term is usually referred to as a monopole term, but as noted by Hanson [24], it scales like the quadrupole term and has a similar radiation pattern. The thickness term is indeed formed by a continuous chordwise distribution of monopoles, but this is not equivalent to a single monopole. The name given to sources in terms of multipoles should therefore be considered very carefully.

- quadrupole noise: this name is chosen here for the sake of simplicity but the name steady overspeed noise would be more appropriate, because this term is reduced here to the noise generated by the steady velocity gradients around the blades and does not include the interaction of incoming turbulence with the potential field (this source is part of the fan broadband noise model developed by Mani [20, 150] and may become significant at high Mach numbers and inflow turbulence levels). Again, the name quadrupole should be considered with caution.

- drag noise is less significant for well-designed blades as the drag coefficient is usually smaller than the lift coefficient by one or two orders of magnitude.
- lift noise is the mechanism common to a number of different sources depending on the steady or unsteady nature of the perturbation observed in the frame locked to the blades:
  - steady lift noise is the first source to have been considered by Gutin [145] in the propeller noise problem. As for the thickness, quadrupole and drag terms, noise is generated here by the mere rotation of steady multipoles.
  - unsteady lift noise is associated to time variations of the pressure distribution on the blades. In the present study, four sources are based on that mechanism:
    - tonal potential field interaction noise
    - tonal wake interaction noise
    - broadband wake interaction noise
    - broadband trailing edge self noise

The sources can also be classified according to considerations more related to modelling aspects. Table 6.4 distinguishes between tonal and broadband noise, and self and interaction noise on the other side. The prediction of interaction noise is usually more prone to inaccuracies than self noise, because not only the blade row generating sound (and its flow characteristics) has to be modelled, the blade row generating the aerodynamic perturbation and the propagation of that perturbation have to be reproduced correctly.

type	tonal noise	broadband noise
self noise	thickness & quadrupole noise steady drag & lift noise	trailing edge noise
interaction noise	wake interaction noise potential field interaction noise	turbulence interaction noise

Table 6.4: Classification of turbofan noise sources

The turbulence interaction noise comprises two different sources that rely on the same mechanism: the interaction with a turbulent wake generated by a blade row located upstream, and the interaction with fan inflow turbulence generated upstream of the engine (for example in the atmosphere). The next Tables 6.5 and 6.6 summarize the mathematical formulation of the different components of the source terms σ (see Eq.(6.42)) for the tonal and broadband noise, respectively:

6.5.2 Modelling of the sources

Decomposition of the source terms

The source term σ summarized in Table 6.3 for the different mechanisms can be written in a more general form:

$$\sigma(r_s, \omega, \tilde{\omega}) = \mathcal{R}(r_s, \omega) \cdot \Psi(r_s, \omega) \cdot \zeta_0(r_s, \tilde{\omega}) \cdot e^{i\phi_0(r_s, \tilde{\omega})} \tag{6.42}$$

The source is decomposed into acoustic and aerodynamic terms. Two non-dimensional acoustic terms depend on the radius r_s and on the acoustic frequency ω expressed in the fixed frame: an acoustic radiation term $\mathcal{R}$ and a chordwise correlation term Ψ originally introduced by Hanson [25], which is mathematically defined as the chordwise Fourier decomposition of the source distribution. The normalized chordwise distributions (denoted h) of blade thickness, surface force and Lighthill's stress are assumed each to be constant along the blade radius. They are normalized such as $\frac{1}{c}\int_{\ell=0}^{c} h(\ell)d\ell = 1$. The acoustic terms verify at zero frequency: $\mathcal{R}(r_s, 0) = 0$ and $\Psi(r_s, 0) = 1$. The correlation function determines the directivity (or

source	$\mathcal{R}$	Ψ	ζ_0	ϕ_0
thickness noise	$k_\ell^2 c^2$	$\frac{1}{c}\int_{\ell=0}^{c} h_T(\ell) e^{-ik_\ell \ell} d\ell$	$\rho_0 W_0^2 \frac{\overline{t}}{c}$	0
quadrupole noise	$k_\ell^2 c^2$	$\frac{1}{c^2}\int_{\ell=-\infty}^{+\infty}\int_{n=0}^{h} h_Q(\ell,n) e^{-ik_\ell \ell - ik_n n} dn d\ell$	$\overline{\rho u_\ell^2}$	0
steady-drag noise	$ik_\ell c$	$\frac{1}{c}\int_{\ell=0}^{c} h_D(\ell) e^{-ik_\ell \ell} d\ell$	$\frac{1}{2}\rho_0 W_0^2 C_D$	0
steady-lift noise	$ik_n c$	$\frac{1}{c}\int_{\ell=0}^{c} h_L(\ell) e^{-ik_\ell \ell} d\ell$	$\frac{1}{2}\rho_0 W_0^2 C_L$	0
unsteady-lift noise	$ik_n c$	$\frac{1}{c}\int_{\ell=0}^{c} h_L(\ell) e^{-ik_\ell \ell} d\ell$	$\frac{1}{2}\rho_0 W_0^2 C_L(\tilde{\omega})$	$m_0 \cdot (\theta_{gust} - \theta_1)$

Table 6.5: Decomposition of the source terms for tonal noise

source	$\lvert\mathcal{R}\rvert^2$	$\lvert\Psi\rvert^2$	$\overline{\lvert\zeta_0\rvert^2}$
trailing edge noise	$(k_n c)^2$	$\left\lvert\frac{1}{c}\int_{\ell=0}^{c} h_L(\ell) e^{-ik_\ell \ell} d\ell\right\rvert^2$	$\lvert S(\tilde{\omega})\rvert^2 \Phi_{pp}(\tilde{\omega})$
turbulence interaction noise	$(k_n c)^2$	$\left\lvert\frac{1}{c}\int_{\ell=0}^{c} h_L(\ell) e^{-ik_\ell \ell} d\ell\right\rvert^2$	$\pi^2 \rho_0^2 W_0^2 \lvert S(\tilde{\omega})\rvert^2 \Phi_{uu}(\tilde{\omega})$

Table 6.6: Decomposition of the source terms for broadband noise

the modal distribution) and the decay of the frequency spectrum. The other term $\zeta_0 e^{i\phi_0}$ is called the aerodynamic excitation pressure and depend on the aerodynamic perturbation frequency $\tilde{\omega}$ expressed in the rotating frame. The phase term inside the exponential models the delay of excitation due to the incoming perturbation (due to tilted wakes, or the skewness of the incoming pertubation).

For the broadband noise sources, the source term is solely modelled through the expectation value of its squared magnitude and its phase is ignored. So Eq.(6.42) becomes:

$$\overline{|\sigma|^2} = |\mathcal{R}|^2 \cdot |\Psi|^2 \cdot \overline{|\zeta_0|^2}$$

Amplitude of the aerodynamic excitation

For the thickness noise the source term of Eq.(6.20) is written:

$$\sigma_T = k_\ell^2 c^2 \cdot \rho_0 W_0^2 \overline{t} \cdot \Psi_T$$

where

$$\Psi_T = \frac{1}{c}\int_{\ell=0}^{c} h_T(\ell) e^{-ik_\ell \ell} d\ell$$

Ψ_T is a non-dimensional chordwise correlation function, which was originally identified by Hanson [25] as a quantity representing the effect of source non-compactness along the blade chord. The function $h_T$represents the non-dimensional chordwise distribution of thickness and verifies $h_T(0) = h_T(1) = 0$.

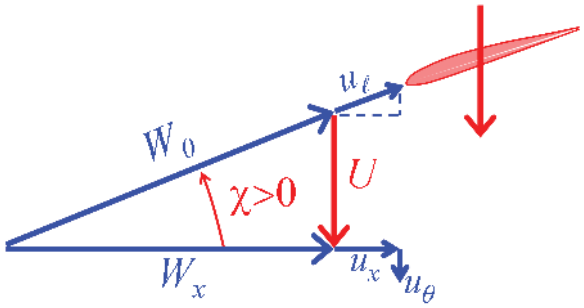

Figure 6.8: Mean flow and perturbation velocities in the fixed and rotating reference frames

For the quadrupole noise source term of Eq.(6.22), we will consider here only the part that is steady in the rotating reference frame, and the Lighthill's tensor element is reduced to the Reynolds stress $T_{ij} = \rho u_i u_j$, where u_i represents the perturbation velocity expressed in the fixed frame of reference (denoted v_i' by Goldstein [144]). Hence the local flow velocity is represented by the axial component $W_x + u_x$ and the circumferential component u_θ. According to Eq.(6.21) the quadrupole source term then reduces to $T_{\ell\ell} = \rho u_\ell^2$, where $u_\ell = u_x \cos\chi - u_\theta \sin\chi = W_\ell - W_0$ denotes the chordwise component of the perturbation velocity observed in the rotating reference frame as specified by Hanson [24] and Peake [45] in the case of propeller blades (see figure 6.8). In the case of a compressor fan stage, the mean flow velocity W_0 in the rotating reference frame is different upstream and downstream of the blade row, leading to a non-zero source term far from the blades. We are confronted here with an inherent limitation of the acoustic analogy: if the left-hand side of Eq.(6.1) misses to reproduce significant propagation effects within the flow, these are included in the right-hand side and are falsely interpreted as a source. Peake [46] suggests that the calculation of the quadrupole fields may simply correspond to distortion effects in the propagation of sound (especially due to large supersonic portions and shocks around the blades). In the case where we have different chordwise velocities W_A and W_B, we can force the quadrupole source to vanish far upstream and downstream of the blade row by setting: $u_\ell^2 = |W_\ell - W_A| \cdot |W_\ell - W_B|$.

The source term is written:

$$\sigma_Q = k_\ell^2 c^2 \cdot \overline{\rho u_\ell^2} \cdot \Psi_Q$$

where

$$\Psi_Q = \frac{1}{c^2} \int_{\ell=-\infty}^{+\infty} \int_{n=0}^{h} h_Q(\ell, n) e^{-ik_\ell \ell - ik_n n} dn d\ell$$

Ψ_Q is the correlation function similar to Ψ_T. The function h_Q represents the non-dimensional distribution of local flow velocity around the airfoil (only the chordwise component) and vanishes upstream and downstream of the airfoil. The term $\overline{\rho u_\ell^2}$ is the mean chordwise stress averaged over the flow domain capted by a blade passage. It is strong at transonic speed where the flow perturbations are large as shown by Hanson [24]. The presence of strong shocks leads to large regions of over- and under-speed around the airfoil. At higher flow velocities, the shocks become oblique and weaker, leading to smaller flow perturbations around the airfoil. The evaluation of the quadrupole term is a delicate task for which no analytical models exist to the knowledge of the author, other than that presented in the previous chapter (see Unsteady Aerodynamics 4). This term can be evaluated more precisely using a full 3D RANS simulation.

For the surface force noise, the source term of Eq.(6.22) is formulated in different ways depending on the problem considered. For tonal noise the formulation by Hanson [26] is used. He writes the chordwise distribution of lift $f_L^{\tilde{\omega}}(\ell)$ (also called local pressure jump) as a product of a chordwise-averaged lift and

a non-dimensional distribution assumed to be independent of the frequency of the impinging gust, from a mathematical perspective, this is a mere separation of the variables $\tilde{\omega}$ and ℓ:

$$f_L^{\tilde{\omega}}(\ell) = \frac{1}{2}\rho_0 W_0^2 C_L(\tilde{\omega}) \cdot h_L(\ell)$$

It follows for the source term:

$$\sigma_L = ik_n c \cdot \frac{1}{2}\rho_0 W_0^2 C_L(\tilde{\omega}) \cdot \Psi_L(\omega) \tag{6.43}$$

where

$$\Psi_L = \frac{1}{c}\int_{\ell=0}^{c} h_L(\ell) e^{-ik_\ell \ell} d\ell$$

Ψ_L is the chordwise Fourier transform of the non-dimensional distribution of loading. $h_L(\ell)$ is the non-dimensional chordwise distribution of loading which verifies $h_L(0) = h_L(1) = 0$ and $\frac{1}{c}\int_{\ell=0}^{c} h_L(\ell) d\ell = 1$, see previous section 4.6. The unsteady lift coefficient is given by:

$$C_L(\tilde{\omega}) = 2\pi \frac{u_n(\tilde{\omega})}{W_0} S(\tilde{\omega})$$

where S is the Sears function [136], for which a model is proposed in chapter 4, Eq.(4.14), valid in incompressible flow and at low frequencies. This formulation presents the advantage of separating the term C_L that depends on the frequency of the excitation $\tilde{\omega}$ from the chordwise correlation function Ψ which is linked to the frequency of acoustic radiation ω. Moreover, the unsteady lift coefficient is a widely used quantity for which substantial research has been done. For the drag noise term, an equivalent formulation is used.

Other authors adopt a different approach than that of Hanson to model the source term σ_L. A more general alternative, where no separation of variables is imposed, is proposed by Amiet [125]:

$$\sigma_L = ik_n c \cdot \pi\rho_0 W_0 u_n(\tilde{\omega}) \cdot \mathcal{L}(\tilde{\omega}, \omega), \text{ where } \mathcal{L} = \frac{\frac{1}{c}\int_{\ell=0}^{c} f_L^{\tilde{\omega}} e^{-ik_\ell \ell} d\ell}{\pi\rho_0 W_0 u_n} \tag{6.44}$$

The quantity $\mathcal{L}$ is called by Amiet chordwise integral of the surface loading, or chordwise aeroacoustic transfer function by Roger and Moreau [36]. The main difference to Hanson's approach is the fact that the distribution of loading may depend on the frequency and the acoustic waves generated along the airfoil may interact with the loading fluctuations (such as the back-scattering of waves coming from the trailing edge).

In broadband noise problems, the relevant quantity is $\overline{|\sigma_L|^2}$, the statistical averaging of the squared magnitude of the source term, which is modelled by the product of a power spectral upwash velocity spectrum Φ_{uu} (denoted S_{ww} in the original papers) for incident turbulence noise and by a wall-pressure spectrum Φ_{pp} for trailing edge noise. More details are found in the studies of Amiet [125, 132], and Roger and Moreau [36]:

$$\text{incident turbulence noise: } \overline{|\sigma_L|^2} = (k_n c)^2 \cdot \pi^2 \rho_0^2 W_0^2 \cdot \Phi_{uu}(\tilde{\omega}) \cdot |\mathcal{L}(\tilde{\omega}, \omega)|^2$$
$$\text{trailing edge noise: } \overline{|\sigma_L|^2} = (k_n c)^2 \cdot \Phi_{pp}(\tilde{\omega}) \cdot |\mathcal{I}(\tilde{\omega}, \omega)|^2$$

The transfer functions $\mathcal{L}$ and $\mathcal{I}$ include the chordwise correlation function but assume a more complex form because they also include back-scattering corrections and account to some extent for the coupling between sources and the sound field they generate. They are basically high-frequency solutions, that can be extended to low frequencies when considering back-scattering corrections. These functions are originally expressed for a non-rotating single airfoil for which $\omega = \tilde{\omega}$, but an extension of this approach to

rotating blades is proposed by Rozenberg [37]. In our approach, the question of rotating and non-rotating sources is treated in a unified way from the beginning. The effects captured by the quantities $\mathcal{L}$ and $\mathcal{I}$ can be alternatively described through Ψ and the Sears function S:

$$\text{incident turbulence noise: } \overline{|\sigma_L|^2} = (k_n c)^2 \cdot |\Psi(\omega)|^2 \cdot \left(\frac{1}{2}\rho_0 W_0^2\right)^2 \cdot \overline{|C_L|^2}(\tilde{\omega})$$

$$\text{, where } \overline{|C_L|^2}(\tilde{\omega}) = 4\pi^2 \frac{\Phi_{uu}(\tilde{\omega})}{W_0^2} |S(\tilde{\omega})|^2$$

$$\text{trailing edge noise: } \overline{|\sigma_L|^2} = (k_n c)^2 \cdot |\Psi(\omega)|^2 \cdot \Phi_{pp}(\tilde{\omega}) |S(\tilde{\omega})|^2$$

By comparison of both formulations and considering a non-rotating blade row generating noise ($\tilde{\omega} = \omega$), we obtain the following equivalence relations:

$$|\mathcal{L}|^2 \approx |\mathcal{I}|^2 \approx |\Psi|^2 \cdot |S|^2$$

An asymptotic expansion at high frequencies yields:

$$\left.\begin{array}{l} |\Psi|^2 \to \frac{1}{kc} \\ |S|^2 \to \frac{M_0}{kc} \end{array}\right\} \Rightarrow |\mathcal{L}|^2 \to \frac{M_0}{(kc)^2} \text{ and } |\mathcal{I}|^2 \to \frac{M_0}{(kc)^2}$$

which is in agreement with the results of Roger and Moreau [36] (although they differ by a multiplicative factor around 2 dB in amplitude). The phase of $\mathcal{L}$ tends to $+\pi/4$, which is also the case for the non-compactness term Ψ (physically representing the time delay between gust excitation and airfoil response).

At low frequencies, the aeroacoustic transfer functions $\mathcal{L}$ and $\mathcal{I}$ have unity amplitude and zero phase (considering an infinite series of back-scattering corrections), as does the product $\Psi \cdot S$.

In summary, the Hanson's approach adopted here is not equivalent to Amiet's approach, because the non-dimensional distribution of loading is the Sears one and does not depend on the gust frequency. However Hanson's approach models the non-compactness of the sources and it provides a similar low- and high-frequency behaviour as in Amiet's work.

Phase of the aerodynamic excitation

The phase of the aerodynamic excitation pressure is given by $\phi_0(r_s)$ and represents the phase of the aerodynamic excitation (incident wake or potential field) and the time delays of excitation that can be induced by the blade geometry (for example sweep and lean). If the quantity responsible for the excitation is convected with the flow (i.e. a wake generated by a blade row or pylon located upstreams as depicted in Figure 6.9), the term ϕ_0 is expressed as follows:

$$\phi_0(r_s) = m_0 \cdot (\tilde{\theta}_{gust} - \theta_1), \text{ where } \tilde{\theta}_{gust} = \tilde{\theta_0} - \tan\beta_{gust} \frac{x_1 - x_0}{r_s}$$

The quantities θ_1 and x_1 are respectively the azimuth and the axial position of the blade edge interacting with the gust (leading edge for a downstream propagating gust, trailing edge otherwise), $\tilde{\theta}_0$ and x_0 are respectively the azimuth and the axial position at which the gust is generated, and $\tilde{\theta}_{gust}$ is the azimuth of the incoming gust centerline as it impinges onto the blade. The tilde sign refers to the relative frame linked to the blade row creating the gust. The circumferential mode order of the gust is m_0. Finally, the quantity β_{gust} represents the gust propagation angle and is given by:

$$\beta_{gust} = \begin{cases} \beta_{rel} \text{ , convected wake} \\ \arctan\left(\dfrac{M_x^2}{1-M_x^2}\tan\beta_{rel}\right) \text{ , potential field in subsonic flow} \\ \arctan\left(\dfrac{M_x^2}{1-M_x^2}\tan\beta_{rel} \pm \dfrac{\sqrt{M_{rel}^2-1}}{1-M_x^2}\right) \text{ , potential field in supersonic flow} \end{cases}$$

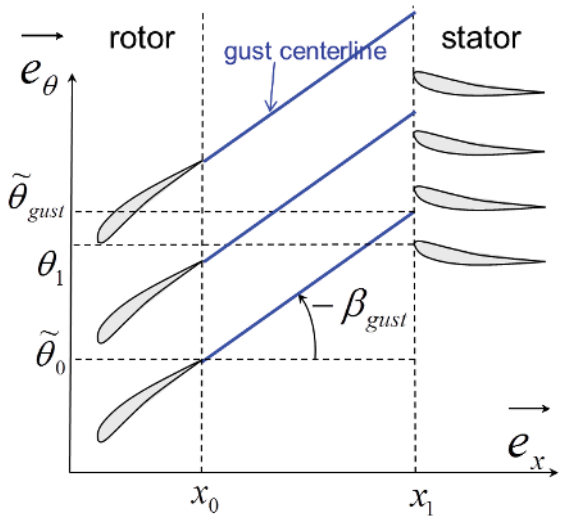

Figure 6.9: Path of gusts as they convect from rotor to stator, in the relative frame

A wake is convected by the flow, so the propagation angle in that case is the flow angle in the reference locked to the blade row generating the wake. A potential field is not convected but propagated at a different angle, which depends strongly on the axial Mach number M_x. Note that for low subsonic flow where $M_x << 1$, the potential field propagation is nearly axial, irrespective of the flow angle. A potential field propagating in supersonic flow ($M_{rel} > 1$) is actually constituted of shocks; in that case the quantity β_{gust} represents the angle normal to the shock front for upstream (-) resp. downstream (+) propagation. In the limit case of sonic axial inflow ($M_x = 1$), it can be shown via an asymptotic expansion that the shocks propagate axially irrespective of the rotor rotation speed and other flow parameters.

As Envia [169] and Guérin [62] pointed out, the radial variations of the quantities θ_{gust} and θ_1, hence of the phase $\phi_0(r_s)$, have an essential impact on tonal noise and may lead to very substantial cancellations of the pressure waves emitted from the blades. For example, the wake generated by rotor blades is tilted increasingly as it convects down to the stator, this is due to the stronger swirl velocity at the hub (which is typical of free-vortex swirl distributions). This effect can be enhanced by a backward sweep of the stator vanes and combined with vanes leaned in the direction of rotation to achieve tonal noise reduction.

6.5.3 Generalized cut-on criterion for efficient radiation

The existence of a strict cut-on condition is typical of in-duct noise propagation. This condition can be presented in the form:

$$\sigma_{mn} < \frac{kR}{\sqrt{1 - M_x^2}}$$

It states that at a given frequency, modes of large azimuthal and radial order cannot propagate any acoustic energy in the duct. This criterion is related to the propagation only, but it provides no further indication on the ability of a mode to be efficiently excited or not. In the free-field case, no strict cut-on/cut-off condition exists. From the expressions for the modal Green's functions in the free-field and in-duct, given respectively in Eq.(6.25) and (6.26), we propose to define a common criterion based on the Bessel function term $J_m(k_r r_s)$. Figure 6.10 shows the values taken by this term as a function of the reduced frequency $k_r r_s$ for $m = 20$ on the left, and of the azimuthal mode order m of the right for $k_r r_s = 20$.

On both sides of the figure, two domains can be distinguished. A domain of large mode order (resp. low frequency) where the Bessel function assumes small values. In that domain, the radiation efficiency decreases rapidly with increasing mode order (resp. with decreasing frequency). At some critical value

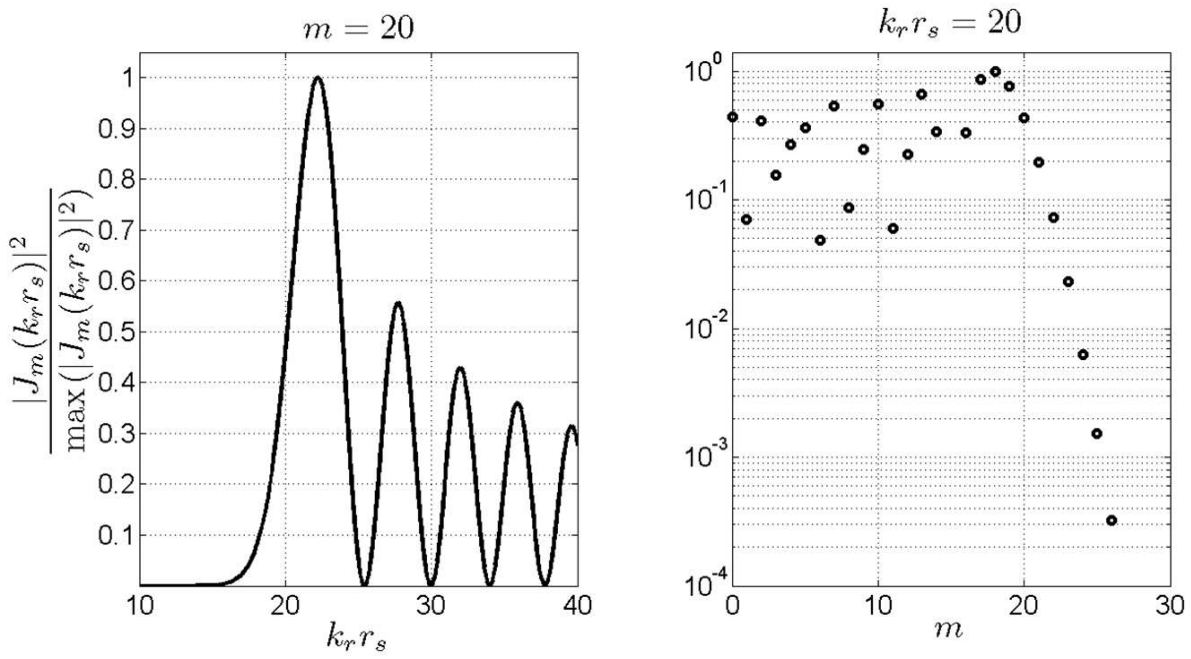

Figure 6.10: Cut-on/cut-off domains visualized via the variations of the Bessel function

roughly corresponding to $|k_r r_s| \approx |m|$, the Bessel function reaches its global maximum value, and its values remain large in average but shows significant oscillations beyond that point. As a result, there is a marked boundary between efficient and inefficient radiation, and the cut-on criterion can be formulated as:

$$|k_r r_s| > |m|$$

If we replace the radial wavenumber by its expression given in Eq.(6.5), we obtain:

$$\sqrt{\left(\frac{kr_s}{m}\right)^2 + M_x^2} \cdot \sin\psi > 1 \tag{6.45}$$

The term $\frac{kr_s}{m}$ can be related to the azimuthal phase velocity. The phase of a harmonic wave is $\phi = \omega t - m\theta$, its azimuthal phase velocity is given by $v_\phi = \frac{d\theta}{dt}|_{\phi=const} \cdot r_s = \frac{\omega}{m} \cdot r_s$, hence $\frac{kr_s}{m} = \frac{v_\phi}{a_0}$. So the left-hand term of Eq.(6.45) can be interpreted as the component of the wave front Mach number pointing towards the observer. In other words, a pressure perturbation can radiate efficiently sound if its wave front velocity point towards the observer is supersonic. In the particular case of noise generated by pressure patterns rotating with the rotor (which verify $\omega = m\Omega$, like for thickness or steady loading noise), the Mach number of the wave fronts is equivalent to the inflow Mach number, Eq.(6.45) becomes:

$$M_{rel}(r_s) > \frac{1}{\sin\psi}$$

Parry and Crighton [170] concluded that for a given observer angle ψ, there exist a radius (so-called Mach radius) on the rotor blade above which the sources radiate efficiently. The Mach radius verifies $M_{rel}(r_s) = \frac{1}{\sin\psi}$ and presents the highest radiation efficiency (global maximum of the Bessel function) Except for the case of sideline radiation ($\psi = \frac{\pi}{2}$), the Mach radius is larger than the sonic radius (radius above which the local inflow of the rotor blades is supersonic). This result can also be related to the cut-off criterion of the Bessel function in Figure 6.10. Note also that in the ducted case the Mach

radius can be identified with the caustic radius of Eq.(6.12). The criterion derived here is valid both for free-field and in-duct sound emission, as it is essentially related to the flow Mach number rather than to the boundary conditions.

Some care must be taken while considering the axial flow Mach number utilized in the cut-on criterion. In accordance with the acoustic analogy approach, this should be the convection Mach number of the moving medium in the fixed frame of reference. However, in some cases such as a CROR engine, there is no unique convection Mach number because the flight Mach number and the local axial Mach number ahead of the rotors are different. So the assumption of the acoustic analogy is violated and the choice of the proper Mach number is not clear: choosing the local Mach number respects the conditions of noise generation, while choosing the flight Mach number, as done by Peake [46], is more representative of the far-field propagation.

6.5.4 Effect of source non-compactness

This effect becomes significant when the spatial extent of the source domain is similar to or larger than the wavelength of the sound generated. Interferences occur between the sound waves emitted by correlated sources and this usually leads to very substantial cancellations at high frequencies. This illustrates the effects of source correlation that take place in each direction of space.

Circumferential correlation

The correlation of sources in circumferential direction is related to blade-to-blade interferences and will therefore affect only tonal noise in the present study. Two different types of behaviour have to be distinguished depending on the cut-on criterion developed in the previous section. If the reduced frequency of the source is not high enough to excite modes that radiate efficiently, the noise level is very sensitive to the azimuthal order of the excited mode and will strongly decrease with increasing mode order, as shown in Figure 6.10. This effect is particularly obvious on single-rotating propellers operating at subsonic conditions: adding one blade to a propeller may result in noise reduction of up to 5 dB. The rapid decrease of acoustic radiation efficiency is analogous to the exponential decay of the potential field presented in a previous chapter 4 (see Eq.(4.2)) where the impact of blade count is similar.

If the cut-on criterion is respected, the radiation efficiency of the modes is high and present some fluctuations depending on the mode order. The sole modes that do not result in destructive interferences are the so-called Tyler and Sofrin modes (see Eq.(6.29)). The ratio of sound power emitted by B correlated point sources to that emitted by the same number of uncorrelated point sources is determined by the number of Tyler & Sofrin modes N_{TS} and the total number of modes N_{tot} that radiate efficiently (the criterion for efficient radiation is presented in the previous section). Figure 6.11 shows the asymptotic behaviour of that sound power ratio as frequency is increased. The ratio $\frac{N_{TS}}{N_{tot}}$ asymptotically tends the constant value B irrespective of the mode order of the incoming perturbation m_0. For broadband noise, the correlation length is assumed small so that neighbouring blades are uncorrelated. In that case, the Tyler and Sofrin rule does not hold and all modes can be excited.

Chordwise correlation

The chordwise correlation function, denoted Ψ in Eq.(6.42), is illustrated in Figure 6.12 for various source distributions, corresponding respectively to the typical thickness distribution of a NACA profile and two loading distributions (one flat distribution and one with a strong peak at the leading edge). These results are presented by Hanson [171] in a more detailed manner. The chordwise correlation function presents a wavy shape that is visible in airfoil broadband noise measurements and predictions (see Amiet [132] and Moreau&Roger [35]). We also observe that smooth distributions present a more rapid decay at high frequencies. The high-frequency asymptotic behaviour of $|\Psi|$ is given by Crighton&Parry [170] in the

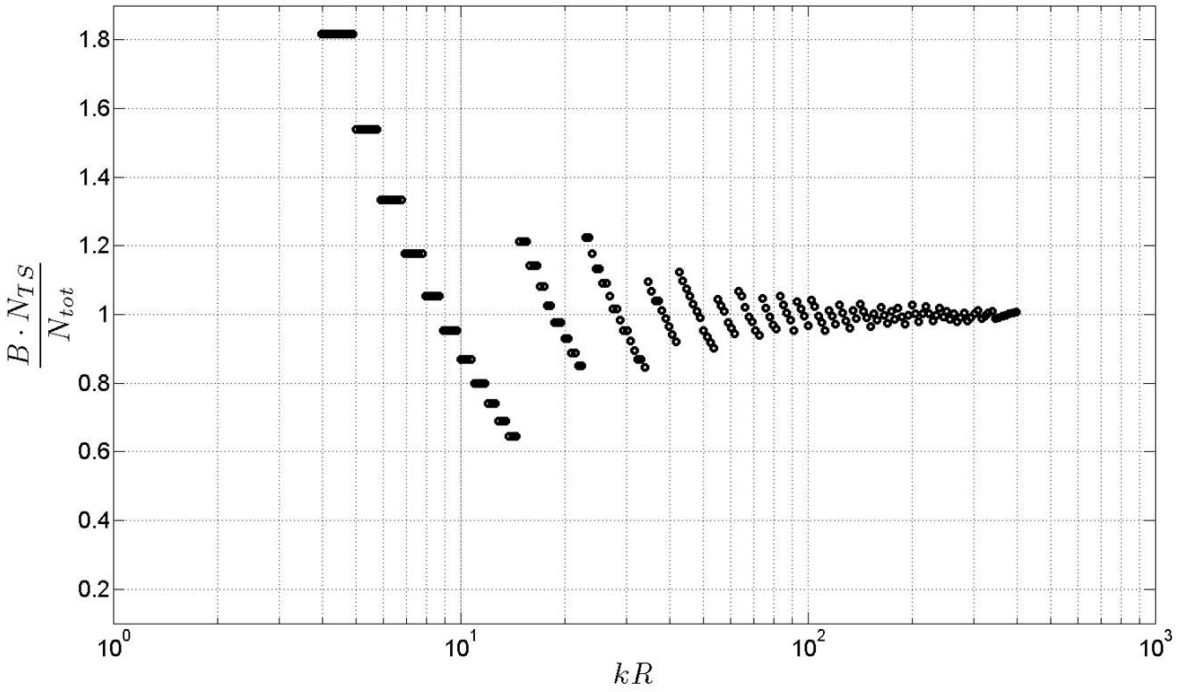

Figure 6.11: Effect of circumferential correlation

form:

$$|\Psi| \propto \frac{\left|\cos\left(\frac{|k_\ell c|}{2} - (1+\nu)\frac{\pi}{2}\right)\right|}{|k_\ell c|^{1+\nu}}$$

The quantity ν is the power exponent of the polynomial asymptotic expansion of the distribution towards the leading and trailing edges. It represents the smoothness of the distribution. The cosine term describes the wavy shape of the spectrum. Local maxima are found at particular values of the chordwise wavenumber k_ℓ, which correspond to the resonance of the sound wave over the blade chord (the chord length is then a multiple of the half wavelength). The black dashed line in Figure 6.12 represents the high-frequency approximation with $\nu = 0.5$. The knowledge of the exact source distribution is necessary to predict accurately noise levels at high frequencies. For broadband noise sources, the chordwise non-compactness is also modelled by the function Ψ, as the turbulent eddies are assumed frozen while they are convected over the blade.

Radial correlation

The effect of radially distributed sources has been studied in two previous publications by Moreau and Guérin [60, 64] and we propose to summarize here the results of these studies. At first glance, the problem of radial correlation differs from those of circumferential and chordwise correlation as the boundary conditions in the free space and in a duct are not identical. However, the previous paragraph has demonstrated the analogy existing between the free-field and in-duct formulations and a consequence is that the ducted and unducted solutions assume the same asymptotic behaviour at high frequencies, as shown in Figure 6.13. The sound power Π radiated by uniformly distributed sources in radial direction

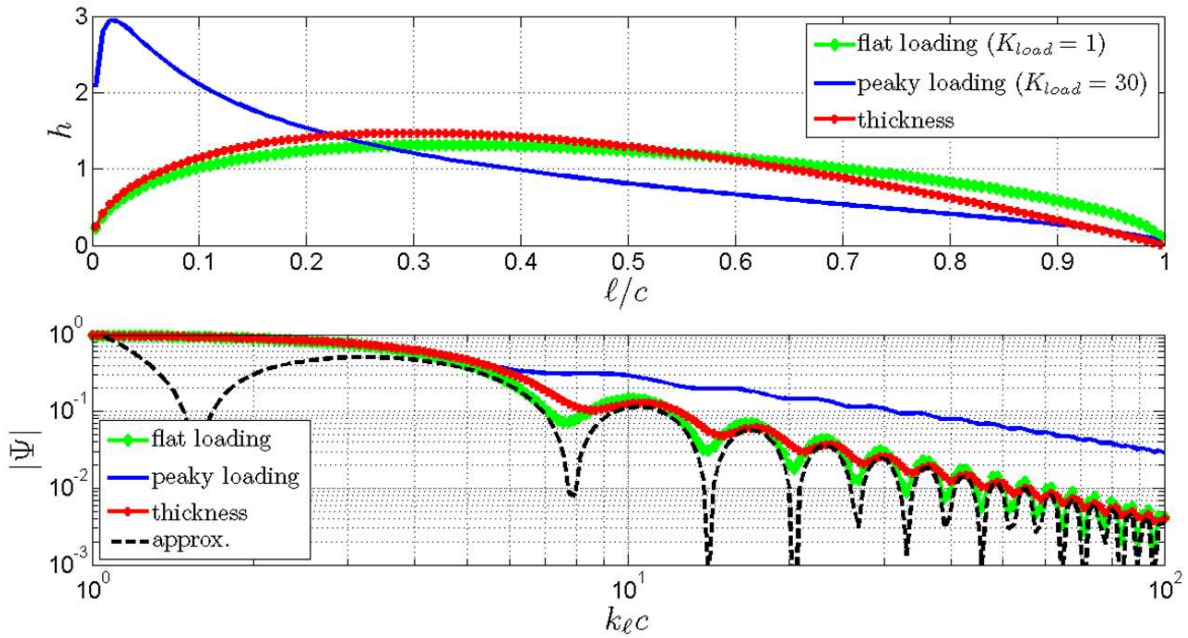

Figure 6.12: Effect of chordwise correlation for various source distributions

is related to the sound power Π_{ref} radiated by an equivalent point source having the same strength σ:

$$\Pi_{ref} = \frac{\sigma^2}{\rho_0 c_0} \frac{R^2}{8\pi}$$

We consider here a single blade to isolate the effect of radial non-compactness from the circumferential one. In Figure 6.13, the ratio $\frac{\Pi}{\Pi_{ref}}$ is represented by the blue solid line in the free-field case and by red circles in the in-duct case. The tonal and broadband noise cases are represented on the upper and lower part of the figure, respectively. At high frequencies (typically for $kR > 20$), the ducted and unducted solutions are nearly identical. At low frequencies, significant differences in levels can be observed due to the reduced number of radial modes and more pronounced resonances observed in the ducted case. It is remarkable to note that the tonal and broadband noise sources have a similar high-frequency behaviour despite their different mathematical modelling. Referring to equations of Table 6.2 with radially constant source strength σ, the sound power Π is proportional to:

$$\text{tonal noise: } \Pi \propto \left(\int \hat{g}_m^\omega dr_s \right)^2$$

$$\text{broadband noise: } \Pi \propto \ell \cdot \int |\hat{g}_m^\omega|^2 dr_s$$

The radial variation of the Green's function $\hat{g}_m^\omega$ is characterized by oscillations around the zero value, which increase with frequency. As a result, in the case of tonal sources, the radial integral of this function decreases to zero with increasing frequency, which may be interpreted as sound wave interferences leading to noise cancellations. The asymptotic law of decay is π/kR and is depicted by the black dashed line in Figure 6.13. For the broadband noise, the integral of the square magnitude of the Green's function tends to a constant finite value, so the radial correlation is not modelled through the oscillations of the Green's function but through the turbulence correlation length ℓ, whose dependency to frequency is described by Eq.(4.13).

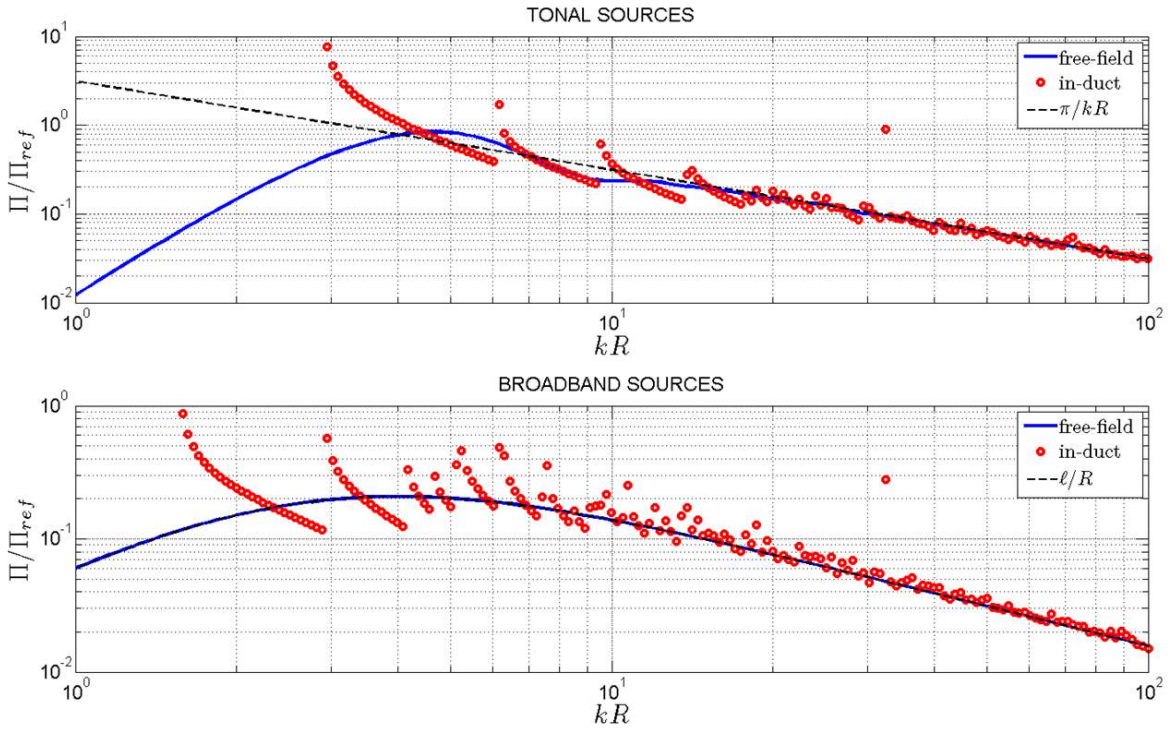

Figure 6.13: Correlation effects for uniformly distributed sources in radial direction

These conclusions hold for a source strength σ constant over the radius, which represents the case where radial noise cancellations are maximum. On a real application, the effect of radial non-compactness will depend on the radial distribution of sources and will be less pronounced if the sources are concentrated around a given radial positions. This is precisely the case for subsonic rotors whose noise is dominated by the blade tip as stated by Parry and Crighton [44]. In supersonic rotors, on the contrary, the sources are more smoothly distributed in the outer region between the tip and the sonic radius.

6.5.5 Application to a single propeller: effect of rotation speed and blade count

In this section we propose to illustrate the effect of rotation speed and blade count of a propeller, and to consider only the tonal self noise sources (thickness, quadrupole, steady lift and drag noise). The application considered is a single-rotating propeller located in the free space with uniform axial flow. Realistic values have been chosen for it geometric and aerodynamic characteristics, these are listed below:

- tip radius $R = 1$, hub-to-tip ratio $\eta = 0.3$
- propeller solidity at meanline radius $\sigma = 0.2$
- twisted but straight blades with zero sweep and lean angles
- radially constant blade chord length
- radially constant mean relative thickness $\frac{\bar{t}}{c} = 0.03$
- radially constant lift and drag coefficients $C_L = 0.5$, $C_D = 0.012$
- radially constant critical Mach number $M_{cr} = 0.87$

Assuming a constant lift coefficient along the radius is not realistic especially near the hub and the tip where lift should vanish. Therefore, the noise levels presented hereafter are overestimated with respect to real noise levels. However, they present realistic trends.

Effect of rotation speed at fixed stagger angle

The relevant parameter to describe the effect of rotation speed is the inflow Mach number of the blade tip observed in the rotating frame, which we call relative tip Mach number $M_{tip,rel}$. This quantity has been varied from the low subsonic to high supersonic values while keeping the blade angle of attack and stagger angle constant; thus the axial velocity and the thrust steadily increase with the rotation speed. Figure 6.14 shows the variations of overall sound power (left-hand side) and of the radially averaged aerodynamic excitation pressure $\overline{\zeta_0}$ (right-hand side) for each of the sources considered. The results are shown for a propeller with 10 blades.

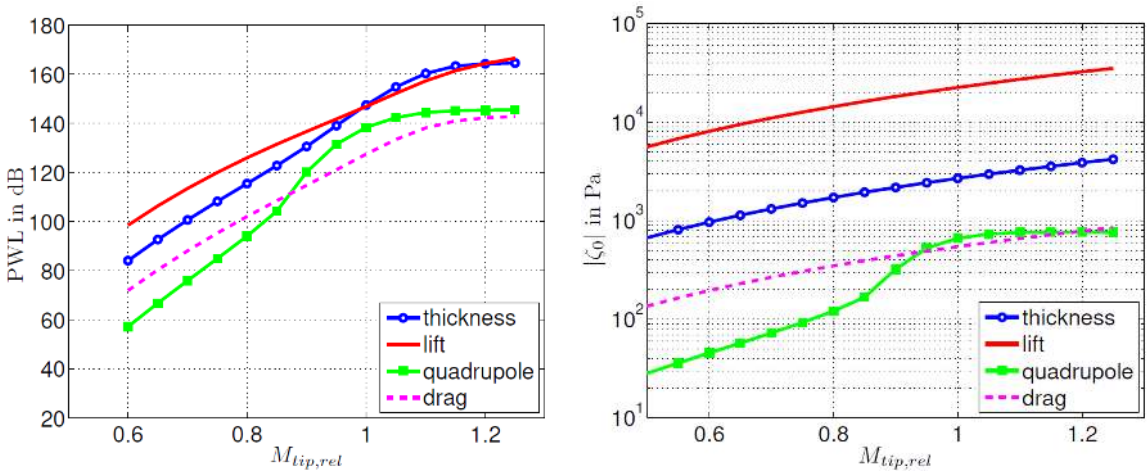

Figure 6.14: Effect of blade tip Mach number $M_{tip,rel}$ on the radiated sound power (left) and on the aerodynamic excitation term (right)

The following remarks can be made:

- Lift noise is the source dominating the low subsonic regime. This is mainly due to the much higher values of the excitation pressure ζ_0 for the lift component than for the thickness, quadrupole and drag component. The drag noise levels are low compared to the other sources over the whole Mach number range, which is explained by the low value of drag coefficient.
- Approaching sonic conditions at the blade tip, thickness noise increases more rapidly and becomes dominant in the transonic domain around $M_{tip,rel} = 1$. This is related to the variations of the radiation term $\mathcal{R}$ appearing in Eq.(6.42): the normal wavenumber k_n decreases whereas the squared chordwise wavenumber k_ℓ^2 increases rapidly.
- Quadrupole noise is negligible at low subsonic speeds but experiences, like thickness noise, a sudden rise in level as transonic conditions are passed (beyond the critical Mach number). The effect is even more pronounced than for thickness noise because of the increase of the excitation pressure at transonic conditions.

Effect of blade count

In a second approach, the blade count of the propeller has been varied while keeping the rotation speed and other aerodynamic parameters constant. The solidity has also been kept constant, so increasing the blade count is accompanied by an equivalent decrease in blade chord length. The variations of overall sound power level are shown in Figure 6.15, separating the subsonic case (left-hand side) from the supersonic case (right-hand side).

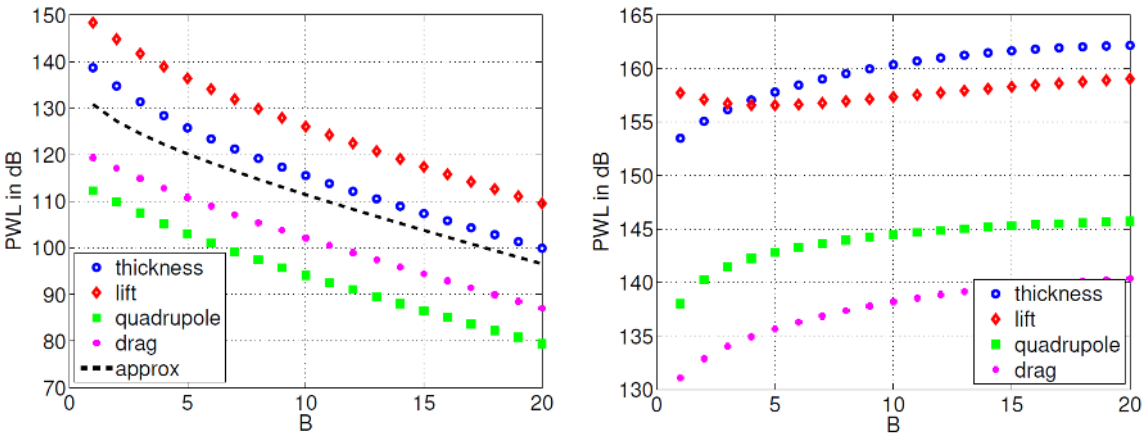

Figure 6.15: Effect of blade count B on the radiated sound power of a subsonic (left, $M_{tip,rel} = 0.8$) and supersonic propeller (right, $M_{tip,rel} = 1.1$)

The blade count affects the radiated sound power of a propeller very differently if the blade tip is subsonic or supersonic. In the subsonic case, represented on the left side of Figure 6.15, noise is extremely sensitive to the blade count: adding one blade decreases noise by approximately 5 dB in the example given here. This is a well-known result, observed by several authors in the past (see the model scale tests on the General Electric CROR named 'UDF' [172, 173]) and which we propose to explain from theoretical considerations. Parry and Crighton [44] demonstrated that the noise of subsonic propellers is dominated by the tip region. Moreover, most of the noise is radiated in the sideline direction ($\psi = \pi/2$). The sound power therefore scales as the squared amplitude of the Bessel term evaluated at the tip:

$$\Pi \propto |J_m(k_r R)|^2 \text{ , where } k_r R = \frac{m M_{tip}}{\sqrt{1 - M_x^2}} \text{ and } m = hB$$

This approximation is depicted in Figure 6.15 by the dashed black line and presents the same dependency on blade count as does the exact solution. The modes excited by a subsonic propeller are cut-off (they do not radiate sound efficiently, but this is compensated by a large excitation pressure), and similarly to the exponential axial decay of a cut-off potential field, more blades lead to more rapid near-field cancellations. In the case of a supersonic propeller, the blade count has a much less pronounced impact on noise. This is because the cut-on limit is passed at some radial station, the modes excited are cut-on and it is not decisive how high above the cut-on limit they are.

Effect of rotation speed at fixed thrust

The thrust of the propeller, the blade count and the chord length are maintained constant, whereas the lift coefficient, the rotation speed and the blade stagger angle are adjusted to satisfy the following relation: $\frac{1}{2}\rho_0 W_0^2 \cdot C_L \cdot \sin\chi = const.$ This quantity is the axial component of the lift force per unit surface, it scales proportionally to the thrust. The result of this parameter study is presented in Figure 6.16

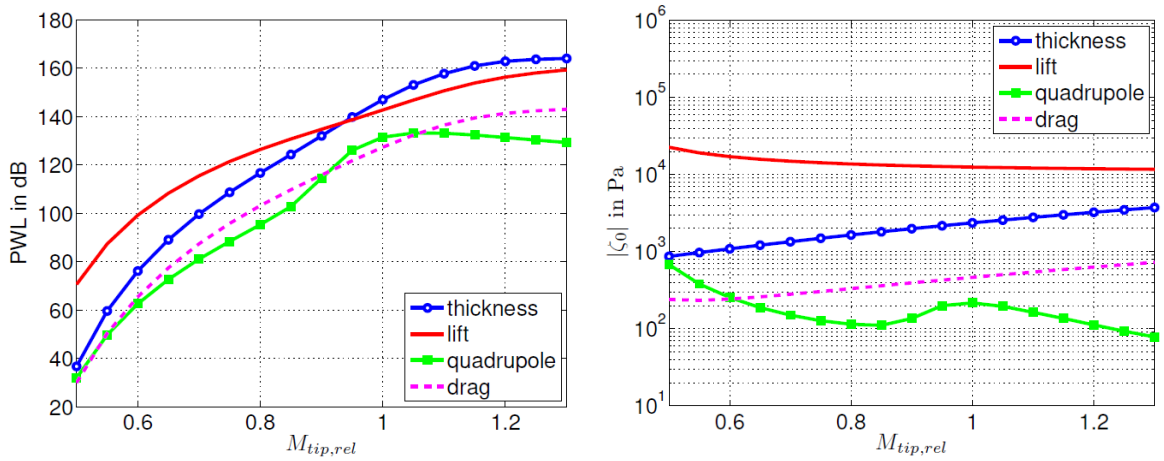

Figure 6.16: Effect of rotation speed (at fixed thrust) on the radiated sound power (left) and on the aerodynamic excitation term (right)

There are some notable differences with the results of Fig.(6.14), especially concerning the steady-lift and quadrupole noise sources. Here, their aerodynamic excitation terms decreases with increasing rotation speed. However, the sound power levels still show a marked increase with rotation speed in the subsonic regime. Again, this can be explained by the tip-dominated Bessel term $|J_m(k_r R)|^2$ mentioned in the previous section. This term is very sensitive to the Mach number for cut-off modes verifying $|k_r R| << |m|$. In the supersonic regime, the increase is much less pronounced (there is even a decrease of quadrupole noise levels). The general increase of noise levels with increasing rotation speed at fixed thrust has been observed experimentally on the 'UDF' CROR by Janardan and Gliebe [172].

6.6 Validation of the acoustic models

Two examples of validation of the noise prediction are now presented. A validation of broadband noise could be performed during a tool benchmarking workshop organized during the last AIAA Aviation conference in 2014 [174]. Flow and noise data obtained from a past comprehensive experiment of NASA on a rotor-stator fan stage (Source Diagnostic Test [175]) were provided to the workshop participants. Therefore the acoustic model of PropNoise could be informed by radial distributions of the mean flow and turbulence measured by hot-wire probes. The acoustic model simulated the broadband wake interaction between the rotor wakes and the stator vanes. The comparison of the prediction sound power with the measured noise data at approach condition is shown in Fig. 6.17. The discrepancy in sound power levels is less than 3 dB over a wide range of frequencies, the predicted overall sound power agrees with the measurement within less than 1 dB, which is a very good result.

The other case of validation concerns the prediction of interaction tones on a rotor-stator fan stage designed by DLR and measured in 2012 [66]. The comparison of the measured and predicted sound power at approach condition is detailed in Table 6.7. At this operating condition, the first BPF harmonic is cut-off. For this calculation, the exact mean flow and turbulence flow data were not available (unlike the SDT case), so PropNoise was started in its stand-alone mode (introduced in Fig. 1.1) and the aerodynamic input to the acoustic model had to be estimated. That may explain the larger inaccuracy of the prediction, which nevertheless remains within a reasonable range of 5 dB for the second and third BPF harmonics; at the fourth BPF, the acoustic response starts to become highly sensitive to the flow and geometry details of the blades, which explains probably the larger discrepancy with the measurements. Another validation exercise on open rotor tones performed with the RANS-informed mode [67] shows that a very good noise estimation can be achieved, at least for subsonic operating conditions like approach.

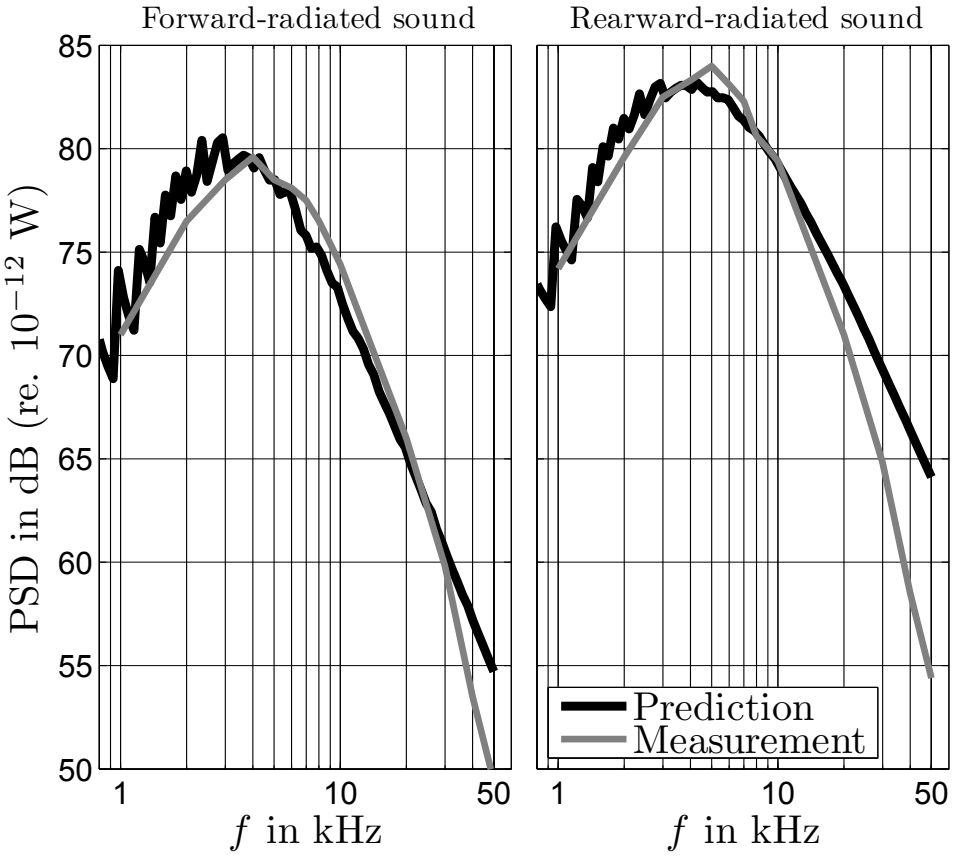

Figure 6.17: Validation of the predicted power spectral density for forward- and rearward-radiated broadband noise

6.7 Jet noise

During the design process of an engine, the choice of the proper thermodynamic cycle is related to the fan pressure ratio and will determine the relative importance of fan noise compared to other engine sources, especially jet noise. In this section a simple estimation of jet noise is proposed based on an empirical scaling law for two broadband jet noise mechanisms: the turbulent-mixing noise and the shock-associated noise. For a cold jet expanding in a non-moving medium, the turbulent-mixing noise scales approximately with the eight power of the jet velocity according to Lighthill [176]. The effect of temperature is neglected because only the cold jet expanding from the bypass is considered here. The mechanism underlying shock-associated noise is still a subject of controversy; one explanation proposed by Christopher Tam is the distortion of turbulent eddies as they convect across the shocks and expansion waves of the jet, thus generating sound. Another explanation attributable to Ulf Michel is the modulation of the turbulent-mixing noise sources by the wavy flow pattern induced by the shocks and expansion waves. The fact that shock-associated noise decreases when turbulent-mixing noise is reduced (for example via a chevron nozzle) would support the latter explanation. Moreover, flow and sound visualizations on a supersonic jet show that the sound radiates from a portion of the jet located further downstream where the shocks are oblique and weak and ought not cause a strong interaction with the turbulence. We propose here a

Table 6.7: Comparison of the measured and predicted tonal sound power of the DLR UHBR fan

OAPWL in dB	2-BPF	3-BPF	4-BPF
measured	102	88	88
predicted	106	85	95

simple scaling law for the overall sound power of jet noise:

$$\Pi = K_{JN} \cdot \rho_0 c_0^3 \cdot A_j \cdot \frac{\left(\frac{V_j+V_0}{2}\right)^4 \cdot (V_j - V_0)^4}{c_0^8} \cdot \left(1 + K_{BBSN} \cdot \beta^4\right), \text{ where } \beta = \sqrt{M_j^2 - 1}$$

Basically, this model states that the shock-associated noise is proportional to turbulent-mixing noise; moreover, it depends on the quantity β^4 which follows the observations of Fisher [177] and Harper Bourne [178]. The empirical constant $K_{JN} = 10^{-5}$ is detailed by Goldstein [137]. The constant $K_{BBSN} = 36$ is calibrated to provide the same level as turbulent-mixing noise for $M_j = 1.08$, according to experimental results of Fisher [177]. The quantity A_j is the cross-section area of the expanded jet. Note that the model is valid for a convergent nozzle only. In that case, the jet Mach number M_j is indeed representative of the shock strength and flow expansion inside the jet. For a well-designed convergent-divergent nozzle however, the jet may be supersonic and fully expanded at the nozzle exit, thus free of shocks.

The variation of jet noise is shown in Figure 6.18 for a nozzle of unity cross-section area and zero flight velocity $V_0 = 0$.

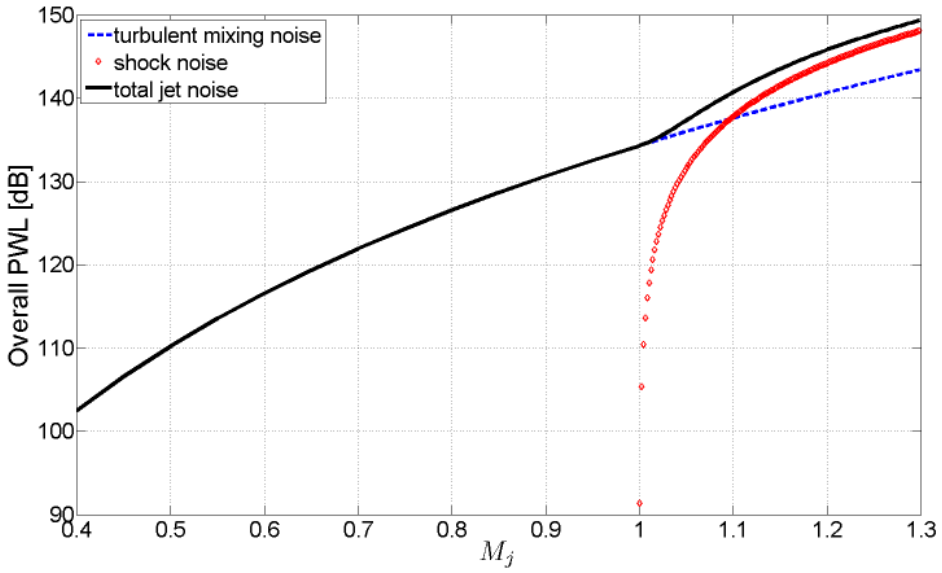

Figure 6.18: Variation of jet noise with fully-expanded jet Mach number in static conditions

6.8 Concluding remarks

A set of models based on a unified application of the acoustic analogy has been derived for rotating-blade noise. The analytical formulations expressed in the frequency domain enable to separate and identify the

various contributors to noise generation and propagation, and to relate them to more intuitive quantities such as mean-flow and geometry parameters. Beyond the assumptions that must be made at some point, and which were detailed at the beginning of this chapter, the acoustic models may in the future be extended in the following ways:

- The integration of noise-damping structures in the nacelle of an engine (also called liners) is a very common and efficient measure to reduce fan noise emissions. Considering liners as part of the acoustic design of an engine thus requires a model for the prediction of the so-called insertion loss (damping coefficient of sound waves). Such a model was derived and published by the author [61]; it is based on the ray structure of acoustic duct modes and necessitates the frequency-dependent impedance of the liner. This quantity must be determined via a liner design module that relates the geometry of the nacelle (especially its length and thickness) to its acoustic damping characteristics. Brambley [179] gives an overview on different liner impedance models available in the literature; the extended Helmholtz resonator model developed by Rienstra [180] is widely used for locally reacting liners.

- The tonal self noise of supersonic rotors is presently overestimated because the propagation of the sound waves is described by a linear model that does not account for the energy dissipation occurring inside shocks. The application of the shock decay model presented in Eq.(4.4) for a potential field should be extended to all acoustic waves. Moreover the scattering of energy from the blade-passing frequencies into other engine orders (which is typical of buzz-saw noise) should be taken into account. A semi-empirical approach was proposed by Pickett [107]; it is based on the statistical modelling of the shock amplitude and shock position.

- Rotor shielding: the transmission of sound through a blade row may be of relevance. In particular transonic rotors are characterized by large supersonic domains inside their blade passage that prevent the sound waves emitted by the stator vanes to propagate upstream and to radiate in the forward arc. Several two-dimensional cascade models were developed in the 1970s: see for example the work of Smith [181], Kaji and Okazaki [182]. An application of these models on a realistic fan has been presented by Jenkins [183] in 2012. A method based on the ray theory may represent here again a simple alternative.

- The steady increase of fan diameter observed on modern and future engine designs must be compensated by a decrease of the nacelle length relative to its diameter in order to maintain the engine weight in a reasonable range. Such short-nacelle designs do not only imply less liner surface and less fan noise damping, they are more prone to inlet flow distortion, which may interact with the front rotor and constitute an additional noise source. The mechanism underlying this source is basically unsteady lift noise (tonal or broadband) and was already treated in this chapter. However, a flow distortion model describing the amplitude and spectral content of the velocity perturbation in relation to the intake length, engine incidence, and flow deceleration inside the intake has to be developed completely as no analytical model available in the literature is known to the author.

- Moreover the short intake cannot prevent completely the acoustic cut-off modes generated by the fan stage to radiate into the far field. To account for that, the decay of cut-off modes should be implemented in a way similar to Eq.(4.2). An in-duct to far-field radiation module should also be included, for example inspired by the work of Morfey [184] or Homicz and Lordi [185] for simple intake resp. nozzle geometries.

- The interaction between neighboring blades of a cascade is neglected in the current model. As a result, each blade reacts to a gust as if it were isolated; correlatively no scattering of the generated pressure waves is considered. Several models have been published to account for the cascade effect, see for example the 3D approach of Posson [38]; such models add a substantial complexity to the analytical description and are highly time consuming. Blandeau et al. [186] stated that the sound power emitted is sufficiently well predicted by the isolated-airfoil response as long as the reduced frequency $\frac{\tilde{\omega} s}{a_0}$ related to the blade passage is larger than one. This corresponds to the minimum

frequency at which the first inter-blade acoustic mode becomes propagating inside the blade passage. The isolated-airfoil assumption is therefore acceptable at high frequencies or for low-solidity blade rows typical for the open rotors.

- The importance of turbulence-associated quadrupole noise relative to the other broadband fan noise sources still has to be clarified. This mechanism describes basically the interaction of turbulent eddies with the potential field surrounding blades: for example the rotor tip self noise or the interaction of incoming turbulence with shocks. The latter source is described as a significant one by Gliebe [187]. The impact of tip noise has been assessed by Ganz et al. [117]. Other authors claim however that the dipole-scaling mechanisms as wake turbulence interaction are dominant. Future theoretical and experimental studies will have to remedy this obvious lack of consense on the community.

A thorough and careful validation of the models will provide the insight necessary to select the most relevant improvements. In the next chapter, the first step of that validation will be addressed by applying the models in the frame of global trend studies. The predictions provided by the models will be discussed with regard to their implications in terms of engine and fan design choices.

Chapter 7

Application of the models

7.1 Introduction

This chapter is dedicated to demonstrate the pre-design capabilities of the aerodynamic and acoustic models presented throughout the previous chapters 2 to 6. A large part of this chapter and the figures shown here have been published and presented by the author at the ASME Turbo Expo Conference 2015 [76], later released as a paper of the Journal of Turbomachinery [188].

Two conceptual parametric studies are presented, which deal with a question that has strongly influenced the evolution of fan designs so far: the impact of tip speed on noise. The steady evolution since the 1950's towards higher bypass ratio engines has enhanced the acoustic role of the fan compared to the jet. The studies presented in this chapter therefore address the following question: does a further decrease in fan pressure ratio and rotor tip speed provide a significant reduction of fan broadband and tonal noise?

The first study proposes a variation of the design fan pressure ratio and evaluates for conventional and contra-rotating fan concepts its impact on noise at three acoustic off-design points. The second study addresses the variation of design rotor tip speed at constant fan pressure ratio. All comparisons are presented at given thrust conditions. Both studies address questions raised by past work performed at NASA, but they also intend to provide a theoretical background which confirms or modifies the guidelines generally accepted. Before that we start with a brief description of the main assumptions specific to the parametric studies.

7.2 Assumptions done for the parametric studies

7.2.1 Aerodynamic and design assumptions

As shown in Fig. 2.1 a simplified modeling of the engine is adopted which considers a single flow channel representing the bypass flow. The thrust is produced solely by the fan stage. The core is ignored, its thermodynamic cycle and its weight are assumed to be independent of the fan design. This approximation gets closer to reality as the engine bypass ratio increases. Although the core engine is not modeled, a theoretical relationship can be established between engine bypass ratio BPR and fan pressure ratio FPR by assuming the power of the low-pressure turbine is fully transmitted to the fan, and the core engine remains independent of the bypass ratio, especially the shaft power of the low-pressure spool ΔH_t^{LPT}:

$$(1 + \mathrm{BPR})\Delta H_t^{FAN} = \Delta H_t^{LPT}$$

where ΔH_t^{FAN} is the enthalpy rise across the fan, which may also be expressed in terms of fan pressure ratio. We obtain:

$$\mathrm{BPR} = \frac{(\Delta H_t)^{LPT}}{H_{t0}} \cdot \frac{1}{\mathrm{FPR}^{(\gamma-1)/(\gamma\eta_{pol})} - 1} - 1 \tag{7.1}$$

The first term of the relation is the non-dimensional total-enthalpy drop of the low-pressure turbine; it is assumed to have a constant typical value of 1.36. The polytropic efficiency of the fan is assumed constant with a value of 0.93 only in this correlation. The result of that relation are depicted in Fig. 7.1. In the rest of the study, variations of the bypass ratio will be expressed in terms of fan pressure ratio.

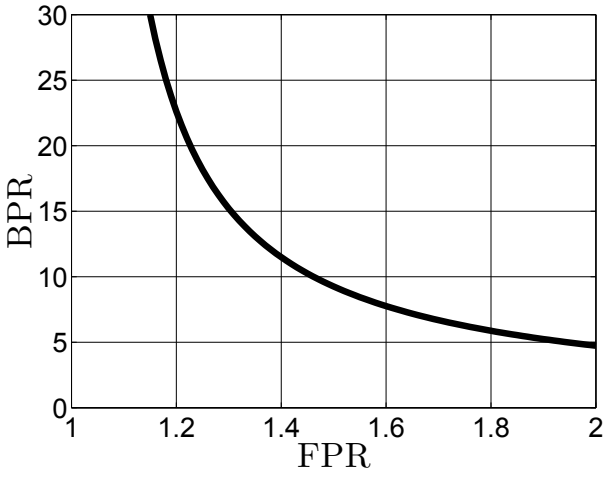

Figure 7.1: Relation between fan pressure ratio and engine bypass ratio

The pressure ratio is related to the enthalpy rise of the fan via the following equation:

$$\mathrm{FPR} = \left(1 + \eta_{ise}\frac{\Delta H_t}{H_{t0}}\right)^{\frac{\gamma}{\gamma-1}} \tag{7.2}$$

The quantity H_{t0} denotes the mass-specific total enthalpy of the flow entering the engine, expressed in the absolute reference frame. ΔH_t is defined similarly and represents the enthalpy rise across the stage. The isentropic efficiency η_{ise} of the fan stage is obtained from the rotor and stator losses. As described in the chapter 2 dedicated to Steady Aerodynamics, the aerodynamic loss results from competing mechanisms: the friction loss is reduced by minimizing the blade surface, hence the solidity; on the other hand, increasing the solidity leads to the reduction of the aerodynamic loading per unit area, which is beneficial for keeping low mixing and shock losses. The aerodynamic model accounts for this trade-off, which allows to determine an optimum solidity that minimizes loss for each specified flow turning. Similarly, the optimum Mach number M_1 results from a balance between large flow diffusion at low rotor tip speed and large skin friction at high speed.

As discussed in chapter 3, the fan design procedure determines these optimum values automatically based on the specification of the fan pressure ratio FPR and the fan-face axial Mach number M_x at the design point, which we defined in cruise. The diameter of the fan is determined by the thrust requirement of the aircraft. Beside the cruise efficiency, the stall margin of the fan has also to be considered to ensure stable operation at the off-design points, especially those located near the surge limit like the sideline point. The final design is impacted in form of increased solidity on the blade rows that generate large loss, which means the rotor of the conventional fan and the rear rotor of contra-rotating configurations. Large stall margin is generally obtained at the cost of a decreased design efficiency [189, 190], for well designed fans near their aerodynamic optimum.

For each of the fans designed automatically by the tool, the off-design points are searched in their respective fan map to provide the true off-design conditions. The relative position of the off-design points within the map may differ significantly depending on the design parameters of the fan, but *the thrust produced is equal for all configurations.* The thrust settings for each operating point were detailed previously in the Steady Aerodynamics chapter 2 in Table 2.4.

7.2.2 Noise-relevant design assumptions

No acoustic optimization has been included during the aerodynamic fan design procedure. However, some assumptions are done and discussed hereafter:

- The blade count is determined automatically for each rotor based on the solidity and on a target value for the blade axial aspect ratio. This latter parameter affects the mechanical properties of the blade and the tip-leakage losses. For ducted configurations, the target rotor aspect ratio is 2.5. The blades of the CROR have an axial aspect ratio around 4. The vane count of the stators are determined with a different approach: the blade number ensures that solely the first BPF is cut-off at approach and only there, it is practically realized by choosing the lowest vane count that satisfies the 1-BPF cut-off at approach. For the contra-rotating concepts, no cut-off of the tones can be achieved.

- The axial distance between the blade rows is not optimized in the present study but set automatically by an amount equal to the maximum axial chord length of front and rear rotors. This design option yields engines with a similar length, thus nacelle surface and weight. But the acoustic impact is fairly high, and this choice is less favorable to low-blade count designs, such as the CRTF and CROR concepts, for which the potential field decays slowly. Precisely this aspect is one of the important acoustic challenges for counter-rotating technologies.

- The length of the intake duct is maintained constant for all configurations and only depends on the cruise engine net thrust: a value near 1.4 m was chosen, this corresponds to a ratio of intake length to fan diameter of 0.5 for FPR=1.2 and 0.9 for FPR=1.6. The aerodynamic and acoustic implications for shorter inlets have not been accounted for. More precisely, cut-off modes (for example generated by a subsonic rotor-locked potential field) may not decay fast enough before radiating at the inlet, or stronger inlet distortions may occur at incidence. Those aspects are currently investigated within dedicated studies at DLR Berlin before being included in the present conceptual design framework at a later point.

Although some validation work has been started and presented, it still remains difficult at the moment to predict absolute levels. This task is all the more challenging if the number of noise mechanisms is large and if the aerodynamic input data have to be estimated for each source. For that reason, the authors consider that summing up the sound power of all sources to provide a single overall fan noise value is not reliable yet and will not be presented in the following of our study. However, in order to facilitate the representation of the results and their discussion, the fan noise sources presented in the two parametric studies following this chapter will be structured in four different groups:

- Tonal self-noise: it is basically related to the acoustic emission of the potential field locked to each rotor. This group includes the so-called thickness noise, steady-lift and steady-drag noise and a quadrupole term. Tonal self-noise is dominant if the relative flow around the rotor is supersonic, because shocks are formed and the acoustic emission becomes particularly efficient.

- Tonal interaction noise: there are basically two mechanisms forming this group, the interaction between the front rotor wakes and the rear blade row and the interaction of the potential field of the downstream blade row with the leading edge of the front rotor. The potential field interaction is primarily strong if the blade count is low (the decay of the perturbations is reduced then) or if the flow Mach number is high (shocks are the expression of a marked potential field and, here again, imply more noise).

- Broadband self-noise: it encompasses a broad range of sources but is limited in our study to the trailing edge noise generated by each blade row. Tip vortex self-noise is not considered.

- Broadband interaction noise: this group contains the interaction of the atmospheric turbulence ingested by the fan with each blade row, and the interaction of the wakes coming from the front rotor and impinging onto the downstream blade row. In our simplified approach, the wake is simply

extrapolated from the meanline radius, the details of the endwall flow (increased turbulence due to the rotor tip vortex for example) are not considered.

It should also be noted that only the sound power generated has been calculated, the propagation of sound, for example its shielding by the rotor or the attenuation by damping material mounted in the nacelle (liners) have not been modeled.

7.3 First parametric study: acoustic impact of the fan pressure ratio

The present study considers the fan noise reduction potential that may be obtained from a variation of the design fan pressure ratio FPR defined in cruise. The fan-face axial Mach number M_x is kept at a constant value of 0.65, which is a realistic value for modern fans in cruise conditions. The fan pressure ratio is varied between 1.7, typical value for today's turbofan engines, and 1.1 which is the domain targeted for the open rotors. For each of these values, optimal fan parameters (such as rotor speed and blade solidities) are automatically determined providing the best isentropic efficiency in cruise along with a sufficient stability margin. The fan diameter is determined based on the thrust requirement in cruise.

The results of this optimization procedure are shown in Fig. 7.2 for the three different fan concepts: the conventional rotor-stator fan stage (TF), the contra-rotating fan (CRTF) and the open rotors (CROR). It is obvious that fan diameter depends inversely on fan pressure ratio, it does however not depend on the concept considered as the thermodynamic cycle is the driving quantity here. The fan efficiency reaches a maximum around FPR=1.1 for the CROR and FPR=1.2 for the ducted configurations, this latter value may be slightly too low compared to common results due to some underestimation of the endwall losses as mentioned above. However, the difference in efficiency between the CRTF and TF is in line with the study of Lengyel [105]: around 1 to 2% , and up to 3% at high values of the fan pressure ratio. The significantly lower efficiency of the CROR is attributed to the high values of the axial Mach number, which can only be controlled in a ducted configuration. The main advantage of the CROR lies in its peak efficiency reached at extremely low pressure ratio without the weight and drag penalty of a large nacelle. The fan degree of reaction depicted in the top right of the figure also shows expected values: the contra-rotating concepts are close to the theoretical optimum at 0.5 (in that case the front and rear rotors produce the same static enthalpy change) whereas the conventional rotor-stator fan has a high reaction around 0.8 [85].

The values of blade count obtained after design are shown in Table 7.1. Usually rotors have an even number of blades for maintenance and balancing reasons, this has not been reproduced here. The match with the values encountered in real turbofans is not exact because this is directly linked to the challenging task of predicting blade solidity correctly as discussed earlier in Fig. 3.11. The rear rotor of the CRTF has more blades than the front rotor to ensure a sufficient aerodynamic stability margin. This is not the case for the CROR, where the front rotor has more blades; here the stability at higher incidence is not provided by an increased solidity but by the variable-pitch system.

The impact of the fan pressure ratio on Mach numbers at the acoustic operating points is shown in Fig. 7.3. Decreasing the fan pressure ratio will reduce the Mach numbers on both front and rear rotors (or stator), as well as the blade solidity, meaning less blades are required for a given aspect ratio. Designing for subsonic tip speeds at sideline and cutback requires a design fan pressure ratio in cruise below 1.35 for the TF and below 1.45 for the CRTF. Current research fans producing low shock noise have a cruise fan pressure ratio around 1.45-1.5 for slightly lower fan-face Mach number.

Decreasing the fan pressure ratio also has a positive impact on the wake severity as demonstrated in Fig. 7.4. The wake severity is represented here by the ratio of the boundary layer thickness at the blade trailing edge θ to the staggered spacing $h = s\cos\chi$. That ratio generally decreases significantly with decreasing fan pressure ratio except at sideline and very low pressure ratio below 1.3. This increase is attributed to the location of the sideline point in the fan map which is closer to the surge line and characterized by strong values of the incidence. The stability margin of very low pressure ratio fans is known to be more critical than designs with higher FPR. This phenomenon is described by Cumpsty [191]

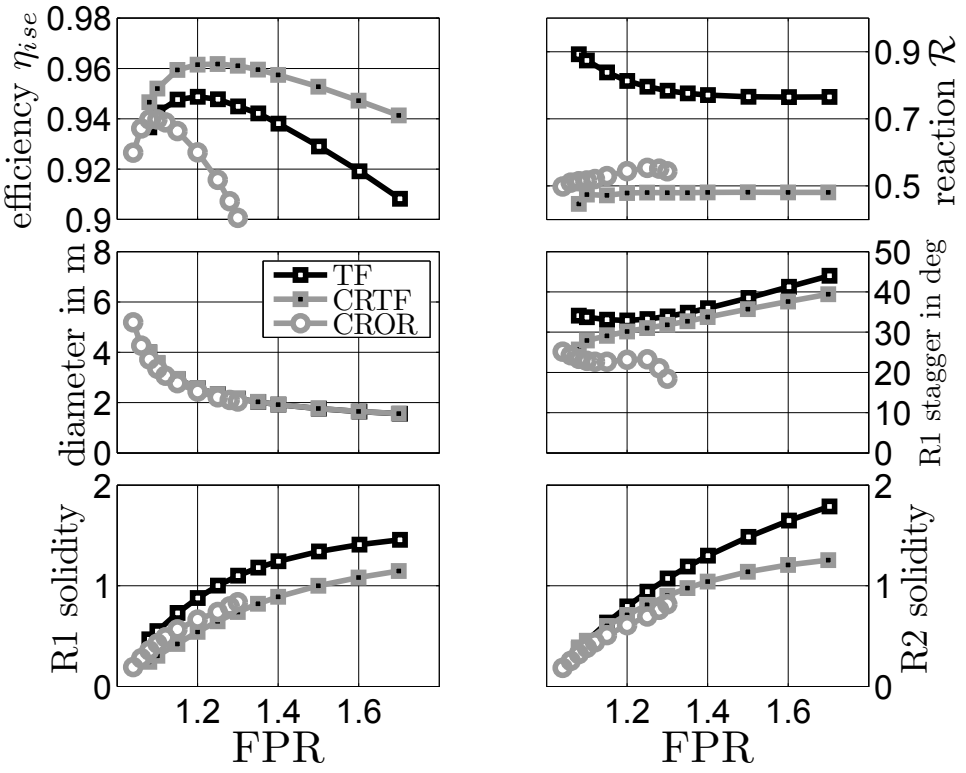

Figure 7.2: Variation of fan performance and geometry with design fan pressure ratio [76]

Table 7.1: Blade count of front and rear rotors (or stator) depending on design fan pressure ratio [76]

TF	FPR	1.1	1.15	1.2	1.3	1.4	1.5	1.6
	R1	8	11	13	16	17	18	18
	R2	13	18	21	26	28	31	32
CRTF	FPR	1.1	1.15	1.2	1.3	1.4	1.5	1.6
	R1	5	6	8	11	13	14	15
	R2	7	9	11	13	15	16	17
CROR	FPR	1.06	1.08	1.1	1.12	1.15	1.2	1.3
	R1	9	11	14	16	19	22	29
	R2	8	10	12	14	16	19	25

and attributed to the unchoked nozzle of low-FPR designs in Cruise conditions. In order to mitigate that effect, a variable-pitch system or a variable-area nozzle would be appropriate to unload the fan and avoid large wakes responsible for increased noise. The lower wake severity of the CRTF is attributable to the more lightly loaded and lower solidity blades.

Before considering the variations of fan noise and its different components, another noise source strongly affected by the fan pressure ratio is simulated: jet noise. The prediction of jet noise is performed with a very simple scaling law based on the exhaust Mach number of the expanded jet and the flight Mach number. It includes an estimate of the turbulent-mixing and shock-induced components. The jet Mach number and jet noise levels are depicted in Fig. 7.5 for each of the operating points. The type of fan concept is irrelevant for jet noise. Decreasing the fan pressure ratio from 1.6 to 1.2 reduces jet

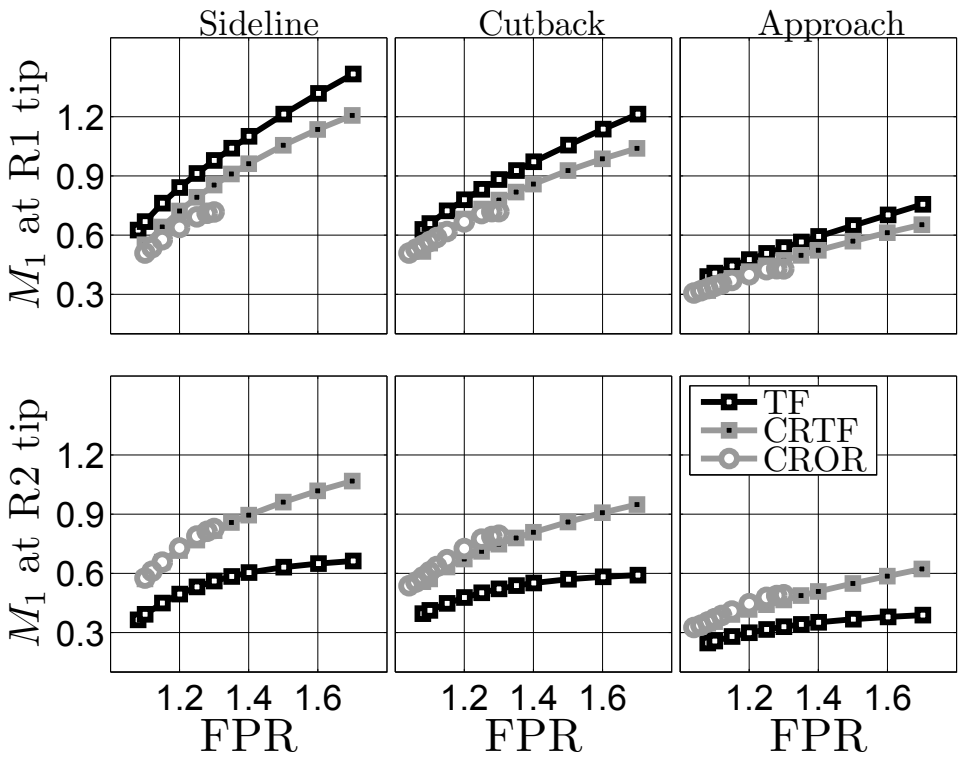

Figure 7.3: Relative Mach numbers at blade tip of front and rear rotors for Sideline, Cutback, and Approach conditions [76]

noise by around 15 dB for each acoustic point, and up to 20 dB in cruise and top of climb owing to the deceleration of the jet below sonic speeds (thus suppressing shock noise). The question is whether fan noise is steadily reduced while decreasing the fan pressure ratio by an amount similar to jet noise or if it reaches a minimum beyond which noise increases again.

The following figures 7.6 to 7.8 show the variation of the different fan noise components with design fan pressure ratio. First, similar trends are observed for the three concepts and for the three acoustic points considered. Reducing the design fan pressure ratio generally affects all fan noise components in a favorable manner. Quantitatively, the variations of the different noise components by decreasing FPR from 1.6 to 1.2 are as follows:

- Tonal self-noise occurring at the sideline and cutback points is cut-off when the rotor tip relative Mach number becomes subsonic. It should be noted that the current model implemented does not account for the non-linear dissipation inside shocks as they travel in the duct. Therefore the level of cuton shock noise is probably overestimated. Nevertheless a substantial noise reduction is achieved by designing for a lower fan pressure below 1.4 (or 1.5 for the CRTF). This aspect is part of the low-noise research strategy of several engine manufacturers.

- Tonal interaction noise is reduced by 10 dB or more at sideline and cutback. The reduction is more pronounced for the conventional fan.

- Broadband self-noise decreases by approximately 5 dB at cutback and approach. At sideline conditions, the noise levels reach a minimum for a fan pressure ratio around 1.3. This is attributable to the increased incidence and wake size, which was mentioned earlier and is specific to low-pressure ratio fans.

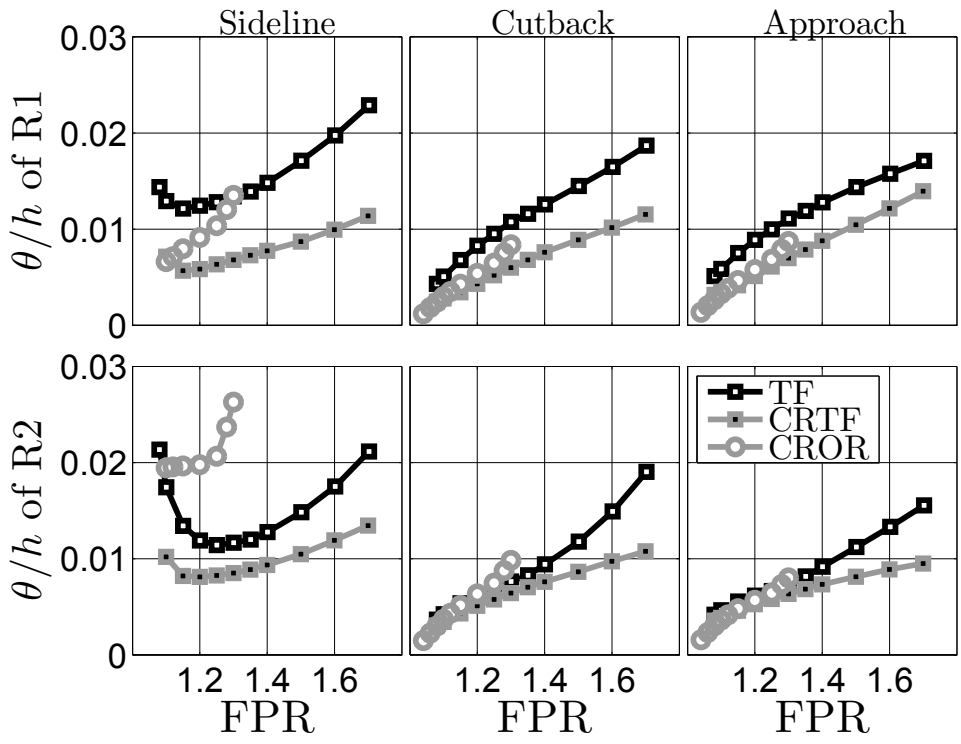

Figure 7.4: Wake size relative to blade spacing for Sideline, Cutback, and Approach conditions [76]

- Broadband interaction noise decreases by up to 10 dB at sideline and cutback, and 5 dB at approach conditions.

In conclusion, an overall reduction of fan noise by around 5 to 10 dB can be achieved for each acoustic point at high speed (sideline and cutback). This is in good agreement with the conclusions of a similar parametric study performed by Gliebe and Janardan in 1993 [192]. Moreover, we also observed that the noise reduction potential at approach condition is less pronounced for low pressure ratio fans. In general, the optimum fan pressure ratio for minimal fan noise emission is located well below the point of optimal fuel consumption and operating costs, which lies in the range 1.4<FPR<1.5 according to different studies [192, 193, 194]. Fans of very low pressure ratio have few blades which enhances the risk of a strong potential-field interaction and requires an increased axial spacing between the blade rows; their stability margin at sideline is more critical, and this would imply either extra solidity, variable-pitch blades or a variable-area nozzle to reduce this margin and the additional loss and noise associated to it, this question has been addressed by Crichton [195].

We will now analyze the results of this study with respect to the relative performance of the three different concepts:

- Tonal self-noise starts at higher FPR for contra-rotating configurations due to the lower Mach numbers. In their range of operations (FPR<1.3) the rotors of the CROR have no supersonic tip speed at sideline and cutback and thus produce no shock noise. The concept of CRTF may assume a fan pressure ratio of up to 1.45 without generating buzz-saw noise at sideline, whereas the conventional fan is limited to 1.35.

- For the tonal interaction noise, the contra-rotating configurations show higher levels, especially at very low pressure ratios below 1.2. In that case, the small blade count would require the distance between both rotors to be substantially increased for the potential field to decay sufficiently.

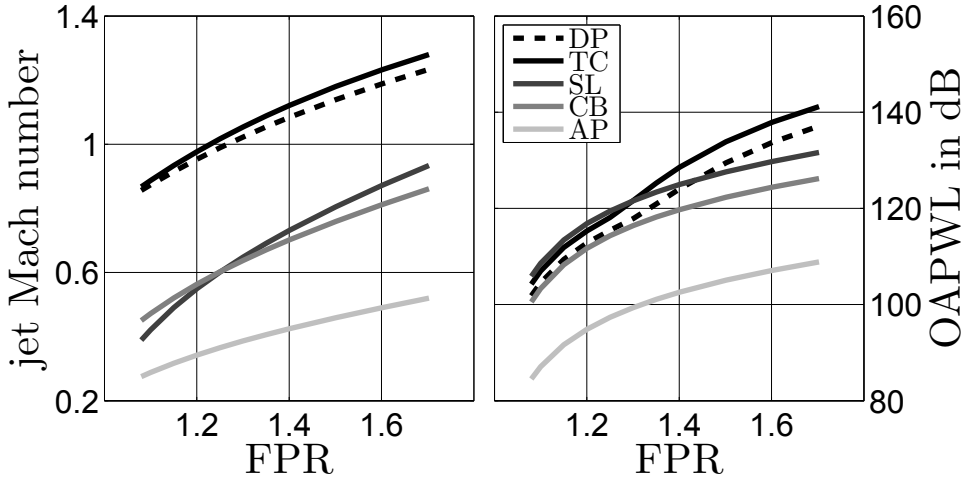

Figure 7.5: Variation of expanded jet Mach number and overall sound power of jet noise with design fan pressure ratio at various operating points [76]

Moreover, the rear rotor of a contra-rotating configuration experiences a high Mach number that the stator does. At approach conditions, the conventional fan present levels lower by 10 dB due to the cut-off design of the first BPF. This is not feasible on contra-rotating rotors as they produce a very rich spectrum of tones that always contain some cut-on modes radiating into the far field.

- The trends for broadband noise are common to the self-noise and the interaction-noise components. The ducted CRTF performs about 5 dB better than the conventional fan, the benefit is more pronounced for high pressure ratio and at higher speeds other than at approach. The strong broadband self-noise emitted by the CROR at sideline conditions is caused by the high incidence of the blades, this problem may be removed by variable-pitch system, which was not modeled in the present study.

Here again, similar results were obtained by Gliebe and Janardan [192]; the two contra-rotating fans concepts they considered showed a noise benefit of 2 to 3 dB against the conventional concepts with the same pressure ratio. They also concluded that the benefit is more pronounced for high pressure ratios. In conclusion, in the domain of design pressure ratios around 1.4, the CRTF seems to be a competitive concept both in terms of aerodynamic performance (2% more efficiency) and in terms of broadband and buzz-saw noise. The challenge is the reduction of the interaction tones, which cannot be cut-off by an appropriate blade number combination and must therefore be controlled by damping surfaces (liners) and a sufficient axial distance between the rotors. In the range of very low pressure ratios, the importance of weight penalties leads to configurations without a nacelle (CROR), this represents a noise challenge, not because there is an increase in sound generation - this is rather the opposite for broadband noise - but due to the absence of liners.

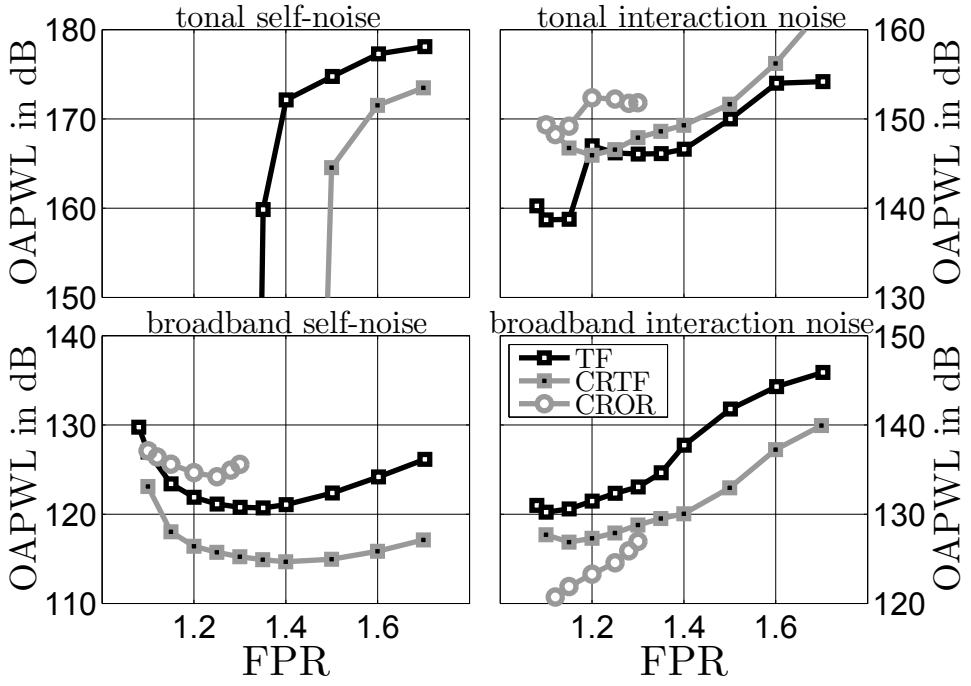

Figure 7.6: Overall sound power of fan noise sources at Sideline condition [76]

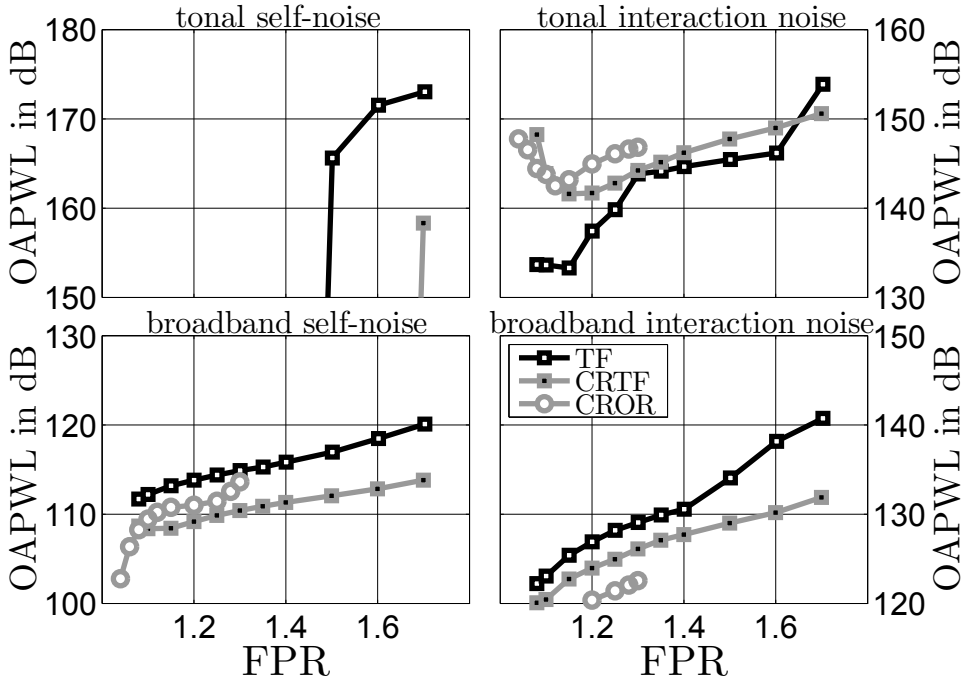

Figure 7.7: Overall sound power of fan noise sources at Cutback condition [76]

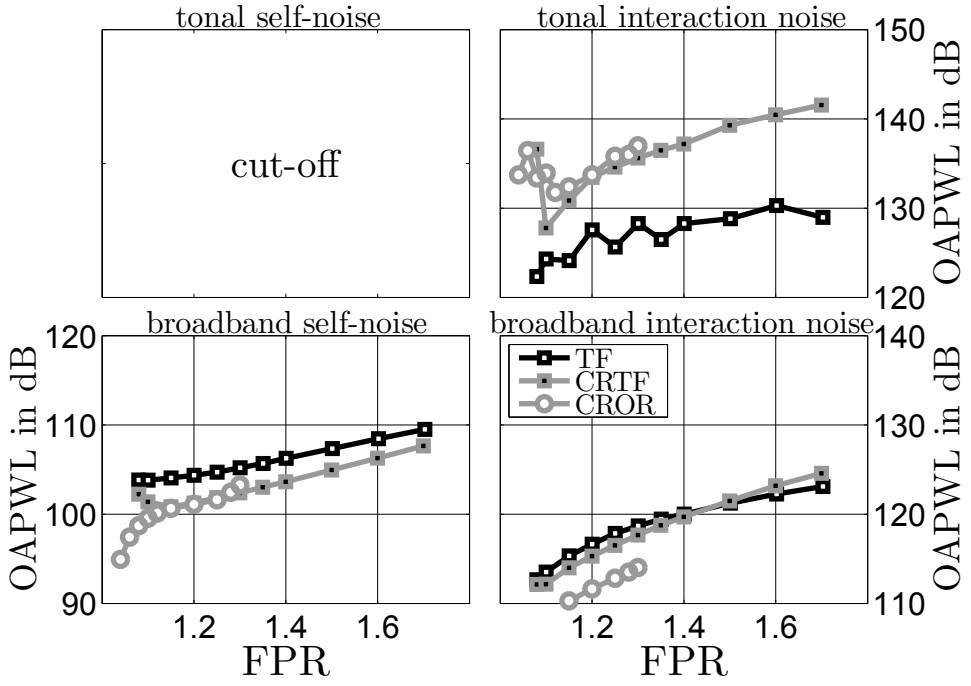

Figure 7.8: Overall sound power of fan noise sources at Approach condition [76]

7.4 Second parametric study: acoustic impact of the design rotor speed at constant fan pressure ratio

The present study considers the further noise reduction potential that may be obtained through appropriate design choices after the fan pressure ratio has been frozen. With a fixed value of FPR and fan-face axial Mach number M_x the size and weight of the nacelle remain unchanged, so does the engine exhaust Mach number and therefore jet noise. Under these conditions, the rotor speed is still a free design parameter to be selected carefully; it directly impacts the flow Mach numbers and thus may be expected to have a positive influence on fan noise. Variations of the rotation speed are considered for a conventional rotor-stator fan stage with a constant axial Mach number of 0.65, and two different values of fan pressure ratio, 1.5 and 1.3, which respectively correspond to recent and future low-noise research fans.

As suggested by the Euler turbomachinery equation Eq.(2.5) decreasing rotor speed U at nearly constant enthalpy rise ΔH_t leads to an increase of the flow turning and a significant modification of the velocity triangles of the stage. The quantity designated loading and denoted ψ is the parameter usually preferred to characterize the problem. It is defined as follows:

$$\psi = \frac{\Delta H_t}{U^2}$$

It should be noted that for a stage with purely axial inflow, the loading and the degree of reaction are not independent and are related through $\psi = 2(1 - \mathcal{R})$. As shown in Fig. 7.9, designs with low loading are characterized by a high rotor inflow Mach number and weakly cambered rotor blades with a large stagger. On the other side, highly loaded designs show a more cambered rotor with a lower stagger angle, and most importantly, a higher stator inflow Mach number and stator flow turning. We consider first the impact of loading on the fan aerodynamic performance and geometry of the blades. As seen in the top left part of Fig. 7.10, an optimum loading that delivers the maximum fan efficiency is found for each fan pressure ratio, the values around 0.5 obtained here are in line with other observations [196, 85]. Designs

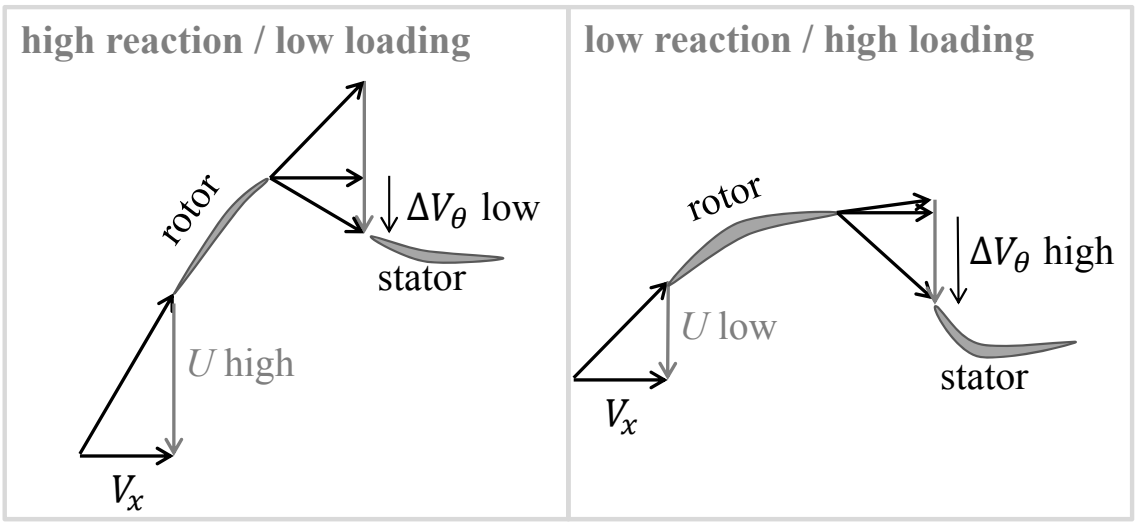

Figure 7.9: Velocity triangles for an axial-flow fan with different degree of reaction and loading [76]

at low loading are characterized by a large rotor Mach number, implying large skin friction and shock loss on the rotor; designs at high loading have high flow turning, implying high stator losses. In general, increasing the loading requires increased solidities on both rotor and stator, which means more blades - if their aspect ratio is kept constant.

The values of blade count obtained after design are shown in Table 7.2.

Table 7.2: Blade count of rotor and stator depending on design value of fan loading [76]

FPR=1.3	ψ	0.29	0.33	0.39	0.47	0.58	0.75
	rotor	13	14	15	16	18	21
	stator	23	24	25	26	28	31
FPR=1.5	ψ	0.40	0.46	0.53	0.62	0.75	0.94
	rotor	16	17	19	22	25	30
	stator	29	30	32	35	39	44

The levels of relative Mach numbers at the rotor and stator blade tip are shown in Fig. 7.11 for the three acoustic operating points: sideline, cutback and approach. Similarly Fig. 7.12 shows the rotor and stator wake size normalized by the staggered spacing of the blades $h = s\cos\chi$. The main acoustic asset of increasing the loading is the strong reduction of rotor Mach number at all operating points; as we will see later, this enables to design for subsonic tip speeds and to cut-off the rotor-alone tones generated by the shocks. However, there are also a number of acoustic drawbacks associated with high loading values: the stator inflow Mach number increases significantly and the wake size is increased on both rotor and stator.

The impact of loading on the different components of fan noise is detailed in the figures 7.13, 7.14 and 7.15. In the same way as done for the first parametric study, we will now discuss the impact of the loading parameter on each component.

- The cut-off of rotor-alone tones associated with shocks is possible if the fan loading is increased to such an extent that the rotor tip velocity becomes subsonic. The noise benefit gained by the

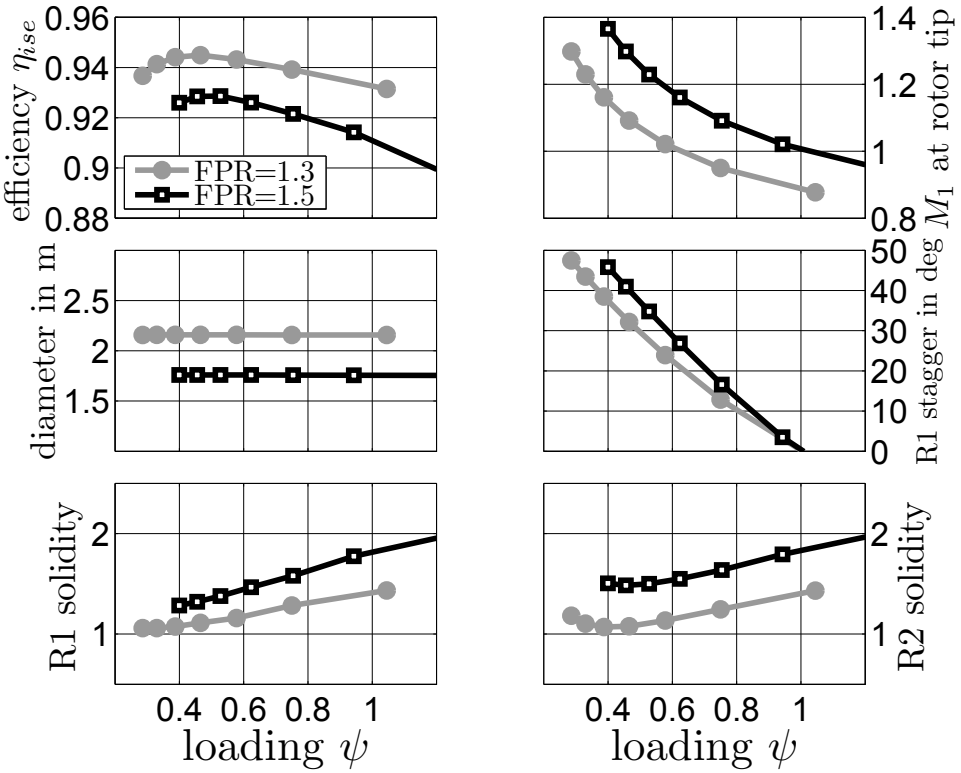

Figure 7.10: Variation of fan performance and geometry with fan loading for two different values of design fan pressure ratio [76]

cut-off is very substantial and in the range of several dB on overall fan noise, despite the slight overestimation of these tones as mentioned earlier.

- Tonal interaction noise decreases with increasing fan loading. This evolution is surprising as it is contrary to that of the broadband interaction described hereafter. The rotor-stator fans designed here have a relatively large number of blades, therefore the potential field interaction is weak and the wake interaction dominates. Unlike its broadband counterpart, the tonal interaction does not seem to be impacted strongly by the size of the wakes, indeed the tonal excitation pressure ζ, see Eq.(6.42), slightly increases with loading but far less than the broadband one. The decrease of noise with loading is partly explained by the decrease of the number of propagating cut-on modes (because the rotation frequency drops). Other aspects (like differences in radiation efficiency depending on the exact modes excited) must be identified to fully explain the trend observed. In general, understanding the evolution of tonal interaction noise is more challenging than for broadband noise: the radial interferences and the small number of modes excited make the acoustic generation more sensitive to small variations.

- Increasing the fan loading has a negative impact on broadband self-noise at all acoustic points: doubling the loading from 0.4 to 0.8 enhances this component by 10 dB at sideline and cutback, and by 5 dB at approach. The reduction of the flow Mach number at the rotor trailing edge is beneficial but cannot compensate sufficiently the increase in wake size and blade number.

- The behavior of the broadband interaction component is less straightforward as it is composed of the interaction between the inflow turbulence ingested by the engine and the rotor turbulent wake interacting with the stator vanes, these mechanisms scaling differently with loading. At low loading,

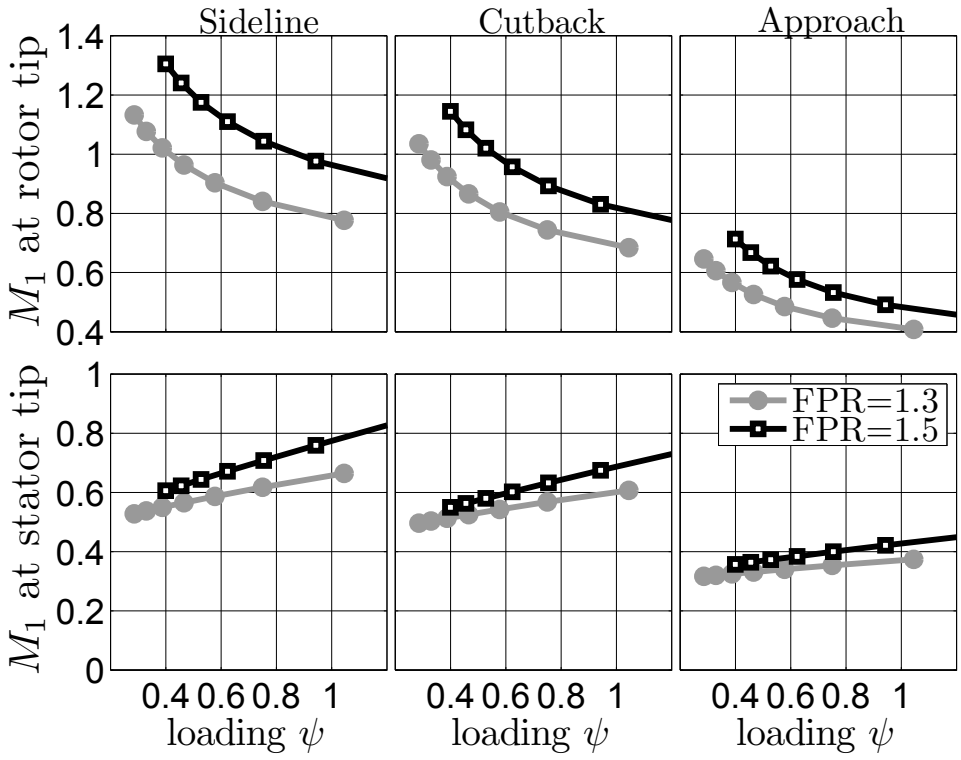

Figure 7.11: Relative Mach numbers at blade tip for Sideline, Cutback, and Approach conditions [76]

the inflow-turbulence noise becomes dominant whereas wake-interaction noise dominates for highly loaded designs. The optimal loading value depends on the turbulence levels ingested by the fan: the lower the turbulence, the lower the optimal fan loading will be. Increasing the fan loading may be of interest for fans operating with a strong inflow distortion.

These trends have to be compared with the results of other studies. Little experience on the acoustic impact of fan loading has been transported so far to the public domain, but three examples are given now to support the conclusions of our study. NASA, working in collaboration with GE on the Source Diagnostic Test fan (SDT), have tested two rotors (so-called R4 and M5) with 10% different rotation speeds for the same fan pressure ratio (around 1.5) and blade count. As expected, the faster rotor M5 showed higher tone levels at high speed, which is due to the increased shock-associated noise. The surprise at that time was the broadband noise level of rotor M5, being lower by 2 to 3 dB at part speeds than for the slower but more heavily loaded rotor R4. The results were published by Woodward, Podboy et al. in two NASA technical reports [197, 198]; it was postulated than the blades of rotor R4 were overloaded and produced larger wakes responsible for the increased noise levels.

Similarly, NASA and Pratt & Whitney worked together on the precursor of the Geared Turbofan called Advanced Ducted Propulsor (ADP) and investigated experimentally the broadband noise of two rotors (called Fan1 and Fan2) having different rotation speeds for the same pressure ratio and blade count. The ADP fan produced a pressure ratio of 1.3. Here again, the slower thus more loaded Fan2 produced slightly more noise at all points, this was reported by Elliott [199] and Heidelberg [200]. The noise increase of Fan2 was attributed by Topol [201] to the higher turbulence levels observed in the tip region; this might be explained by the stronger tip vortex forming on blades operating at a high lift coefficient.

Finally, Rolls-Royce plc. working with the University of Cambridge as part of the EU-funded project RESOUND (1998-2001) re-designed a fan primarily to reduce its rotor-alone noise source component [202].

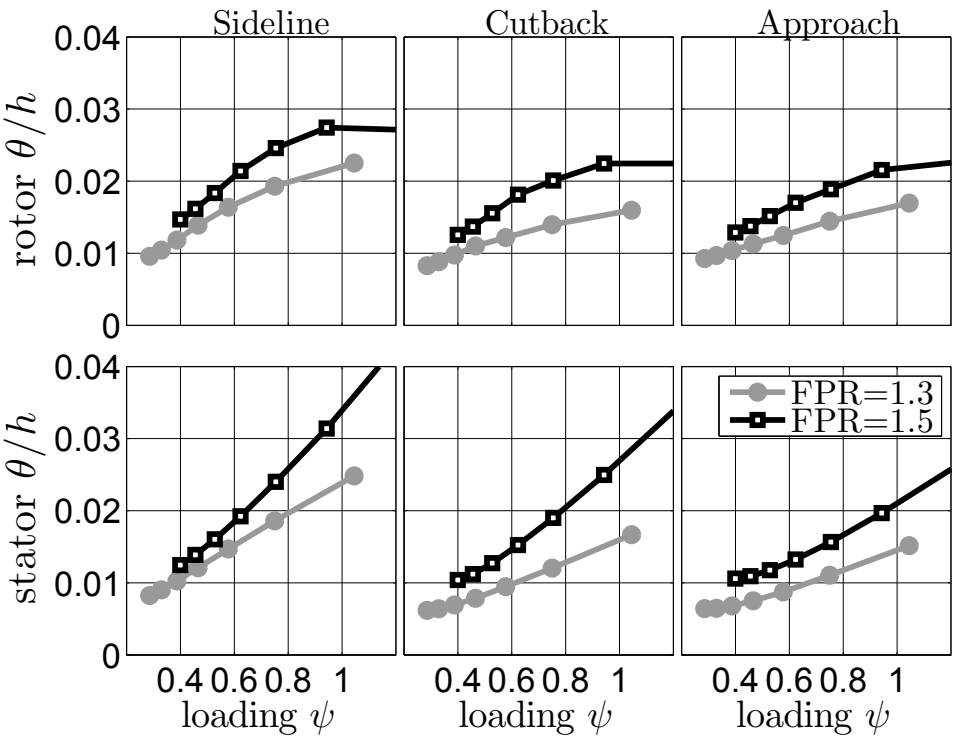

Figure 7.12: Wake size relative to blade spacing for Sideline, Cutback, and Approach conditions [76]

The datum fan and the new fan, called LNR1, both had a pressure ratio around 1.8 and 26 rotor blades. LNR1 had a tip speed 15% lower than the datum fan. The tests were carried in the ANCTF facility in Ansty, England. As expected, the low tip-speed design cut off the rotor-alone tones, so a large tone noise reduction by 5 to 10 dB was measured. However, the broadband noise levels did not decrease. An increase in wake interaction noise was suspected, which offset the benefit of the lower tip speed.

These three examples are in agreement with the conclusions of the present study: a reduction of the fan tip speed accompanied with an increase of the fan loading leads to the suppression of buzz-saw noise but this may be at the cost of an increase in broadband noise. As a result, there is an optimum value of fan loading for noise emission, which does not necessarily coincide with the aerodynamic optimum. The exact position of the acoustic optimum depends on the cut-on limit of rotor-alone tones and on the severity of the shocks responsible for the steep rise in buzz-saw noise. Shock management (operation close to choking with minimum incidence) is discussed by Crichton [196].

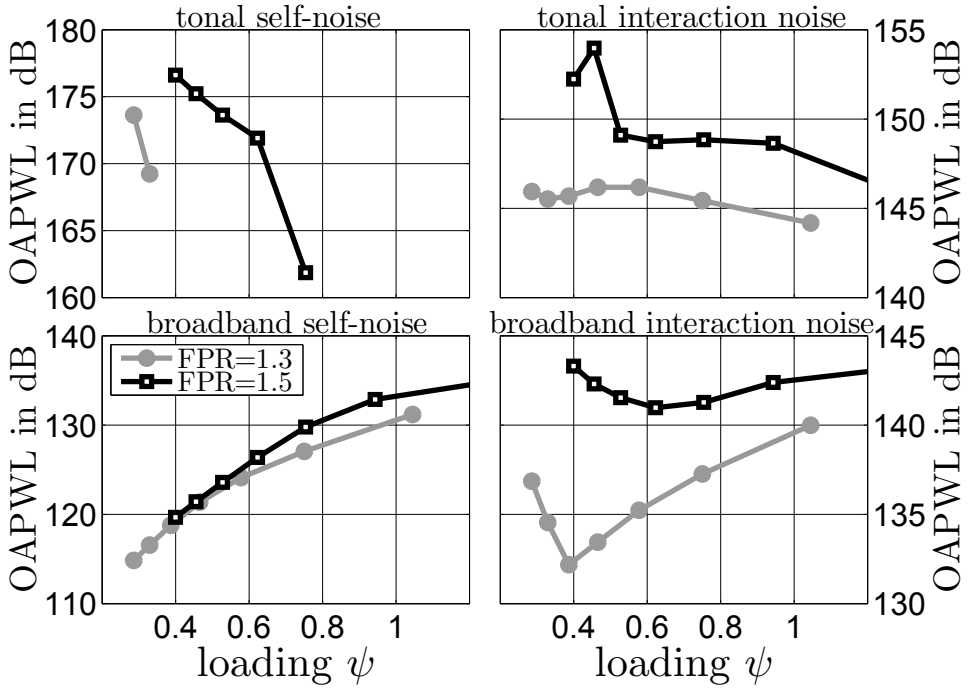

Figure 7.13: Overall sound power of fan noise sources at Sideline condition [76]

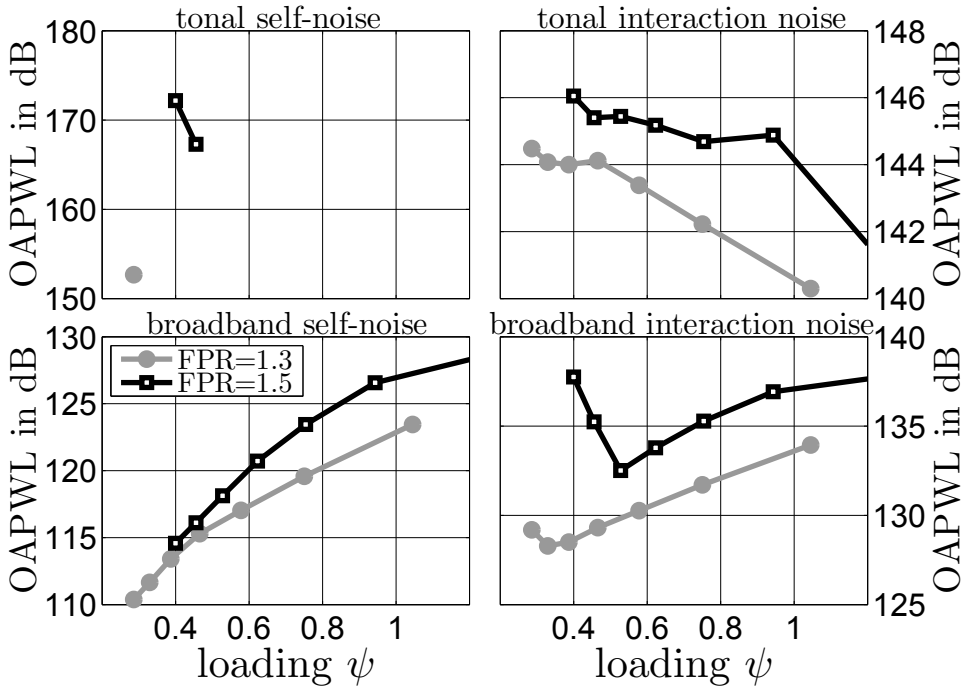

Figure 7.14: Overall sound power of fan noise sources at Cutback condition [76]

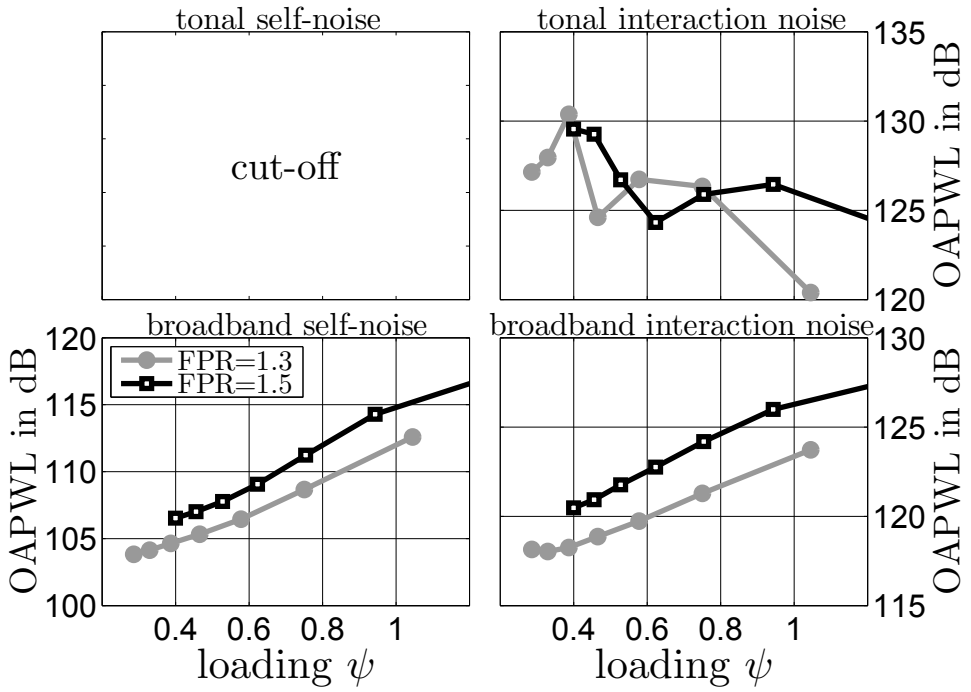

Figure 7.15: Overall sound power of fan noise sources at Approach condition [76]

7.5 Conclusions about the parameter studies

A conceptual study (presented at the ASME Turbo Expo [76] and edited in the Journal of Turbomachinery [188]) integrating the assessment of fan aerodynamic performance and fan noise emission has been performed to evaluate the impact and benefit of designs with a low rotor speed on equal thrust basis. As this study is situated on the preliminary design level, a number of simplifications was made to represent the fan geometry and flow features with analytical models, for example only the bypass is considered and a meanline approach is adopted to predict the fan aerodynamic performance. For the acoustic prediction, a fully analytical description of the different fan noise sources is applied, which is not based on the empirical correlations usually used at the pre-design level, and accounts for ducted/unducted and single-/contra-rotating fan configurations on the same basis. Two parameter studies have been conducted with this integrated analytical prediction framework. The scope of the first parameter variation is the influence of the design fan pressure ratio and the comparison between the different concepts TF, CRTF and CROR. The main conclusions are summarized here:

- The reduction of design fan pressure ratio beyond the subsonic tip speed limit (which is reached around FPR=1.35 for a conventional fan at sideline) provides continuously lower noise levels of the fan broadband and fan tonal interaction components.
- The flattening of the noise benefit is reached for very low pressure ratios which are well below the fuel-burn optimum located around FPR=1.4. Therefore there is a motivation to consider Ultra-High-Bypass-Ratio engines as good candidates for future low-noise propulsive systems. Nacelle integration and weight become the prominent challenges which also affect the acoustic design: the axial distance between the blade rows is critical in view of the low blade count, the short intake cannot ensure a small inflow distortion and the noise attenuation by liners is limited.
- The noise benefit provided by low fan pressure ratio is more pronounced at sideline and cutback than at approach conditions, where anyway airframe and jet-flap interaction are strong noise components.

- For a fan in the domain around FPR=1.4, the contra-rotating ducted turbofan CRTF should be regarded as a serious competitor to the conventional fan. Besides the fact that the fan isentropic efficiency is improved by roughly 2%, it generates no buzz-saw noise and shows reduced broadband noise levels.

A second study evaluates the impact of a reduction of the rotor speed at constant pressure ratio, for a conventional rotor-stator fan stage.

- The main asset of reducing rotor speed is the ability to cut-off the rotor-alone tones if the inflow in the relative frame remains subsonic at sideline.
- However this must be done at the cost of a substantial increase in broadband noise. Both rotor and stator have a higher loading, meaning that the blades generate thicker boundary layers, larger wakes and more intense turbulence. The noise induced by the rotor tip flow, although not addressed here, will follow a similar trend owing to the increase of the lift coefficient.
- Tonal interaction noise seems to be reduced with increased loading, which is a reverse and unexpected trend compared to broadband noise. A number of mechanisms (i.e. number of propagating modes) apparently compensates the increase in wake size. A closer look at the evolution of each acoustic parameter should explain this trend.
- Anyway there is an optimum fan loading for each fan pressure ratio that primarily depends on the onset of buzz-saw noise. Designing for transonic fans with weak shocks might be the appropriate strategy to minimize broadband noise and overall fan noise, if the fan operates with a relatively clean inflow. If the inflow distortions are strong, as it may be the case in embedded engines or with short nacelles, designing for highly loaded fans might be acoustically preferable: the number of rotor blades and the relative flow Mach numbers at which the disturbances impinge on to the rotor will both be lower, which will result in a weaker interaction between the front rotor and the inflow distortion.

The conclusions of both studies agree with the results of other design exercises and experiments published in the past, especially concerning the noise potential of low fan pressure ratio [192] and the neutral [202] or negative impact of increased loading on broadband noise [197, 199]. The work presented in this paper provides therefore a theoretical background for important low-noise design guidelines which are more or less empirical but have been accepted and adopted so far within the engine community. The next objective is to go beyond the state-of-the-art designs by further exploiting the present fan noise prediction framework.

Chapter 8

Conclusions and outlook

8.1 Feasibility of acoustic pre-design by analytical methods

The contribution of the present work to the field of fan noise research is to propose a stand-alone theoretical environment, independent of external tools, for the assessment of axial-flow fan configurations during the preliminary design phase of an engine. The approach is based on models that are mainly analytical in nature, but also resort to some empirical correlations when necessary. The problem of fan noise emission, that is often described as complex, is separated into its elementary components and simplified in a drastic manner which is more appropriate to capture the acoustic impact of design parameters at the engine level.

The detailed description and derivation of the aerodynamic and acoustic models presented in chapters 2 to 6 has shown the similarities shared by ducted and unducted configurations, and by the single- and contra-rotating fans. Therefore the various characteristics proper to each fan concept can be predicted with the same set of models, and compared to each other *on a common theoretical basis*. This contributes to legitimate the approach based on simplified models and to demonstrate the feasibility of acoustic pre-design with this approach.

The previous chapter has shown realistic applications of the models in the context of global trend studies and validation on specific configurations. On the one hand, the exercise of validation has demonstrated on a limited number of cases that the models can provide sensible results which are comparable to experiments. On the other hand, global trend studies have demonstrated that the models can be applied over a wide range of the design space, thereby delivering clear trends which are in agreement with experimental observations and trend studies available in the literature. This too supports the idea of the feasibility of acoustic pre-design with an analytical approach.

Finally, two aspects must be mentioned on which the success of pre-design methods also depends. First, analytical models are very fast: the wall-clock time for the full simulation of a fan configuration from aerodynamic design to acoustic assessment at five operating points typically takes less than half an hour. This aspect is particularly important during pre-design studies, in which a vast design space must be explored. Second, analytical models assume a didactic role that improves insight into the driving mechanisms and helps to anticipate good design choices.

8.2 Main conclusions on the model predictions

We now summarize the most important conclusions suggested by the parametric studies of the previous chapters. The results mentioned in this section are confirmed by state-of-the-art or by experiments, so they are not affected by the relative inaccuracy of the models. The section 8.3 will discuss the domain of validity and possible improvements for the models.

8.2.1 Comparison of the fan concepts

The three fan concepts considered as potential candidates to equip future civil aircraft engines are the conventional ducted turbofan TF, the contra-rotating ducted fan CRTF, and the contra-rotating open rotors CROR. The most remarkable features of these concepts can be described as follows:

- **Contra-rotating technology:**
  - The rotation of the rear blade row allows for more flexibility in the aerodynamic design of the fan stage. In particular it is possible to design for a stage degree of reaction around 0.5 (which means equal distribution of static-enthalpy rise on both rotors). The fall-off in performance observed away from the optimal design region is less pronounced on contra-rotating fans, thus enabling a design at higher values of pressure ratio and axial Mach number without too much performance penalty.
  - As the work input can be distributed over two rotors, the aerodynamic loading is reduced, therefore the required solidity and number of blades are smaller, thus increasing the choke margin. In all, these effects represent a benefit of 2 to 3 % in fan isentropic efficiency compared to a conventional rotor-stator stage with the same pressure ratio. This also has positive implications in terms of broadband noise, which tends to be lower than the conventional turbofan by around 2 dB.
  - The tonal self-noise of the front rotor can be significantly diminished due to its lower inflow Mach number. As a result the onset of buzz-saw noise can be delayed towards higher values of fan pressure ratio, which makes CRTF an interesting competitor to TF at FPR=1.4 and above.
  - An acoustic drawback is the strong tonal interaction between the potential field of the rear rotor and the trailing edge of the front rotor. The high inflow Mach number of the rear rotor is responsible for a strong potential field at source, which has on top of that a slow axial decay owing to the low blade count. Sufficient axial distance between both rotors must be therefore guaranteed, making the fan stage less compact.
  - No cut-off of the blade passing frequency and its harmonics can be achieved by adapting the rotation speeds or the blade counts.
  - Tonal sound generation occurs at relatively low frequencies (lower rotation speed and blade count), or equivalently large wavelengths. Therefore introducing sweep and lean to generate radial interferences is acoustically less efficient than on a conventional rotor-stator stage. Moreover, the performance of acoustic liners may be reduced as the depth of the damping cells is constrained by the thickness of the nacelle.
- **Unducted rotors:**
  - The main benefit of open configurations is the absence of an external nacelle producing additional drag and weight. This is of particular interest for stages with a very low pressure ratio (below 1.2).
  - The other side of the coin is that the axial Mach number just upstream of the stage cannot be controlled. On a conventional turbofan the nacelle decelerates the flow in cruise; the fan-face Mach number is then usually maintained around 0.6 by sizing the nozzle exhaust area accordingly. In the unducted case, there is a thrust-induced axial velocity that is superimposed to the flight speed, leading to fan-face Mach numbers well above 0.8 and limiting the isentropic efficiency of the fan.
  - Apart from the different flow Mach numbers affecting the strength of the sound sources, there are no fundamental differences concerning the sound propagation and radiation from ducted and open configurations. In both cases, a cut-off limit can be identified beyond which acoustic modes decay exponentially inside a duct or radiate very poorly in free field. This cut-off limit

is related to the subsonic or supersonic velocity of the sound wave front, it is not caused by the geometric boundary conditions of the problem. For sources of equal strength exciting cut-on modes the sound power is nearly identical in the ducted and open problems.

- The amount of surface available for noise-damping materials is much smaller in the absence of an external nacelle. This aspect, combined with the high inflow Mach numbers and the acoustic questions inherent to the contra-rotating technology, is the reason why the CROR concept is regarded as challenging for noise emission.

- **Conventional turbofan:**

  - The ducted rotor-stator fan stage has remained the technology of choice for all civil aircraft engines for many decades, and the large experience gained over its many years of service is a decisive asset in a conservative branch like aeronautics. The conventional fan is characterized by its relative simplicity, with only one rotating blade row.
  - The role played by each blade row is clearly differentiated: the rotor is responsible for the work input and generates most of the loss whereas the stator function is only to remove the swirl from the rotor and to ensure an axial exhaust flow. The stator contribution to the total loss is usually below 30%. For those reasons, the global performance of the stage strongly depends on the quality of the rotor aerodynamic design, while the design of the stator is less critical.
  - The distinct roles of the rotor and stator imply dedicated noise-mitigation measures that are specific to each blade row. The reduction of tonal self-noise (buzz-saw noise) and the wake size are a priority for the rotor, but this has to be carefully balanced to cope with severe requirements on efficiency and stability margin. Noise mitigation may be more drastic on the stator: for example with pronounced sweep and lean angles of the vane leading edges combined with a low vane count which permits inverse cut-off design and low broadband noise levels.

8.2.2 Choice of the design fan pressure ratio and fan loading

The second aspect addressed by the trend studies of the previous chapter is related to the impact of two key design parameters: the fan pressure ratio and the fan loading, for a rotor-stator ducted stage. The following general conclusions can be drawn:

- **Impact of the fan pressure ratio:**

  - This parameter varies inversely to the bypass ratio and to the diameter of the fan. The main benefit of low FPR is the improvement in engine propulsive efficiency due to the lower jet exhaust velocity. At some point however, the drag and weight penalties of the enlarged nacelle annihilate the propulsive benefit.
  - Reducing the pressure ratio also affects the fan performance in a positive manner: the aerodynamic loads on the blades are reduced. This means smaller wakes and less broadband noise; the Mach numbers of the flow impinging both rotor and stator are reduced too, which decreases the noise generation of all sources, especially the tonal self-noise of rotors (buzz-saw noise).
  - The thermodynamic, aerodynamic and acoustic virtues of low pressure-ratio fans explain the very pronounced trend toward large high-bypass-ratio engines observed since the earliest hours of civil aeronautics. Currently, ultra-high-bypass ratio engines with a fan pressure ratio around 1.3 are targeted by engine manufacturers to tap the full potential of this strategy.
  - There are however some new challenges related to low-pressure-ratio fans. Their low-solidity blades make them less prone to support strong positive incidences encountered at off-design points like Sideline or Approach, which are precisely located closer to the aerodynamic stability limit because the nozzle is unchoked in Cruise conditions. This aspect leads to a reduction of the stability margin, which must be restored with help of an auxiliary device such as a

variable-area nozzle, variable-pitch blades or air bleed via openings in the intake. The latter option may induce strong spurious noise sources, while the variable-geometry options may bring an aerodynamic and acoustic benefit.

- Another challenge related to large engines is the short nacelle necessary to limit the weight and drag penalty. In addition to the reduced surface available for liners, new noise sources may appear such as the interaction of the front rotor with inflow distortions triggered by the short intake at incidence. Alternatively, it is possible to bypass this problem by replacing the large engine by a number of smaller propulsion systems (all still having a low fan pressure ratio) distributed over the airplane. This strategy is called distributed propulsion and can be realized through a joint effort from airliners and engine manufacturers.

- **Impact of the fan loading:**
  - At constant fan pressure ratio, this parameter varies inversely to the design speed of the front rotor, and represents the aerodynamic load of the rotor disc. For a stage with a purely axial inflow, increasing the loading is equivalent to decreasing the stage degree of reaction, which corresponds to a redistribution of the static-enthalpy rise from the front rotor to the stator.
  - Varying the fan loading at constant pressure ratio has no impact on the fan diameter and size of the nacelle, so it may represent a noise reduction strategy worth considering if one desires to avoid the questions raised by high-bypass-ratio engines mentioned above. In particular, the inflow Mach number of the front rotor can be substantially decreased by increasing the loading, thereby suppressing buzz-saw noise, and weakening the interaction with inflow distortions.
  - However, in that case, the Mach number of the rear blade row increases as does the interstage swirl. This means aerodynamically more demanding conditions for the rear blade row, and globally a shift closer to the stability margin of the stage. Moreover the flow turning of the front rotor also increases. As a result, the blade wakes are larger and cause more broadband noise for high-loading designs.
  - Consequently, the effect of fan loading is not as straightforward to assess as for the fan pressure ratio: there is a balance to find between competing noise generation mechanisms. To accept a certain amount of supersonic flow over the rotor in order to maintain reasonable broadband noise levels may be an inevitable compromise for turbofans with medium to high fan pressure ratio (FPR > 1.35 in Cruise). In that case, effective mitigation of buzz-saw noise is a central aspect of fan noise reduction strategies.

Beyond the confirmation of academic knowledge, many of the conclusions presented here confirm the qualitative rules that form current state-of-the-art in the field of fan aerodynamic and acoustic design. The past evolution of engine fans and modern research trends can be understood and reproduced via the theoretical framework proposed here.

8.3 Prediction capability of the models

The previous section has summarized the global trends predicted by the models which turn out to describe well past and current evolutions of engine fans. In this section we propose an overview focused on the specific aerodynamic and acoustic models, their ability or inability to capture phenomena and possible extensions or improvements that may be envisaged for future work.

- **Models for steady flow and aerodynamic performance:**
  - One of the strongest simplifications is the meanline approach, which assumes that the evolution of flow quantities along a single streamline, called the meanline, can provide the global performance and that the entire flow field can be extrapolated from this meanline. That approach turned out to capture correctly many important features of axial-flow stages both in

terms of design rules and off-design behavior, however some difficulties were encountered and are summarized hereafter.

- First, the impact of several design parameters is correctly reproduced. Large blade solidity and duct contraction (MVDR) both play an aerodynamically stabilizing role (flow separation is prevented) but this is at the cost of friction loss, hence there exists an optimal value which increases with fan loading and pressure ratio. Similarly, increasing the design speed for a specified fan pressure ratio and mass flow has a stabilizing effect but it also implies more friction and possibly shock loss. The higher the pressure ratio the higher the optimal design speed should be. The aerodynamic superiority of contra-rotating fans is properly predicted by the models, as are their main differences compared to conventional fans: lower blade solidity and rotation speed of the front rotor, weaker sensitivity of the peak performance to design specifications. Finally, the models identify design features related to stability-margin requirements: stages with low pressure ratio need a variable-pitch system or variable-area nozzle; the rear rotor of a CRTF has a higher blade solidity than the front rotor.
- Two aspects must be mentioned, for which the models do not provide a good correlation with observations. First, the impact of the axial Mach number at the fan face is significantly underestimated. Indeed, for a constant fan pressure ratio, the models predict a decrease of the rotor speed with increasing axial Mach number which is motivated by the reduction of shock losses. This trend is contrary to results from another more accurate study performed with a 3D RANS flow solver. The other aspect is that the solidity of rotors resp. stators is generally under- resp. over-predicted by the models. This might be related to the dependence of loss to rotation, to Mach number (high for rotors, low for stators), or to the presence of a tip clearance.
- The behavior of the models when applied at off-design conditions (that means for a fixed fan geometry) shows sensible trends: the Top-of-Climb point is located at a slightly higher speed than design and shifted toward choking; the Sideline has a larger incidence than the design incidence, owing to the large thrust requirement at relatively low Mach number. The higher incidence also observed at Approach is due to the less pronounced acceleration of the flow over the spinner than that observed at higher axial Mach numbers. Moreover, the Sideline and Approach points are located more closely to the stability margin for low-pressure-ratio fans than for high-pressure-ratio fans.
- A widely recognized obstacle to performance prediction models is the complex flow that prevails in endwall regions. There have been many suggestions to tackle this aspect but none accepted as a reliable correlation in compressor applications. Here we have simply chosen to ignore the endwall and tip loss, except for the friction loss induced by the hub and casing surfaces.
- The prediction of deviation is another topic that usually strongly relies on empirical correlations. The model implemented here reproduces for low-solidity blades the inviscid lift coefficient in the limit of an isolated airfoil and zero-deviation for infinitely large solidity. The contribution of the boundary layer thicknening is not accounted for. This explains the inaccuracy of fan pressure ratio near the stability limit. Moreover the absence of Mach-number-dependent deviation model may explain why the fan pressure ratio is overestimated at high rotation speeds.
- One of the largest difficulty for analytical models or empirical correlations is to describe correctly the transition between the subsonic and supersonic regimes in terms of loss. The academic distinction between the boundary layer loss and the shock loss may not be the most appropriate approach because these contributions do not superimpose linearly and interact with each other increasingly as the inflow velocity gets supersonic. An alternative model proposed by Freeman and Cumpsty [87] based on the continuity and momentum equations applied on flat plates may be a starting point for future improvements.
- The relatively inaccurate prediction of the mass flow rate at which choking occurs in the fan map is inherent to the meanline approach. Indeed, near choking there is a strong redistribution

of mass flow from the upper region of the blade (usually choked) toward the lower part which is not choked due to low Mach numbers. This redistribution cannot be captured by a single-radius approach.

- The meanline approach also has some limitations at strongly off-design conditions where the radial distribution of work load and swirl significantly departs from the free-vortex distribution. Nevertheless, this latter distribution is realistic near the design point because it corresponds to a radially constant circulation around the blades, thus minimizing the vortex-induced drag of ducted fans. For open configurations where the blade circulation is forced to zero at the blade tip, the free vortex assumption is more subject to errors.

- **Models for unsteady aerodynamics:**

  - Due to the massive development of numerical simulations, the interest for analytical solutions of wake, turbulence and potential fields prevailing around blades has remained limited after the 70's. However these quantities are essential for fan noise prediction. The present stand-alone method had to resort to such analytical models.
  - The prediction of the wake size directly depends on the drag coefficient provided by the steady-flow and performance models discussed above. The assumption is made that the wakes have a Gaussian shape and are symmetrical on the suction and pressure sides. This is not valid in the vicinity of the blade trailing edge, where local flow acceleration at the edge of the boundary layers may occur. Moreover, the model also departs from reality in the endwall regions where stronger vortex systems are encountered. The downstream development of the wake is predicted by a coupled system of momentum and continuity equations supported by an empirical correlation for the entrainment of boundary layer mass flow. This model correctly reproduces the slower wake decay in the presence of a positive pressure gradient.
  - The estimation of the turbulence intensity and its decay behind a blade row is addressed only by empirical correlations so far; these would require more extensive validations. In particular the increased background turbulence between the wakes (which is higher than the inflow turbulence) seems to be a significant contributor to broadband noise, although its origin is not clearly identified yet. It might be attributed to the strong adverse pressure gradient experienced by the flow across a compressor blade row, which amplifies velocity fluctuations and in particular the background turbulence. A two-transport-equation turbulence model as used in the RANS approach (i.e. $k-\omega$ model) may replace the empirical correlation to describe the streamwise decay.
  - The decay of the potential field can be described fully analytically in a ducted configuration based on the dispersion equation. However the initial strength of the potential field is related empirically to the lift and thickness of the blades. As for the aerodynamic loss model, the transition between subsonic and supersonic regimes represents a difficulty for analytical models dedicated to the potential-field-strength prediction and to the lift coefficient.
  - The gust response function, currently implemented for an isolated flat plate, can be extended to account for neighboring blades, which should provide a slightly lower and more accurate estimate of the acoustic levels at low frequencies. The high-order terms of the response function like flow incidence, leading edge thickness, and profile camber may also improve the accuracy of prediction, especially in the case of turbine blades.

- **Acoustic models:**

  - A fully analytical formulation has been derived from Goldstein's fundamental linear equation for sound generation in the presence of rotating solid surfaces. The source terms have been separated from the propagation terms and the similarities between the free-field/in-duct problems on the one side, and tonal/broadband noise on the other side, have been demonstrated. The presence of the duct walls does not fundamentally modify the sound power radiated by

a source of given strength, a cut-off limit can be identified beyond which sound waves with higher mode order or lower frequency radiate very poorly into the far field. This condition is linked to the subsonic nature of their phase speed.

- The strong assumptions imposed for broadband noise can be released to provide more general validity to the models. In particular, abandoning the hypothesis of small-scale turbulence allow considering large-scale eddies ingested by an engine (typical of conditions near the ground, or with a short nacelle at incidence) and to bypass the need for a model of integral length scales. However, the consequence is that two-point statistics of the turbulent flow field are needed, which are difficult to measure, simulate or even more to model analytically. Apart from that aspect, the broadband sources modeled currently are of dipole type and linked to blade unsteady lift. Extension to quadrupole sources that account for the distortion of eddies while being convected across a blade row might provide new insight. There is very little experience on the importance of quadrupole broadband noise, it is suspected to be relevant only at high Mach numbers.
- For ducted configurations, the current models ignore the contribution of cut-off modes to the radiated sound field. With the development of short nacelles such simplification is not valid anymore, above all because inflow distortions generally excite cut-off modes. A radiation model from the intake plane into the far field is necessary to obtain an estimation of the sound power carried by these modes to the observer. Apart from that, including cut-off modes may deliver smoother trends which better correspond to the actual acoustic behavior of fans.
- The shielding exerted by the rotor on the sound waves emitted by the stator in the upstream direction plays a dominant role at high Mach number regimes. In that case the forward-arc radiation is dominated by tonal self-noise from the rotor and interaction noise is masked. A transmission model through blade rows accounting for full shielding when sonic flow conditions are reached is required for proper estimation of forward fan noise at supersonic speeds.
- As the acoustic models are currently fully linear, the decay of pressure amplitude observed during shock propagation is not modelled. This implies that tonal self-noise produced by supersonic rotors is over-predicted. A non-linear shock propagation model accounting for energy dissipation and scattering is needed to model buzz-saw noise, typical of supersonic rotors.

Provided the large number of different models implemented and the wide range of topics they cover, the perspective of a comprehensive validation must be planned for the next years to come. Some work related to that has been started and presented here, but a large part of the efforts must focus on further assessment of both single models and global predictions. Therefore, access to high-quality experimental data from clearly identified fan noise source experiments is needed.

8.4 Further extensions of the method and outlook

In addition to the various model improvements suggested in the previous section, the method adopted for acoustic assessment and design can be extended. One extension, still remaining in the stand-alone frame, could be to integrate more advanced acoustic criteria within the design procedure: for example, the variation of blade number, or the optimization of axial distance between the front and rear rotors. The coupling with a tool dedicated to automated optimization (such as 'AutoOpti' developed by the Fan and Compressor Department of DLR Cologne) represents an alternative likely to extract the best potential out of the aerodynamic and acoustic models. It is also possible to go beyond the stand-alone approach and the dependency on analytical performance models, as we have seen that the proper prediction of the aerodynamic input is essential for acoustics. The aerodynamic modules (for design and steady aerodynamics) can be bypassed by feeding the acoustic analytical models with the flow field obtained from a three-dimensional CFD simulation (provided e.g. by the flow solver 'TRACE' of the DLR Institute of Propulsion). In that case, the flow data must be extracted and extrapolated to the locations

where sound is emitted. Thus the overall accuracy of the noise prediction is significantly improved by an amount equivalent to the quality of the CFD flow solution. Models for unsteady aerodynamics are still necessary because a RANS solution does not provide the turbulence spectra required for broadband noise. As a further step, this hybrid approach (analytical acoustic models informed by a RANS solution) may be integrated into an optimization procedure to explore the design space in a more extensive manner and to discover three-dimensional blade shapes that provide a substantial noise reduction combined with a high aerodynamic performance.

8.5 Afterwords

As a conclusion, the numerous and very strong simplifications assumed to handle the problem of fan aerodynamic and acoustic design with analytical models may be easily striking at first. Approximations, inaccuracies are questions the user of such models is faced at continuously. That does not mean, however, that their output is something out of which no helpful result can be identified. On the contrary, despite the strongly simplified formulations, or maybe precisely thanks to them, the analytical models capture sensible clear trends which are in line with the evolution of engine fans and accompany them from a theoretical point of view.

The fact that analytical models are robust, applicable on a wide range of cases and require few computational resources makes them powerful to explore vast design spaces typical of turbomachines and guide the engineers rapidly toward the regions with the best potential. In that respect, they are complementary to high-fidelity tools such as unsteady RANS or LES/DES simulations. They may also represent a valuable support to appraise the results produced by more advanced tools, whose calculations, internal assumptions and limitations are not as straightforward to understand as those of analytical models.

Bibliography

[1] A. Moreau and S. Guérin. The impact of low-speed fan design on noise: an exploratory study. In *ASME Turbo Expo*, 2015. GT2015-43163.

[2] T. Lengyel-Kampmann, C. Voß, E. Nicke, K.-P. Rüd, and R. Schaber. Generalized optimization of counter-rotating and single-rotating fans. In *ASME Turbo Expo 2014*, Düsseldorf, Germany, 2014. GT2014-26008.

[3] E. Envia, D. Tweedt, R. Woodward, D. Elliott, B. Fite C. Hughes, G. Podboy, and D. Sutliff. An assessment of current fan noise prediction capability. In *14th AIAA/CEAS Aeroacoustics Conference*, 2008.

[4] M. Heidmann. Interim prediction method for fan and compressor source noise. Technical report, NASA Technical Memorandum X-717763, 1979.

[5] K. Kontos, P. Janardan, and P. Gliebe. Improved NASA-ANOPP noise prediction computer code for advanced subsonic propulsion systems - Volume 1: ANOPP evaluation and fan noise model improvement. Technical report, NASA Contractor Report 195480, 1996.

[6] J. Hough and D. Weir. Aircraft noise prediction program (ANOPP) - Fan noise prediction for small engines. Technical report, NASA, 1996. Contractor report CR-1398300.

[7] M. Heidmann and C. Feiler. Noise comparisons from full-scale tests at nasa lewis research center. Technical report, NASA, 1973. Technical Momerandum TM X-68289.

[8] C.S. Ventres, M.A. Teobold, and W.D. Mark. Turbofan noise generation. volume 1: Analysis. Technical report, NASA Report CR-167952, 1982.

[9] H.D. Meyer and E. Envia. Aeroacoustic analysis of turbofan noise generation. Technical report, NASA Report CR-4715, 1996.

[10] M. Nallasamy and E. Envia. Computation of rotor wake turbulence noise. *Journal of Sound and Vibration*, 282:649–678, 2005.

[11] D. Topol. Rotor wake/stator interaction noise - predicitions versus data. In *13th AIAA Aeroacoustics Conference*, Tallahassee, Florida, 1990. AIAA-90-3951.

[12] D. Philbrick and D. Topol. Development of a fan noise design system. part 1: system design and source modelling. In *15th AIAA Aeroacoustics Conference*, Long Beach, California, 1993. AIAA-93-4415.

[13] D. Topol. Development of a fan noise design system. part 2: far-field radiation and system evaluation. In *15th AIAA Aeroacoustics Conference*, Long Beach, California, 1993. AIAA-93-4416.

[14] D. Hanson. Coupled two-dimensional cascade theory for noise and unsteady aerodynamics of blade row interaction in turbofans. volume 1: theory development and parametric studies. Technical report, NASA, 1994. Contractor report 4506.

[15] D. Hanson. Turbulence / cascade interaction: spectra of inflow, cascade response, and noise. In *4th AIAA/CEAS Aeroacoustics Conference*, Toulouse, France, 1998. AIAA-98-2319.

[16] D. Hanson. Theory for broadband noise of rotor and stator cascades with inhomogeneous inflow turbulence including effects of lean and sweep. Technical report, NASA, 2001. Contractor report 2001-210762.

[17] S. Glegg. Broadband noise from ducted prop fans. In *15th AIAA Aeroacoustics Conference*, Long Beach, California, 1993. AIAA-93-4402.

[18] S. Glegg. Broadband fan noise generated by small scale turbulence. Technical report, NASA CR-207752, 1998.

[19] S. Glegg. The response of a swept blade row to a three-dimensional gust. *Journal of Sound and Vibration*, 227:29–64, 1999.

[20] B. Morin. Broadband fan noise prediction system for gas turbine engines. In *5th AIAA/CEAS Aeroacoustics Conference*, Seattle, Washington, 1999. AIAA-99-1889.

[21] R. Mani. Noise due to interaction of inlet turbulence with isolated stators and rotors. *Journal of Sound and Vibration*, 17:251–260, 1971.

[22] R. Mani. Isolated rotor noise due to inlet distortion or turbulence. Technical report, NASA, 1974. Contractor report CR-2479.

[23] R. Mani and K. Bekofske. Experimental and theoretical studies of subsonic fan noise. Technical report, NASA, 1976. Contractor report CR-2660.

[24] E.J. Kerschen and P.R. Gliebe. Noise caused by the interaction of a rotor with anisotropic turbulence. *AIAA Journal*, 19:717–723, 1981.

[25] P. Gliebe, R. Mani, H. Shin, B. Mitchell, G. Ashford, S. Salamah, and S. Connell. Aeroacoustic prediction codes. Technical report, NASA Report CR-2000-210244, 2000.

[26] D. Hanson. The importance of quadrupole sources in prediction of transonic tip speed propeller noise. *Journal of Sound and Vibration*, 62:19–38, 1979.

[27] D. Hanson. Helicoidal surface theory for harmonic noise of propellers in the far field. *AIAA Journal*, 18:1213–1220, 1980.

[28] D. Hanson. Noise of counter-rotation propellers. In *AIAA/NASA 9th Aeroacoustics Conference*, Williamsburg, Virginia, USA, 1984. AIAA-84-2305.

[29] E. Envia. An asymptotic theory of supersonic propeller noise. Technical report, NASA, 1992. Contractor report 191110.

[30] F. Farassat. Linear acoustic formulas for calculation of rotating blade noise. *AIAA Journal*, 19:1122–1130, 1980.

[31] F. Farassat. Prediction of advanced propeller noise in the time domain. *AIAA Journal*, 24:578–584, 1986.

[32] F. Farassat and K. Brentner. The acoustic analogy and the prediction of the noise of rotating blades. *Theoretical and Computational Fluid Dynamics*, 10:155–170, 1998.

[33] H. Atassi, A. Ali, O. Atassi, and I. Vinogradov. Scattering of incidence disturbances by an annular cascade in a swirling flow. *Journal of Fluid Mechanics*, 499:111–138, 2004.

[34] H. Atassi and I. Vinogradov. Modelling broadband fan noise and comparison with experiments. In *13 AIAA/CEAS Aeroacoustics Conference*, 2007. AIAA-2007-3691.

[35] M. Logue, H. Atassi, D. Topol, and J. Gilson. Aerodynamics and acoustics of a 3D annular cascade - comparison with a 2D linear cascade. In *16th AIAA/CEAS Aeroacoustics Conference*, 2010.

[36] D. Stephens and S. Morris. Sound generation by a rotor interacting with a casing turbulent boundary layer. *AIAA Journal*, 47:2698–2708, 2009.

[37] S. Moreau and M. Roger. Competing broadband noise mechanisms in low-speed axial fans. *AIAA Journal*, 45:48–57, 2007.

[38] M. Roger and S. Moreau. Extensions and limitations of analytical airfoil broadband noise models. *International Journal of Aeroacoustics*, 9:273–306, 2010.

[39] Y. Rozenberg, S. Moreau, M. Henner, and S. Morris. Fan trailing-edge noise prediction using rans simulations. In *16th AIAA/CEAS Aeroacoustics Conference*, Stockholm, Sweden, 2010. AIAA-2010-3720.

[40] H. Posson and M. Roger. Experimental validation of a cascade response function. *AIAA Journal*, 49:1907–1918, 2011.

[41] A. Carazo, M. Roger, and M. Omais. Analytical predicition of wake-interaction noise in counter-rotation open rotors. In *17th AIAA/CEAS Aeroacoustics Conference*, Portland, Oregon, 2011. AIAA-2011-2758.

[42] A. Pagano, M. Barbarino, D. Casalino, and L. Federico. Tonald and broadband noise calculations for aeroacoustic optimization of propeller blades in a pusher configuration. In *15th AIAA/CEAS Aeroacoustics Conference*, Miami, Florida, 2009. AIAA-2009-3138.

[43] B.G. Marinus, M. Roger, R.A. Van den Braembussche, and W. Bosschaerts. Mutlidisciplinary optimization of propeller blades: focus on the aeroacoustic results. In *17th AIAA/CEAS Aeroacoustics Conference*, 2011.

[44] S. Magne, S. Moreau, A. Berry, and Marlène Sanjosé. Aeroacoustic prediction of an automotive cooling fan. *Journal of the Canadian Acoustical Association*, 39, 2011.

[45] A. Parry. *Theoretical prediction of counter-rotating propeller noise*. PhD thesis, University of Leeds, 1988.

[46] A. Parry and D. Crighton. Asymptotic theory of propeller noise - part i : subsonic single-rotation propeller. *AIAA Journal*, 27:1184–1190, 1989.

[47] N. Peake and D. Crighton. An asymptotic theory of near-field propeller acoustics. *Journal of Fluid Mechanics*, 232:285–301, 1991.

[48] N. Peake and D. Crighton. Lighthill quadrupole radiation in supersonic propeller acouctics. *Journal of Fluid Mechanics*, 223:366–382, 1991.

[49] C. Morfey. Sound generation in subsonic turbomachinery. *ASME Journal of Basic Engineering*, 92:450–458, 1970.

[50] C. Morfey. The acoustics of the axial flow machines. *Journal of Sound and Vibration*, 22:445–466, 1972.

[51] C. Morfey. Rotating blades and aerodynamic sound. *Journal of Sound and Vibration*, 28:587–617, 1973.

[52] P. Joseph, K. Britchford, and P. Loheac. A model of fan broadband noise due to rotor-stator interaction noise. In *5th European Conference on Turbomachinery Fluid Dynamics and Thermodynamics*, Prague, Czech Republic, 2003.

[53] Q. Zhou and P. Joseph. A frequency domain method for the prediction of broadband noise from an open rotor. In *10th AIAA/CEAS Aeroacoustics Conference*, 2004. AIAA-2004-3038.

[54] V. Blandeau, P. Joseph, and Tester B. Broadband noise prediction from rotor-wake interaction in contra-rotating propfans. In *15th AIAA/CEAS Aeroacoustics Conference*, Miami, Florida, 2009. AIAA-2009-3137.

[55] V. Blandeau and Ph. Joseph. On the validity of amiet's model for propeller trailing-edge noise. In *16th AIAA/CEAS Aeroacoustics Conference*, Stockholm, Sweden, 2010. AIAA-2010-3797.

[56] M. Kingan. Open rotor broadband interaction noise. In *18th AIAA/CEAS Aeroacoustics Conference*, Colorado Springs, Colorado, 2012. AIAA-2012-2304.

[57] J. Schulten. Frequency-domain method for the computation of propeller acoustics. *AIAA Journal*, 26:1027–1035, 1988.

[58] H. Brouwer. A lifting line model for propeller noise. In *12th AIAA7CEAS Aeroacoustics Conference*, San Antonio, Texas, 1989. AIAA-89-1079.

[59] K. Heinig. *Ein Beitrag zur Berechnung der Schallemission mehrstufiger Verdichter und Turbinen von Flugzeugtriebwerken.* PhD thesis, Technical University of Berlin, 1994.

[60] A. Moreau and L. Enghardt. A first step towards a parametric model for fan broadband and tonal noise. In *Proceedings of the DAGA Conference, Dresden, Germany, 2008*, 2008.

[61] A. Moreau and L. Enghardt. Improvement of a parametric model for fan broadband and tonal noise. In *Proceedings of the Acoustics08 Conference, Paris, France*, 2008.

[62] S. Guérin, A. Moreau, and U. Tapken. Relation between source models and acouctics duct modes. In *16th AIAA/CEAS Aeroacoustics Conference*, Miami, Florida, 2009. AIAA-2009-3364.

[63] A. Moreau, S. Guérin, and S. Busse. A method based on the ray structure of acoustic modes for predicting the liner performance in annular ducts with flow. In *DAGA / NAG Conference*, Rotterdam, Netherlands, 2009.

[64] S. Guérin and A. Moreau. Accounting for sweep and lean in the design-to-noise of rotor-stator stages. In *Proceedings of the DAGA Conference, Berlin, Germany*, 2010.

[65] A. Moreau and S. Guérin. Development and application of a new procedure for fan noise prediction. In *16th AIAA/CEAS Aeroacoustics Conference*, Stockholm, Sweden, 2010. AIAA-2010-4034.

[66] A. Moreau and S. Guérin. Similarities of the free-field and in-duct formulations in rotor noise problems. In *17th AIAA/CEAS Aeroacoustics Conference*, Portland, Oregon, 2011. AIAA-2011-2759.

[67] A. Moreau, S. Guérin, L. Enghardt, A.L. Le Denmat, E. Nicke, S. Weber, S. Diehl, and P. Koch. The new nwb ventilator: a practical case of design-to-noise. In *18th AIAA/CEAS Aeroacoustics Conference*, Colorado Springs, Colorado, 2012. AIAA-2012-2178.

[68] A. Moreau and S. Oertwig. Measurements compared to analytical prediction of the sound emitted by a high-speed fan stage. In *19th AIAA/CEAS Aeroacoustics Conference*, Berlin, Germany, 2013. AIAA-2013-2047.

[69] S. Guérin, A. Moreau, C. Menzel, and C. Weckmüller. Open-rotor noise prediction with a RANS-informed analytical method. In *18th AIAA/CEAS Aeroacoustics Conference*, Colorado Springs, Colorado, 2012. AIAA-2012-2303.

[70] N. Cumpsty and E. Greitzer. Ideas and methods of turbomachinery aerodynamics: a historical view. *Journal of Propulsion and Power*, 20:15–26, 2004.

[71] W. Swan. A practical method of predicting transonic-compressor performance. *Journal of Engineering for Power*, 83:322–330, 1961.

[72] H. Grieb, G. Schill, and R.Gumucio. A semi-empirical method for the determination of multistage axial compressor efficiency. In *ASME Paper No 75-GT-11*, 1975.

[73] C.C. Koch and L.H. Smith. Loss sources and magnitudes in axial-flow compressors. *Journal of Engineering for Power*, pages 411–422, 1976.

[74] D. Miller and D. Wasdell. Off-design prediction of compressor blade losses. In *Institution of Mechanical Engineers Conference Proceedings C423/028*, pages 249–260, 1987.

[75] P. Wright and D. Miller. An improved compressor performance prediction model. In *Institution of Mechanical Engineers Conference Proceedings C279/87*, 1991.

[76] S. Lieblein. Loss and stall analysis of compressor cascades. *Journal of Basic Engineering*, pages 387–400, 1959.

[77] J.D. Denton. Loss mechanisms in turbomachines. *Journal of Turbomachinery*, 115:621–656, 1993.

[78] F. Weinig. *Die Stroemung um die Schaufeln von Turbomaschinen: Beitrag zur Theorie axial durchstroemter Turbomaschinen*. Barth, Leipzig, 1935.

[79] N. Scholz. *Aerodynamik der Schaufelgitter - Band I*. Verlag G. Braun Karlsruhe, 1965.

[80] A.D.S. Carter and H.P. Hughes. A theoretical investigation into the effect of profile shape on the performance of aerofoils in cascade. Technical report, Britisch Aeronautical Research Council, 1946.

[81] A.D.S. Carter. The low speed performance of related aerofoils in cascades. Technical report, Britisch N.G.T.E. Report n R.55, 1949.

[82] S. Lieblein. Experimental flow in two-dimensional cascades. Technical report, NASA SP-36, 1956.

[83] S. Lieblein. Incidence and deviation-angle correlations for compressor cascades. *Journal of Basic Engineering*, 82:575–584, 1960.

[84] M. Cetin, A. Uecer, C. Hirsch, and G. Serovy. Application of modified loss and deviation correlations to transonic axial compressors. Technical report, AGARD Report No.745, 1987.

[85] B. Lakshminarayana. *Fluid dynamics and heat transfer of turbomachinery*. John Wiley & Sons, 1996.

[86] N.A. Cumpsty. *Compressor Aerodynamics*. Longman Scientific & Technical, Harlow, England, 1989.

[87] H. Grieb. *Verdichter für Turbo-Flugtriebwerke*. Springer Verlag, 2009.

[88] C. Freeman and N. Cumpsty. Method for the prediction of supersonic compressor blade performance. *Journal of Propulsion*, 8:199–208, 1992.

[89] P. Levine. Two-dimensional inflow conditions for a supersonic compressor with curved blades. *Journal of Applied Mechanics*, pages 165–169, 1957.

[90] J. E. Cahill. Identification and evaluation of loss and deviation models for use in transonic compressor stage performance prediction. Master's thesis, Virginia Tech, 1997.

[91] S. Lieblein, F.C. Schwenk, and R.L. Broderick. Diffusion factor for estimating losses and limiting blade loadings in axial-flow.compressor blade elements. Technical report, NACA RM E53D01, 1953.

[92] E. Greitzer. Review - axial compressor stall phenomena. *Journal of Fluids Engineering*, 102:134–151, 1980.

[93] I. Day. Axial-compressor performance during surge. *Journal of Propulsion and Power*, 10:329–336, 1994.

[94] H. Schlichting. *Boundary-layer theory*. McGraw-Hill, 6th edition edition, 1968.

[95] W. Koenig, D. Henneke, and L. Fottner. Improved blade profile loss and deviation angle models for advanced transonic compressor bladings: Part i - a model for subsonic flow. *Journal of Turbomachinery*, 118:73–87, 1996.

[96] G. Miller, G. Lewis, and M. Hartmann. Shock losses in transonic compressor blade rows. *Journal of Engineering for Power*, pages 235–242, 1961.

[97] A.J. Wennerstrom. Low aspect ratio axial-flow compressors: why and what it means. *Journal of Turbomachinery*, 111:357–365, 1989.

[98] C.C. Koch. Stalling pressure rise capability of axial-flow compressor stages. *Journal of Engineering for Power*, 103:645–655, 1981.

[99] S. Smith. A simple correlation of turbine efficiency. *Journal of the Royal Aeronautical Society*, 69:467, 1965.

[100] B. Kaplan, E. Nicke, and C. Voss. Design of a highly efficient low-noise fan for ultra-high bypass engines. In *ASME Paper No GT2006-90363*, 2006.

[101] D. Goerke, A.L. Le Denmat, T. Schmidt, F. Kocian, and E. Nicke. Aerodynamic and mechanical optimization of cf/peek blades of a counter-rotating fan. *ASME Turbo Expo 2012*, 7:21–33, 2012. GT-2012-68797.

[102] G. Bloch. *Flow losses in supersonic compressor cascades*. PhD thesis, Virginia Polytechnic Institute and State University, 1996.

[103] A.-L. Aulich, D. Görke, M. Blocher, E. Nicke, and F. Kocian. Multidisciplinary automated optimization strategy on a counter-rotating fan. In *ASME Turbo Expo 2013*, San Antonio, Texas, 2013. GT2013-94259.

[104] J.D. Mattingly, W.H. Heiser, and D.T. Pratt. *Aircraft engine design - 2nd edition*. AIAA Education Series, 2002.

[105] T. A. Ward. *Aerospace propulsion systems*. Wiley, 2010.

[106] N. Kemp and W. Sears. Aerodynamic interference between moving blade rows. *Journal of the Aeronautical Sciences*, 20:585–597, 1953.

[107] G.F. Pickett. The prediction of the spectral content of combination tone noise. In *AIAA/SAE 7th Propulsion Joint Specialist Conference*, Salt lake City, Utah, 1971. AIAA-71-730.

[108] D. Hanson. Near-field frequency-domain theory for propeller noise. *AIAA Journal*, 23:499–504, 1985.

[109] C.L. Morfey and M. J. Fischer. Shock-wave radiation from a supersonic ducted rotor. *Aeronautical Journal of the Royal Aeronautical Society*, 74:579–585, 1970.

[110] A. Carazo. *Semi-analytical prediction of wake-interaction noise in coutner-rotating open rotors*. PhD thesis, Ecole Centrale de Lyon, 2012.

[111] R. Raj and B. Lakshminarayana. Characteristics of the wake behind a cascade of arifoils. *Journal of Fluid Mechanics*, 61:707–730, 1973.

[112] A. Ravindranath and B. Lakshminarayana. Mean velocity and decay characteristics of the near and far wake of a compressor rotor blade of moderate loading. *Journal of Engineering for Power*, 102:535–548, 1980.

[113] B.D. Reynolds. Characteristics of the wake of a lightly loaded compressor or fan rotor. In *AIAA 15th Conference*, Washington D.C., 1979. AIAA-79-0550.

[114] M. Roger. Sur l'utilisationd'un modle de sillage pour le calcul du bruit d'interaction rotor-stator. *Acustica*, 80:238–246, 1994.

[115] A. Silverstein, S. Katzoff, and W.K. Bullivant. Downwash and wake behind plain and flapped airfoils. Technical report, NACA Report n651, 1939.

[116] I. Wygnanski, F. Champagne, and B. Marasli. On the large-scale structures in two-dimensional, small-deficit, turbulent wakes. *Journal of Fluid Mechanics*, 168:31–71, 1986.

[117] U. Ganz, P. Joppa, J. Patten, and D. Scharpf. Boeing 18-inch fan rig broadband noise test. Technical report, NASA Report CR-1998-208704, 1998.

[118] M.R. Head. Entrainment in the turbulent boundary layer. Technical report, British Aeronautical Research Council Report n3152, 1960.

[119] J.E. Green. Application of head's entrainment method to the prediction of turbulent boundary layers and wakes in compressible flow. Technical report, British Aeronautical Research Council Report n3788, 1976.

[120] A. A. Townsend. *The structure of turbulent shear flows*. Cambridge University Press, 1956.

[121] A. Lyrio. *An integral method for the computation of steady and unsteady turbulent boundary layer flows, including the transitory stall regime in diffusers*. PhD thesis, Stanford University, 1981.

[122] A. Veldman. A simple interaction law for viscous-inviscid interaction. *Journal of Engineering Mathematics*, 65:367–383, 2009.

[123] J. Prato and B. Lakshminarayana. Investigation of compressor rotor wake structure at peak pressure rise coefficient and effects of loading. *Journal of Turbomachinery*, 115:487–500, 1993.

[124] S. Glegg, E. Kawashima, F. Lachowski, W. Devenport, and N. Alexander. Inflow distortion noise with non-axisymmetric flow. In *19th AIAA/CEAS Aeroacoustics Conference*, Berlin, Germany, 2013. AIAA-2013-2286.

[125] R. Amiet. Acoustic radiation fro an airfoil in a turbulent stream. *Journal of Sound and Vibration*, 41:407–420, 1975.

[126] B. Reynolds and B. Lakshminarayana. Characteristics of lightly loaded fan rotor blade wakes. Technical report, NASA Report CR-3188, 1979.

[127] A. Moreau and L. Enghardt. Ranking of fan broadband noise sources based on an experimental parametric study. In *15th AIAA/CEAS Aeroacoustics Conference*, Miami, Florida, 2009. AIAA-2009-3222.

[128] V. Jurdic, P. Joseph, and J. Antoni. Investigation of rotor turbulence wakes through cyclostationary spectral analysis. *AIAA Journal*, 47:2022–2030, 2007.

[129] T.R. Camp and H.W. Shin. Turbulence intensity and length scale measurements in multistage compressors. *Journal of Turbomachinery*, 117:38–46, 1995.

[130] W. Willmarth and F. Roos. Resolution and structure of the wall pressure field beneath a turbulent boundary layer. *Journal of Fluid Mechanics*, 22:81–94, 1965.

[131] M. Goody. Empirical spectral model of surface pressure fluctuations. *AIAA Journal*, 42:1788–1794, 2004.

[132] R. Amiet. Noise due to turbulent flow past a trailing edge. *Journal of Sound and Vibration*, 47:387–393, 1976.

[133] G. Corcos. The structure of the turbulent pressure field in boundary-layer flows. *Journal of Fluid Mechanics*, 18:353–378, 1964.

[134] J. Remmler, J. Christophe, J. Anthoine, and S. Moreau. Computation of wall pressure spectra from steady flow data for noise prediction. *AIAA Journal*, 48:1997–2007, 2010.

[135] S. Glegg, B. Morin, O. Atassi, and R. Reba. Using rans calculations of turbulent kinetic energy to provide predictions of trailing edge noise. In *14th AIAA/CEAS Aeroacoustics Conference*, Vancouver, Canada, 2008.

[136] W.R. Sears. Some aspects of non-stationary airfoil theory and its practical application. *Journal of the Aeronautical Sciences*, 8:104–108, 1941.

[137] M. Goldstein. *Aeroacoustics*. McGraw-Hill International Book Company, New York, 1976.

[138] M. Goldstein and H. Atassi. A complete second-order theory for the unsteady flow about an airfoil due to a periodic gust. *Journal of Fluid Mechanics*, 74:741–765, 1976.

[139] E. Kerschen, C. Tsai, and M. Myers. *Influence of airfoil shape and incidence angle on high-frequency gust interaction noise*, chapter VI, pages 765–782. Springer New York, 1993.

[140] J.M.R. Graham. Similarity rules for thin aerofoils in non-stationary subsonic flows. *Journal of Fluid Mechanics*, 43:753–766, 1970.

[141] J. Adamczyk. Passage of a swept airfoil through an oblique gust. *Journal of Aircraft*, 11:281–287, 1974.

[142] N. Kemp and G. Homicz. Approximate unsteady thin-airfoil theory for subsonic flow. *AIAA Journal*, 14:1083–1089, 1976.

[143] M. Lighthill. On sound generated aerodynamically - I. General theory. *Proceedings of the Royal Society of London. Series A*, 211:564–587, 1952.

[144] M. Goldstein. Unified approach to aerodynamic sound generation in the presence of solid boundaries. *Journal of the Acoustical Society of America*, 56:497–509, 1974.

[145] L. Gutin. On the sound field of a rotating propeller. *Journal of Technical Physics*, 12:76–83, 1936.

[146] N. Curle. The influence of solid boundaries upon aerodynamic sound. *Proceedings of the Royal Society of London. Series A*, 231:505–514, 1955.

[147] J.E. Ffowcs-Willams and D.L. Hawkings. Theory relating to the noise of rotating machinery. *Journal of Sound and Vibration*, 10:10–21, 1969.

[148] D. Hawkings. Multiple tone generation by transonic compressor. *Journal of Sound and Vibration*, 17:241–250, 1971.

[149] C. Lowis and P. Joseph. Determining the strength of rotating broadband sources in ducts by inverse methods. *Journal of Sound and Vibration*, 295:614–632, 2006.

[150] R. Mani, P. Gliebe, and P. Ho. Fan broadband noise model development. Technical report, NASA CR-198457, 1997.

[151] H. Atassi, S. Subramaniam, and J. Scott. Acoustic radiation from lifting airfoils in compressible subsonic flow. In *13th AIAA Aeroacoustics Conference*, Tallahassee, Florida, 1990. AIAA-90-3911.

[152] V. Wells and A. Han. Acoustics of a moving source in a moving medium with application to propeller noise. *Journal of Sound and Vibration*, 184:651–663, 1995.

[153] C. Weckmüller, S. Guérin, J. Wellner, and U. Michel. Ffowcs-williams & hawkings formulation for the convective wave equation and permeable data surface. In *16th AIAA/CEAS Aeroacoustics Conference*, Stockholm, Sweden, 2010. AIAA 2010-3710.

[154] S. Rienstra and A. Hirschberg. *An introduction to acoustics*. Lecture notes, Eindhoven University of Technology, 2006.

[155] C. Morfey. Sound transmission and generation in ducts with flow. *Journal of Sound and Vibration*, 14:37–55, 1971.

[156] F. Holste. *Ermittlung der aerodynamischen Laermquellen und Berechnung des abgestrahlten Schallfeldes mittels der im Nahfeld gemessenen Druckschwankungen am Beispiel eines Triebwerksmodells*. PhD thesis, Technical University of Berlin, 1995.

[157] C. Chapman. Sound radiation from a cylindrical dcut. part 1: ray structure of the duct modes and of the external field. *Journal of Fluid Mechanics*, 281:293–311, 1994.

[158] E. Rice, M. Heidmann, and T. Sofrin. Modal propagation angles in a cylindrical duct with flow and their relation to sound radiation. In *17th Aerospace Sciences Meeting*, New Orleans, Louisiana, 1979. AIAA-79-0183.

[159] C. Morfey. Acoustic energy in non-uniform flows. *Journal of Sound and Vibration*, 14:159–170, 1971.

[160] D. Blokhintsev. The propagation of sound in an inhomogeneous and moving medium. *Journal of the Acoustical Society of America*, 18:322–328, 1946.

[161] D. Blokhintsev. Acoustics of a nonhomogeneous moving medium. Technical report, NACA TM-1399, 1956.

[162] I. Garrick and C. Watkins. A theoretical study of the effect of forward speed on the free-space sound-pressure field around propellers. Technical report, NACA Technical Note 3018, 1953.

[163] C. Cantrell. *Modern Mathematical Methods for Physicists and Engineers*. Cambridge University Press, 2000.

[164] S. Rienstra. An analytic green's function for a lined circular duct containing uniform mean flow. In *11th AIAA/CEAS Aeroacoustics Conference*, Monterey, California, 2005. AIAA-2005-3020.

[165] J. Tyler and T. Sofrin. Axial flow compressor noise studies. *Transactions of the Society of Automotive Engineers*, 70:309–332, 1962.

[166] C. Tam and L. Auriault. Jet mixing noise from fine-scale turbulence. *AIAA Journal*, 37:145–153, 1999.

[167] P. Morse and K. Ingard. *Theoretical acoustics*. Princeton University Press, 1986.

[168] H. Atassi and M. Logue. Fan broadband noise in anisotropic turbulence. In *15th AIAA/CEAS Aeroacoutics Conference*, Miami, Florida, 2009. AIAA-2009-3148.

[169] E. Envia and M. Nallasamy. Design selection and analysis of swept and leaned stator concept. *Journal of Sound and Vibration*, 228:793–836, 1999.

[170] D. Crighton and A. Parry. Asymptotic theory of propeller noise - part ii : supersonic single-rotation propeller. *AIAA Journal*, 29:2031–2037, 1991.

[171] D. Hanson. Influence of propeller design parameters on far-field harmonic noise in forward flight. *AIAA Journal*, 18:1313–1319, 1980.

[172] B. Janardan and P. Gliebe. Acoustic characteristics of counter-rotating fans from model scale tests. In *AIAA 12th Aeroacoustics Conference*, San Antonio, Texas, 1989.

[173] P. Gliebe. Aeroacoustics in turbomachines and propellers - future research needs. In *6th International Symposium on Unsteady Arodynamics, Aeroacoustics and Aeroelasticity of turbomachines and propellers*, University of Notre Dame, Indiana, 1991.

[174] E. Envia and J. Coupland. Fan Broadband Noise Workshop - AA-39 Panel Session in 20th AIAA/CEAS Aeroacoustics Conference - URL: www.oai.org/aeroacoustics/FBNWorkshop, 2014.

[175] R. Woodward. Comparison of far-field noise for three significantly different model turbofans. Technical report, NASA, 2008. NASA/TM-2008-215136.

[176] M. Lighthill. On sound generated aerodynamically - II. Turbulence as a source of sound. *Proceedings of the Royal Society of London. Series A*, 222:1–32, 1954.

[177] M. Fisher, P. Lush, and M. Harper Bourne. Jet noise. *Journal of Sound and Vibration*, 28:563–585, 1973.

[178] M. Harper-Bourne and M. Fisher. The noise from shock waves in supersonic jets. In *AGARD Conference of Noise Mechanisms*, 1973.

[179] E. Brambley. Review of acoustic liner models with flow. In *Acoustics2012 Conference*, Nantes, France, 2012.

[180] S. Rienstra. Impedance models in time domain, including the extended helmholtz resonator model. In *12th AIAA/CEAS Aeroacoustics Conference*, Cambridge, Massachusetts, 2006. AIAA-2006-2686.

[181] S. Smith. Discrete-frequency sound generation in axial-flow turbomachines. Technical report, Aeronautical Research Council, 1973. Report n 3709.

[182] S. Kaji and T. Okazaki. Propagation of sound waves through a blade row. i. and ii. *Journal of Sound and Vibration*, 11:339–375, 1970.

[183] G. Jenkins, P. Joseph, and C. Powles. Multimode blockage due to rotors and apllication to turbomachinery broadband noise. In *18th AIAA/CEAS Aeroacoustics Conference*, Colorado Springs, Colorado, 2012. AIAA-2012-2130.

[184] C. Morfey. A note on the radiation efficiency of acoustic duct modes. *Journal of Sound and Vibration*, 9:367–372, 1969.

[185] G. Homicz and J. Lordi. A note on the radiative directivity patterns of duct acoustic modes. *Journal of Sound and Vibration*, 41:283–290, 1975.

[186] V. Blandeau, P. Joseph, G. Jenkins, and C. Powles. Comparison of sound power radiation from isolated airfoils and cascades in a turbulent flow. *Journal of the Acoustical Society of America*, 129:3521–3530, 2011.

[187] P. Gliebe, P. Ho, and R. Mani. Uhb engine fan broadband noise reduction study. Technical report, NASA Report under Contract NAS3 26617, 1995.

[188] A. Moreau and S. Guérin. The impact of low-speed fan design on noise: an exploratory study. *Journal of Turbomachinery*, 138, 2016.

[189] A. Oyama and M.-S. Liou. Multiobjective optimization of a multi-stage compressor using evolutionary algorithm. In *AIAA Conference*, 2002. AIAA-2002-3535.

[190] J. Sorokes. Range versus effficiency - striking the proper balance. In *Proceedings of the 41st Turbomachinery Symposium*, Houston, Texas, 2012.

[191] N.A. Cumpsty. Preparing for the future: reducing gas turbine environmental impact. In *ASME Turbo Expo 2009*, Orlando, Florida, USA, 2019. GT2009-60367.

[192] P. Gliebe and A. Janardan. Ultra-high bypass engine aeroacoustic study. Technical report, NASA, 1993. NASA/CR-2003-212525.

[193] D. Daggett, S. Brown, and R. Kawai. Ultra-efficient engine diameter study. Technical report, NASA Report CR-2003-212309, 2003.

[194] M. Guynn, J. Berton, K. Fisher, W. Haller, M. Tong, and D. Thurman. Refined exploration of turbofan design options for an advanced single-aisle transport. Technical report, NASA Technical Memorandum TM-2011-216883, 2011.

[195] D. Crichton, L. Xu, and C. Hall. Preliminary fan design for a silent aircraft. *Journal of Turbomachinery*, 129:184–191, 2007.

[196] D. Crichton. *Fan design and operation for ultra low noise*. PhD thesis, Cambridge, 2007.

[197] R. Woodward, C. Hughes, R. Jeracki, and C. Miller. Fan noise source diagnostic test - far-field acoustic results. In *8th AIAA/CEAS Aeroacoustics Conference*, Breckenridge, Colorado, 2002. AIAA-2002-2427.

[198] G. Podboy, M. Krupar, C. Hughes, and R. Woodward. Fan noise Source Diagnostic Test - LDV measured flow field results. In *8th AIAA/CEAS Aeroacoustics Conference*, Breckenridge, Colorado, 2002. AIAA-2002-2431.

[199] D. Elliott and J. Dittmar. Some acoustic results from the NASA / Pratt and Whitney Advanced Ducted Propulsor model. In *38th Aerospace Sciences Meeting and Exhibit*, Reno, Nevada, 2000. AIAA-2000-0351.

[200] L. Heidelberg and D. Elliott. A comparison of measured tones for two low noise propulsion fans. In *6th AIAA/CEAS Aeroacoustics Conference*, Hawaii, 2000. AIAA-2000-1989.

[201] D. Topol, C. Ingram, M. Jarkin, C. Roche, and R. Thulin. Advanced subsonic technology (AST) 22-inch low noise research fan rig prelimiary design of ADP-type Fan3. Technical report, NASA Report CR-2004-212718, 2004.

[202] C. Bewick, M. Adams, J. Schwaller, and L. Xu. Noise and aerodynamic design test of a low tip speed fan. In *7th AIAA/CEAS Aeroacoutics Conference*, Maastricht, the Netherlands, 2001. AIAA-2001-2268.